Skolkovo Institute of Science and Technology

OPTICAL AND MECHANICAL PROPERTIES OF DIATOM STRUCTURES

Doctoral Thesis

by

JULIJANA CVJETINOVIC

DOCTORAL PROGRAM IN PHYSICS

Supervisor
Professor Dmitry Gorin
Co-advisor
Professor Alexander Korsunsky

Moscow - 2023

I hereby declare that the work presented in this thesis was carried out by myself at Skolkovo Institute of Science and Technology, Moscow, except where due acknowledgement is made, and has not been submitted for any other degree.

Candidate (Julijana Cvjetinovic)
Supervisor (Prof. Dmitry Gorin)
Co-advisor (Prof. Alexander Korsunsky)

Abstract

Nanostructured natural objects featuring advanced properties serve as an endless source of inspiration for the development of new materials and devices. A rich gallery of such objects are the skeletons of diatom algae – Nature's glass (silica) lace. The neat slender structures resemble woven lace that combines elegance with strength and durability, and provoke the effort to explore the organization and properties of the objects created and refined by nature over millions of years of evolution.

Diatoms have gathered considerable attention due to their ecological significance and their potential as valuable resources for sustainable biofuels and high-value commodities, including pigments, vitamins, and omega fatty acids. characteristics make diatoms an intriguing subject of research and emphasize the need to closely monitor their growth to ensure optimal biomass production. While microscopy-based cell counting remains a widely utilized technique for monitoring algal growth, its effectiveness diminishes with the rapid division of notably small cell species, particularly after several days of culture. Furthermore, benthic species have a propensity for prolific mucus secretion, posing a challenge in accurately enumerating cells within microvolumes. Given this limitation in conventional cell counting, especially during long-term cultivation, the first part of this thesis turns to explore the potential of optical methods for monitoring the growth of diverse freshwater and marine diatoms in suspension. Fluorescence and photoacoustic signals displayed by diatom species exhibit growth phase-dependent patterns, which have been confirmed using spectroscopic methods. These methods provide rapid, non-invasive insights into the physiological state of the algae, without intricate preparatory procedures and mitigating the risk of introducing contaminants into the medium. The optical setup with a central

wavelength of 505 nm was fabricated to monitor changes in diatom concentrations. Various diatom strains characterized by diverse morphologies, sizes, and volumes were examined, revealing a linear correlation between the measured transmission and concentration, suggesting its applicability for monitoring diatom growth in bioreactors.

Beyond their ecological importance and biomass production, diatom unique structure serves as a wellspring of inspiration for the development of advanced hybrid nanostructure designs mimicking multi-scale porosity to achieve outstanding mechanical and optical properties. Consequently, the second part of the thesis aims to gain insights into the mechanical behavior of diatom cleaned frustules and living cells under both static and dynamic loading conditions, which holds relevance not only for foundational research, but also for the potential application of these systems as functional materials in novel devices. The mechanical characteristics of both cleaned *Coscinodiscus oculus-iridis* frustules and living cells were examined using atomic force microscopy (AFM) and *in situ* scanning electron microscopy (SEM) nanoindentation techniques. The Young's modulus of wet diatom cells showed a notably higher value compared to cleaned frustules, attributed to the influence of silica hydration and support from the organic material. Moreover, the thin uppermost layer, characterized by an array of nanometer-sized pores, resulted in a lower Young's modulus value when compared with the thicker inner layer. Under cyclic loading, it was observed that the compliance of the silica frustule increased with an increasing number of cycles, without experiencing complete rupture. The relationship between structure and mechanical properties directly influences the vibrational behavior of the frustule, acting as a complex micrometer-sized mechanical system. This study marks the first experimental verification of the numerically calculated resonance frequencies using AFM method.

By studying the optical and mechanical properties of diatoms in tandem, a holistic view of their interdependent structure-property relationships can provide insights into materials design. Therefore, another important aspect of this research is to investigate the role of the hierarchical design in determining the optical properties of diatoms. The periodic structure of *Coscinodiscus oculus-iridis* frustule, studied by Fourier modal method, enhances light transmittance and light intensity in the range of λ = 400–500 nm, which corresponds to the optimal absorption range of chlorophyll *a*, a key photosynthetic pigment. The simulation reveals distinct interference patterns of light intensity beneath the frustule, aiding in efficient light utilization by chloroplasts.

Through the functionalization, diatom properties and the range of applications can be further upgraded and expanded. In the third section of this thesis, a novel approach involving the combination of freezing-induced loading and layer-by-layer methods has been employed to functionalize the surface of diatomite with gold nanoparticles. The resulting hybrid structure was evaluated as a Surface-Enhanced Raman Spectroscopy (SERS) platform. This combined method led to an amplified signal from Rhodamine 6G, showcasing its potential utility as an effective SERS platform with implications for sensing applications.

Lessons from Nature's nanostructuring of diatoms open up pathways to new generations of nano- and microdevices for electronic, electromechanical, photonic, liquid, energy storage, and other applications.

Thesis related publications

1. **Cvjetinovic J**, Luchkin S, Statnik E, Davidovich N, Somov P, Salimon A, Korsunsky A, Gorin D. Revealing the static and dynamic nanomechanical properties of diatom frustules—Nature's glass lace. *Scientific Reports*. 2023; 13, 5518: 1-12.

(The main and corresponding author, IF 4.996, Q1)

2. **Cvjetinovic J**, Salimon I, Novoselova M, Sapozhnikov Ph, Shirshin E, Yashchenok A, Kalinina O, Korsunsky A, Gorin D. Photoacoustic and fluorescence lifetime imaging of diatoms. *Photoacoustics.* 2020; 18; 100171.

(The main and corresponding author, IF 9.656, Q1)

3. **Cvjetinovic J**, Merdalimova A, Kirsanova M, Somov P, Salimon A, Korsunsky A, Gorin D. SERS Platform Based on Diatomite Modified by Gold Nanoparticles Using a Combination of Layer-by-Layer Assembly and Freezing-Induced Loading Method. *Physical Chemistry Chemical Physics*. 2022; 24: 8901-8912.

(The main and corresponding author, IF 3.945, Q1)

4. **Cvjetinovic J**, Perkov S, Kurochkin M, Sergeev I, German S, Bedoshvili Ye, Davidovich N, Korsunsky A, Gorin D. Concentration dependence of optical transmission and extinction of different diatom cultures. *Journal of Biomedical Photonics and Engineering*. 2023; 9(1):1-9.

(The main and corresponding author, IF 1.4, Q2)

5. **Cvjetinovic J**, Bedoshvili Ye, Nozdriukhin D, Salimon A, Korsunsky A, Gorin D. Photonic tools for evaluating the growth of diatom colonies during long-term batch cultivation. *Journal of Physics: Conference Series*. 2022; 2172; 012011.

(The main and corresponding author)

6. **Cvjetinovic J**, Nozdriukhin D, Bedoshvili Ye, Salimon A, Korsunsky A, Gorin A. Assessment of diatom growth using fluorescence imaging. *Journal of Physics: Conference Series*. 2021; 1984; 012017.

(The main and corresponding author)

7. **Cvjetinovic J**, Bedoshvili Ye, Nozdriukhin D, Efimova O, Salimon A, Volokitina N, Korsunsky A, Gorin D. In situ fluorescence/photoacoustic monitoring of diatom algae. *SPIE Proceedings* XVIII; 2021; 11641; 116410G.

(The main and corresponding author)

8. Aggrey P, Nartey M, Kan Y, **Cvjetinovic J**, Andrews A, Salimon A, Dragnevski K, Korsunsky A. On the diatomite-based nanostructure-preserving material synthesis for energy applications. *RSC Advances*, 2021; 11; 31884-31922.

(Wrote several sections of the review article, IF 4.036, Q1)

9. Korsunsky A, Bedoshvili Ye, **Cvjetinovic J**, Aggrey P, Dragnevski K, Gorin D, Salimon A, Likhoshway Ye. Siliceous diatom frustules - a smart nanotechnology platform. *Materials today: Proceedings*. 2020; 33(4):2032-2040.

(Wrote several sections of the review article, IF 1.46, Q2)

10. **Cvjetinovic J**, Salimon A, Novoselova M, Sapozhnikov Ph, Kalinina O, Korsunsky A, Gorin D. Photoacoustic visualization of diatom algae. *Limnology and Freshwater Biology*. 2020; 4.

(The main and corresponding author)

11. Salimon A, Sapozhnikov Ph, Everaerts J, Kalinina O, Besnard C, Papadaki C, **Cvjetinovic J**, Statnik E, Kan Y, Aggrey P, Kalyaev V, Lukashova M, Somov P, Korsunsky A. A Mini-Atlas of diatom frustule electron microscopy images at different magnifications. *Materials Today: Proceedings*. 2020; 33(4):1924-1933.

(Participated in collecting SEM images, IF 1.46, Q2)

12. Sapozhnikov Ph, Salimon A, Korsunsky A, Kalinina O, Senatov F, Statnik E, **Cvjetinovic J**. Features of formation of colonial settlements of marine benthic diatoms on the surface of synthetic polymer. *Marine Biological Journal*. 2020; 5(2):88-104.

(Participated in writing of the manuscript)

13. Salimon A, **Cvjetinovic J**, Kan Y, Statnik E, Aggrey A, Somov P, Salimon I, Everaerts J, Bedoshvili Ye, Gorin D, Likhoshway Ye, Sapozhnikov Ph, Davidovich N, Kalinina O, Dragnevski K, Korsunsky M. On the Mathematical Description of Diatom Algae: From Siliceous Exoskeleton Structure and Properties to Colony Growth Kinetics, and Prospective Nanoengineering Applications, in the book The Mathematical Biology of Diatoms, ed. Janice L. Pappas, Scrivener Publishing LLC, 2023; 63-102.

(Performed experiments related to the colony growth kinetics, wrote several sections, performed final editing)

14. **Cvjetinovic J**, Nozdriukhin D, Mokrousov M, Novikov A, Novoselova M, Tuchin V, Gorin D. Enhancement of contrast in photoacoustic – fluorescence tomography and cytometry using optical clearing and contrast agents, in the book Handbook of Tissue Optical Clearing, ed. Valery Tuchin, Dan Zhu, Elina Genina, Taylor and Francis Group, CRC Press, 2022

(The main and corresponding author)

Other publications

1. M. R. Chetyrkina, **J. Cvjetinovic**, F. S. Fedorov, S. V. Perevoschikov, E. S. Prikhozhdenko, B. F. Mikladal, Y. G. Gladush, A. G. Nasibulin, D. A. Gorin. ACS Photonics 2022, 9, 10, 3429–3439 (Q1, IF 7.077)

2. T. O. Abakumova, O. I. Gusliakova, **J. Cvjetinovic**, O. I. Efimova, E. V. Konovalova, A. A. Schulga, T. S. Zatsepin, D. A. Gorin, A. M. Yashchenok, and S. M. Deyev. *ACS Applied Nano Materials*. 2022, 5, 8, 10744–10754 (Q1, IF 6.14)

3. Kan Y, Bondareva JV, Statnik ES, **Cvjetinovic J**, Lipovskikh S, Abdurashitov AS, Kirsanova MA, Sukhorukhov GB, Evlashin SA, Salimon AI, Korsunsky AM. *Nanomaterials*. 2022; 12(6):998. (Q1, IF 5.719)

4. Kaydanov, N, Perevoschikov, S, German, S, Romanov, S, Ermatov, T, Kozyrev, A, **Cvjetinovic, J**, Machnev, A, Noskov, R, Kosolobov, S, Skibina, J, Nasibulin, A, Zakian, C, Lagoudakis, P, Gorin, D. *ACS Photonics*, 2021, 8(11), 3346-3356 (Q1, IF 7.077)

5. Y. Kan, **J. Cvjetinovic**, E. S. Statnik, S. V. Ryazantsev, N. Yu. Anisimova, M. V. Kiselevskiy, A. I. Salimon, A. V. Maksimkin, A. M. Korsunsky. *Materials Today Communications* 24 (2020) 101052 (Q2, IF 3.662)

Conferences

1. **Cvjetinovic, Julijana**; Salimon, Alexey; Novoselova, Marina; Sapozhnikov, Philipp; Kalinina, Olga; Korsunsky, Alexander; Gorin, Dmitry. Photoacoustic and fluorescence lifetime imaging of diatoms. The VIIth Vereschagin Baikal Conference. 2020, Irkutsk, Russia (oral talk)

2. **Cvjetinovic, Julijana**; Salimon, Alexey; Korsunsky, Alexander; Novoselova, Marina; Sapozhnikov, Philipp; Kalinina, Olga; Bedoshvili, Yekaterina; Gayer, Alexey; Efimova, Olga; Yaschenok, Alexey; Gorin, Dmitry. Diatoms: where photoacoustics meets fluorescence. The XXIV Annual Conference Saratov Fall Meeting. 2020, Saratov, Russia (oral talk)

3. **Cvjetinovic, Julijana**; Bedoshvili, Yekaterina; Nozdriukhin, Daniil; Efimova, Olga; Salimon, Alexey; Volokitina, Nadezhda; Korsunsky, Alexander; Gorin, Dmitry. In situ fluorescence/photo acoustic monitoring of diatom algae. SPIE Photonics West Digital forum. 2021, San Francisco, USA (oral talk)

4. **Cvjetinovic, Julijana**; Nozdriukhin, Daniil; Bedoshvili, Yekaterina; Efimova, Olga; Salimon, Alexey; Somov, Pavel; Korsunsky, Alexander; Gorin, Dmitry. Monitoring of diatom algae growth using fluorescence and photoacoustic imaging techniques. SPb Photonic, Optoelectronic, & Electronic Materials (SPb POEM). 2021, Saint Petersburg, Russia (oral talk)

5. **Cvjetinovic, Julijana**; Gorin, Dmitry. Photoacoustic contrast agents for in vitro/in vivo visualization. II Международная научно-практическая конференция «Фундаментальная наука для практической медицины-2021» (Basic science for practical medicine-2021). 2021, Elbrus, Russia (oral talk)

6. **Cvjetinovic, Julijana**; Bedoshvili, Yekaterina; Davidovich, Nickolai; Salimon, Alexey; Korsunsky, Alexander; Gorin, Dmitry. Photonic tools for studying freshwater and marine diatoms during long-term cultivation. The XXV Saratov Fall Meeting. 2021, Saratov, Russia (oral talk)

7. **Cvjetinovic, Julijana**; Nozdriukhin, Daniil; Kirsanova, Maria; Somov, Pavel; Salimon, Alexey; Korsunsky, Alexander; Gorin, Dmitry. Hybrid materials based on diatomite modified by gold nanoparticles: fabrication and photoacoustic characterization. SNAIA (Smart NanoMaterials: Advances, Innovation and Applications). 2021, Paris, France (oral talk)

8. **Cvjetinovic, Julijana**; Nozdriukhin, Daniil; Bedoshvili, Yekaterina; Davidovich, Olga; Efimova, Olga; Davidovich, Nickolai; Somov, Pavel; Salimon, Alexey; Korsunsky, Alexander; Gorin, Dmitry. Photonic methods for studying diatom algae. UK-Russia conference – Advanced materials to combat cancer. 2021, Lancaster, United Kingdom (oral talk)

9. **Cvjetinovic, Julijana**; Bedoshvili, Yekaterina; Davidovich, Nickolai; Luchkin, Sergey; Salimon, Alexey; Korsunsky, Alexander; Gorin, Dmitry. Optical properties of diatom algae: research methods and potential applications. The 6th International Conference on the Physics of Optical Materials and Devices AND The 5th International Workshop of Persistent and Photostimulable Phosphors (IWPPP-5). 2022, Belgrade, Serbia (oral talk)

10. **Cvjetinovic, Julijana**; Merdalimova, Anastasiia; Kirsanova, Maria; Somov, Pavel; Nozdriukhin, Daniil; Salimon, Alexey; Korsunsky, Alexander; Gorin, Dmitry. Nanostructured biosilica exoskeletons functionalized by gold nanoparticles as

SERS-active materials. The XXVI Saratov Fall Meeting. 2022, Saratov, Russia (oral talk)

11. **Cvjetinovic, Julijana**; Luchkin, Sergey; Statnik, Eugene; Davidovich, Nickolai; Bedoshvili, Yekaterina; Somov, Pavel; Salimon, Alexey; Korsunsky, Alexander; Gorin, Dmitry. The nanomechanics of diatom silica exoskeletons. The 13th International Conference on Key Engineering Materials (ICKEM 2023). 2023, Istanbul, Turkey (oral talk)

12. **Cvjetinovic, Julijana**; Dyakov, Sergey; Maksimov, Eugene; Davidovich, Nickolai; Salimon, Alexey; Lagoudakis, Pavlos; Korsunsky, Alexander; Gippius, Nikolay; Gorin, Dmitry. Diatom optics: unlocking the potential of biogenic photonic crystals. BRICS Workshop on biophotonics II. 2023, Saratov, Russia (oral talk)

13. **Cvjetinovic, Julijana**; Perkov, Sergei; Kurochkin, Maxim; Sergeev, Igor; German, Sergey; Bedoshvili, Yekaterina, Davidovich, Nickolai; Korsunsky, Alexander; Gorin, Dmitry. Optical characteristics of diatoms: relationship between concentration and transmission/extinction. Workshop on current trends in biophotonics. 2023, Nizhny Novgorod, Russia (oral talk)

Acknowledgements

First and foremost, I would like to express my sincere gratitude to my advisor, Prof. Dmitry Gorin for his guidance and tutoring. I could not have achieved the accomplishments inside or outside this thesis work without his constant encouragement, resourcefulness and diligence which have set the high standard for my PhD research. I would also like to express my deep appreciation for the help and guidance from my co-advisor, Prof. Alexander Korsunsky, a tutor of great knowledge, vision and wisdom. Their faith in the potential of diatom study have been the source of my inspiration, and the key driving forces for me to pursue the wonderful researches presented in this work.

I extend my heartfelt appreciation to the Jury members for their invaluable contributions to the refinement and polishing of my thesis. Their insightful feedback and guidance have played a pivotal role in shaping the final version.

I would like to thank Dr. Alexey Salimon for introducing me to the world of diatoms, for his support, ideas and guidance throughout my PhD studies. I would also like to extend my gratitude towards Dr. Yekaterina Bedoshvili and Prof. Nickolai Davidovich for providing me with the diatom cultures and being the best collaborators. Their help in the study of diatom structure, feedbacks and discussions have been of great value for my thesis work. I would also like to thank Dr. Sergey Luchkin, Eugene Statnik and Pavel Somov for their help with the study of mechanical properties, Prof. Sergey Dyakov and Prof. Nikolay Gippius for the numerical calculations of optical properties, Prof. Vladimir Drachev and Prof. Pavlos Lagoudakis for patiently listening to my talks and providing useful advice.

My special thanks also go to Dr. Sergei German for help with monitoring diatom division in a microfluidic cell, Dr. Maxim Kurochkin and Sergei Perkov for development of optical setup to measure changes in diatom concentrations, Daniil Nozdriukhin for fabrication of the first version of bioreactor, Stanislav Perevoschikov for calculations of diatom resonance frequencies, Anastasiia Merdalimova for performing Raman measurements of gold-coated diatomite. I have been inspired by their approaches in solving many complicated scientific problems. I am beyond grateful to my dear colleagues and friends Dr. Yuliya Kan, Margarita Chetyrkina and Maksim Mokrousov for their company, support, pleasant memories and many fruitful discussions that we usually had over a cup of tea. I have also had the great pleasures working with all the wonderful colleagues from Biophotonics and HSM Laboratories.

I would also like to acknowledge the Center for Photonic Science and Engineering, “Bioimaging and Spectroscopy” Core Facility as well as Advanced Imaging Core Facility at Skoltech and Russian Science Foundation for support through grant No. 22-14-00209.

Last but not least, I would like to express my sincere gratitude to my family members for their endless love and support throughout my academic journey. My parents, sister, niece and my grandparents have been my source of inspiration, constantly encouraging me to pursue my dreams and reminding me of the importance of hard work and discipline. At the very last, I would like to thank my husband Andrey for everything he did for me. I could not have made so far without his company, unwavering support, patience and love. Thank you for being there for me every step of the way.

Table of contents

Abstract 3

Thesis related publications 6

Conferences 10

Acknowledgements 13

Table of contents 15

List of Symbols, Abbreviations 21

List of Figures 22

List of Tables 40

Chapter 1. Introduction 41

Chapter 2. Literature review 47

2.1 Introduction to the world of diatoms 47

2.2 Hierarchical structuring of diatom algae 56

2.3 The mechanical properties of diatoms 61

2.4 The optical properties of diatoms 67

2.4.1 Light focusing and concentration 70

2.4.2 Light trapping 73

2.4.3 Spectral light filtration 75

2.4.4 Photoluminescence 77

2.4.5 Potential applications based on the optical properties 81

2.5 The modification and applications of diatoms 83

2.5.1 Surface modification 83

2.5.2 Genetic or metabolic modification 85
2.5.3 Incorporation of nanoparticles 85
2.5.4 Physical modification 85
2.5.5 Different applications of diatoms 86
2.6 On the MEMS perspective 89
2.7 On the importance of diatom algae in addressing specific issues 93
Chapter 3. Experimental section 95
3.1 Diatom algae cultivation 95
3.1.1 Sampling diatoms from natural populations. Isolation and introduction into clonal cultures of certain species of diatoms. Cultivation of various types of freshwater and marine diatoms ... 95
3.1.2 Cultivation of diatoms in the incubator 98
3.2 Monitoring of the growth of diatoms 100
3.2.1 IVIS SpectrumCT In vivo Imaging system 100
3.2.2 Spectroscopy measurements 101
3.2.3 RSOM monitoring 101
3.2.4 Monitoring of the growth of diatoms using microfluidic cell 102
3.2.5 Monitoring of diatom concentration changes using photoacoustic imaging 105
3.2.6 Setup for optical monitoring of diatom concentration changes .. 106
3.3 Cleaning of diatom cells from organic components 108
3.4 Characterization of the morphology and structure of diatoms 109
3.4.1 Scanning electron microscopy 109
3.4.2 Transmission electron microscopy 110

3.5 Visualization of living diatom cells 111
3.5.1 Optical microscopy 111
3.5.2 Confocal laser scanning microscopy 111
3.5.3 Operetta High Content Imaging System 112
3.5.4 Fluorescence lifetime imaging microscopy (FLIM) 113
3.6 Study of mechanical properties of diatoms 113
3.6.1 Preparation of samples for SEM nanoindentation and AFM 113
3.6.2 AFM measurements 114
3.6.3 In situ SEM nanoindentation 116
3.7 Study of resonance frequencies of diatoms 117
3.7.1 Numerical simulation using COMSOL Multiphysics 117
3.7.2 AFM measurements 118
3.8 Study of optical properties of diatoms 118
3.8.1 Numerical simulations using Fourier modal method 118
3.8.2 Extinction spectroscopy of individual diatoms 119
3.8.3 Chloroplast distribution study using FLIM 119
3.9 Modification of diatomite with gold nanoparticles 120
3.9.1 Gold nanoparticle synthesis 120
3.9.2 Fabrication of gold-coated diatomite 120
3.9.3 Zeta potential measurements 121
3.9.4 SEM study of prepared samples 121
3.9.5 TEM and EDX measurements 121
3.9.6 Photoacoustic visualization of gold-coated diatomite 122
3.9.7 SERS measurements of gold-coated diatomite 122

Chapter 4. Monitoring and characterization of diatom colonies 123
4.1 Background 124
4.2 Monitoring of freshwater pennate diatoms 128
4.3 Monitoring of the growth of marine centric diatoms 134
4.4 Monitoring changes in diatom concentrations 140
4.4.1 Photoacoustic imaging 140
4.4.2 Monitoring of diatom concentration changes using a developed optical setup 145
4.5 Summary 152
Chapter 5. Visualization of living and cleaned individual diatoms 155
5.1 Background 155
5.2 Morphology of frustules of different species 157
5.3 Distribution of chloroplasts in selected diatom species 161
5.4 FLIM visualization 163
5.5 Summary 168
Chapter 6. Mechanical properties of diatoms 170
6.1 Background 170
6.2 Morphology and topography study: from micro to nanoscale 173
6.3 AFM and AMFM studies of mechanical properties of diatoms 176
6.4 Compliance of cleaned frustules: Static vs. dynamic approach 182
6.5 In situ SEM nanoindentation 187
6.6 Vibrational eigenmodes of diatom frustules 190
6.7 Summary 204
Chapter 7. Optical properties of diatoms 206

7.1 Background 206
7.2 The diatom model 207
7.3 Reflection and transmission 208
7.3.1. The solar spectra at different depths in water 212
7.4 Light intensity distribution 215
7.4.1 Light intensity at specific incident angles 215
7.4.2 Light intensity integrated over all incident angles and all polarizations 217
7.4.3 Light intensity depending on the distance between two valves and polarization 221
7.4.4 Chloroplast migration in diatom frustules: responses to varied light intensity conditions 223
7.5 Summary 224
Chapter 8. Modification of diatomite 226
8.1 Gold nanoparticle characterization 226
8.2 Characterization of gold-coated diatomite 228
8.3 SEM study of degree of coverage of diatomite surface by gold 229
8.4 TEM and STEM-EDX study 231
8.5 Analysis of degree of diatomite functionalization by gold nanoparticles using photoacoustic imaging 232
8.6 Gold-decorated diatomite as a SERS platform 235
8.7 Summary 238
Chapter 9. Conclusions and Outlook 240
Appendix A 245

Appendix B 249

Appendix C 253

Appendix D 254

Appendix E 260

Bibliography 264

List of Symbols, Abbreviations

AFM – atomic force microscopy

AMFM – amplitude modulation- frequency modulation

BANSAM – Bio-Assisted Nanometer Size Additive Manufacturing

BF-TEM – Bright-field transmission electron microscopy

DI – deionized

DMT – Derjaguin-Muller-Toropov

FIL – freezing-induced loading

FLIM – fluorescence lifetime imaging microscopy

FMM – Fourier modal method

HAADF – high angle annular darkfield

EDX – energy dispersive X-ray

LbL – Layer-by-layer

MEMS – microelectromechanical systems

NEMS – nanoelectromechanical system

PAH – polyallylamine hydrochloride

RSOM – Raster scanning optoacoustic mesoscopy

SEM – scanning electron microscopy

SERS – Surface enhanced Raman spectroscopy

STEM – scanning transmission electron microscopy

TCSPS – time-correlated single-photon-counting

TEM – transmission electron microscopy

List of Figures

Figure 1. Research design and methodology 44

Figure 2. Phylogenetic diversity of eukaryotes showing the four major lineages of phytoplankton highlighted in bold typeface (prasinophytes, coccolithophorids, diatoms and dinoflagellates). Adopted from Ref.[13]. Reproduced with permission from John Wiley & Sons, Inc. 47

Figure 3. Left – Cover page of Ernst Haeckel's Kunstformen der Natur. Right – Plate 84 devoted to diatomea. Adopted from Ref.[18]. Reproduced with permission from Elsevier Ltd. 49

Figure 4. Diatom terminology. 1–3: Frustule terminology; 4–6: Examples of two major orders of diatom based on frustule shape—elliptical (pennate) (4 and 5) or circular (centric) (6) in valve view; these make up the two orders of diatoms (Pennales and Centrales, respectively). 4 and 5: Pennate diatom; 4: Valve view; 5: Connective view. 6: Centric diatom. 7: Symmetry axes. 8–11: Diatom species showing Raphe. 12 and 13: Diatom species showing pseudoraphe. 14: Structural details of the cell wall. Adopted from Ref.[23]. Reproduced with permission from Springer New Delhi.....50

Figure 5. Centric diatoms (1–3, 5–7); pennate diatoms (4, 8–12). Adopted from Ref.[14] (Courtesy of M.V. Kravchishina, Ph. V. Sapozhnikov, O.Y. Kalinina, SIO RAS). Reproduced with permission from Scrivener Publishing. 52

Figure 6. Shape classification of diatom frustules. Adopted from Ref.[28]. Reproduced with permission from Springer. 53

Figure 7. Different representatives of thalassiosiroids (1–6) and coscinodiscoids *Coscinodiscus radiatus* (7, 8). Adopted from Ref.[14] (SEM images are courtesy of M.V.

Kravchishina, light microscopy images are taken by Ph. V. Sapozhnikov, SIO RAS). Reproduced with permission from Scrivener Publishing. 54

Figure 8. Typical structure of multilevel pores (Coscinodiscus sp.). a) 3D model; b) arrays of foramen and second-level pores, scale bar 1 μm; c) array of sieve pores, scale bar 2 μm; d) array of nanopores on girdle band, scale bar 1 μm. Adopted from Ref.[28]. Reproduced with permission from Springer.....57

Figure 9. Biosilicification in diatoms. a) *Thalassiosira pseudonana* diatom (credit to University of Washington). b) Biosilicification mechanisms in the formation of hierarchical silica-based honeycomb-like structure of diatom skeleton. Adopted from Ref.[42]. Reproduced with permission from Wiley-VCH.....58

Figure 10. Schematic illustrations of: a) formation, b) reproduction of diatom frustules. Adopted from Ref.[28]. Reproduced with permission from Springer. 60

Figure 11. Glass needle tests: Live single cells of *T. punctigera* (a–c) and *F. kerguelensis* (d–f), in chains (e,f). Pressures applied along the girdle bands, (a,d), across the girdle bands (b,e), and across the centre of the valves (c,f). g) Forces necessary to break frustules. Scale bars, 10 μm. Adopted from Ref.[48]. Reproduced with permission from Springer Nature. 62

Figure 12. a) Low-resolution AFM image of the internal plate after nanoindentation. b) Series of indentation points (solid arrows) obtained using a force of 1.5-3 μN. c) Typical force penetration curve showing loading and unloading parts (dashed arrows). d) AFM image showing nanoindentation performed on an areola rib at higher applied load (12 μN). White scale bar is 10 μm. Adopted from Ref.[45]. Reproduced with permission from American Chemical Society.....64

Figure 13. Ashby plot of strength vs. density for naturally occurring biological materials, including diatoms. Adopted from Ref.[49]. Reproduced with permission from Taylor and Francis Ltd. 65

Figure 14. Overview of relevant features that differ between the diatom in its natural habitat and rinsed diatom valve measured using an optical setup (a). b) A diatom valve rinsed of organic material, c) A living diatom in water, d) A mapping showing how spectrum of transmitted light changes with depth. Adopted from Ref.[65]. Reproduced with permission from Springer Netherlands. 69

Figure 15. Left: The intensity distribution of the transmitted light at the distance (z) of 4 μm (top) and 104 μm (bottom): the red line is the experimental recorded one, the black line is the numerically estimated. Right: The corresponding images of the diatom surface recorded by a CCD at the two distances considered. Adopted from Ref.[73]. Reproduced with permission from Optica Publishing Group. 71

Figure 16. Distance z* of maximum intensity of the transmitted spot as a function of the wavelength of the incoming light beam. Adopted from Ref.[74]. Reproduced with permission from Optica Publishing Group. 72

Figure 17. Optical images of the diffraction patterns obtained from the different regions of C. wailesii valve. a) No diatom was present in the beam path. b-d) The frustule valve was present in the beam path. The color of the central spot changed according to the location of the partial photonic band gap. Adopted from Ref.[72]. Reproduced with permission from Optica Publishing Group. 74

Figure 18. Transmittance spectra of a frustule using the following alignment: a) Incident light passing through the side wall of the frustule, b) Incident light passing through the frustule perpendicular to the side wall. Optical microscopy images of: c)

parallel, d) perpendicular alignments. Adopted from Ref.[77]. Reproduced with permission from Japan Society of Applied Physics.....75

Figure 19. Transmittance spectra for: a - *Coscinodiscus concinnus*, cleaned frustules. b - *C. granii* cleaned frustules. c - *C. concinnus*, dried cells with cell content. d - *C. granii*, dried cells with cell content. Adopted from Ref. [65]. Reproduced with permission from Springer Netherlands. 76

Figure 20. *Thalassiosira* photoluminescence spectrum in dry air (continuous line), in 167 ppb of NO_2 in dry air (dashed line) and in 10 ppm of NO_2 in dry air (dotted line). Adopted from Ref [82]. Reproduced with permission from Elsevier Ltd. 78

Figure 21. The micro-photoluminescence spectra of diatom frustule were measured by: a) 325 CW laser and b) 355nm pulse laser acted the excitation laser sources. Adopted from Ref.[85]. Reproduced with permission from Optica Publishing Group. 79

Figure 22. Diatom biosilica optical properties and their potential applications 82

Figure 23. Scheme of the surface modification techniques of diatoms in pharmaceutical applications. Adopted from Ref. [104] Reproduced with permission from MDPI. 84

Figure 24. Various applications of diatoms. 87

Figure 25. Mode shapes and natural frequencies of *Coscinodiscus* sp. (centric) and *Ulnaria acus* (pennate) observed in the simulation using COMSOL Multiphysics. Adopted from[148]. Reproduced with permission from Elsevier Ltd.....90

Figure 26. The example of FIB-SEM milling of diatom species (destructive method). Adopted from Ref.[14]. Reproduced with permission from John Wiley & Sons, Inc. 91

Figure 27. Ptychography of *Aulacoseira* diatom cells (courtesy of T.E.J. Moxham, University of Oxford / Diamond Light Source, U.K.) Adopted from Ref.[14]. Reproduced with permission from John Wiley & Sons, Inc. 92

Figure 28. A scheme of the diatom algae incubator 100

Figure 29. Scheme of a setup with a microfluidic cell for monitoring the growth of diatoms using optical microscopy 103

Figure 30. a) Photography of the whole experiment setup, b) Photography of microfluidic cell. 104

Figure 31. Experimental setup for monitoring changes in the diatom algae concentration. (a) Direct LED light coupling in multimode optical fiber. (b) Artistic representation of an optical system for measuring the transmission of algae in a nutrient medium depending on their fractional dilution. (c) Schematic representation of the experimental setup key components for transmission measurements. (d) Emission spectrum of LED. 106

Figure 32. Calibration of a stiff diamond probe (k=400 N/m) on a fused silica reference sample. a) Topography, b) The stiff diamond cantilever, c) The DMT model, d The Hertz model), e) Hardness depending on the applied force. [39] 115

Figure 33. Absorption range of different algae pigments[182] 128

Figure 34. Photography of: a) incubator, b) LED strip above cell culture flasks, c) cell culture flasks with diatoms. 129

Figure 35. A. sibiricum: a) SEM image, b) culture growth during three days after inoculation, c) optical image of two diatoms during cell division, d) confocal images of: cells fixed formaldexyde and stained with DAPI (blue, nucleus; red, chlorophyll).....130

Figure 36. (a) Images of cell culture flasks containing diatoms obtained using the IVIS platform (top view), (b) The average radiant efficiency of diatoms during the cultivation period, (c) Normalized fluorescence spectra of *A. sibiricum* cells, (d) Comparison of fluorescence intensity at 680 nm and average radiant efficiency depending on the cultivation time.....132

Figure 37. (a) RSOM images of *A. sibiricum* diatoms mixed with agarose gel at 11-99 MHz, 11-33 MHz (red), 33-99 MHz (green) after 7, 28, 45, 60, 90, and 100 days of cultivation. Scale bar: x, y-axis – 0.5 mm. Red color corresponds to a low-frequency signal emitted by larger samples. A high- frequency signal, shown with green bars, is emitted by smaller structures. (b) The dependence of mean pixel intensity on the cultivation time, (c) Extinction spectra collected at different periods of cultivation, (d) Comparison of extinction at 523 nm and mean pixel intensities at 11-33 MHz and 33-99 MHz, as functions of the cultivation time.....133

Figure 38. SEM images of: a) *Coscinodiscus* sp. (21.0407-OA), b) *B. titiana* (0.0212-OH). c) Images of flasks containing diatoms obtained using IVIS imaging system, d) Total radiant efficiency depending on the cultivation time of both strains. 134

Figure 39. Fluorescence spectra of: a) *Coscinodiscus* sp., c) *B. titiana*. Comparison of normalized fluorescence intensity at 680 nm and normalized total

radiant efficiency depending on the cultivation time of: b) *Coscinodiscus* sp., d) *B. titiana*. 1-lag phase, 2-exponential growth, 3-stationary phase, 4-decline. 135

Figure 40. a) RSOM images of 4 different cultures obtained during 32 days of cultivation, b) Mean pixel intensity vs. cultivation time for all strains. 137

Figure 41. Extinction spectra of: a) *Coscinodiscus* sp., b) *B. titiana*, c) *Ulnaria acus*. Normalized extinction at maximum wavelengths of: d) *Coscinodiscus* sp., e) *B. titiana*, f) *Ulnaria acus*. 138

Figure 42. (a) RSOM image of different concentrations of *K. amoena* embedded in agarose gel at frequencies of 11–99 MHz. Inset: Photograph of different dilutions of *K. amoena* in agarose gel drops, where 1 – Agarose gel; 2 – Stock suspension; Diluted suspensions: 3 - 1:2; 4 – 1:4; 5 – 1:8; 6 – 1:16; 7 – 1:32; 8 – 1:64; 9 – 1:128. (b) RSOM image of *K. amoena* at low frequencies (LF). (c) RSOM image of *K. amoena* at high frequencies (HF). Scale bar (a,b,c): x-axis – 1 mm, y-axis – 1 mm, z-axis – 0.2 mm. (d) Volume of 3D objects vs. the concentration of diatoms mixed with agarose gel. AF – all frequencies. (e) Volume of 3D objects vs. the concentration of diatoms. (f) Mean pixel intensity vs. the concentration of diatoms mixed with agarose gel. 141

Figure 43. (a) Extinction spectra of different concentrations of *K. amoena* embedded in agarose gel. Chl a – chlorophyll a, Chl c – chlorophyll c. (b) Dependence of photoacoustic signal and extinction at 532 nm on concentration of diatoms mixed with agarose gel. 144

Figure 44. Brightfield microscopy images of marine centric diatoms: (a) *Biddulphiopsis titiana* (0.0212-OH), *Coscinodiscus oculus-iridis* (0.1211-OD): (b) top view, (c) side view, (d) *Coscinodiscus* sp. (21.0407-OA). Fluorescence images of marine centric diatoms: (e) 0.0212-OH, 0.1211-OD: (f) top view, (g) side view, (h)

21.0407-OA. Brightfield microscopy images of freshwater pennate diatom strains: (i) *Amphipleura* sp. (Ov 466), (j) *Hannaea baicalensis* (BK 479), (k) *Asterionella formosa* (BZ 33), (l) *Ulnaria acus* (15k 595). Fluorescence images of freshwater pennate diatoms: (m) Ov 466, (n) BK 479, (o) BZ 33, (p) 15k 595. 147

Figure 45. Optical measurements of diatom cultures. Light intensity as a function of the relative concentration of diatom cells. Light intensity was normalized on the measurements of nutrient medium. Scatter plot represents measured values, solid lines represent linear fit.....148

Figure 46. Spectrophotometric and fluorescence measurements of diatoms. (a) Extinction spectra. (b) Dependence of extinction (λ = 505 nm) on the diatom concentration. Scatter plot represents extinction values normalized on the nutrient medium extinction. Solid lines represent linear fit. (c) Fluorescence intensity spectra. Excitation wavelength: 430 nm. (d) Dependence of fluorescence intensity on the diatom concentration. Scatter plot represents fluorescence intensity values normalized on the nutrient medium values.....150

Figure 47. The dependence of linear fit slopes on the volume of diatom cells. The red circles represent slopes of linear fit in extinction measurements. The blue squares represent absolute values of slopes of linear fit in transmission measurements on the custom-made setup.....152

Figure 48. SEM images of different pennate: (a) *Nitzschia graciliformis*, (b) *Ulnaria acus*, (c) *Asterionella formosa*, (d) *Amphipleura* sp., (e) *Hannaea baikalensis* and centric diatom frustules: (f) *Coscinodiscus oculus-iridis*, (g) *Coscinodiscus* sp., (h) *Biddulphiopsis titiana*. Insets: enlarged view of individual frustules.....157

Figure 49. Visualization of pennate diatoms using laser scanning microscopy. a) Confocal image of *U. acus* (15k 595) after PDMPO staining, b) 3D confocal image of U. acus, c) Fluorescent image of *N. graciliformis*, d) Bright field image of *N. graciliformis*, e) Confocal image of *Amphipleura* sp. (Ov 466) after PDMPO staining, f) 3D confocal image of a dividing cell of *Amphipleura* sp., g)-h) 3D images of *Amphipleura* sp., i) Confocal image of *A. formosa* (BZ 33) after PDMPO staining, j) 3D -confocal image of *A. Formosa*. Scale bar: a, b, c, d, i, h - 10 μm; e, g, j – 5 μm. 161

Figure 50. Visualization of *C. oculus-iridis* (strain 0.1211-OD) using laser scanning microscopy. a) Confocal image of a fixed *C. oculus-iridis* cell stained with LysoTracker Yellow and DAPI (lateral view), b) 3D image of a dividing cell with nuclei (lateral view), c) 3D image of a divided cell without a nucleus, d) 3D image image of a dividing cell, e) Confocal image of a fixed *C. oculus-iridis* cell (top view), f) 3D image of a cell without a nucleus (top view), g) 3D image of a cell with a nucleus (top view). Red: chlorophyll autofluorescence, green: newly formed valves, blue: nucleus. Scale bar: a, e – 20 μm; b, c, f, g – 5 μm. 162

Figure 51. Transmission bright field (left) and FLIM images (right) of different pennate diatoms. Excitation wavelength: 638 nm (*K. amoena*), 402 nm (*H. karadagensis*, *A. sibiricum*, *E. silesiacum*) 164

Figure 52. Transmission bright field (left) and FLIM images (right) of different centric diatoms. Excitation wavelength: 402 nm. 167

Figure 53. Study objects, biomimetic approach and research methodology. a) Samples used in this study: cleaned frustule (organic matter removed), external and internal sides of cleaned frustules, diatom cell containing organic components, b) SEM

images of the MEMS microphone and the membrane perforation (inset). Adapted with a permission from[146]. c) SEM image of diatom frustule showing the porous structure (inset), d) Schematic diagrams of two modes of AFM measurement: force vs distance and amplitude modulation-frequency modulation (AMFM), e) In situ nanoindentation inside SEM column, f) Schematic illustration of a copepod crushing diatom cell with the help of a silica tooth as an example of indentation in nature. 171

Figure 54. SEM images of: a) the cleaned diatom frustule consisting of a hypotheca and an epitheca joined together by girdle bands, b) the frustule FIB cross-section showing areola walls c, d) outer surface of the valve, e details of the external side of the valve: cribrum, f) cribellum, g) inner surface of the valve, h) details of the internal side of the valve: rimoportulae, i) foramen. AFM topography of: j) an outer surface of the cleaned frustule decorated with porous domes (cribrum), k) foramen holes on the inner surface of a cleaned frustule, l) a surface of a wet diatom cell forming a hilly terrain, m) close view of regularly spaced pores on the outer surface (cribellum) of a wet diatom cell. [39] 175

Figure 55. AFM study of cleaned frustules and wet diatom cells. Topography of a measured: a) inner side and b) outer side of cleaned frustule, c) wet diatom cell. Young's modulus of: d) inner and e) outer surface of cleaned frustule, f) wet diatom cell. [39] 177

Figure 56. Inner surface of a frustule measured by the stiff diamond probe (k=400 N/m). a) Topography before nanoindentation, b) topography after nanoindentation with indicated Young's modulus values calculated using DMT model, c) force-indentation and force-deflection curves collected at specific indentation points. [39] 178

Figure 57. AFM indentation at specific points of a cleaned inner valve. a Inner surface of a frustule measured by the stiff probe after indentation at specific points by applying different indentation force, b Young's modulus calculated using the Derjaguin-Muller-Toropov (DMT) model at different applied forces after averaging over 10 points, c the dependence of hardness on the applied force. [39].....179

Figure 58. The AMFM study of cleaned frustules and wet diatom cells. External side of the cleaned valve: a) Topography, b) The AMFM Young modulus, c) The AMFM Young modulus profile along the white line shown in Figure 60b. Internal side of the cleaned valve: d) Topography, e) The AMFM Young modulus, f) The AMFM Young modulus profile along the white line shown in Figure 60e. External side of the wet diatom cell: g) Topography, h) The AMFM Young modulus, i) The AMFM Young modulus profile along the white line shown in Figure 60h. 181

Figure 59. Compliance of cleaned frustules: static vs. dynamic approach. A) Young's modulus depending on the distance from the edge towards the center of the outer surface of the valve. Inset: topography of outer surface of a cleaned frustule. The measurements were carried out using AFM by pressing the diamond probe on the sample with a force of 7.7 μN along each green line. b) Compliance vs. relative radial position calculated using the Green's function of a point force, c) SEM images of whole diatom frustule acquired during different stages of nanoindentation in the SEM column, d) Calculated compliance vs. cycle number. [39] 184

Figure 60. a) SEM image of a measured cleaned diatom upper valve, b) Displacement vs. time, the whole region – 300 seconds, c) Displacement vs. time, a short time interval – 5 seconds, d) Compliance vs. cycle number, e) SEM image of a measured cleaned diatom frustule, f) Displacement vs. time, the whole region – 300

seconds, g) Displacement vs. time, a short time interval – 5 seconds, h) Compliance vs. cycle number. Amplitude 1 μm, period 1s. [39] 185

Figure 61. The deformation response of the frustule valve to local indentation 186

Figure 62. In situ SEM nanoindentation of cleaned frustules and dried diatom cells. a) SEM images of air-dried diatom cells measured by nanoindentation in the SEM column, b) SEM images of cleaned frustules. Scale bar, 10 μm. c) Force-displacement curves obtained during indentation of dried cells, d) Calculated area under the force-displacement curves of dried and cleaned diatoms equal to work done, e) The case of a layered structure of the frustules of some diatoms, potentially responsible for difference in the obtained force-distance curves. [39] 188

Figure 63. Force-displacement curves of cleaned frustules obtained by in situ SEM nanoindentation. a) force-displacement curves for forces up to 25 mN, b) magnified view of force-displacement curves for forces up to 1 mN. [39] 189

Figure 64. a) Flowchart of modelling steps using COMSOL Multiphysics. b) SEM image of AFM chip after FIB-assisted welding of diatom frustules, right: enlarged view of the samples. Schematic illustrations of two AFM approaches: c) thermal vibrations, d) external modulation. 194

Figure 65. a) Experimental frequencies of thermal vibrations collected from different parts of the diatom frustule, as shown in the optical microscopy insets on the right side. The spectra were smoothed to avoid spurious spectral lines. The raw spectra are shown in Appendix B. b) Calculated vibrational eigenmodes of diatom frustules with indicated frequencies and quality factors.....195

Figure 66. Amplitude-frequency spectra of different parts of diatom frustules obtained by mechanical excitation in the region: a) 0-8 MHz, b) 0-3 MHz. Phase frequency spectra collected at different positions in the region: c) 0-8 MHz, d) 3-7.8 MHz. 198

Figure 67. Thermal vibration spectra of diatoms with diameter: (a) 72 μm, (c) 60 μm, (e) 70 μm, with enlarged view of peaks on the right. Externally modulated vibration spectra of the same diatoms. Optical microscopy images of the samples and positions of the laser spot are shown on the right. 200

Figure 68. a) 3D AFM image of the diatom frustule. b) Horizontal and vertical profiles of diatom frustule as shown in the image c). d) Topography of the surface layer. 202

Figure 69. SEM images of C. oculus-iridis. Top view of: a), b) upper layers, c) inner layer. Cross sections of: d) the whole frustule, e) upper layer, f) inner layer...207

Figure 70. The schematic of a 3D model of diatom frustule including structural parameters used for calculations. Blue: water ($n = 1.33$), green: silica ($n = 1.45 \pm 0.03i$) 208

Figure 71. Reflection (upper row) and transmission (bottom row) of diatoms in main, diffraction and all channels. Incidence from the top.....209

Figure 72. Reflection (upper row) and transmission (bottom row) of diatoms in main, diffraction and all channels. Incidence from the bottom. 210

Figure 73. The transmission spectra of diatoms and non-periodic structure of the same thickness.....211

Figure 74. Extinction spectra of: a) individual living diatoms, b) individual cleaned frustules with corresponding images showing where the spectra were collected. 212

Figure 75. a) Solar spectra and b) normalized solar spectra at different depths in water, c) modelled color of water as a function of depth.....213

Figure 76. Light intensity simulation at λ=420 nm, θ=0°, φ=0° on the surface of the frustule. 216

Figure 77. Light intensity simulation at λ=420 nm, θ=45°, φ=0° on the surface of the frustule. 217

Figure 78. a) Vertical cross-sections of two model structures: 1 (with cavity) and 2 (without cavity). b) Maximal and c) mean light intensity over a horizontal cross-section with coordinate z for both structures (with and without cavity).....218

Figure 79. Left: Vertical cross-sections of light intensity distribution for structure 1 (with cavity) and structure 2 (without cavity). Right: Horizontal cross-sections of light intensity distribution at the coordinates z=2288 nm and nm z=3738 nm for structure 1 (with cavity) and structure 2 (without cavity). 219

Figure 80. FLIM images of *C. oculus-iridis* showing distribution of chloroplasts in the frustule: a) top view, b) side view.....220

Figure 81. a) Two model structures: 1 - with cavity and 2 - without cavity for distance between valves g=5μm. Maximal light intensity distribution calculated for: b) S- and d) P- polarizations. Mean light intensity distribution calculated for: c) S- and e) P- polarizations. 221

Figure 82. Maximal light intensity distribution calculated for two model structures for distance between valves g=25μm: a) S- and c) P- polarizations. Mean light intensity distribution calculated for: b) S- and d) P- polarizations.....222

Figure 83. a) Typical BF-TEM image of gold nanoparticles (scale bar, 20 nm), b) Size distribution histogram of synthesized gold nanoparticles, c) Extinction spectrum of AuNPs, d) Zeta potential distribution of AuNPs.....227

Figure 84. a) A schematic representation of layer-by-layer approach, b) Extinction spectra of AuNPs and diatomite decorated with different number of PAH/AuNPs bilayers, c) Zeta potential depending on the layer number. 229

Figure 85. SEM images of gold-coated diatomite consisting of one (left), three (middle), and five (right) PAH/AuNPs bilayers. 230

Figure 86. Diatomite-$(PAH/Au)_3$: a, b) HAADF-STEM image, c, d) TEM images, e) HAADF-STEM image, corresponding elemental EDX maps and f) EDX spectrum.....231

Figure 87. RSOM images of 2-fold diluted diatomite coated with different number of PAH/AuNPs bilayers (up) and the corresponding mean pixel intensity depending on the dilution (down).....233

Figure 88. RSOM images of gold nanoparticles and stock suspensions of diatomite coated with different number of PAH/AuNPs bilayers at: a) 11-99 MHz, b) 11-33 MHz, c) 33-99 MHz frequency range, d) Mean pixel intensity depending on the sample, e) comparison of the extinction at 532 nm and mean pixel intensities at 11-33 and 33-99 MHz. 1-Diatomite-$(PAH/Au)_1$, 2-Diatomite-$(PAH/Au)_2$, 3-Diatomite-(PAH/Au)3, 4-Diatomite-$(PAH/Au)_4$, 5-Diatomite-$(PAH/Au)_5$. Scale bar, 200 μm.234

Figure 89. Surface-enhanced Raman spectra of Rhodamine 6G obtained using gold-coated diatomite hybrid materials with a different number of PAH/AuNPs bilayers. 235

Figure 90. Division of C. oculus-iridis in the microfluidic cell 247

Figure 91. Monitoring of the division of *C. oculus-iridis* in the microfluidic cell during temperature changes. 248

Figure 92. Structural details of *Ulnaria acus* 15K595 cells (TEM). Cross sections - a, b; longitudinal sections, c, d. The arrows in Figure 1b show plastoglobules, and in Figure 1c, a fragment of the forming girdle rim. Symbols: GA - Golgi apparatus; H - hypotheca; m - mitochondrion; P - pyrenoid; E - epitheca; N – nucleus, NS - nucleolus. Scale: a, c, d – 1 μm; b – 500 nm. 249

Figure 93. Details of the cell structure of *Coscinodiscus oculus-iridis*. a) general view of the cell, cross section, the arrow shows the nucleolus; b) section through the chloroplast (arrow – plastoglobules); c) section through the mitochondrion (arrow— polysaccharide layer); d) fragment of a chloroplast section (black arrow, thylakoid; white arrow, anastomosis between stacks of thylakoids); e) Section fragment through the chloroplast (arrow – plastoglobule) and transport vesicle (asterisk). Scale: a – 5 μm; b – 1 μm; c-e - 500 nm. Designations as in the previous Figure 92. 251

Figure 94. Details of the cell structure of *Hannaea baicalensis*. A) general view of the cell, cross section; b) enlarged fragment of figure 48a; c) section through a part of the chloroplast without a pyrenoid; d) cross section of mitochondria; e) section of the Golgi apparatus adjacent to the chloroplast. Scale: a, c – 1 μm; b, d, e – 500 nm. Designations as in Figure 92. 252

Figure 95. Raw spectra of frequencies of thermal vibrations of the diatom frustule collected at different spots. 253

Figure 96. Convergency check in Fourier modal method. In simulation, Ng=97 is used.....254

Figure 97. Maximal and mean light intensity distribution calculated for two model structures for distance between valves g=10 μm for S- and P- polarizations. 254

Figure 98. Maximal and mean light intensity distribution calculated for two model structures for distance between valves g=15 μm for S- and P- polarizations. 255

Figure 99. Maximal and mean light intensity distribution calculated for two model structures for distance between valves g=20 μm for S- and P- polarizations. 255

Figure 100. Light intensity calculated for: S- (upper row) and P-polarization (bottom row), within horizontal cross-sections of samples with height g=5, 10, 15, 20, 25 μm. 256

Figure 101. Light intensity calculated for P-polarization within vertical cross-sections of samples with height g=5, 10, 15, 20, 25 μm in yz plane. 256

Figure 102. Light intensity calculated for S-polarization within vertical cross-sections of samples with height g=5, 10, 15, 20, 25 μm in yz plane. 257

Figure 103. Light intensity calculated for P-polarization within vertical cross-sections of samples with height g=5, 10, 15, 20, 25 μm in xz plane. 257

Figure 104. Light intensity calculated for S-polarization within vertical cross-sections of samples with height g=5, 10, 15, 20, 25 μm in xz plane. 258

Figure 105. Light distribution inside the diatom frustule calculated for the wavelength λ=450 nm: a) Vertical cross-section, b) Horizontal cross-sections at z=3.8

μm, z=6.4 μm, z=10 μm. c) The dependence of wavelength of incident light on the angle of incidence. 259

Figure 106. Distributions of peak intensities of two prominent peaks of Rhodamine 6G (1362 cm^{-1} – up, 1509 cm^{-1} – down).....261

Figure 107. Calibration curve for R6G.....262

List of Tables

Table 1. The summary of results of nanoindentation and bending experiments of diatoms.....66

Table 2. Summary of studies on optical properties of diatoms.....81

Table 3 Comparison of the volume of 3D objects obtained by using the ImageJ program with the calculated volume of diatom cells in an agarose gel drop.....141

Table 4. The size and morphology of the studied diatom cultures 146

Table 5. Comparison of the coefficient of determination (COD) for spectrophotometric measurements with optical measurements on the custom device. 151

Table 6. Diatom model parameters.....193

Table 7. Experimentally obtained and calculated resonance frequencies and quality factors.....197

Table 8. Calculated resonance frequencies for diatom frustules with diameters 60, 70 and 72 μm 199

Table 9. Raman and SERS intensities.....236

Chapter 1. Introduction

The investigation of diatoms traces its origins to the late eighteenth century. However, substantial progress in the field materialized during the early nineteenth century, as diatoms gathered the attention of microscopists in the wake of notable improvements in microscope resolution. Diatoms are of planetary ecological importance, making a huge contribution to biomineralization and carbon dioxide capture by accounting for approximately 20% of oxygen production via photosynthesis[1–3]. As primary producers, they also constitute a foundational component of the food web and serve as a source of valuable renewable resources – complex organic compounds (lipids, polyunsaturated fatty acids, pigments, etc.) [4,5] and highly porous silica[6]. To optimize the growth conditions and the processes of diatom algae biomass production, it is important to monitor their growth over extended periods within controlled laboratory environments. The need for developing novel optical methods of monitoring the growth arises from the limitations of traditional methods. Traditional methods of monitoring diatom growth involve manual counting of cells, which is time-consuming and labor-intensive[7]. Moreover, these methods are prone to errors and may not provide accurate measurements of growth rates, particularly in the case of the rapid division of small cell species. The optical methods outlined in this thesis, encompassing fluorescence and photoacoustic visualization, offer notable advantages in comparison to conventional approaches. They provide non-invasive, real-time information about the physiological state of the algae, without the need for complex preparatory procedures and with a reduced risk of introducing contaminants into the medium. This aids in optimizing growth conditions for biotechnology applications and assessing the impact of environmental changes on diatom populations.

However, diatoms gather attention not solely for their ecological significance but also for the distinctive characteristics of their highly porous silica cell wall. A unique micro- and nano-scale architecture of diatom silica exoskeletons provides exceptional optical and mechanical properties, offering potential for the development of advanced materials. In order to design effective technologies and materials, a deep understanding of the fundamental properties and structure of natural materials is needed. After a thorough study of the literature, no reports were found on a fundamental and systematic study of the relationship between the structural and topographic features of diatom frustules, as well as wet and air-dry cells containing organic material, and their mechanical characteristics under static and dynamic loading. Given the fact that the diatom frustule itself can be considered as a nanostructured membrane, the determination of the mechanical properties of both membranes and cells with all organic components present seems extremely important and necessary both from the point of view of fundamental research and from the point of view of the use of these systems as functional materials for new devices. By characterizing the mechanical properties of diatom frustules, insights can be gained into their capacity to withstand external forces and protect the cell from damage. Leveraging a biomimetic approach, it becomes feasible to fabricate micro-electro-mechanical systems (MEMS) devices based on diatoms, hybrid membranes, and sensitive optoacoustic microphone arrays for minimally invasive endoscopic procedures.

Another important aspect of my research is to investigate the role of the hierarchical structure in determining the optical properties of diatom frustules. By using advanced imaging techniques such as electron microscopy and fluorescence lifetime imaging microscopy as well as numerical simulations, the goal is to study the

interaction of light with the highly porous hierarchical frustule, taking into account the chloroplast distribution within, and how they contribute to the overall optical performance of the nature-based photonic crystal.

The optical properties of diatoms, such as their light scattering and absorption efficiencies, are of interest in the development of new sensors and devices for environmental monitoring, as well as for photonic and biomedical applications[8,9]. Despite some work being done in the field of studying optical properties of diatoms, which are considered as natural photonic crystals, many questions remain unanswered. These include inquiries into the impact of the periodic multilayered structure on the distribution of light intensity, and its potential correlation with the distribution of chloroplasts within the diatom frustule.

Another important aspect for future application of diatom frustules is the modification of the surface to further improve their properties. For example, modifying the surface of diatomite with gold nanoparticles has the potential to create a composite material for sensing applications. Various techniques have been suggested for the functionalization of diatomite with gold nanoparticles[10–12]. Nevertheless, there remains a demand for improved control of the deposition procedure, achieving uniform coverage, and enabling the creation of multilayered and functional coatings. Gold nanoparticles on the surface of diatomite can act as a catalyst for chemical reactions, while the porous structure of diatomite can provide a large surface area for adsorption of pollutants or other molecules. Additionally, the combination of gold nanoparticles and diatomite holds promise in biomedical applications, capitalizing on the distinct attributes of both materials including biocompatibility, expanded surface area, and customizable surface chemistry, to forge novel and inventive solutions.

To address the needs and challenges discussed above, this thesis undertakes a comprehensive investigation of diatoms on three levels, encompassing the study of colonies in suspension, individual living diatoms, as well as purified frustules and diatomite powder, as schematically shown in Figure 1. The main tasks of the thesis are:

1. To monitor the diatom growth using optical and spectroscopic methods;
2. To study optical and mechanical properties of individual living diatom cells as well as cleaned frustules without organic components;
3. To modify the surface diatomite powder with gold nanoparticles.

In order to fulfill these objectives, a variety of methods and approaches have been used, tailored to the specific scope of each investigation, as depicted in Figure 1.

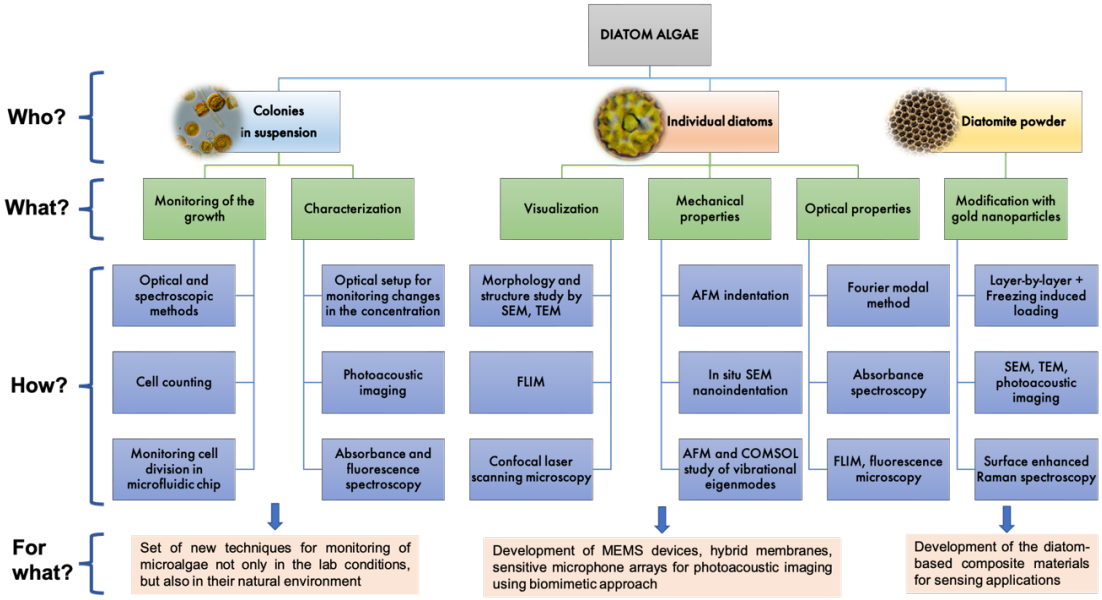

Figure 1. Research design and methodology

By revealing the underlying relationship between the diatom structure, properties and function, this dissertation aims to contribute to the understanding of these fascinating organisms and the development of new approaches and practices to address

the problem of efficient diatom monitoring. By combining physics, biology, and materials science, new insights into the natural world can be uncovered, and new technologies that benefit society can be developed.

According to the aforementioned objectives, the thesis is structured into nine chapters:

Chapter 1: Introduction

- This chapter includes a brief overview of the research area, novelty and motivation.

Chapter 2: Literature review

- This chapter includes a review of diatom algae, their properties, modification techniques and applications.

Chapter 3: Experimental section

- This chapter describes the cultivation of diatoms, preparation of samples and experimental approaches used to study them.

Chapter 4: Monitoring and characterization of diatom colonies

- This chapter covers fluorescence and photoacoustic monitoring and spectroscopic characterization of diverse diatom cultures throughout their extended cultivation under controlled laboratory conditions.

Chapter 5: Visualization of living and cleaned individual diatoms

- This chapter initiates the investigation of individual diatoms using scanning electron microscopy, confocal microscopy and fluorescence lifetime imaging microscopy to visualize both intact living cells and cleaned frustules without organic constituents.

Chapter 6: Mechanical properties of diatoms

- This chapter shows results of the nanomechanical characterization of *Coscinodiscus oculus-iridis* diatom silica frustules, as well as of air-dried and wet cells with organic content in the static and dynamic regime using atomic force microscopy and *in situ* nanoindentation in the column of scanning electron microscope. The second section of this chapter presents the outcomes pertaining to the experimental validation, employing an AFM optical system, of the numerically predicted vibrational mode calculations of *Coscinodiscus oculus-iridis*.

Chapter 7: Optical properties of diatoms

- In this chapter, the Fourier modal method has been used to present and analyze the mechanisms governing the optical properties of *Coscinodiscus oculus-iridis* frustules. This exploration aims to unravel how the structural features of diatom frustules are fine-tuned to enhance the interaction of light with chloroplasts.

Chapter 8: Modification of diatomite

- In this chapter a modification of diatomite powder by gold nanoparticles using layer-by-layer technology in combination with a freezing-induced loading approach is demonstrated. The obtained composite structures are characterized by dynamic light scattering, extinction spectroscopy, scanning and transmission electron microscopy, photoacoustic imaging technique, and tested as a platform for surface-enhanced Raman scattering using Rhodamine 6G.

Chapter 9: Conclusions and Outlook

- This part of the thesis summarizes the research findings and introduces prospects for future research endeavors.

Chapter 2. Literature review

2.1 Introduction to the world of diatoms

Phytoplankton is a diverse group of photosynthetic microorganisms that includes diatoms, dinoflagellates, cyanobacteria, coccolithophores and other types of algae. It is estimated that these single-celled primary producers of organic matter account for about half of the global fixation of carbon, and are responsible for the export of fixed carbon to the deep ocean through the biological carbon pump[13]. The main functional groups of marine phytoplankton include nitrogen fixers (cyanobacteria), silicifiers (diatoms), and calcifiers (coccolithophores). Phylogenetic diversity of these eukaryotes is illustrated in Figure 2.

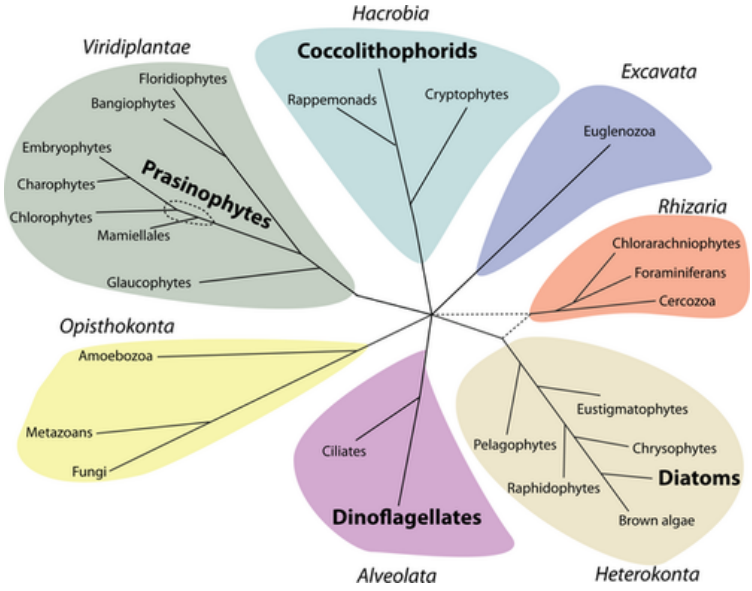

Figure 2. Phylogenetic diversity of eukaryotes showing the four major lineages of phytoplankton highlighted in bold typeface (prasinophytes, coccolithophorids, diatoms and dinoflagellates). Adopted from Ref.[13]. Reproduced with permission from John Wiley & Sons, Inc.

At present, diatoms are considered to be an extensive taxonomic group of unicellular microorganisms at the type or division level (Biota: Chromista, Kingdom: Harosa, Subkingdom: Heterokonta, Infrakingdom: Bacillariophyta, Phylum). Despite the fact that many species of diatoms are capable of forming colonies of considerable size, at the individual level they remain unicellular. Figures on the origination period of diatoms as an evolutionary group of marine organisms differ depending on the method of study. There are several specific assumptions about the lifetime of diatoms depending on the various studies on their age. Thus, according to the estimation using the molecular clock method, they may be as old as 240 million years[14,15]. However, paleontological approaches—revolving around an age analysis of ancient microfossils—indicate that diatoms were separated as a group in the world ocean about 145 million years ago[16]. The paleontological approach with respect to the diatoms should now be considered as more reliable.

Humans have been fascinated by the intricate structure of diatom frustules for well over a century. Figure 3 contains reproduction of plates from Ernst Haeckel's "Kunstformen der Natur"[17] published in 1899–1904. Haeckel made hand drawings as the basis for fabricating engraving plates, in a manner similar to that used by Hooke in preparation of his Micrographia treatise[18]. Their beauty fascinated even Charles Darwin, who mentioned them in his work "On the origin of species by means of natural selection, or the preservation of favoured races in the struggle for life": "Few objects are more beautiful than the minute siliceous cases of diatoms, were they only created to be admired under the microscope?"[19]

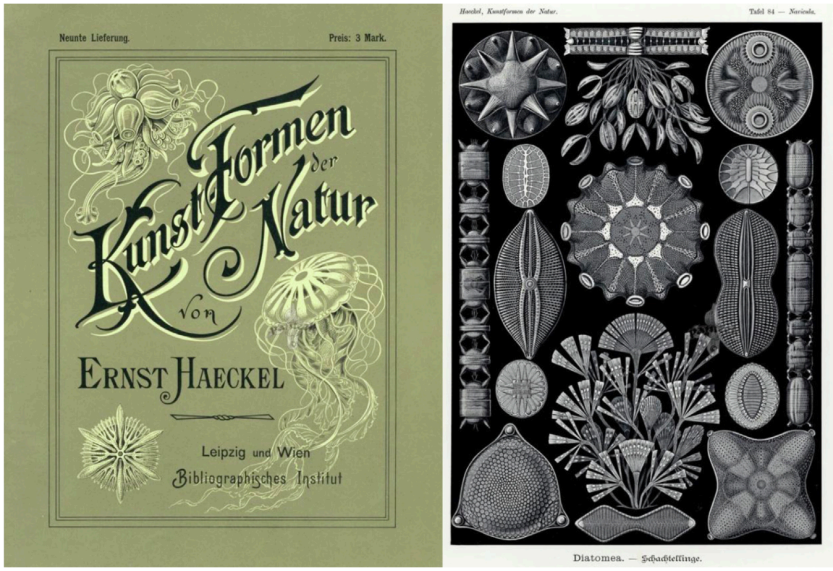

Figure 3. Left – Cover page of Ernst Haeckel's Kunstformen der Natur. Right – Plate 84 devoted to diatomea. Adopted from Ref.[18]. Reproduced with permission from Elsevier Ltd.

According to the taxonomy used by Algaebase.org[20], the diatoms include the centric species with multiradial and bipolar symmetry (classes *Coscinodiscophyceae* and *Mediophyceae*), and pennate species with bilateral symmetry (class Bacillariophyceae)[21]. The latter includes the subclasses *Fragilariophycidae* and *Urneidophycidae* (without raphe on the valve) and *Bacillariophycidae* (with raphe)[21]. They appear as individual cells or colonies in different shapes (filaments, chains, ribbons, fans, zigzags, or stellate), either as free-floating (planktonic) or attached to the substrate (benthic or periphytic)[22]. Figure 4 shows basic diatom terminology, division and structural elements[23].

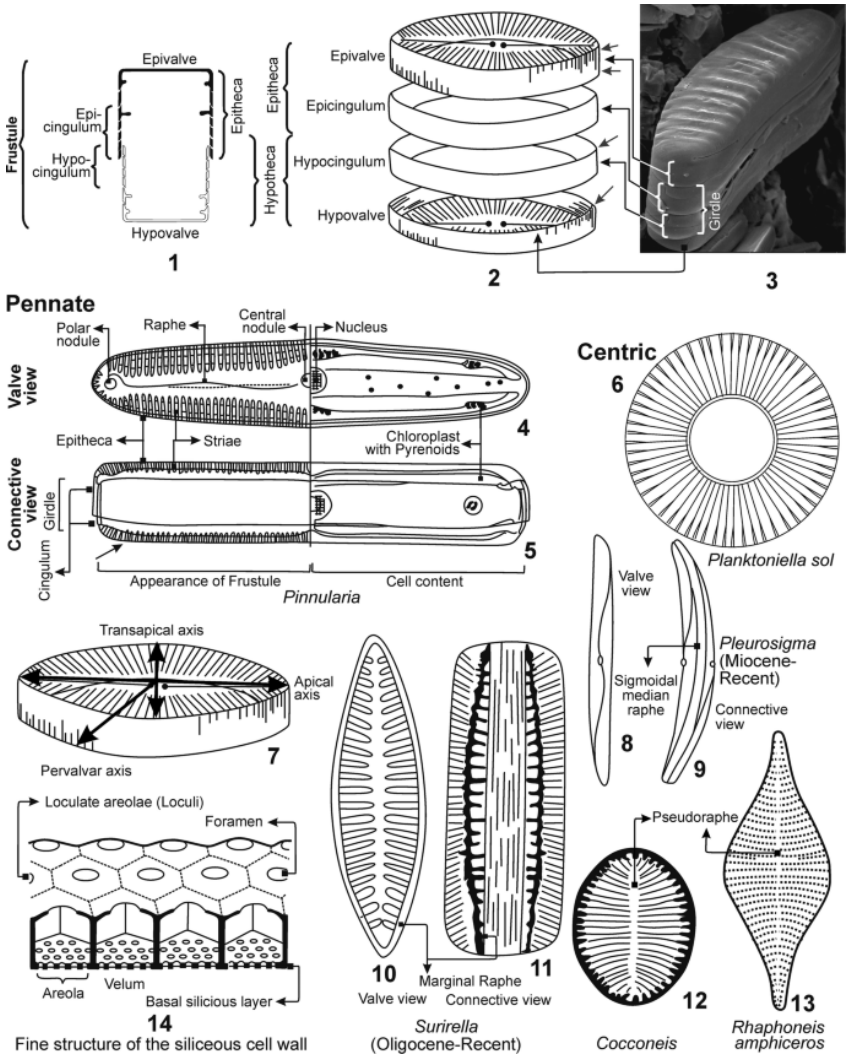

Figure 4. Diatom terminology. 1–3: Frustule terminology; 4–6: Examples of two major orders of diatom based on frustule shape—elliptical (pennate) (4 and 5) or circular (centric) (6) in valve view; these make up the two orders of diatoms (Pennales and Centrales, respectively). 4 and 5: Pennate diatom; 4: Valve view; 5: Connective view. 6: Centric diatom. 7: Symmetry axes. 8–11: Diatom species showing Raphe. 12 and 13: Diatom species showing pseudoraphe. 14: Structural details of the cell wall. Adopted from Ref.[23]. Reproduced with permission from Springer New Delhi.

The frustule consists of two intersecting halves: the upper, called the epitheca, and the lower, the hypotheca[24], which fit into each other, resembling a Petri dish, with sizes varying from 2 μm up to several mm. Diatoms, originating in fluctuating salinity lagoons, developed silicon shells in response to variable environmental conditions. Evolving over time, they diversified into various habitats, from aquatic to semi-aquatic environments. Diatoms now thrive in oceans, rivers, lakes, and even on diverse surfaces like rocks, tree bark, and soil. Some species have adapted to extreme conditions, residing on high-altitude rocks and the skin of whales [25]. They inhabit both water columns (plankton) and the depths (benthos) of water bodies. Additionally, diatoms can be found on macroalgae, invertebrates, fish, and floating objects. Notably, certain diatoms have successfully colonized artificial polymers, forming specialized communities capable of withstanding challenging conditions in polluted waters. Planktonic diatoms are most often endowed with a radial symmetry of the shell, whereas benthic diatoms display bilateral symmetry (Figure 5). In terms of the number of species, pennate (bilaterally symmetric) diatoms clearly predominate over the centric diatoms accounting for only 19% of the nearly 17,000 diatom species within the accepted taxonomic description[20]. However, planktonic species, mainly centric ones, are responsible for the bulk of diatom population by numbers and volume, especially in nutrient-rich and well illuminated marine waters. According to some estimates, diatoms are the largest group of eukaryotic algae, numbering over 100,000 known species[26,27].

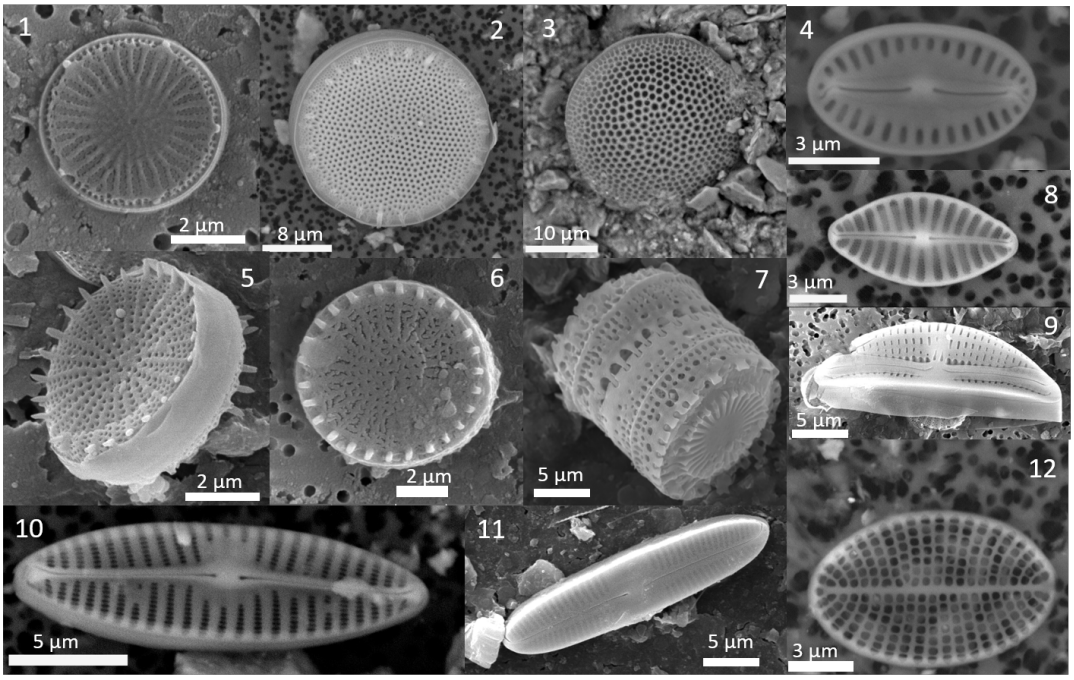

Figure 5. Centric diatoms (1–3, 5–7); pennate diatoms (4, 8–12). Adopted from Ref.[14] (Courtesy of M.V. Kravchishina, Ph. V. Sapozhnikov, O.Y. Kalinina, SIO RAS). Reproduced with permission from Scrivener Publishing.

According to Zhang et al.[28], the diatom frustules may be classified into three categories: rod shaped, flake shaped and generic 3D shape, as illustrated in Figure 6. The plane of the valve surface is defined as XY-plane. The major axis of the valve is X, while the minor axis of the valve is Y (for pennate diatoms only; for centric diatoms: X=Y). The valve-through axis is z-axis, and the length of the line connecting the centers of epivalve and hypovalve is Z.

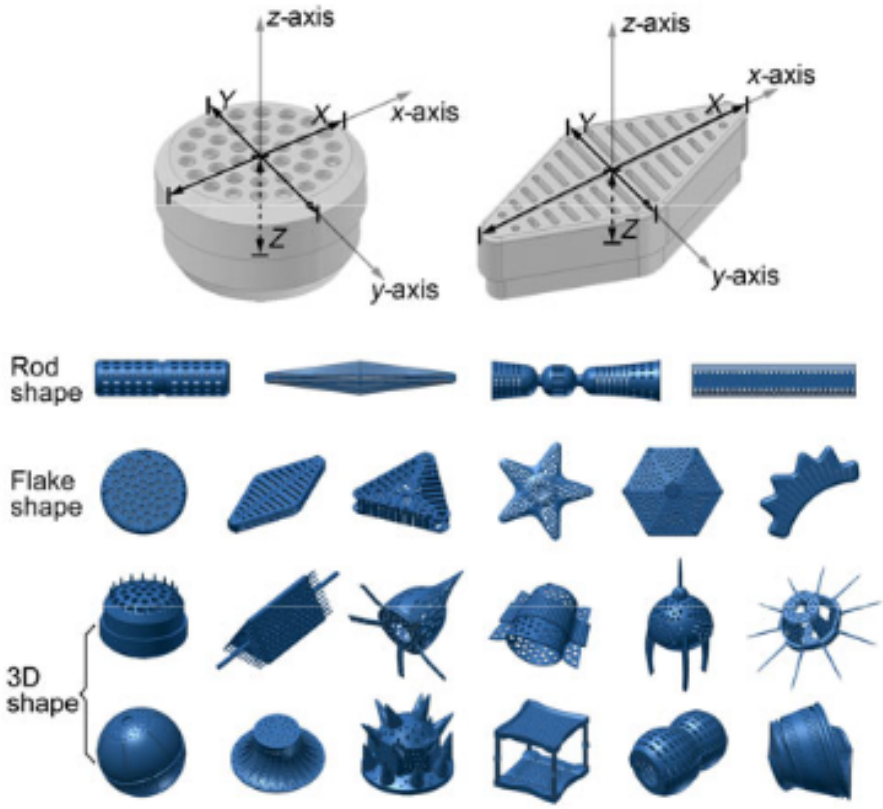

Figure 6. Shape classification of diatom frustules. Adopted from Ref.[28]. Reproduced with permission from Springer.

The diatom's complex adaptations allow it to survive, carry out metabolic functions, and reproduce successfully in any biotope. Many of them are reflected in the form of their shells, in the way the pores are arranged, the configuration of the pore apparatus itself, sutures, outgrowths, in the size of the cells and the thickness of the shell. Diatom shells reflect the evolutionary path and adaptive response of the species to the varying environmental conditions in which it has evolved. Mobile diatoms (class *Bacillariophyceae*)[29] capable of sliding at different speeds among thickets or sediment particles have a bilateral shell shape and are endowed with special devices for locomotion – variously organized raphes[14]. The forms with radial symmetry of the

frustule are grouped into the *Coscinodiscophyceae* class. These diatoms have characteristic adaptations that allow them to float in the water column: singly or in colonies. The coscinodiscoids shown in Figure 7 hover due to the large size of single cells, have thin-walled shells and contain large vacuoles in the cells, which balance their density with the surrounding water[14].

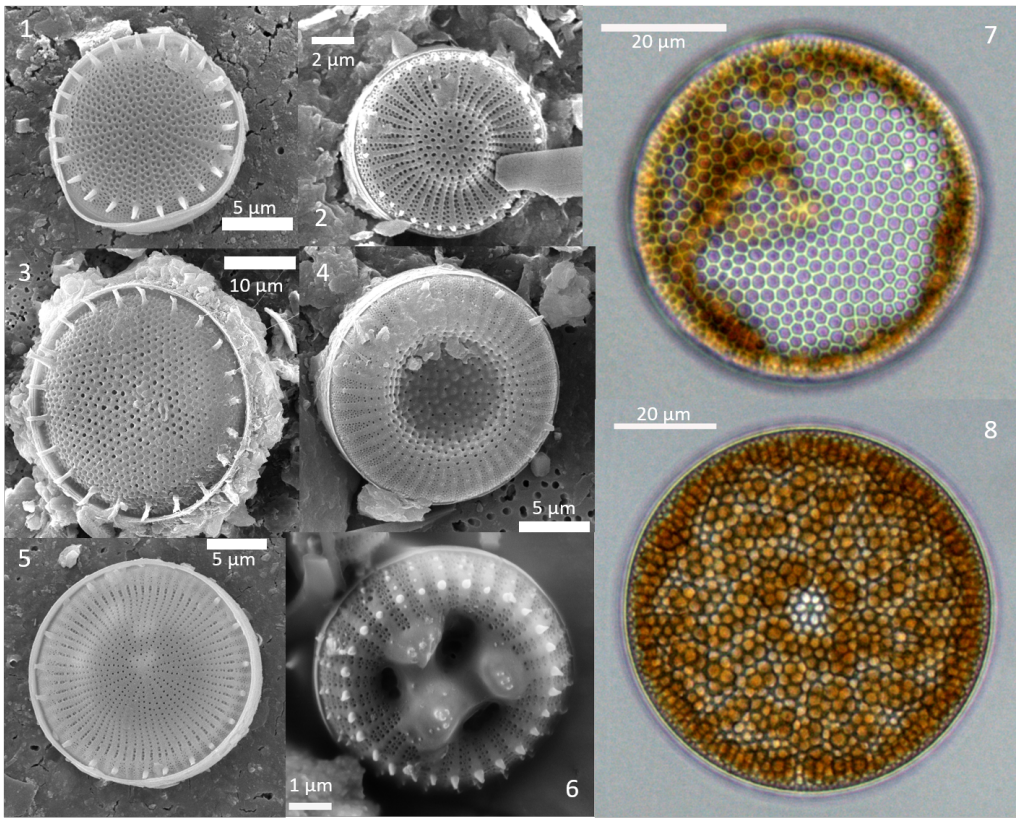

Figure 7. Different representatives of thalassiosiroids (1–6) and coscinodiscoids *Coscinodiscus radiatus* (7, 8). Adopted from Ref.[14] (SEM images are courtesy of M.V. Kravchishina, light microscopy images are taken by Ph. V. Sapozhnikov, SIO RAS). Reproduced with permission from Scrivener Publishing.

In the context of visualizing and monitoring growth, this thesis explores both types of diatoms. A centric diatom species was selected for the study of optical and mechanical properties, owing to its intricate multilayered structure. Studying both marine centric and freshwater pennate diatoms is important for a comprehensive understanding of diatom growth dynamics. These two types represent distinct ecological niches, each with its own set of environmental conditions. Monitoring both allows for a broader insight into how various factors influence diatom growth rates in different habitats. This comparative approach aids in developing a more comprehensive understanding of the ecological factors affecting diatom populations and their responses to environmental changes. Additionally, it provides a basis for evaluating potential applications of diatoms across diverse aquatic environments.

The presence of a silica exoskeleton ensures the performance of many vital functions of the unicellular micro-organisms – the interaction and exchange of gases, nutrients and other metabolites between diatom cells and the surrounding environment, protection from external mechanical influences, attachment to substrates, filtration, regulation of metabolism processes, control of light absorption during photosynthesis and the protection of DNA from UV radiation[27,30–32].

Due to the large number of pores of various sizes, diatom frustules have a high specific surface area, high adsorptivity and porosity, high mechanical stability, biocompatibility and low toxicity[33]. Cultivating diatoms in large quantities is straightforward and doesn't demand complex infrastructure or costly resources. This simplicity renders diatom cultivation a cost-effective means of obtaining biomass abundant in valuable compounds. Additionally, utilizing diatom silica for biotechnological applications provides an economical alternative to synthetic silica,

which involves labor-intensive and potentially hazardous production processes[34]. This is especially noteworthy considering the plentiful and naturally occurring sources of diatomite[35,36]. To proliferate in the shallow well-illuminated waters in the presence of predators, diatoms must protect themselves from various mechanical influences. The intricate architecture of the frustule provides structural integrity while allowing for flexibility[37]. Additionally, the specific arrangement of the silica filaments within the frustule contributes to its overall strength and resistance to mechanical stresses. This combination of stability and lightness allows diatoms to effectively withstand external forces, such as water flow and turbulence, ensuring their survival in diverse aquatic environments.

2.2 Hierarchical structuring of diatom algae

Essentially, hierarchical structure refers to the thoughtful and purposeful organization of material building blocks at each dimensional level in order to create multifunctional structures and mechanisms[14]. Nature provides numerous examples of successful hierarchical structuring in soft and hard tissues to satisfy the diverse and frequently contradictory requirements posed by the varying environments of living organisms[38].

The hierarchical structuring of diatom algae is a fascinating area of study that has been attracting the attention of researchers for many years. At the macroscopic level, diatoms exhibit a wide range of shapes and sizes, which are decorated by the intricate patterning of their frustules. These patterns are highly complex and can vary greatly between different species, making them an important tool for taxonomic classification. At the microscopic level, the frustule is composed of a series of layers

that are arranged in a hierarchical manner[6,39]. The outermost layer is typically composed of large, irregularly shaped pores that allow for the exchange of nutrients and gases with the surrounding environment. Beneath this layer, there is a series of smaller pores that are arranged in a regular pattern. These pores are thought to play a role in the control of water flow around the diatom cell, which is important for nutrient uptake and waste removal. The innermost layer of the frustule is composed of a dense, highly ordered lattice structure that is responsible for the overall strength and rigidity of the cell wall. This lattice structure is made up of silica nanoparticles that are arranged in a hierarchical manner, with smaller particles forming the building blocks for larger structures. Such hierarchical structure is well demonstrated in Figure 8a[28].

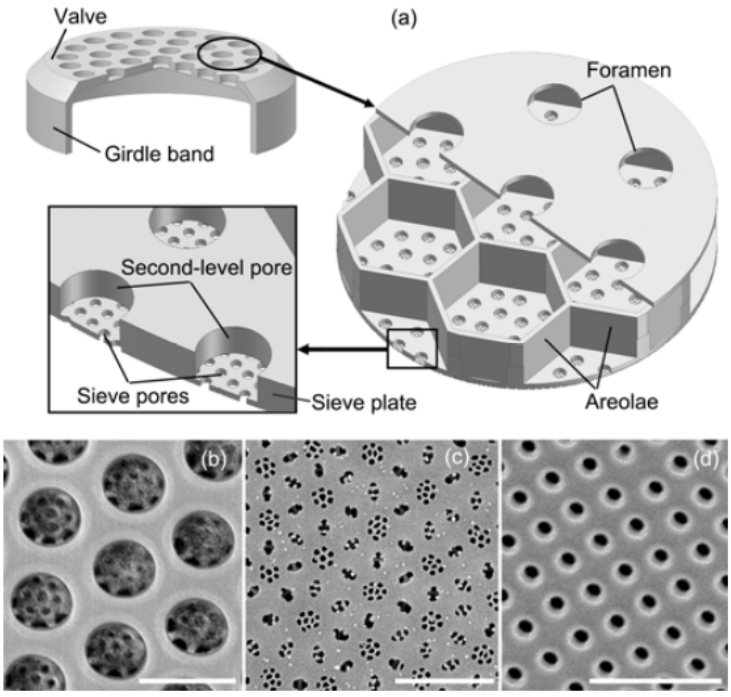

Figure 8. Typical structure of multilevel pores (Coscinodiscus sp.). a) 3D model; b) arrays of foramen and second-level pores, scale bar 1 μm; c) array of sieve pores, scale bar 2 μm; d) array of nanopores on girdle band, scale bar 1 μm. Adopted from Ref.[28]. Reproduced with permission from Springer.

Figure 8b shows regular array of large pores – foramen; a circular or hexagonal chamber – areola, under the foramen; second-level pores with a diameter of 200 nm, located at the bottom of the areolae. Sieve pores with diameter 40 nm are distributed inside second-level pores (Figure 8c). The mantle and girdle band also contain numerous pores, as shown in Figure 8d. It is also believed that the formation of these patterns is the result of a self-organized phase separation process[40]. Recent advances in imaging techniques, such as SEM [41] and X-ray tomography [41], have allowed researchers to study the hierarchical structuring of diatom algae in unprecedented detail[27].

Certain hierarchical multifunctional architecture of a diatom frustule is DNA-coded and biologically driven. For example, the biosilicification process in diatoms is demonstrated on *Thalassiosira pseudonana* (Figure 9)[42].

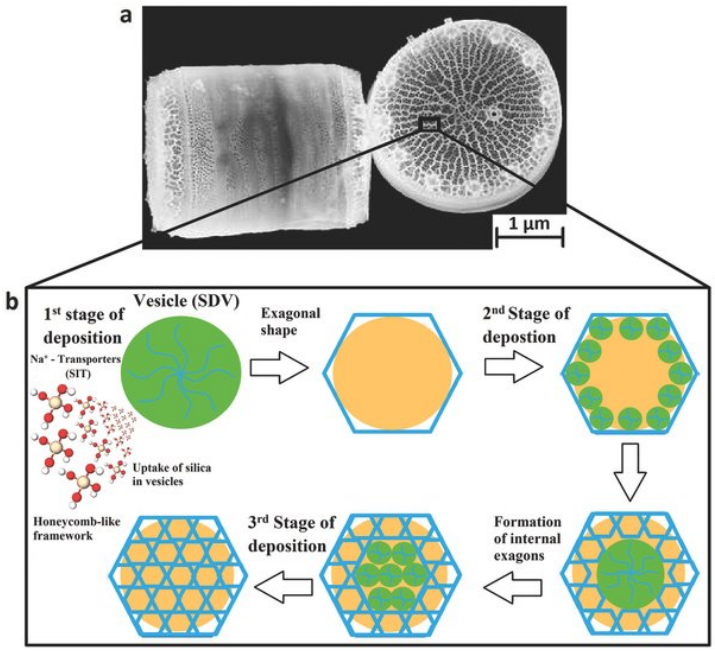

Figure 9. Biosilicification in diatoms. a) *Thalassiosira pseudonana* diatom (credit to University of Washington). b) Biosilicification mechanisms in the formation of hierarchical silica-based honeycomb-like structure of diatom skeleton. Adopted from Ref.[42]. Reproduced with permission from Wiley-VCH.

Diatom frustules formation is a complex process that involves the synthesis and assembly of a silica shell, which serves as a protective layer and structural support for diatoms. The process requires water-soluble silicic acid $Si(OH)_4$, which is transported by silica transport vesicles (STV) to the silica deposition vesicles (SDV) where the valves are formed[28] as shown in Figure 10a. The silanol groups of $Si(OH)_4$ are hydrolyzed in SDV and form Si-O-Si bonds. Silaffins proteins and long chain polyamines (LCPA) in SDV catalyze the hydrolysis reaction and influence the valve structure[43]. Firstly, the framework structure is produced, followed by the thickening of the valve and development of microstructure. During the division the diatom cell separates into two; each half inherits one valve and undergoes an identical frustule formation process. This process results in two new cells with symmetrically placed valves, but with different sizes labelled as 1 and 2; the newly formed "half-thecas" in SDV are slightly smaller (labeled as 2 and 3) (Figure 10b). After the first division, the two daughter cells have frustules composed of 1–2 and 2–3 separately. After the second division, four daughter cells are produced, and so on. Every act of division reduces the size of frustule by dozens of nanometers, but without the change in the pore size. When the size of a cell reduces to below two-thirds of the biggest cell, the cells undergo a unique form of cell division called the auxospore formation, which allows them to restore their size and morphology.

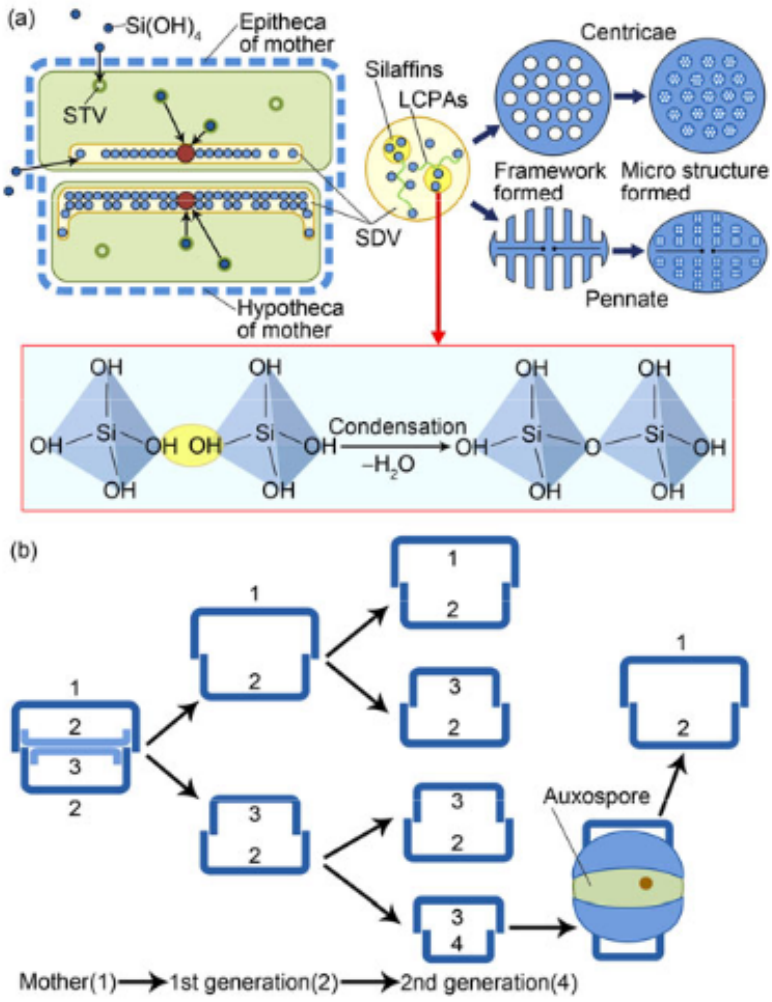

Figure 10. Schematic illustrations of: a) formation, b) reproduction of diatom frustules. Adopted from Ref.[28]. Reproduced with permission from Springer.

Nevertheless, the fine local mechanisms of phase separation in silica deposition vesicles at the nanometer scale still needs to be systematically studied to be understood. This would open the pathways for these processes to be directed and customized, and potentially used to implement the paradigm of Bio-Assisted Nanometer Size Additive Manufacturing (BANSAM)[14]. BANSAM assumes the transition to nature-like fabrication technologies in the 21st century that are simultaneously green, sustainable, non-carbon, and possess nanometer tolerance.

2.3 The mechanical properties of diatoms

The material, shape and thickness of the frustules, as well as the spatial order of the pores and the topology of the channels connecting them determine such mechanical properties as stiffness, strength and natural oscillation frequency. However, the fine structure of the frustule porosity and the nanomechanical properties associated with it present challenges for the experimental study involving the application and detection of forces at scales relevant to the diatom cell. The elastic modulus, hardness, and tensile strength of various diatom species were studied using various experimental methods such as nanoindentation[44], AFM probing[45–47], and bending with glass microneedles[48]. In a groundbreaking study by C.E. Hamm et al.[48] the mechanical performance of the diatom frustule was assessed by performing loading tests with calibrated glass microneedles which led to the conclusion that the frustules evolved to provide necessary mechanical protection for the cells against predators, as shown in Figure 11.

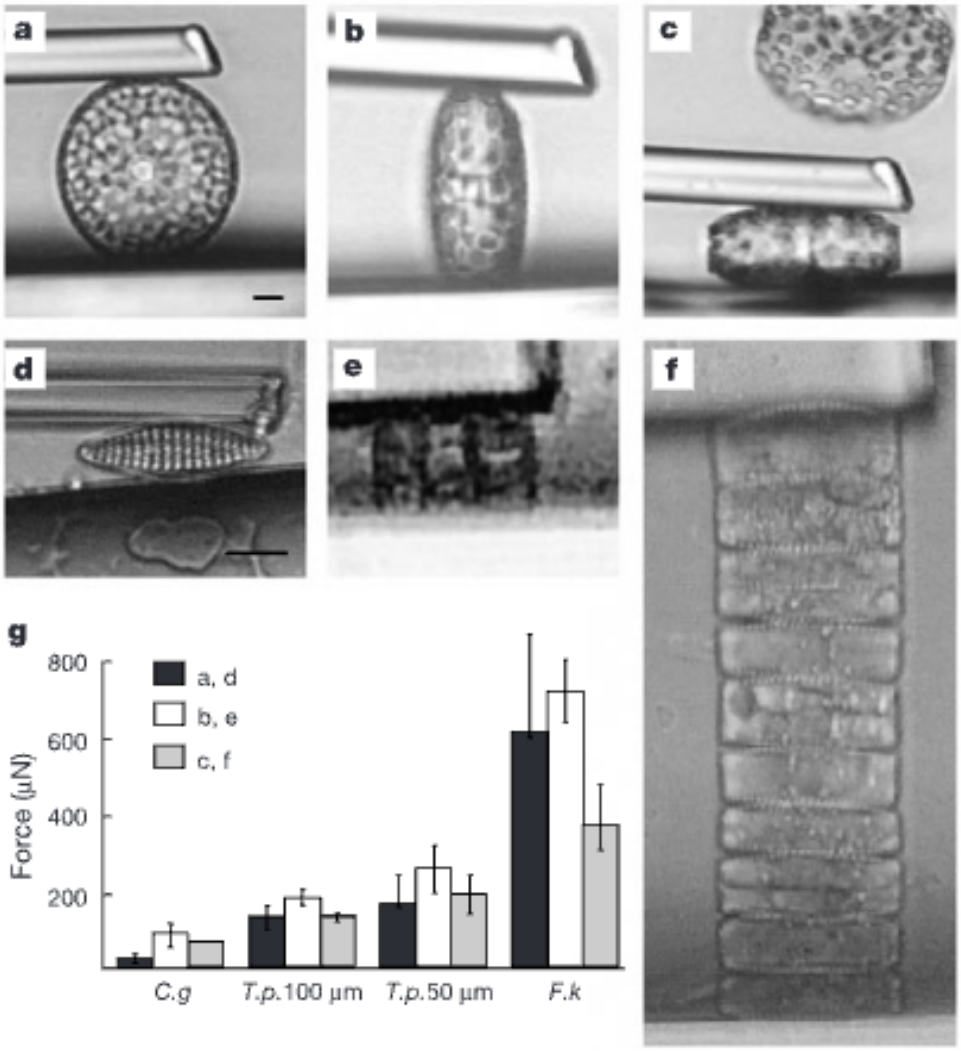

Figure 11. Glass needle tests: Live single cells of *T. punctigera* (a–c) and *F. kerguelensis* (d–f), in chains (e,f). Pressures applied along the girdle bands, (a,d), across the girdle bands (b,e), and across the centre of the valves (c,f). g) Forces necessary to break frustules. Scale bars, 10 μm. Adopted from Ref.[48]. Reproduced with permission from Springer Nature.

The first AFM studies on the mechanical behavior of diatom silica nanostructure were done in 2001 on dried diatoms by Almqvist et al.[47] They measured elasticity and hardness of the diatom *Navicula pelliculosa* semi-quantitatively with a

resolution down to approximately 10 nm and found that Young's modulus varied from seven GPa to hundreds of GPa, depending on the location. At the same time, hardness values ranged from 1 GPa to 12 GPa. These results confirmed that micromechanical characteristics are not restricted only to the biosilica itself, but they are also influenced by the hierarchical three-dimensional morphology of the porous structures of the exoskeleton on scales from nanometers to micrometers. Also, the change in mechanical properties can potentially be explained by differences in silica content and phase of development of a frustule.

Later, Losic et al.[45] mapped the nanoscale mechanical properties of *Coscinodiscus* sp. at different locations along the frustule using an AFM nanoindenter and calculated the hardness and elastic modulus from force penetration curves. AFM nanoindentation tests confirmed significant variations of the elastic modulus E (1.7-15.6 GPa) and hardness H (0.076-0.53 GPa) depending on frustule morphological features as pore size, porosity, and distance between pores. The lowest values were obtained on the cribellum and the girdle band. The location of the indentation, different biomineralization processes, and the quality of the nutrition can also influence the micromechanical properties of diatom frustules. Figure 12 shows AFM images of the internal plate with a series of indentations performed at various positions from the central region to the periphery and a typical force penetration curve.

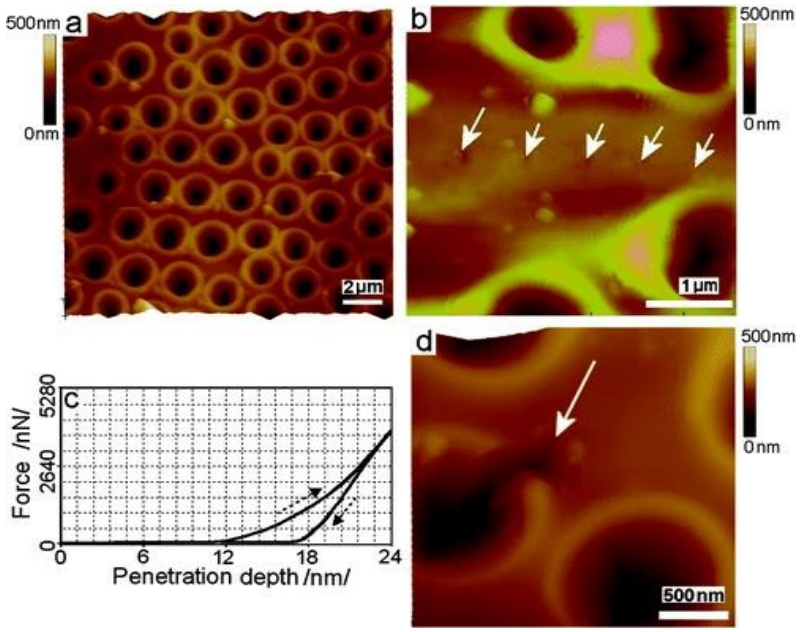

Figure 12. a) Low-resolution AFM image of the internal plate after nanoindentation. b) Series of indentation points (solid arrows) obtained using a force of 1.5-3 µN. c) Typical force penetration curve showing loading and unloading parts (dashed arrows). d) AFM image showing nanoindentation performed on an areola rib at higher applied load (12 µN). White scale bar is 10 µm. Adopted from Ref.[45]. Reproduced with permission from American Chemical Society.

Overall, the studies performed by AFM and nanoindentation demonstrated significant variations of the elastic modulus depending on the location[44,45,47] which may be due to the porous structure, nonuniform distribution of pores having different sizes and shapes, orientation of the frustule, location of the indent, etc. As suggested in Ref.[47], improved instrumentation and the study of several species under physiological conditions are needed to gain more knowledge about the native mechanical properties and their link to morphogenesis, i.e., the process of silica biomineralization.

Coscinodiscus sp. were also tested in situ by three-point bending. Aitken et al.[21] analyzed the bending of the beam with a square cross section and obtained a brittle fracture of the diatom frustule at the average stress of 1.1 GPa and strain 3.0% with the elastic modulus of 36.4 ± 8.3 GPa. Moreover, they estimated the relative frustule density near 30% and got the highest strength-to-density ratio, approximately 1700 N·m/kg among all known biologic materials, as provided by Ashby plot[49] in Figure 13.

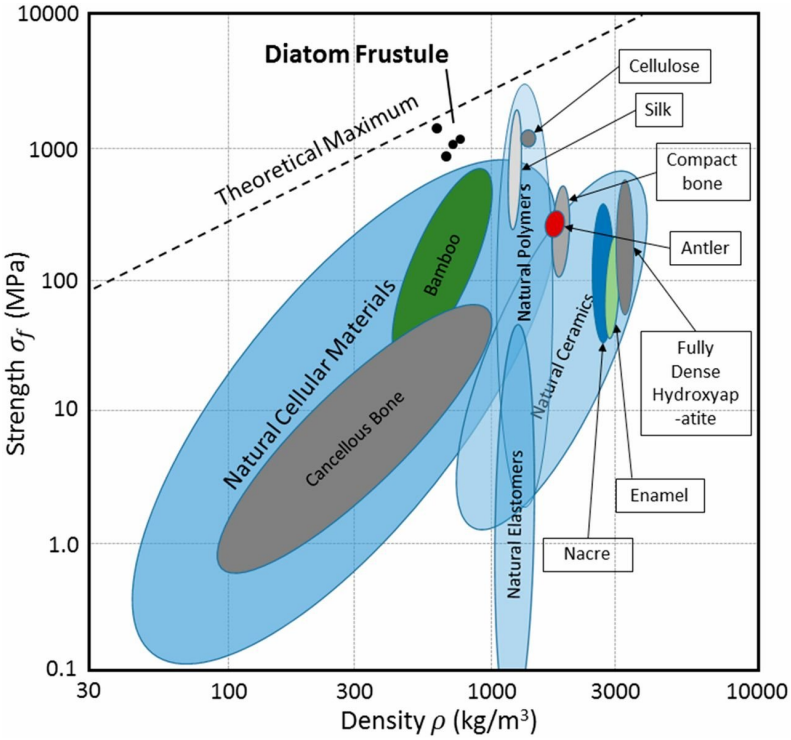

Figure 13. Ashby plot of strength vs. density for naturally occurring biological materials, including diatoms. Adopted from Ref.[49]. Reproduced with permission from Taylor and Francis Ltd.

Aitken et al.[21] proved the given results via nanoindentation of the girdle band of the frustule with modulus from 21.0 ± 7.7 GPa at 28 nm to 39.7 ± 8.3 GPa at 217 nm, which corroborates with the mechanics of the bending test. These results clearly

showed how Nature builds shells for live organisms simultaneously with the record lightweight and strength.

The summary of results of nanoindentation and bending experiments of diatom algae is shown in Table 1.

Table 1. The summary of results of nanoindentation and bending experiments of diatoms.

Genus	Test Type	Specimen Location	Stress or Load, mN	Strain or Penetration Depth, nm	Young's Modulus, GPa	Hardness, GPa	Reference
Coscinodiscus	A*	girdle	1.1 ± 0.3 GPa	3.5 ± 0.7 %	36.4 ± 8.3	–	21
	B**			28	21.0 ± 7.7	–	
			–	217	39.7 ± 8.3	–	
Coscinodiscus	B	center	– 0.01–0.03	60–100	1.1–10.6	0.10–1.03	50
Synedra	B	center	0.01	20	13.7–18.6	0.85–1.41	
Coscinodiscus	A	–	2.81 ± 0.15	2000	36.4 ± 8.3	–	51
Coscinodiscus	B	center	0.02–0.07	300–500	0.591–2.768	0.033–0.116	44
	B	edge	0.02–0.07	300–500	0.347–2.446	0.076–0.120	
Didymosphenia	B	–	0.1–1.4	1000–6000	31.8	–	52
Coscinodiscus	B	center	0.12	200	1.562	–	53
Navicula pelliculosa	B	transapical rib	0.01–0.05	4 – 8	7 – 25	–	47
		central rib		2.5 – 5	15 – 30		
		central nodule		1.5 – 4	30 – hundreds of GPa	–	

*A = three-point bending
**B = nanoindentation

Following an extensive review of the literature, it became evident that there was a notable absence of systematic investigations concerning the interplay between the structural and topographical aspects of diatom frustules, along with wet and air-dry

cells containing organic material, and their mechanical behavior under both static and dynamic loading conditions. This knowledge gap prompted the decision to embark on a study of these aspects. The choice to employ AFM and *in situ* nanoindentation within the SEM column in both static and dynamic modes was motivated by the need to comprehensively investigate the mechanical properties of diatoms at nano- and microscale levels. This approach allows for a thorough exploration of how cleaned diatom frustules and living cells respond to various loading conditions, capturing both the static and dynamic aspects. Moreover, AFM methods provides a nanoscale resolution, enabling a detailed examination of the structural and topographical features of diatom frustules, as well as wet and air-dried cells containing organic material. This systematic and multi-modal approach helps to elucidate the nuanced mechanical behavior of these organisms, shedding light on their potential applications as building blocks for miniature devices and sensors.

2.4 The optical properties of diatoms

Growth, behavior, and development of phototrophic organisms are strongly influenced by light. Over the course of evolution, several species of animals and plants have developed highly efficient photonic crystals[54,55]. Bio-inspired technology encounters challenges due to the current limitations in engineering techniques and the impracticality of mass-producing artificial devices that precisely replicate natural structures. Nevertheless, there are still several potential applications showing promise in this field. Therefore, it becomes increasingly apparent that a bottom-up fabrication approach would be ideally suited for exploiting the ability of living organisms themselves to manufacture micro- and nano-optical devices [56].

Low refractive index and extremely low absorption coefficient of nanoscaled well-organized silica materials make the latter an intriguing subject of optical studies[57]. The species-specific patterns of pores, ridges, and indentations on the silica cell walls endow diatoms with unique appearances under high magnification. These microscale structures have profound implications for the interaction between light and diatoms, as the porous silica induces diffraction and interference based on the dimensions, forms, and configurations of the pores and ridges[8,58–62].

In recent years, considerable attention has been devoted to investigating the optical properties of diatom algae, particularly with regard to their scattering and absorption of light. Diatoms in their living state are known to efficiently absorb light in the blue, green, and ultraviolet wavelengths, and to scatter light across a broad range of angles, which is attributed to the presence of chloroplasts[63,64]. This proficiency in capturing light energy renders diatoms crucial constituents in aquatic food webs. When light enters water, it is absorbed more strongly than in air and becomes partially polarized. Blue light penetrates much deeper depending on the concentration of dissolved matter and particles, whereas red, orange, and yellow light are quickly absorbed by water, as shown in Figure 14[65]. However, the majority of studies examining the optical properties of diatoms focus on cleaned frustules, neglecting the presence of organic material. Furthermore, many of these investigations are conducted or simulated in air, which is contrary to the aquatic natural habitat of diatoms. In this sense, the calculated effects of these experiments and simulations cannot provide complete biological answers to how living diatoms benefit from the interaction between frustule and light. These differences between measurements on cleaned frustules and diatoms in their natural habitat are shown in Figure 14.

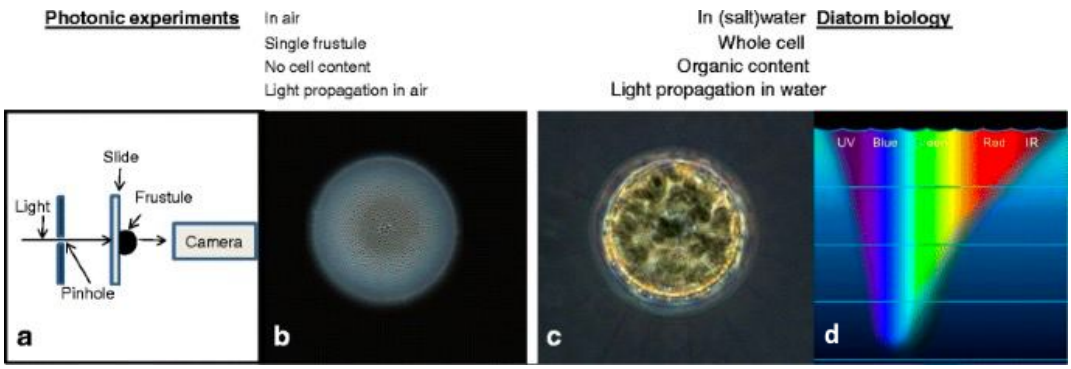

Figure 14. Overview of relevant features that differ between the diatom in its natural habitat and rinsed diatom valve measured using an optical setup (a). b) A diatom valve rinsed of organic material, c) A living diatom in water, d) A mapping showing how spectrum of transmitted light changes with depth. Adopted from Ref.[65]. Reproduced with permission from Springer Netherlands.

Moreover, the orientation of diatoms also affects the light propagation inside the frustules. In the natural environment, light usually falls on diatoms from the outer (convex) side, but it is quite possible that it can also be affected by the inner (concave) side when passing through the cell [65].

The interaction of light with the complex internal structure of diatom frustules can be described mathematically using the theory of wave propagation in periodic structures[66]. The periodicity and complex three-dimensional architecture of diatom frustules give rise to intriguing diffraction phenomena that have been investigated for their fundamental understanding and potential applications[8,62,67–69]. The diffraction of light by diatom frustules occurs due to the interaction of light waves with the complex surface structure of the frustule. The pores and ridges on the frustule's surface act as diffraction gratings, which split the incident light into a spectrum of colors and produce

interference patterns[70]. The diffraction patterns produced by diatom frustules can be used to create high-resolution optical devices, such as lenses and filters[71,72]. By understanding the principles behind this phenomenon, scientists can develop new technologies that are more efficient, smaller, and more precise than those currently available.

2.4.1 Light focusing and concentration

Diatoms can concentrate light into a single point by scattering and refracting it with the walls of their frustules. This allows the diatoms to concentrate the light into a specific area which can be used for photosynthesis or other metabolic processes. The process of light focusing in diatoms is important for the survival of the species, as it allows them to absorb more light for photosynthesis and therefore create more energy for the organism[69].

In the study by De Stefano et al.[73], the light concentration and focusing ability of *Coscinodiscus wailesii* (*C. wailesii*) were studied using a red laser beam with a diameter 100 μm. The results showed that the beam diameter was reduced by about 12 times at a distance of 104 μm from the valve position, acting like a lens (Figure 15).

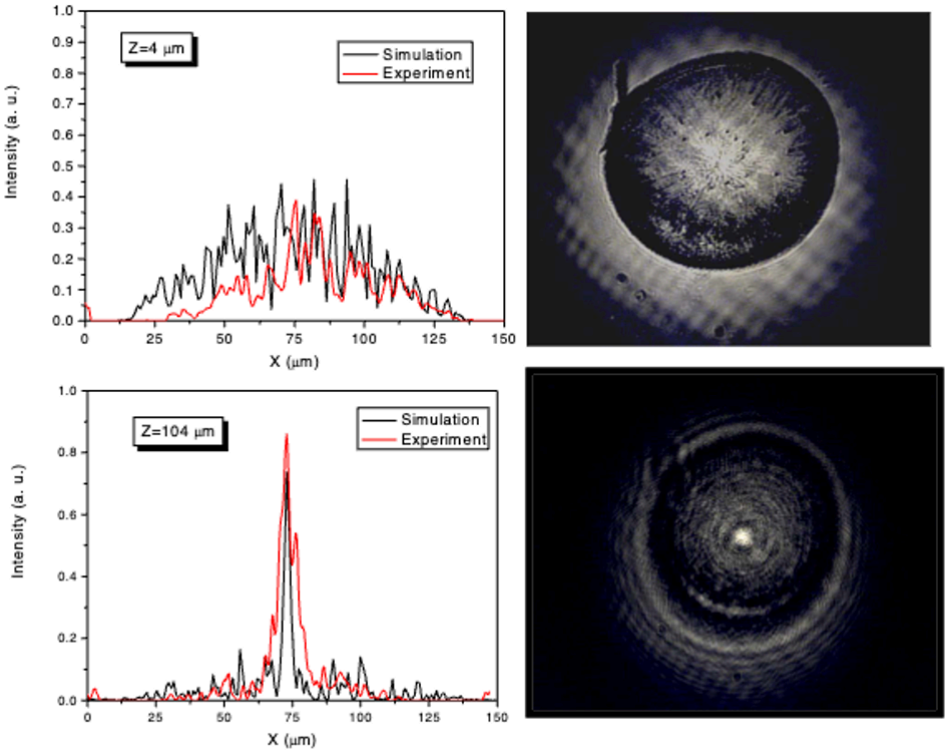

Figure 15. Left: The intensity distribution of the transmitted light at the distance (z) of 4 μm (top) and 104 μm (bottom): the red line is the experimental recorded one, the black line is the numerically estimated. Right: The corresponding images of the diatom surface recorded by a CCD at the two distances considered. Adopted from Ref.[73]. Reproduced with permission from Optica Publishing Group.

The focusing of light to a spot size smaller than the pinhole diameter at a certain distance from the valve was due to the way the light waves passed through the valve's areolae. De Tomassi et al. explained such behavior by the regular pore pattern and the superposition of the diffracted wave fronts.[74]

The focusing distance of the laser beam was found to be wavelength dependent, as shown in studies on *C. wailesii* (Figure 16)[74] and *Arachnoidiscus* sp., where a 633 nm laser beam was focused at a distance 163 μm.[62]

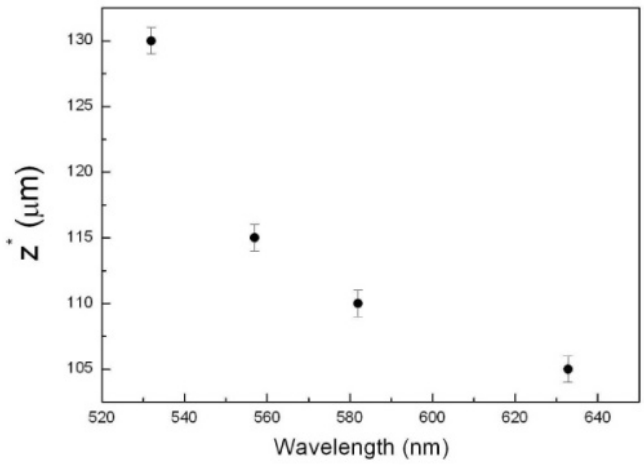

Figure 16. Distance z* of maximum intensity of the transmitted spot as a function of the wavelength of the incoming light beam. Adopted from Ref.[74]. Reproduced with permission from Optica Publishing Group.

In that way, the spatial distribution of the pores in the periodic structure of the valve affects light propagation, so the valve can be considered as multifocal lens. Romann et al.[32] investigated waveguide ability and multifocal lens properties of *Coscinodiscus centralis* and *C. wailesii* using confocal hyper-spectral imaging and found that multiple light cones were transmitted through the centric valve at several wavelengths, including 485, 535, 625, and 675 nm. Additionally, they showed that the intensity of transmitted light depends on the orientation of the valve, with light intensity decreasing when the incident light illuminates the internal side of the valve and increasing when it illuminates the external side.[32] The experiment also found that tilting the incident light at an angle of 10 degrees did not change the concentration behavior of the frustule. This suggests that the material is able to maintain its optical properties even when the angle of incident light is changed, which is important because it suggests

that silica-based biomaterials may have potential applications in industries that require stable and consistent optical properties, such as in the production of optical fibers or lenses. However, it is important to note that this experiment was conducted on a limited number of species and further research is needed to fully understand the optical properties of silica-based biomaterials in different environments and with different species.

2.4.2 Light trapping

The light trapping ability of *Coscinodiscus* sp. in photovoltaic application was demonstrated in the study by Chen et al. The first band diagram simulations for valve and girdle bands of *Coscinodiscus granii* (*C. granii*) showed that the generated photonic crystal modes depend on the periodicity of the structure, slab thickness, and incident wavelength.[75] However, some authors suggested that to exhibit a complete 2-D photonic crystal band-gaps, a refractive index contrast in the material of about 2 is needed.[76]

In the experiment conducted by Kieu et al.[72] *C. wailesii* diatom valve was fixed on top of an optical fiber and irradiated with a coherent supercontinuum broadband laser with the spectral range of 400-1700 nm in a small region of about 20 micrometers in order to study the diffracted and transmitted light through the valve as a function of the lattice constant in the periodic structure. When the valve was irradiated with different wavelengths at different angles, it generated colorful transmitted patterns in a hexagonal pattern (Figure 17), as a result of the interaction with the periodic structure of the diatom valve.

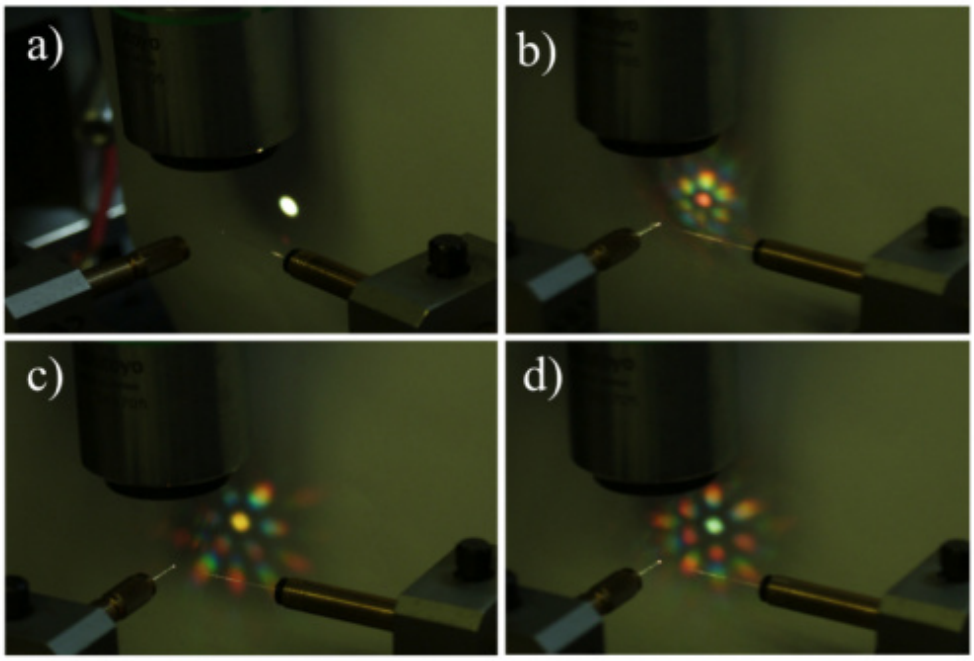

Figure 17. Optical images of the diffraction patterns obtained from the different regions of C. wailesii valve. a) No diatom was present in the beam path. b-d) The frustule valve was present in the beam path. The color of the central spot changed according to the location of the partial photonic band gap. Adopted from Ref.[72]. Reproduced with permission from Optica Publishing Group.

A study performed using a microfiber spectroscopic method found that the cylindrical frustule of the diatom *Melosira variance* (*M. variance*) has photonic crystalline characteristics that assist light absorption depending on the orientation[77]. A transmittance valley was observed between 400 and 500 nm when irradiated through its internal side, but not when it was irradiated perpendicular to the silica side wall, as shown in Figure 18[77]. The periodicity of the refractive index in the structure was found to be related to the observed transmitted spectra.

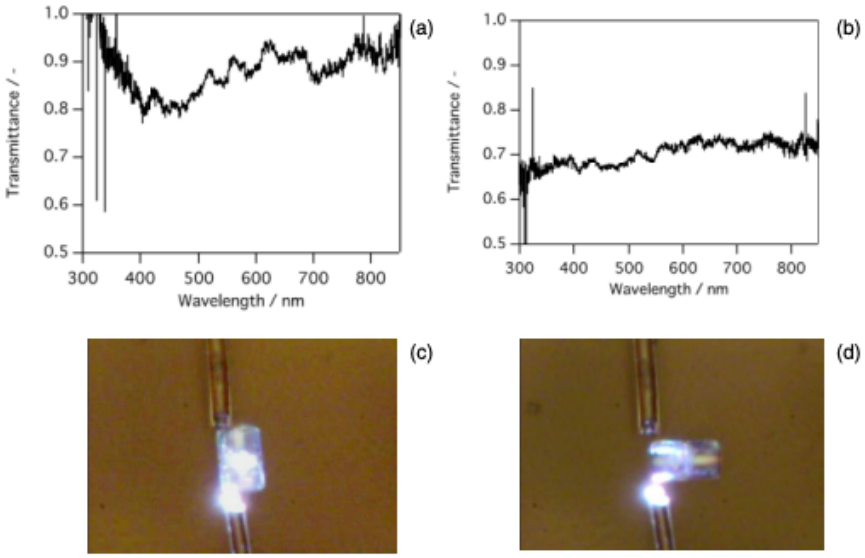

Figure 18. Transmittance spectra of a frustule using the following alignment: a) Incident light passing through the side wall of the frustule, b) Incident light passing through the frustule perpendicular to the side wall. Optical microscopy images of: c) parallel, d) perpendicular alignments. Adopted from Ref.[77]. Reproduced with permission from Japan Society of Applied Physics.

2.4.3 Spectral light filtration

Spectral light filtration is an important process in the life cycle of diatoms. To produce energy and food in the process of photosynthesis, they need to be able to access light in the water. However, light levels can vary, so the diatoms must have to filter the light in order to get the most out of their photosynthesis. Diatoms use their cell walls to absorb some of the light that enters their environment. The cell walls are made of a transparent silica, which allows most of the light to pass through. However, some of the light is filtered out as it passes through the diatoms' cell walls which helps them better regulate and take advantage of the light that is available.

Ellegaard et al.[65] investigated the protective properties of frustules and found that the frustules of certain diatom species were effective at protecting cells from harmful radiation. The samples were more transparent to the light in the visible range of the spectrum, than in the UV range, as shown in Figure 20.

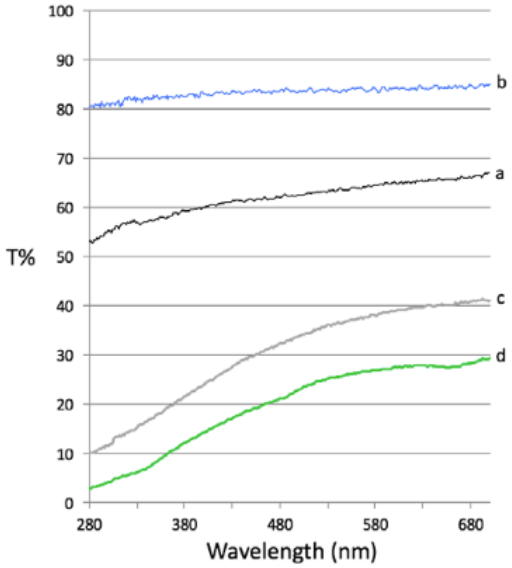

Figure 19. Transmittance spectra for: a - *Coscinodiscus concinnus*, cleaned frustules. b - *C. granii* cleaned frustules. c - *C. concinnus*, dried cells with cell content. d - *C. granii*, dried cells with cell content. Adopted from Ref. [65]. Reproduced with permission from Springer Netherlands.

M. varians frustules exhibit wavelength-dependent filtering behavior, with enhanced transmission of red light and absorption in the blue range[60]. On the other hand, Ferrara et al. showed that circular valve of *Arachnoidiscus* sp. absorb more green and red wavelengths[62]. In the realm of transmission measurements, specific spectral regions bear great significance in diatom biology. Chlorophyll *a*, the principal pigment governing the photosynthetic process, predominantly absorbs in the blue and red segments of the visible spectrum, while carotenoids, also vital in photosynthesis, mainly absorb in the green region[63]. Conversely, the examination of the interaction

between UVB radiation and diatom valves assumes importance in evaluating the extent to which silica nanopatterned valves can shield living organisms from DNA-damaging radiation. Evolutionary processes appear to have shaped frustules with the dual purpose of optimizing visible light absorption and minimizing damage induced by UVB irradiation. Thus, it is evident that the evolutionary advantage of frustules lies not only in their mechanical properties but also in their capacity to manipulate light in a differentiated manner based on wavelength.

2.4.4 Photoluminescence

Diatom shells contain various pigments, including chlorophylls and carotenoids, which absorb light and transfer the energy to other molecules, resulting in the emission of light, or luminescence. The photoluminescence (PL) properties of diatom algae have been extensively studied in recent years due to their potential use in bioluminescence applications. According to studies[78,79], upon illumination of the porous silicon (Si) and porous silica (SiO_2) by UV wavelengths, they emitted PL peaks in the visible spectral region.

The PL properties of diatom algae have been studied using spectroscopy, fluorimetry, and imaging techniques. De Tomassi et al.[80] showed that the intrinsic photoluminescence from frustules is strongly influenced by the surrounding atmosphere, since during the exposure to gases, the induced luminescence changes in the optical intensity and position of peaks. Photoluminescence responses of *Thalassiosira rotula* valves when exposed to different gases and volatile substances were demonstrated in the study by De Stefano et al.[81] The frustules were irradiated by 325 nm laser light which resulted in a multiband PL between 450 and 690 nm. Such

result was attributed to oxidized silicon nanocrystals (533 nm), porous silicon (609 nm), and hydrogenated amorphous silicon (661 nm).

The PL properties of the frustules were then tested with different gases. The valves' PL was quenched with electrophilic gases, which are attracted to electrons, while it was enhanced for nucleophilic ones, which are attracted to positively charged ions. For example, the PL was quenched when exposed to $NO_{2(g)}$ flux, showing high sensitivity in the order of sub-ppm level, as shown in Figure 20. This sensitivity was strongly dependent on the structure, porosity, and gas nature.[82]

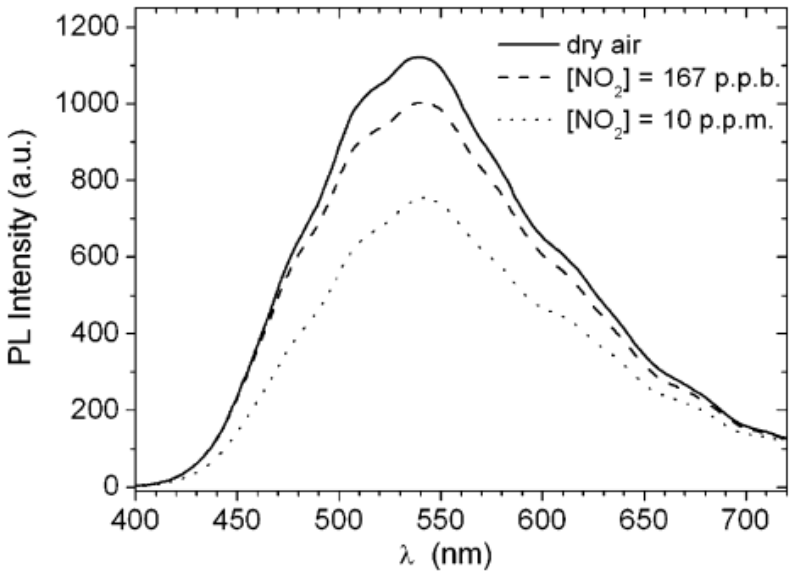

Figure 20. *Thalassiosira* photoluminescence spectrum in dry air (continuous line), in 167 ppb of NO_2 in dry air (dashed line) and in 10 ppm of NO_2 in dry air (dotted line). Adopted from Ref[82]. Reproduced with permission from Elsevier Ltd.

Some studies demonstrated the photoluminescence of chemically modified diatoms. For example, the results obtained by Townley et al. showed that intact frustules of *C. wailesii* exhibited a broad PL peak in the range of 500-650 nm upon

irradiation with 442 nm laser[83]. However, frustules that were grown with nickel sulfate showed a quenched PL. This suggests that the chemical modification of frustules can affect their PL properties. De Stefano et al.[84] found that green PL of diatoms peaked between 520 and 560 nm, can be attributed to Si–H groups, but also to the presence of nanostructures which enhance the light emission by quantum confinement. Antibody doped frustules showed high sensitivity (1.2 ± 0.2 nm·μM^{-1}) and detection limit (100 nM^{-1}) when irradiated by 325 nm laser[84], while frustules from *Psammodictyon panduriforme* exhibited emission peaks at 417 nm and 534 nm due to oxygen-vacancy defects[85]. Under pulse laser excitation, the results showed a single narrow emission peak near 475 nm, which may be explained as a consequence of a putative quantum confinement effect due to the mesoporous silica and the quasi-regular pores in the frustules' structure. The PL spectra obtained in the study are shown in Figure 21[85].

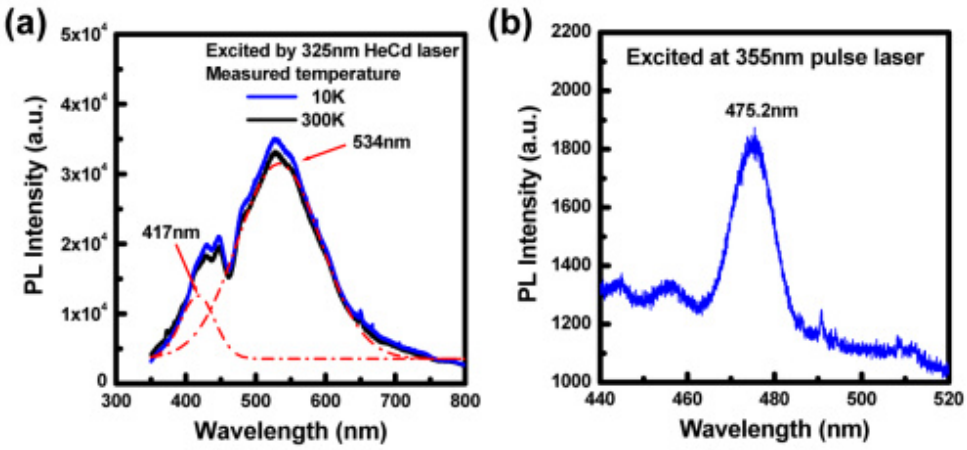

Figure 21. The micro-photoluminescence spectra of diatom frustule were measured by: a) 325 CW laser and b) 355nm pulse laser acted the excitation laser sources. Adopted from Ref.[85]. Reproduced with permission from Optica Publishing Group.

Arteaga-Larios et al.[86] studied the UV-excited photoluminescence emitted by the diatoms and compared it between both species of diatoms, of different ages, and with the PL of synthetic porous SiO_2. They also conducted morphometric analysis of the size and arrangement of pores to observe any correlation with the PL of two diatom species of different ages. The UV-excited PL displayed four clearly defined peaks within the blue-region spectrum, on top of the broad PL characteristic of synthetic porous silicon dioxide. The observed PL shifts are correlated with a substantial increment of Si-OH groups adsorbed on the frustule surface, as revealed by Fourier transform infrared spectroscopy.

As suggested in the study[87], the different defect states in the material cause different levels of electron excitation, which in turn causes the emission of light in the blue and green regions. The oxygen defect centers, specifically, allow for the emission of light in the blue region, while the neutral oxygen vacancy and self-trapped excitons are responsible for the emission of light in the green region.

Table 2 summarizes the studies on optical properties of diatoms.

Table 2. Summary of studies on optical properties of diatoms

Species	Method	Main results	References
C. wailesii	Spectroscopy	The beam diameter was reduced by about 12 times at a distance of 104 μm from the valve position	[73]
C. wailesii	Spectroscopy	Focus distance depends strongly on the wavelength.	[74]
Arachnoidiscus sp.	Spectroscopy, digital holography	A 633 nm laser beam was confined at a distance 163 μm.	[62]
M. variance	Microfiber spectroscopic method	Light absorption depending on the orientation, with a transmittance valley observed between 400 and 500 nm when irradiated through its internal side	[77]
C. granii & concinnus	Spectroscopy	Valves more transparent in the visible region than in UV region of the spectrum	[65]
C. wailesii & C. centralis	Confocal hyperspectral imaging	Light trapping depends on wavelength and the valve orientation, but not on the incident angle	[32]
C. granii	Spectroscopy	The generated crystal photonics modes depend on the periodicity of the structure, slab thickness, and incident wavelength	[76]
M. variance	Spectroscopy	Enhanced transmission of red light and absorption in the blue range	[60]
T. rotula	Spectroscopy	PL of diatoms was suppressed in the presence of electrophiles, while it was amplified when exposed to nucleophilic gases.	[81]
C. wailesii	Spectroscopy	Diatoms displayed a broad PL peak in the range 500-650 nm. Frustules grown with nickel sulfate exhibited suppressed PL properties.	[83]
C. concinnus	Spectroscopy	PL of modified frustules demonstrates heightened sensitivity to antibodies.	[84]
Psammodictyon panduriforme	Spectroscopy	Diatoms exhibited emission peaks at 417 nm and 534 nm due to oxygen-vacancy defects.	[85]
Gomphora, Gomphocymbella	Spectroscopy	The PL shifts are associated with a notable increase in Si-OH groups adsorbed onto the frustule surface.	[86]

2.4.5 Potential applications based on the optical properties

Beyond the aesthetic appeal of diatom frustules, their optical characteristics find practical applications and serve as inspiration for novel technologies[72,88,89]. Their

sensitivity to changes in the environment around them means that diatoms can be used as biosensors to detect chemicals or other factors. The nanoscale structures of diatom cell walls have also inspired new approaches to nanofabrication, such as using diatoms as templates to create replicas of their pores and ridges in materials like metals, plastics, and ceramics. Diatoms demonstrate how intricately patterned microscale structures can be engineered to produce remarkable optical effects.

Figure 22 summarizes optical properties and some of the potential applications of diatom micro- and nano-structures made of silica.

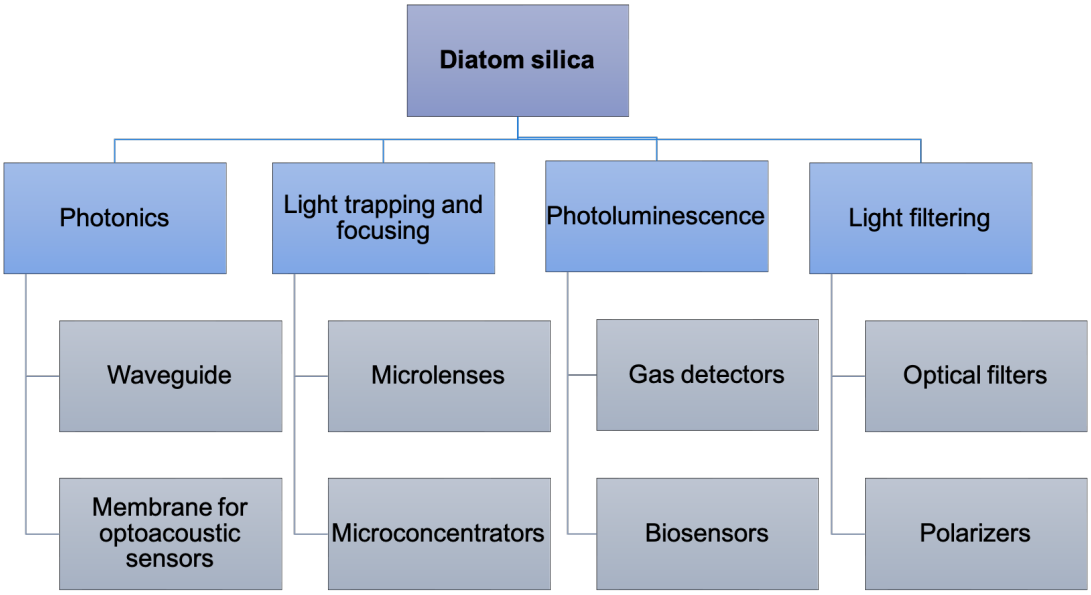

Figure 22. Diatom biosilica optical properties and their potential applications

The interest in diatom frustules as prototypical photonic crystals for microelectronic technology arose relatively recently and has already been reflected in a number of high-profile publications[90–96].

Aulacoseira and *Thalassiosira* frustules have been employed for detecting trace amounts of pure gases such as NO(g), H_2(g), and NO_2(g)[82,97]. Diatoms have the ability

to trap light, which can enhance the amount of light harvested by solar cells[76]. In addition, frustules from diatoms can be modified with TiO2 to improve the efficiency of Dye Sensitized Solar Cells (DSSC) technology[93].

Diatoms can be modified with molecules that can endow them with an ability to attract specific target molecules or pathogens. Researchers have experimented with the immobilization of proteins, antibodies, DNA and other biomolecules on the surface of diatom shells that can interact with a specific analyte, leading to detectable optical changes. Photoluminescence modulation in antibody functionalized diatom frustules of *Amphora sp*. was used by Viji et al.[98] to detect BSA protein at mM level, whereas Selvaraj et al.[99] used the same species to detect Salmonella typhi at detection limit of 10 pg. The review of diatom-based biosensors is provided in the article[87].

Diatom silica has potential for photonics applications due to the nanoscale 3D structures of frustules, which can be modified with luminescent dyes for luminescent materials or metallic nanoparticles for nano-plasmonic sensors for label-free chemical and biological sensing.[100–102]

2.5 The modification and applications of diatoms

There are different ways of modifying diatom algae that can transform them into a custom-designed micro/nanomaterial with desirable properties for various applications.[103]

2.5.1 Surface modification

One of the most common methods of diatom modification is surface modification, which aims to enhance the surface properties of the diatom algae, such as hydrophilicity, surface charge, and increase the surface area for higher catalytic

activities. Schematic representation of different functionalization techniques for pharmaceutical applications are shown in Figure 23.[104]

Figure 23. Scheme of the surface modification techniques of diatoms in pharmaceutical applications. Adopted from Ref. [104] Reproduced with permission from MDPI.

Surface modification can be achieved by changing the chemical composition of the surface using various techniques such as chemical treatment, plasma treatment, or thermal treatment. Some of the most widely used functionalization approaches include noncovalent and covalent functionalization and chemical conversion of diatomite[94]. The surface of siliceous diatom frustules containing reactive silanol (Si-OH) groups can be readily modified with different functional groups, such as –SH, –NH2, –COOH, −CHO for the immobilization of different biomolecular probes (DNA, proteins, antibodies)[105] and drug loading[106–110].

2.5.2 Genetic or metabolic modification

Diatoms' genes can be modified or transferred to enhance their properties. Genetic modification can be achieved using various techniques such as gene cloning, transfection, or CRISPR-Cas9 gene editing[111–113]. Genetic modification can alter the structure and composition of the diatom cell walls, enhancing their desirable properties, such as efficient CO_2 fixation, higher lipid production, and increased tolerance to environmental challenges.[113] Moreover, diatoms can be bioengineered by modifying their metabolism pathways through genetic or metabolic engineering. This method aims to optimize the metabolic pathways of diatoms for the production of desired products such as biofuels, high-value chemicals, and proteins. Bioengineering of diatoms can be achieved by overexpressing the genes involved in the desired metabolic pathways, or by deleting the genes involved in the non-desired metabolic pathways.

2.5.3 Incorporation of nanoparticles

The incorporation of nanoparticles into the diatom frustules can enhance the structural, optical, and electrical properties of diatoms. Nanoparticles can be incorporated into diatoms via electrostatic or bio-mineralization processes, enhancing their properties such as increased catalytic activity, improved mechanical strength, and higher optical absorption. The possibility to insert semiconducting or metallic elements, such as germanium[64,114,115], nickel[83], titanium[116–118], aluminium[119], europium[120], tin[121], zirconium[121,122], in diatom frustules for applications in sensing, optoelectronics, solar energy harvesting, catalysis, and biomedicine is thoroughly explained in the review[123].

2.5.4 Physical modification

Physical modification methods, such as mechanical milling or sonication, can be used to change the size and morphology of diatoms, enhancing their properties such

as increased surface area, porosity, and size distribution. This method can also be used to reduce the size of the diatoms, making them more suitable for applications such as drug delivery and tissue engineering.[103]

2.5.5 Different applications of diatoms

The abundance and versatility of diatoms opens up wide opportunities for choosing the optimal types of structures with desirable characteristics. Nanostructured silica exoskeletons of diatoms are readily available both through cultivation by aquaculture methods and through the extraction of diatomite, widespread sedimentary rock, which is widely used for the production of refractory and heat-insulating materials, as feed in animal husbandry, for filtration and sorption of various substances, including oil spills[35]. These applications exploit the standard features of diatom frustules – the chemical composition, the developed multilayered structure and the presence of an internal cavity as a thermal barrier. At the same time, such features of the specific structure of diatom exoskeletons as a diverse morphology and complex topology of nanosized pores, which determine the spectrum of natural vibration frequencies, as well as structural characteristics (stiffness and strength under quasi-static loading), have not yet been used in engineering devices.

The particular spatial organization of nano- and micropores of the diatom frustules offers promising prototypes of functional systems and elements for targeted drug delivery[124,125], electrochemical energy storage[36,126], photovoltaics[127], metamaterials[128], catalysis[129,130], filtration[131], metal modification and removal[96,123] and many others[132–134]. Some potential applications of diatoms are schematically represented in Figure 24.

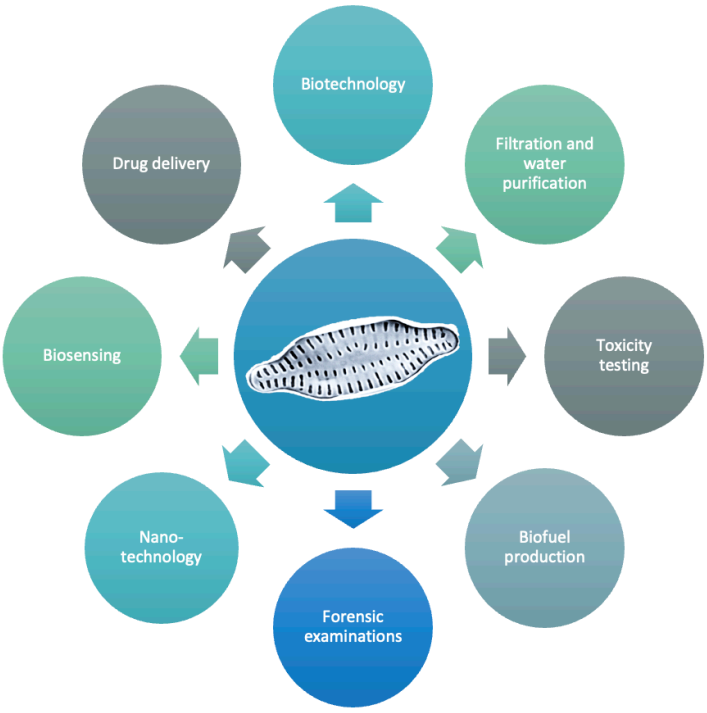

Figure 24. Various applications of diatoms.

Losic and co-workers demonstrated the functionalization of diatomaceous earth with dopamine-modified iron-oxide nanoparticles and proved their capability to be used as magnetically guided micro-carriers for non-invasive and targeted drug delivery.[108] Silver nanoparticles/diatomite nanocomposites exhibited antibacterial effect against infectious pathogens.[135,136]

Jantschke et al. used two approaches—covalent linking and layer-by-layer assembly (LbL)—to decorate diatom frustules with noble metal (Ag, Pt, Au) and semiconductor (CdTe) nanoparticles for surface-enhanced Raman spectroscopy (SERS) of components, for catalysis, and to obtain enhanced image quality in scanning electron microscopy.[137] Fischer and co-workers used a covalent-coupling method to prepare gold nanoparticle-decorated diatom biosilica and successfully applied the

obtained catalysts for the oxidation of D-glucose to D-gluconic acid.[138] Pannico et al. used a method based on electroless deposition of gold to cover diatom frustules and showed that such composites could be used as a support for SERS.[12] According to the study by Kong et al., diatomite decorated with plasmonic nanoparticles served as a lab-on-a-chip device for on-chip chromatography and label-free biosensing of small molecules from complex biological samples.[139]

Moreover, an ultrasensitive SERS immunoassay based on diatom biosilica with integrated gold nanoparticles has been developed for the detection of interleukin 8 (IL-8) in blood plasma.[10] The results confirmed that diatom frustules increase the sensitivity of the immunosensor when compared with a conventional flat glass-based sensor. It was also demonstrated that diatom shells functionalized with gold nanoparticles via a photo-deposition process could be used for the harvesting and detection of biological analytes, such as bovine serum albumin (BSA), and chemical pollutants (mineral oil) in low dilutions down to 10^{-16} M for BSA and 50 ppm for mineral oil leading to applications in biotechnology, medicine, safety, monitoring and control of environmental hazards.[140,141] Polyethylene glycol (PEG)-modified diatomite decorated with gold nanoparticles by one-pot liquid-phase synthesis demonstrated the potential for usage as advanced nanodevices adding imaging features to the nanocomplexes.[142] Recently, Braceño et al. showed that diatom biosilica modified with gold nanoparticles by In-situ and Ex-situ methods represents a promising candidate for controlled release of the gentamicin in simulated body fluid.[143] The experimental findings showed that while In-situ method resulted in a slower release, the Ex-situ method showed a faster release of gentamicin by using gold/cetyl-trimethylammonium bromide (CTAB) nanoparticles.

2.6 On the MEMS perspective

The requirements of small size, specific optical properties, low density and high strength are important for numerous applications, especially in silicon photonics [144,145] and for MEMS[146,147] as well as nanoelectromechanical systems (NEMS). Dimensional and structural correspondence between diatom exoskeletons and MEMS devices for high-sensitivity microphones serve as a starting point for seeking further opportunities to create nanotechnology components using biomimetics and biotechnology[148]. To underpin the development of theoretical concepts in this area, comprehensive studies are required to include structural and mechanical characterization which remain small in number and limited to specific diatom species. Consequently, studies devoted to the possible use of diatom frustules as a basis for MEMS elements[149,150] rely on unproven hypotheses or numerical simulation results[151] that need validation.

Successful fabrication of nanostructured silicon structures reduced from diatomaceous silica earth and firmly integrated into silicon wafers shows that neat nanostructured objects obtained in the framework of the BANSAM paradigm[14,132,152] can be readily applied as elements in smart electronic chip technologies. Since diatoms are able to colonize silicon monocrystalline wafers[6], a simple technique of guided, highly precise deposition of single diatom cells might be developed for mass production of NEMS and MEMS containing diatom frustules as an integral part of a sensor, such as a microphone, or an energy harvesting element.

The description of vibration behavior for a single openwork architected element is a relatively simple task for modern computational math. Numerous finite element analysis (FEA) or finite element modelling (FEM) software packages are available on the market such as Ansys, COMSOL and many others. These software tools are capable

of predicting main modes of vibrations and eigenfrequency spectra processing 3D-meshed geometrical models of diatom frustules fixed to the infinitely thick substrates in a manner (boundary conditions). Figure 26 exemplifies typical results of FEM analysis of diatom frustule vibrational patterns[148].

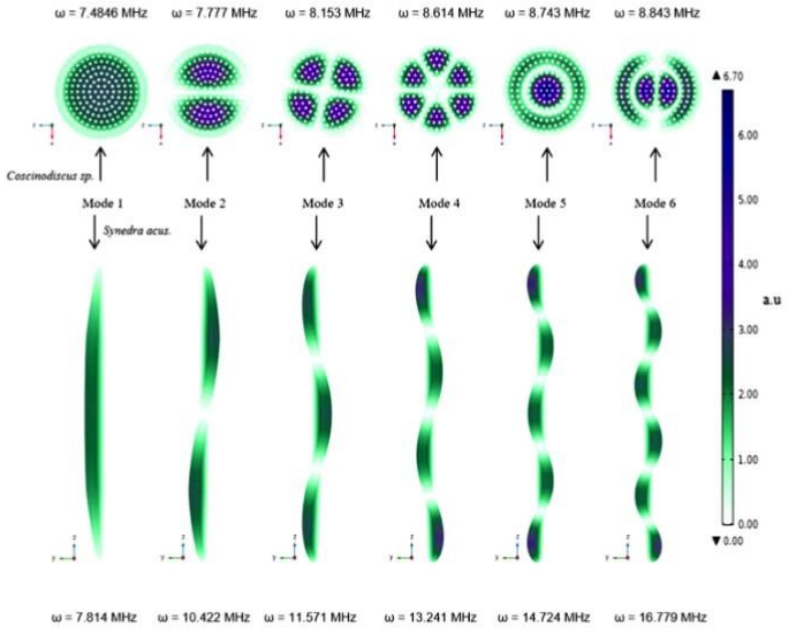

Figure 25. Mode shapes and natural frequencies of *Coscinodiscus* sp. (centric) and *Ulnaria acus* (pennate) observed in the simulation using COMSOL Multiphysics. Adopted from[148]. Reproduced with permission from Elsevier Ltd.

Calculated values of eigenfrequencies of *Ulnaria acus* and *Coscinodiscus* sp. are as high as 7-17 MHz, which is undoubtedly very attractive for NEMS and MEMS elements and microelectronics in general. It is important to note that elastic modulus of amorphous hydrated silica (22.4 GPa) was input for calculations. One can suggest that the reduction of silica to silicon will increase eigenfrequencies a few times due to the dimensional thinning and material stiffening (Young's modulus of silicon is 140-180 GPa). The values of calculated eigenfrequencies for the geometrical models of diatoms

are in good agreement with the data of photoacoustic measurements, which has recently been conducted for several species of live diatoms[153–155]. Live diatoms, as believed, absorb the energy of laser pulses in chlorophyll molecules and convert some part of absorbed energy to a wide spectrum of vibrations resonating with frustules' vibrations at eigenfrequencies. The drawback of this computational Math applied to this aspect of diatom science is quite obvious – simple 3D geometrical models of frustules capture the rough details of frustules neat architecture only. Two approaches have been put forward to deal with difficulty:

- Parametrization of a simplified analytical solution adopted from continuum mechanics of thin shells as demonstrated by Abdusatorov et al.[148]

- the development of destructive (through FIB-SEM milling – Figure 26) or non-destructive tomography (e.g., using ptychography with help of synchrotron coherent beam – Figure 27).

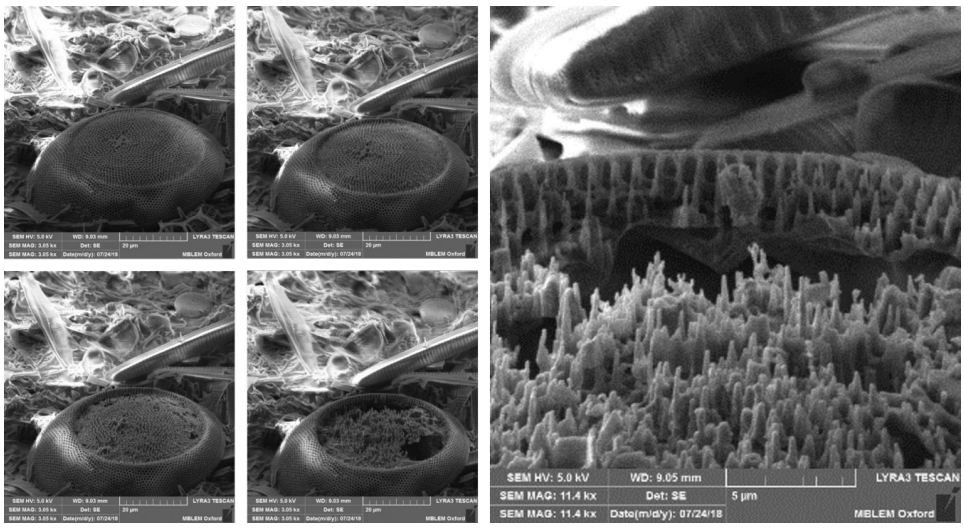

Figure 26. The example of FIB-SEM milling of diatom species (destructive method). Adopted from Ref.[14]. Reproduced with permission from John Wiley & Sons, Inc.

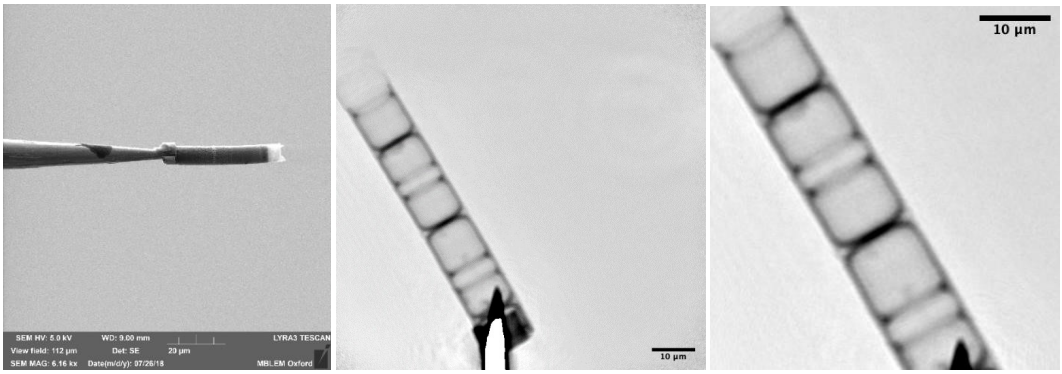

Figure 27. Ptychography of *Aulacoseira* diatom cells (courtesy of T.E.J. Moxham, University of Oxford / Diamond Light Source, U.K.) Adopted from Ref.[14]. Reproduced with permission from John Wiley & Sons, Inc.

Parameterization techniques are relatively simple since they require to calibration and fitting of few parameters for the series of vibration modes, the i-th eigenfrequency of which obeys to formula[14,148]:

$$\omega_i \propto \sqrt{\frac{E}{\rho}} \frac{1}{D} \left[a_i \frac{t}{D} + b_i \right] P_i \left(\frac{d}{D} \right) \quad (1)$$

where E, ρ, D, d and t are Young modulus, density, diatom principal size (outer diameter for centric and longest size for pennate diatoms), pore diameter and frustule thickness, respectively. Parameters a_i and b_i as well as morphology factor P_i are to be fitted and experimental measurements are vital in this case in order to retrieve the values of parameters from the correlation analysis.

A 3D reconstruction of the frustule architecture facilitates the creation of a corresponding 3D model, which enables computations of mechanical properties pertinent to MEMS.

2.7 On the importance of diatom algae in addressing specific issues

In summary, the following list of advantages of diatoms discussed in the preceding Literature Review emphasizes their valuable attributes across diverse applications and specific issues discussed in the Introduction section.

- Hierarchical structure: The hierarchical structure of diatom frustules, comprising intricate nanostructured features such as pores, ribs, and patterns, provides a level of complexity and control that can be challenging to achieve with man-made materials and fabrication techniques. This complexity allows for fine-tuning of the material properties and morphology of the diatom shell, which can be beneficial for improving the performance of the microphone. Additionally, the dimensions of diatom frustules closely align with the requirements for high-sensitivity microphones.
- Biomimicry and Nature-inspired design: Diatoms have evolved over millions of years, developing natural structures optimized for their survival and environmental adaptation. By utilizing diatom shells as MEMS devices, researchers can draw inspiration from Nature's design principles and apply them to microphone technology. Biomimicry often leads to innovative solutions and improved performance in specific applications, making diatoms an attractive option for those seeking to explore nature-inspired design approaches in MEMS technology.
- Scalability: Diatoms offer the potential for large-scale production as they can rapidly grow and proliferate, providing an abundant and renewable source of raw biomaterials.

- Biocompatibility: The biogenic silica composition of diatom frustules makes them biocompatible and suitable for applications involving interaction with biological systems and fabrication of biosensors.
- Environmental adaptability: Diatoms demonstrate adaptability to diverse environmental conditions, making them appealing in applications where extreme environments are involved, thus offering advantages over man-made materials that might deteriorate or fail. Utilizing diatom shells in MEMS devices can contribute to sustainability goals by reducing reliance on resource-intensive or environmentally unfriendly manufacturing processes associated with conventional MEMS materials.
- Unique optical properties: Diatom frustules exhibit fascinating light manipulation characteristics, including diffraction, light concentration and focusing, light trapping, photoluminescence. Such properties can be utilized in photonics and development of optical sensors.

Chapter 3. Experimental section

Chapter 3 provides a detailed account of the methodologies used in the research, encompassing the cultivation of diatoms and the preparation of samples. This chapter presents a comprehensive repository of the processes and techniques employed and provides a strong foundation for the research, ensuring clarity, replicability, and credibility of the findings.

3.1 Diatom algae cultivation

3.1.1 Sampling diatoms from natural populations. Isolation and introduction into clonal cultures of certain species of diatoms. Cultivation of various types of freshwater and marine diatoms

Marine diatoms were isolated from planktonic and benthic samples. Clones of radial centric diatoms *Coscinodiscus oculus-iridis (Ehrenberg) Ehrenberg* and *Coscinodiscus* sp., were subsequently isolated from the plankton samples at the surface water layer (depth of about 1–2 m) in the Tsushima Strait to the north of Okinashima Island and from the pier of the Karadag Scientific Station (Crimea), respectively. A benthic sample was taken in the form of a scraping of fouling from the surface of stones at a depth of about half a meter in a small bay near the settlement of Caleta de Caballo (Lanzarote Island, Canary Islands archipelago) and the polar centric diatom *Biddulphiopsis titiana (Grunow) von Stosch & R. Simonsen* was isolated from it. The samples were placed in plastic containers and delivered to the laboratory of algae and microbiota of the Karadag scientific station[156]. All diatom samples were isolated by micropipetting single cells of diatom species of interest, which gave rise to clonal cultures[157]. According to the Medlin and Kaczmarska system[158], *C. oculus-iridis* and *Coscinodiscus* sp. belong to the class *Coscinodiscophyceae*, while *B. titiana* belongs to

the class *Mediophyceae*. Clonal marine diatom cultures were kept in 100 ml Erlenmeyer glass flasks filled with 40–50 ml medium. A modified ESAW medium was used as a culture medium[159]. ESAW medium is an artificial sea water with a composition similar to natural sea water. To maintain the exponential growth phase, the cultures were reseeded once every 7–10 days. The culture flasks were placed in a room kept at 20 ± 2°C near a window oriented to the north to prevent direct sunlight.

Benthic diatom species *K. amoena* were collected from the tidal zone of Gdansk Bay, Baltic Sea in the area of Zelenogradsk, in early June 2016[155]. The salinity of the interstitial water across the collection sites, as well as the water salinity of the tide pools, was 5 ppt. Samples were collected in the mid-littoral zone during the low tide in the form of strips of sand with a width of 1.5 cm, length up to 15 cm and a depth of 0.7 0.9 cm, by using a 0.5-l polyethylene terephthalate (PET) bottle. Then, the sample container was filled with water from a nearby tide pool. The specimen was not fixed, but it was preserved alive and subsequently delivered to Moscow. The material in the bottle was placed on the windowsill of the laboratory to ensure natural diffuse lighting and an alternating day/ night regime. The temperature ranged from 17 to 26 °C, and the material was kept in the same plastic bottle for 3 years. The cap of the bottle was slightly loose so as not to hamper the gas exchange between the internal space of the container and the external environment and accommodate room temperature variation. The water capacity of the sample (water + sand at the bottom of the bottle) was 400 ml. The amount of water evaporated from the sample container was recovered by trickling distilled water down the inner wall of the bottle, once the evaporation achieved more than 5 mm from the initial level. This was done to avoid the fouling diatoms inhabiting the PET bottle close to the water surface being osmotically stressed. During the growth

period of the accumulation culture, no minerals were fed. At the end of June 2016, the microscopic colonies of *K. amoena* were observed on the surface of sand grains in the ground sample. Permanent preparations were used to identify the species. The frustules were purified from organic components with concentrated sulfuric acid and were embedded in rosin. The macroscopic monocultural colonies of *K. amoena*, appearing as brown spots with ramified edges (diameter, 2–3 mm), were observed on the inner surface of the PET bottle in October 2017. By mid-July 2019, a complete brown coating had already been formed by the colonies on the inner wall of the bottle. As part of this coating, *K. amoena* cells were arranged in a dense one-layer pattern and formed a complex ornamented mosaic.

Freshwater diatom strains *Amphipleura* sp. (strain № Ov 466), *Asterionella formosa* (BZ 33), *Hannaea baicalensis* (BK 479), *Nitzschia graciliformis* (BK 611, 2.5BK 576), *Ulnaria acus* (15K 595), *Achnanthidium sibiricum* (256) and *Encyonema silesiacum* (459) were isolated from the natural populations of the lake Baikal and river Yenisei. Cell isolation into monoclonal cultures was carried out according to the previously described protocol in the Limnological Institute, Siberian Branch, Russian Academy of Sciences (Irkutsk, Russia)[160]. Freshwater diatom cultures were grown on DM medium[161] in flasks at around 8 °C and illumination of 16 μM $m^{-2}s^{-1}$ using a 12/12 hour artificial light/dark cycle.

All cultures were successfully delivered to Moscow and grown at the Skolkovo Institute of Science and Technology in T-25 culture flasks (Eppendorf, Germany) in a volume of 40 ml. Freshwater diatoms were grown in refrigerators equipped with a phytolamp to provide optimal illumination at a temperature of 10 ± 1 °C, while marine cultures were grown in natural diffused light, on the laboratory windowsill, with

alternating day and night, in the temperature range from +19 to + 22 ˚C. [Cultivation was performed by the author]

3.1.2 Cultivation of diatoms in the incubator

Some part of the freshwater diatoms (*A. sibiricum*, *U. acus*, *E. silesiacum*) has been grown in a specially designed incubator in cell culture flasks "T-25" (Eppendorf, Germany), with sterile filter caps, which provide the gas exchange between the internal space of the flask and the external environment. Each flask contained approx. 30 mL of DM medium. The cultivation temperature was maintained at about 12 ± 1 °C, while the blue and red light-emitting diodes (LEDs) with a 12:12 day-night cycle promoted the growth of the strains.

The Algae reactor of two parts: the control unit, maintaining suitable conditions for diatom algae well-being, and the growth chamber. The entire reactor is powered by a 220V AC, transformed into 12V by two independent power supply units (50W for light controlling and 150W for water cooling system). The control unit consists of two independent circuits: the first to control the day-night regime and light brightness, the second one for thermal regulation placed in the PC case. A dry-contact time relay (220V supply, 12V regulation) provides the day-night cycle with the ability to set on and off by a day of the week and time of day. In the same circuit, a smooth PWM light power controller with an operating frequency of 10 kHz (which prevents flickering of the lighting) is integrated.

In the thermal regulation circuit, the purified water from the growth chamber is sucked by an impeller pump into a water block located on the 80W Peltier element's cold side. The hot side of the Peltier element is cooled by a maintenance-free liquid cooling system with a peak dissipated power of 250 W. Feedback of the Peltier element

and the pump is carried out through continuous temperature monitoring by a thermostatic controller with two sensors at the point where water is sucked into the system and water is released back into the core chamber. This way, the temperature inside the growth chamber could be maintained down to 10°C with high precision. The control unit is combined with the growth chamber with quick-release connectors on the rear panel: a 3.5 mm jacks for temperature sensors and a 12V DC-DC connector for power supply and control of the lighting system. Two silicone hoses connect the water circuit to the pump and the chilled water block.

The growth chamber is a vessel, the walls of which are insulated with layers of foamed polyethylene to maintain the temperature. Inside the growth chamber, a rack is located, in which the temperature sensors and the inlet and outlet hoses are mounted. Inside this frame, another frame on which the cultural flasks with diatoms are rest. On the top cover of the growth chamber, made of 8 mm acrylic (thermal barrier), a lighting system is mounted: two LED strips with LEDs that correspond to the bands of maximum light absorption by chlorophyll (phyto light). The strips are stacked to the aluminum profile, which is both a supporting structure and a radiator, and are directed to the cultural flasks at the bottom. The scheme of the incubator is shown in Figure 28. [Incubator was fabricated by Daniil Nozdriukhin]

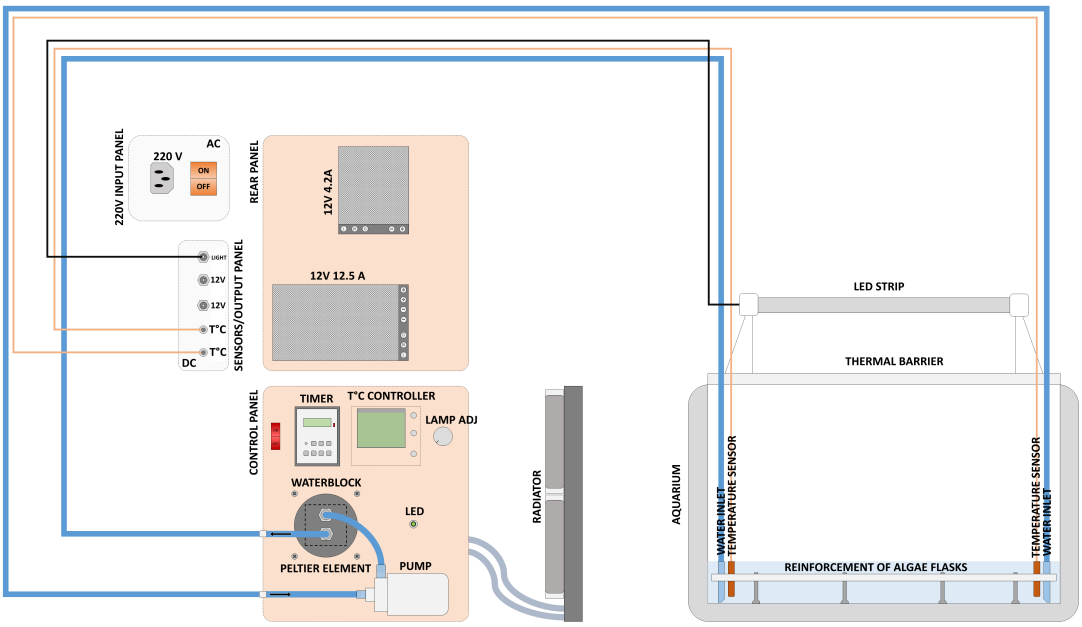

Figure 28. A scheme of the diatom algae incubator

3.2 Monitoring of the growth of diatoms

3.2.1 IVIS SpectrumCT In vivo Imaging system

The IVIS SpectrumCT In Vivo Imaging System (Xenogen Corp., California, USA) was used to monitor the growth of diatoms during long-term cultivation. Different diatom cultures *(A. sibiricum, Coscinodiscus* sp., *Biddulphiopsis titiana* and *Ulnaria acus)* were monitored over a long period of time up to 100 days. Visualization of samples cultivated in 40 ml cell culture flasks was carried out without preliminary sample preparation. The frame with flasks containing diatom cultures cultivated in the incubator was transferred directly from the incubator to the chamber of the setup for monitoring. The fluorescence signal was excited by optical radiation at a wavelength of 465 nm and recorded at 680 nm. The images were acquired and analyzed with Living Image 4.7.3.

Besides, suspensions of diatoms in a 96-well plate and diatoms mixed with agarose gel were also visualized. To prepare diatom-agarose phantoms, in one case, 3 µL of a diatom suspension was mixed with 7 µL of 1 % agarose gel (A9045-5G, Sigma Aldrich, Germany) and pipetted into a petri dish. In another case, 15 µL of diatoms were mixed with 35 µL of melted agarose. Agarose drop served as a reference sample. [Monitoring of the growth of diatoms was performed by author]

3.2.2 Spectroscopy measurements

To verify the results, fluorescence spectra were obtained using an Infinite M Nano+ spectrophotometer (Tecan Trading AG, Switzerland). The fluorescence excitation wavelength was 465 nm, and the emission was recorded in the region of 620–750 nm.[153–155,162,163] The extinction spectra were also collected in the wavelength range 400–700 nm on the specific days during cultivation. [Spectroscopic measurements have been performed by the author]

3.2.3 RSOM monitoring

To monitor the growth of diatoms using RSOM Explorer P50, cultures of *A. sibiricum* (strain 256), *C. oculus-iridis* (strain 0.1211-OD), *Coscinodiscus* sp. (strain 21.0407-OA), *B. titiana* (strain 0.0212-OH), and *U. acus* (strain 15k 595) were mixed with agarose gel and measured on the certain days during cultivation. For this purpose, a mixture of 3 µl of diatom suspension with 7 µl of 1% melted agarose was prepared. Drops of diatoms immersed in agarose gel were pipetted onto the bottom of a Petri dish and, after solidification, filled with deionized water to ensure coupling between the ultrasonic sensor and samples. Diatom-agarose drops were scanned with a scanning step of 20 µm and the field of view up to 12 × 12 × 3 mm. The images were processed using the ImageJ software. The average pixel intensity in the region of interest was

found from the MIP RGB images by analyzing color image histograms that show the average pixel intensity for the red (11-33 MHz) and green (33-99 MHz) channels. [RSOM monitoring of diatom growth has been performed by the author]

3.2.4 Monitoring of the growth of diatoms using microfluidic cell

For in situ monitoring of the process of growth and division of diatoms, a microfluidic cell was developed with the ability to adjust the temperature (from 10 to 40 °C), medium flow rate (1-6000 µl/min) and CO_2 content (0.01-5 vol.). The schematic diagram of the monitoring device is shown in Figure 29.

The flow cell is made in the form of a microfluidic chip. The cell body was cast from Sylgard 184 polydimethylsiloxane elastomer (Dow Corning, USA). The casting mold was made by photopolymer 3D printing using SLA technology. A spacer was used to prevent inhibition of polymerization of the elastomer. The flow cell has a central working channel 1 mm wide, which in the middle has an expansion of up to 5 mm. This makes it possible to reduce the flow rate in the region of observation of the growth of diatoms. The entrance and exit from the channel are carried out using fluoroplastic tubes with an outer diameter of 1 mm. To reduce the number of air bubbles in the tubes, a peristaltic pump (Figure 29 (pump 1)) is installed at the outlet of the cell, and the cell inlet tube is immersed directly into the nutrient medium receiver. A cavity is formed around the main channel in the chip, forming a pressure suction cup. This cavity is connected through a PTFE tube to a compact membrane vacuum pump. When creating a vacuum, the suction cup securely presses the flow cell against the glass slide and provides a tight connection between the main channel and the glass. Such a scheme of the device allows one to quickly disassemble and assemble the flow cell for washing, it is very compact and easy to use. In terms of size, such a cell practically does not differ

from a non-separable one and is installed on a standard microscope slide with a standard preparation driver.

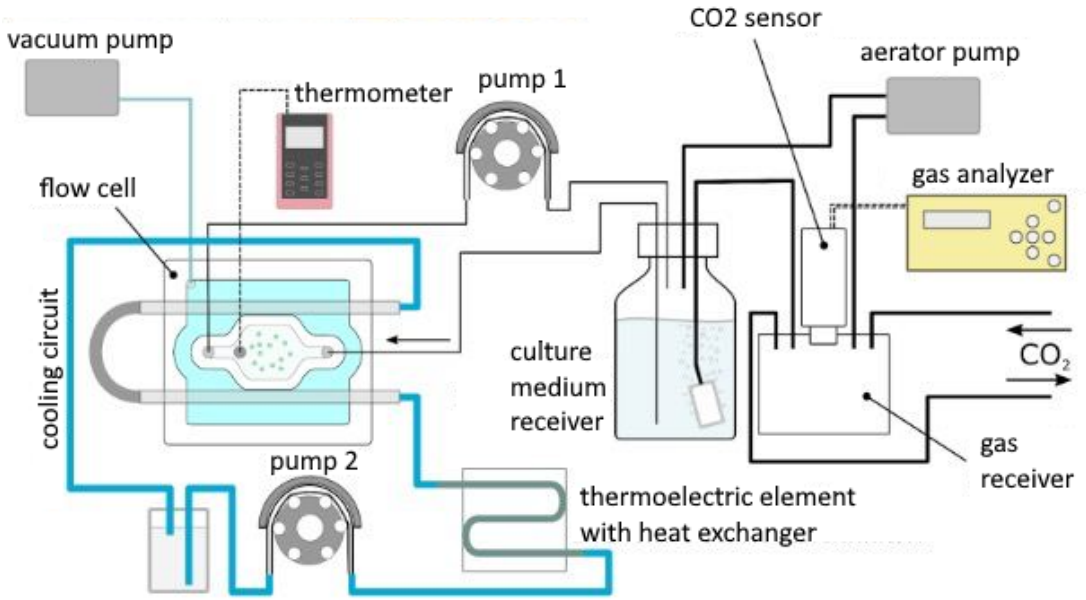

Figure 29. Scheme of a setup with a microfluidic cell for monitoring the growth of diatoms using optical microscopy

The cooling system of the flow cell is liquid. Two stainless steel tubes with a diameter of 1.2 mm are installed in the cell body. The tubes are connected in series to the cooling circuit. The presence of metal tubes built into the cell body allows it to be cooled more evenly. As a cooler in the cooling circuit, a thermoelectric element (TV-71-1.0-1.3, Kryotherm, Russia) with a copper heat exchanger is used, to which a coil made of a 2 mm stainless steel tube is soldered, which is included in the cell cooling circuit. The reverse side of the Peltier element is cooled by a copper-aluminum radiator, which is blown by a fan. The Shenchen Lab V-1 peristaltic pump (Shenchen, China) is used as a pump in the cooling system circuit (Figure 29 (pump 2). The flow rate in the cooling system is 2 ml/min. A 40% aqueous ethanol solution is used as the coolant in

the cooling circuit, since pure water freezes in the heat exchanger when the flow cell is strongly cooled. A k-type thermocouple is installed in the main channel to control the temperature. The temperature is measured using a UNI-T UT325 thermometer (Uni Trend Group, China) connected to a PC.

An aerator is installed in the nutrient medium receiver to accelerate the exchange of gases between the nutrient medium and the gas receiver. The aerator pump constantly pumps gas through the gas receiver and delivers it to the aerator atomizer. To control the CO_2 content in the gas receiver, a sensor is installed, connected to the Hobbit-T-CO2 gas analyzer (Informanalitika Group, Russia). CO_2 is supplied to the gas receiver from a cylinder through a reducer and a throttle, which allow accurate dosing of gas in small quantities. [The microfluidic cell was developed by Dr Sergei German; monitoring of the diatom growth and division was performed by the author]

The division of diatoms was monitored by installing a microfluidic cell in an inverted fluorescent microscope NIB-FL (LOMO-Microsystems, St. Petersburg, Russia), as presented in Figure 30.

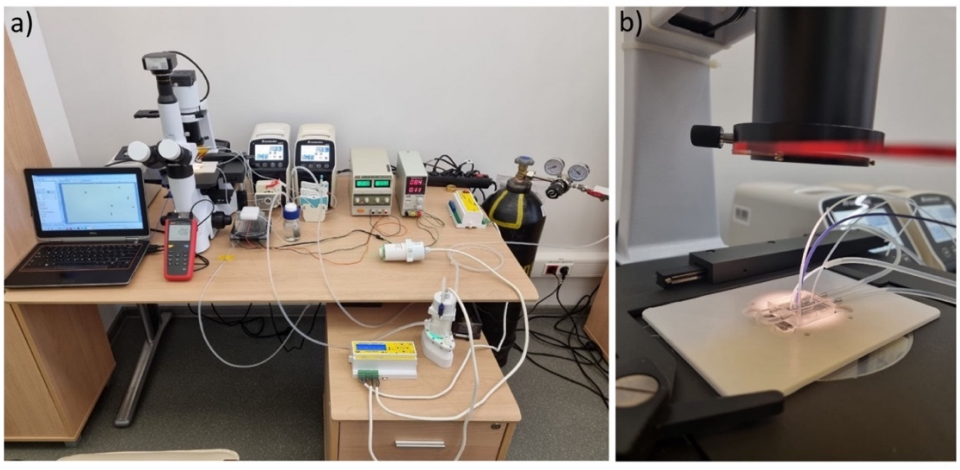

Figure 30. a) Photography of the whole experiment setup, b) Photography of microfluidic cell.

3.2.5 Monitoring of diatom concentration changes using photoacoustic imaging

Before measurements, *K. amoena* stock suspension was removed from the bottom of the plastic bottle and was diluted 1:2 seven times. A 0.1-g portion of agarose (Low type 1-B, A-0576, Sigma-Aldrich, Germany) was mixed with 10 ml of distilled water at 120 °C to obtain agarose gel. The concentration was determined with a hemocytometer (Goryaev's chamber). Different *K. amoena* concentrations (1080, 540, 270, 135, 67.5, 33.8 16.9, and 8.4 cells/µl) were mixed with agarose (3 µl of the suspension plus 7 µl of 1 % melted agarose). *K. amoena*-free agarose and *K. amoena*–agarose mixtures (in descending order of dilutions) were pipetted into a petri dish that was subsequently filled with water and placed in the imaging chamber of an RSOM Explorer P50 setup (iThera Medical GmbH, Germany). The photoacoustic signal of the agarose-gel-embedded *K. amoena* was excited by a Wedge HB frequency-doubled flashlamp-pumped Nd:YAG laser (Bright Solutions, Pavia, Italy) at an excitation wavelength of 532 nm (repetition rate, 1–2 kHz; pulse energy, 200 µJ; pulse length, 2.5 ns). The agarose–diatom samples were scanned over an 11 × 11 × 2.5 mm field of view with a raster step size of 20 µm. The axial and lateral resolution capabilities of the RSOM system were 10 µm and 40 µm, respectively. Induced photoacoustic signals were detected with a custom-made spherically focused $LiNbO_3$ detector (center frequency, 50 MHz; bandwidth, 11–99 MHz; focal diameter, 3 mm; focal distance, 3 mm). [Monitoring of diatom concentration changes using photoacoustic imaging has been performed by the author]

3.2.6 *Setup for optical monitoring of diatom concentration changes*

An optical setup developed for monitoring changes in algae concentrations is shown in Figure 31a-c.[162] A light emitting diode (LED) with a central wavelength of 505 nm was used as a light source. This wavelength was chosen to match the absorption maximum of carotenoids[164] presented in diatoms, such as fucoxanthin and beta-carotene[63]. The emission spectrum of LED is shown in Figure 31d.

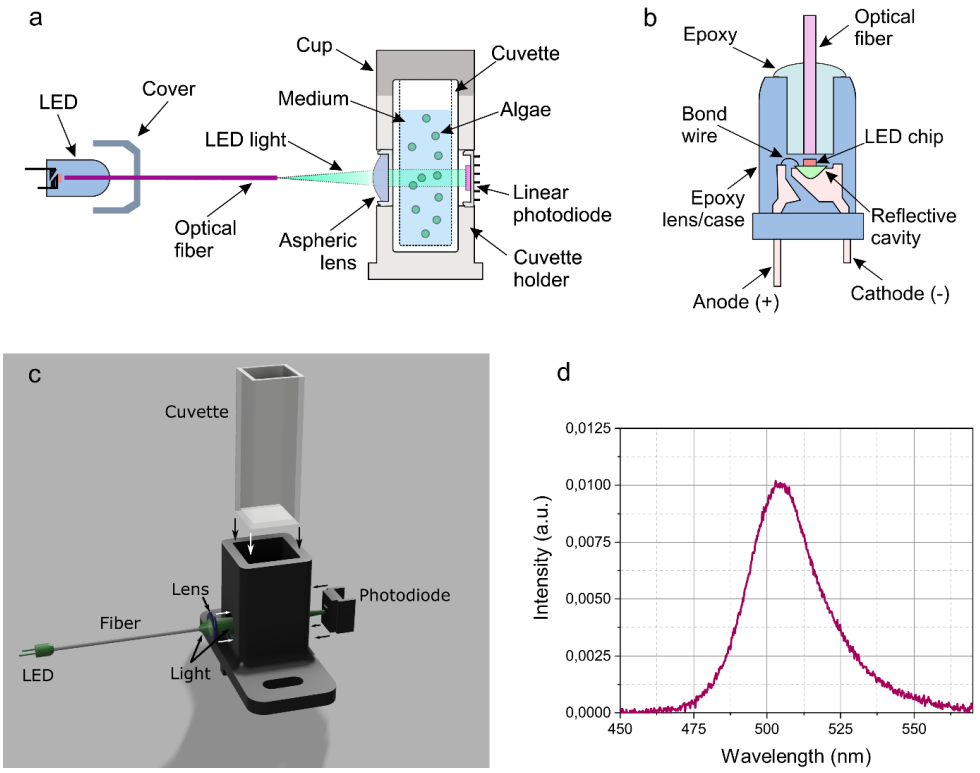

Figure 31. Experimental setup for monitoring changes in the diatom algae concentration. (a) Direct LED light coupling in multimode optical fiber. (b) Artistic representation of an optical system for measuring the transmission of algae in a nutrient medium depending on their fractional dilution. (c) Schematic representation of the experimental setup key components for transmission measurements. (d) Emission spectrum of LED.

Emitted light was coupled in a multimode optical fiber with 105 μm core for spatial filtering then collimated by f=7.5 mm aspheric lens, passed through plastic cuvette with analyzed volume of algae suspended in nutrient medium and measured by a linear photodiode (PD) with preamplifier (OPT101P, Texas Instruments, USA).

The data transfer between the optical system and the personal computer was performed using a microcontroller Arduino Nano. The LED and the photodiode were powered by a 5V voltage source. The diameter of the probe light beam was 1.5 mm. The PD square shaped photosensitive area size was 1.7x1.7 mm. Discretization frequency for Arduino analog-to-digital converter (ADC) was set to 100 Hz. A python code was used to read the data from Arduino, and calculate mean value and standard deviation over 12000 measurements during 2 minutes. To avoid external illumination influence, the optical setup was covered with a non-transparent enclosure.

LED illumination was coupled into an optical fiber by placing the end of the optical fiber to the LED light-emitting crystal at a distance of 200 μm. For this purpose, a 350 μm diameter hole was drilled in the LED transparent body under the optical control of a stereomicroscope ADF S645. An optical fiber was placed in the LED drilled hole and fixed using epoxy resin as shown on Figure 31b. The resulting output power of the LED light output of the collimating aspheric lens was 8.5 μW. Mounting elements of the optical system were produced by photopolymer printing approach.

To verify cell counting ability of the experimental setup, 7 diatom strains were examined.[162] For optical measurements, 1.5 mL of each strain were put into a plastic cuvette in the experimental setup. A custom python script was used to record light intensity values for 2 minutes, and, subsequently, average them over measurement time and calculate standard deviation. For spectrophotometric measurements, 200 μl was

taken each time from a 1.5 ml plastic cuvette. The sample was diluted accordingly by adding the same amount (200 µl) of the medium into the cuvette. In that way, for each strain the sample was diluted x1.154 times. This new sample was placed into the experimental setup, and new light intensity values were recorded. This procedure of dilution and measurement was repeated 11 times for each strain. The well-plate with the same 12 dilutions for each of 7 diatoms strains was placed into a spectrophotometer Tecan Infinite M Nano+ (Tecan Trading AG, Männedorf, Switzerland). For all the initial diatoms concentrations extinction and fluorescence spectra (the excitation wavelength was set to 430 nm) were measured. Then for each sample extinction value and fluorescence intensity were measured. Extinction was measured at the wavelength of 505 nm. The fluorescence intensity was registered at 680 nm. [Setup for optical monitoring of diatom concentration changes was developed by Dr Maxim Kurochkin and Sergei Perkov; measurements were performed by the author]

3.3 Cleaning of diatom cells from organic components

Purification of diatoms from organic material by chemical (acid) treatment consists of several stages. In the case of a marine culture in the initial medium, it is replaced with distilled water for 3 days, after which the cells are washed several times with distilled water to remove the remaining salts with centrifugation in a 5340 centrifuge (Eppendorf, Germany) (500 × g, 5 min). To remove a thick polysaccharide layer between the shell and the cell of freshwater diatom species, they were first washed 3 times in 6% sodium dodecyl sulfate (SDS) for 30 min at 95°C and successively washed with distilled water. The next step is boiling in concentrated nitric acid for 1-2 hours at 95°C. The boiling process can be repeated the next day by adding fresh nitric acid. After centrifugation (500×g, 5 min) and washing with distilled water at least 8

times, concentrated hydrochloric acid (36%) was added and left for 24 hours, followed by washing. Cleaned shells were stored in 50% ethanol to avoid bacterial growth and other possible contamination. [Cleaning of diatom cells has been performed by the author]

3.4 Characterization of the morphology and structure of diatoms

3.4.1 Scanning electron microscopy

A variety of scanning electron microscopes were used to image diatom samples over the course of 4 years, depending on the purpose and the need for high resolution images. To study diatom cultures before purification, as well as after acid treatment, a scanning electron microscope TESCAN VEGA 3 (TESCAN ORSAY HOLDING, Brno, Czech Republic) was used. Samples were mounted on an aluminum holder using double-sided carbon tape and visualized without sputtering at 10 kV.

SEM images of *Coscinodiscus oculus-iridis* were acquired using a TESCAN CLARA (Brno, Czech Republic) electron microscope. Samples were mounted on a standard aluminum stub using carbon adhesive tape and visualized without sputter coating in a high vacuum at 1 keV landing energy and 30 pA beam current. The cross-sections of cleaned diatom samples were obtained by focused ion beam (FIB) under high vacuum in a TESCAN SOLARIS S9000 (TESCAN ORSAY HOLDING, Brno, Czech Republic) electron microscope.

Scanning electron microscope (Quattro S, Thermo Fisher Scientific, USA) was used to investigate the appearance, morphology, and dimensions of *K. amoena* diatoms. Before SEM analysis, 20 µl of a stock suspension of *K. amoena* was deposited on a precleaned crystalline silicon substrate and three-stage drying in a vacuum oven (50 °C for 5 h, 80 °C for 3 h, and 100 °C for 1 h) was carried out to eliminate any organic

components. Samples were analyzed without sputter coating at an accelerating voltage of 2.5–5 kV. [155] Such microscope was also used to examine the morphology of precleaned frustules of A. sibiricum at an accelerating voltage of 3 kV.

FIB-SEM TESCAN SOLARIS S9000 (Tescan, Czech Republic) electron microscope was used to study the surface of *A. sibiricum* frustules at the energy of 1 keV with a MiAngle BSE detector. [The author acquired scanning electron microscopy images using the TESCAN VEGA 3 and Quattro S microscopes, while Pavel Somov obtained images using other mentioned microscopes]

3.4.2 Transmission electron microscopy

To describe the ultrastructure, the cells of several strains were fixed for transmission electron microscopy (TEM) with a mixture of 2.5% glutaraldehyde (Sigma-Aldrich, Germany) and 1% paraformaldehyde (Sigma-Aldrich, Germany) in the medium for 1 hour, then in solution 2.5% glutaraldehyde and 2% paraformaldehyde in phosphate buffer (0.1 M, pH 7.4) with the addition of tannic acid (Sigma-Aldrich, Germany) for 2.5 h. After that, the cells were washed with the same phosphate buffer and post-fixed in 1% osmium oxide solution (Sigma-Aldrich, Germany). The further procedure of dehydration and inclusion in the embedding medium was done as described previously[165]. Sections were obtained using a Diatome diamond knife (Germany) and stained with uranyl acetate and lead citrate. Sections were examined with a transmission electron microscope at an accelerating voltage of 80 kV. The micrographs were taken with a Mega View II Zeiss digital camera. [Transmission electron microscopy images of diatom ultrastructure were obtained together with Dr Yekaterina Bedoshvili]

3.5 Visualization of living diatom cells

3.5.1 Optical microscopy

Diatoms were visualized and counted under the inverted luminescent microscope NIB-FL (LOMO-MA, Russia) using PH10x and PH40x objectives. Images were taken with an UltraHD-4k (35k/s) camera.

3.5.2 Confocal laser scanning microscopy

A. sibiricum diatoms were studied by confocal microscopy using Zeiss Axio Observer.Z1 inverted microscope with PlanApochromat 40×/1.3 Oil DIC (UV) VIS-IR M27 objective and confocal unit LSM 800 (Carl Zeiss Microscopy GmbH, Germany).[154] The microscope is equipped with four solid-state lasers for illumination of the samples at 405, 488, 561, and 647 nm, three GaAsP PMT detectors, and one T-PMT detector for transmission light detection. Diatoms were imaged using Airyscan detector for higher resolution confocal scanning with appropriate filters. Before measurements, diatoms were stained with DAPI (4′,6 diamidino-2-phenylindole, Sigma Aldrich) to visualize nucle. Briefly, the diatom cells were fixed with 4 % formaldehyde for one hour and washed with 0.1 M phosphate buffer (pH 7.4) twice. The cells were collected by centrifugation at 2000 × g for 10 min, followed by DAPI (final concentration, 10 μg/mL) staining. Subsequently, the cells were rinsed twice with the phosphate buffer and mounted using Fluoromount Aqueous Mounting Medium (Sigma Aldrich). DAPI fluorescence was excited with a 405 nm laser, and the emission was registered in the 420-470 nm region. The images were obtained and processed with ZEN 2.3 imaging software.[154]

Laser scanning microscopy (LSM) was used to observe the DNA material of diatom cells and newly formed valves during division. To accomplish this task, *U. acus*,

N. graciliformis, *Amphipleura* sp., *A. Formosa*, *C. oculus-iridis* were exposed to the vital dye PDMPO (Thermo Fisher Scientific, USA) or LysoTracker Yellow (Thermo Fisher Scientific, USA) at a concentration of 5 μg/ml for 1 day, after which they were fixed with a 4% solution of paraformaldehyde in phosphate buffer (0 .1 M, pH 7.4) for 1 hour, washed with phosphate buffer three times and, in the case of LysoTracker Yellow staining, additionally stained with DAPI (10 μg/ml, for 10 min). The cells were then embedded in Mowiol® 40-88 (Sigma-Aldrich, Germany) and examined using an LSM 710 laser scanning microscope (Zeiss, Germany). Chlorophyll autofluorescence was excited by a laser with a wavelength of 561 nm and its radiation was recorded in the range of 650–723 nm. Fluorescence of Lysotracker Yellow H-123 was excited by a laser with a wavelength of 488 nm; its radiation was recorded in the range of 496-647 nm. DAPI fluorescence was excited by a laser with a wavelength of 405 nm; its emission was registered in the ranges of 410-492 nm. Fluorescence of PDMPO was excited by a laser with a wavelength of 405 nm, the radiation was recorded in the range of 441–587 nm. 3D reconstruction obtained from 100 optical sections (thickness along the z axis 14.3-50 μm).

3.5.3 Operetta High Content Imaging System

For fluorescent visualization, 100 μl of each diatom strain (*Asterionella formosa* – strain BZ 33, *Amphipleura* sp. – strain Ov 466, *Hannaea baicalensis* – strain BK 479, *Ulnaria acus* – strain 15k 595, *Biddulphiopsis titiana* - strain 0.0212-OH, *Coscinodiscus oculus-iridis* - strain 0.1211-OD, *Coscinodiscus* sp. - strain 21.0407-OA) was placed in the individual well of 96-well plate (CellCarrier Ultra, PerkinElmer, USA) and imaged with a x20 and x60 magnification objectives using the Operetta High Content Imaging System (Perkin Elmer, USA) in the fluorescence mode. The

chlorophyll autofluorescence was excited at 410-430 nm, while the emission was registered at 650-700 nm. The obtained images were processed using Harmony 4.1 software (Perkin Elmer, USA).[162]

3.5.4 Fluorescence lifetime imaging microscopy (FLIM)

Fluorescence lifetime imaging microscopy (FLIM) measurements of diatoms and image processing were done using a MicroTime 200 STED microscope (PicoQuant GmBH, Germany), a 402- and 638-nm laser as the excitation source, and a 690-nm bandpass filter. Measurements were carried out at a pulse rate of 40 MHz, a pulse duration of 40 ps, and a maximum power of 50 μW. Fluorescence lifetime images were acquired in the time domain. The laser beam was focused on diatom cells with a 100 × 1.4 NA oil immersion objective (UplanSApo, Olympus, Japan). According to the dwell time of 0.2 ms with a pixel size of 0.200 μm/px, the total image acquisition time was 40 s for an image size of 400 × 400 pixels—i.e. 80 × 80 μm.[155]

[Visualization of living diatom cells using all above-mentioned methods has been performed by the author]

3.6 Study of mechanical properties of diatoms

3.6.1 Preparation of samples for SEM nanoindentation and AFM

Cleaned diatom frustules and air-dried living cells were prepared for AFM and in situ SEM nanoindentation measurements.[39] Purification of diatoms from organic material consists of several stages. For the purpose of bacterial destruction of organic matter, the medium was first filled with distilled water and left for 3 days. After that it was washed with DI water several times to remove the remaining salts by centrifugation using the Centrifuge 5340 (Eppendorf, Germany) (500 × g, 5 min). After removing salt, the cell suspension was boiled in concentrated nitric acid for 2-3 hours. The boiling

process was repeated the next day adding fresh nitric acid. The suspension was subsequently centrifuged (500 × g, 5 min) and rinsed with DI water at least 8 times. The cleaned frustule suspension was pipetted onto a silicon wafer and air-dried for further measurements. Air-dried living diatom cells containing cellular material were also placed on a silicon wafer and used for in situ SEM nanoindentation. A vial with live diatoms in water was transferred into the AFM glovebox. A drop of water with diatoms was placed on a silicon substrate. After water evaporation the live diatom cells were measured using the AFM. The diatom samples were imaged with intact and separated frustules or the so-called valves. Separated frustules settled on the substrate exposing their interior concave surface and exterior convex surface. [Samples were prepared by the author]

3.6.2 AFM measurements

AFM measurements were performed using Cypher ES microscope (Asylum Research, Oxford Instruments) installed inside an Ar filled glove box (MBraun). Topography was measured in a tapping mode using a single crystal diamond probe with 147 kHz first resonance frequency and 3.5 N/m spring constant. Nanomechanical properties were measured in the AM-FM viscoelastic mapping mode and by force-distance curve acquisition using stiff (DRP_IN purchased from TipsNano, Estonia, k=400 N/m, Fres=750 kHz) and soft (HA_NC/FD purchased from TipsNano, Estonia, k=3.5 N/m, Fres=147 kHz) single crystal diamond probes. Nanoindentation was performed on the concave surface of a separated frustule using the stiff (k=400 N/m) diamond probe. All AFM probes were calibrated on a TGT1 test grating in order to measure radius of curvature of the tip apex and on a fused silica reference sample in order to test models for fitting experimental data. The stiff probe was additionally

calibrated on a diamond coated silicon wafer in order to get accurate values of the displacement and spring constant (Figure 32). Force-distance curves on the inner surface of the cleaned frustule and on the wet diatom cell were acquired by the stiff diamond probe (k=400 N/m) under the maximum force load of 8 µN. Force-distance curves on the outer surface of the cleaned frustule were obtained by the soft diamond probe (k=3.5 N/m) under the maximum force load of 100 nN because the cleaned cribrum is brittle and often breaks when measured by the stiff probe. Besides, the outer surface bends as a membrane under the stiff probe.

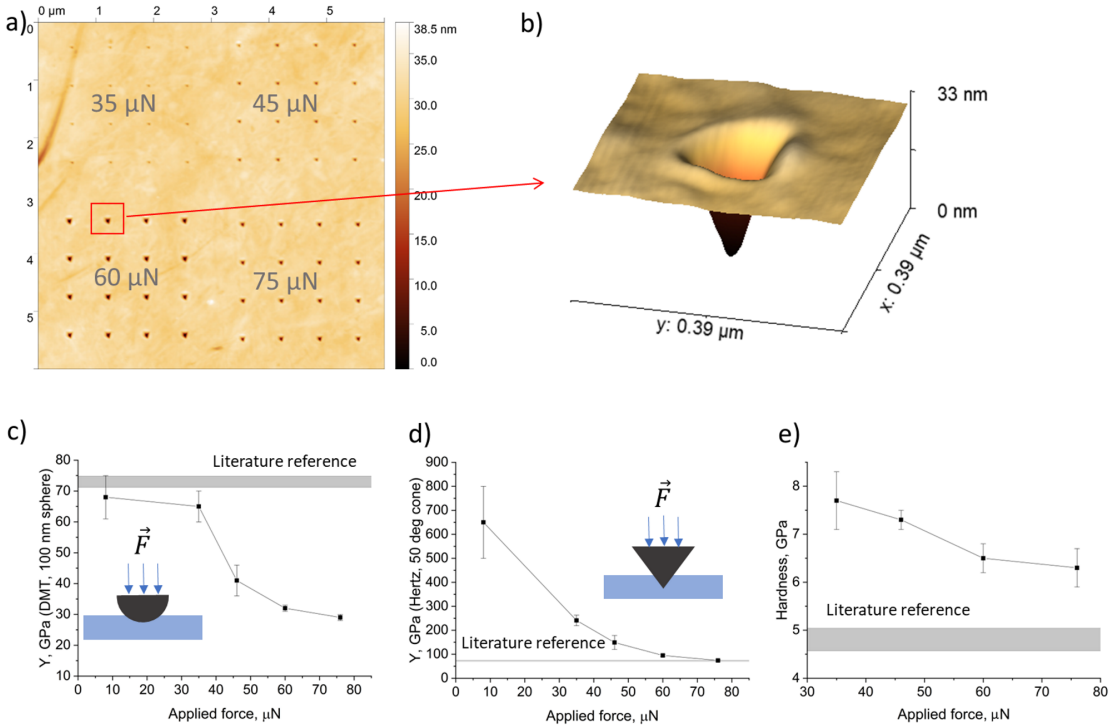

Figure 32. Calibration of a stiff diamond probe (k=400 N/m) on a fused silica reference sample. a) Topography, b) The stiff diamond cantilever, c) The DMT model, d The Hertz model), e) Hardness depending on the applied force. [39]

The stiff diamond cantilever has a spherical tip apex with R ≈ 100 nm and a pyramid body with half angle ≈ 45 deg (Figure 32b). During indentation the contact geometry changes from spherical at low force to pyramidal at high force. Different models were used to fit force-distance curves and calculate Young's modulus. Using the reference fused silica sample (Figure 32a) it was established that at the low indentation force (≤20 μN) where the tip-sample contact geometry is mainly determined by the tip apex (assuming flat surface) the DMT (Derjaguin-Muller-Toropov) model gives results in agreement with literature reference, which can be found elsewhere (Figure 32c). Here the DMT model assumes a spherical indent with R=100 nm made of synthetic diamond, and the sample's Poisson ratio 0.15. At the high indentation force (>70 μN) where the tip-sample contact geometry is mainly determined by the tip body, the Hertz model gives adequate results (Figure 32d). The Hertz model assumes a conical indent with 50° half angle made of synthetic diamond, and the sample's Poisson ratio 0.15. For the diatom samples, low loading force was applied, and the DMT model was employed, except for the hardness measurements. Image processing and analysis was performed using Gwyddion software.[39][AFM measurements were performed by Dr Sergei Luchkin]

3.6.3 In situ SEM nanoindentation

The Alemnis Standard Assembly (ASA) indentation platform (Alemnis, Gwatt, Switzerland) was used to perform in situ nanoindentation testing of cleaned frustules and air-dried living diatom cells placed on silicon wafer inside the chamber of a TESCAN SOLARIS S9000 SEM (TESCAN ORSAY HOLDING, Brno, Czech Republic). In the current work, the ASA tester was equipped with a flatpunch conductive diamond indenter with the diameter of 2.5 μm on the cutting edge and 60°

cone angle. The experiment implied synchronization of two parallel processes like SEM images acquisition and indentation test. In order to achieve the best SEM resolution considering design limitations of the devices, ASA platform was tilted on 20° and moved to the working distance of ~7 mm. The SEM images were recorded under the following conditions: high voltage of 5 kV, beam current of 1 nA, spot size of 15 nm, pixel size of 40 nm and recording speed of 0.5 fps. The nanoindentation testing was done in both static and dynamic modes. The static mode was done under the regime of the linear depth control where the test consisted of three stages as indenter approach, holding and indenter retraction. The dynamic mode included a sinusoidal signal instead of a holding stage. The penetration depth was estimated for each diatom cell height before the test. [In situ SEM nanoindentation has been performed with the participation of Pavel Somov and Eugene Statnik]

3.7 Study of resonance frequencies of diatoms

3.7.1 Numerical simulation using COMSOL Multiphysics

In silico calculations were done with COMSOL Multiphysics by the finite-element method. The geometrical dimensions of the computational model were taken from the corresponding SEM images of the diatom. For evaluation of vibrational eigenfrequencies, the COMSOL Multiphysics Structural Mechanics module was used. The density and Poisson ratio of the silica were described previously[148]. The Young's modulus value was obtained in our study on the mechanical properties[39]. All these values are shown in Table 6. Fixed boundary conditions were applied to the lower part of the diatom. [Numerical simulations were performed with the help of Stanislav Perevoschikov]

3.7.2 AFM measurements

Before AFM measurements, cleaned diatom frustules were prepared according to the procedure described in the section 3.3. After that, a drop of a cleaned frustule suspension was applied to a precleaned silicon wafer. The transfer of diatom frustule from a silicon substrate to an AFM chip was carried out using a nanomanipulator inside the chamber of a TESCAN Solaris microscope. Individual frustules were subsequently welded to the chip using FIB to ensure that they would not come off the surface during measurements and gold-sputtered using magnetron sputtering machine Quorum Q150R ES (Quorum, England) at sputter current 25 mA. AFM measurements were performed using Cypher ES microscope (Asylum Research, Oxford Instruments) installed inside an Ar filled glove box (MBraun). Measurements were performed by obtaining frequencies of thermal vibrations with the subsequent FFT analysis and by mechanical excitation followed by detection via a lock-in amplifier. The measurements of frequencies of thermal vibrations (without piezodriver swing) are used to search for natural frequencies and calibrate the stiffness and amplitude of the AFM probes to avoid spurious frequencies. Image processing and analysis was performed using Gwyddion software. [Samples were prepared by the author; measurements were performed with the help of Dr Sergei Luchkin]

3.8 Study of optical properties of diatoms

3.8.1 Numerical simulations using Fourier modal method

In numerical simulations, the shell is approximated by a periodic structure constituting a multidimensional array of pores in a silica matrix. To calculate the near-field field distribution of the transmitted and reflected waves, a Fourier modal method (FMM) was used[166]. Calculations were performed in MATLAB. To speed up the

process, calculations were parallelized on a 40-core computing server. The formalism of the FMM includes splitting the periodic structure into elementary planar layers, homogeneous in Z direction. The solutions to Maxwell's equations for each layer are found by expansion of the electric and magnetic fields into Floquet-Fourier harmonics. In these numerical simulations the Fourier series is truncated on 97 harmonics to strike a balance between computational efficiency and accuracy. This number of harmonics provides a sufficiently detailed representation of the diatom frustule's complex structure, allowing for meaningful and accurate results without unnecessarily increasing computational demands. [Numerical simulations were performed by Prof Sergey Dyakov]

3.8.2 Extinction spectroscopy of individual diatoms

To measure UV-VIS steady-state extinction spectra of individual living diatom cells and cleaned frustules, a combined system consisting of a stabilized deuterium UV light source SLS204 and a stabilized tungsten-halogen lamp SLS201L/M (Thorlabs, USA) coupled to CCD detectors Flame and Maya2000Pro (Ocean Insight, USA) was used. [Extinction spectra were collected by the author]

3.8.3 Chloroplast distribution study using FLIM

Fluorescence lifetime imaging was also performed in the time-correlated single-photon-counting (TCSPC) mode using the confocal system DCS-120 (Becker&Hickl, Berlin, Germany) installed on the Eclipse Ti2 (Nikon, Tokyo, Japan) microscope. Excitation was performed with a 473 nm picosecond laser BDS-SM-473-LS-101 (Becker&Hickl, Berlin, Germany) with a 30 ps duration impulse driven at 50 MHz repetition rate synchronized with hybrid detector HMP-100-40 (Becker&Hickl, Berlin,

Germany) via board SPC-150 (Becker&Hickl, Berlin, Germany). [FLIM images were acquired by the author]

3.9 Modification of diatomite with gold nanoparticles

3.9.1 Gold nanoparticle synthesis

Gold nanoparticles were synthesized by standard citrate synthesis. 88 μL of 1 M $HAuCl_4$ aqueous solution was diluted to 50 mL by deionized water and heated up to boiling. While boiling, 8.9 mL of 1% sodium citrate tribasic dihydrate was added. The resulting solution (concentration, 2×10^{12} particles/mL) was stirred at boiling temperature for 1 h, then slowly cooled, and stored in the fridge at +4 °C. Gold nanoparticle size and zeta potential were characterized by ZetaSizer Nano ZS analyzer (Malvern Panalytical, Malvern, UK), extinction spectrum was collected by Infinite M Nano+ (Tecan Trading AG, Switzerland). [Synthesis was performed by the author]

3.9.2 Fabrication of gold-coated diatomite

Before modification, diatomite powder was washed with DI water two times. A standard LbL procedure consists of depositing alternating layers of oppositely charged materials with washing steps in between. Firstly, 20 mg of negatively charged diatomite were suspended in positively charged polyallylamine hydrochloride (PAH) solution (2 mL; 0.1% PAH in 0.15 M sodium chloride), followed by agitation in a vortex for 15 min. After this standard adsorption procedure, the samples were washed three times with DI by centrifugation using the Centrifuge 5340 (Eppendorf, Germany) (664 × g, 3 min). Gold nanoparticles were subsequently deposited onto the PAH-coated diatomite using FIL approach. Namely, 2 mL of gold nanoparticle solution (10^{12} particles/mL) were added, and the mixture was placed in a freezer (−20°C) in a continuously rotating flask for 2 h. After the water was completely frozen, the samples were thawed at room

temperature, centrifuged at 664 × g for 3 min, and washed at least three times with DI water, resulting in the formation of a bilayer consisting of a polyelectrolyte/nanoparticle composite. Depending on the sample, the cycle was repeated up to five times to obtain a multilayered composite structure. The resulting composites were stored in water. [Gold-coated diatomite samples have been fabricated by the author]

3.9.3 Zeta potential measurements

Zeta-potential measurements of gold-coated diatomite[94] were performed upon deposition of each layer using ZetaSizer Nano ZS analyzer (Malvern Panalytical, Malvern, UK). All samples were diluted in DI water and placed in the U-cuvette. Measurements were carried out at 25 °C and repeated three times. [Zeta potential measurements were conducted by the author]

3.9.4 SEM study of prepared samples

Diatomite modified by gold nanoparticles was imaged with FIB-SEM TESCAN SOLARIS S9000 (Tescan, Czech Republic) under a high vacuum at 5 keV landing energy, 300 pA beam current and with registration of the signal using a backscattered electron detector. Samples were analyzed without applying a conductive coating. [SEM images were acquired with the help of Pavel Somov]

3.9.5 TEM and EDX measurements

Bright field TEM (BF-TEM) images, high angle annular darkfield scanning transmission electron microscopy (HAADF-STEM) images, and energy-dispersive X-ray (EDX) spectra and compositional maps were acquired in STEM-mode on an aberration corrected FEI Titan Themis Z (ThermoFisherScientific, Breda, Netherlands) transmission electron microscope equipped with a Super-X detection system and operated at 120 kV. Specimens were prepared by depositing a drop of gold-coated

diatomite solution onto a holey copper grid with a carbon/lacey supporting layer and letting them dry in the air followed by transferring into TEM columns. [TEM/EDX measurements were performed in Advanced Imaging Core Facility, Skoltech]

3.9.6 Photoacoustic visualization of gold-coated diatomite

The photoacoustic signals from the gold-coated diatomite composites were obtained using RSOM setup Explorer P50 (iTheraMedical GmbH, Germany) as described in the section 3.2.5. For the purpose of imaging, a 2-fold serial dilution of stock suspensions of gold-coated diatomite was performed 5 times. 3 µl of these suspensions were mixed with melted agarose gel (7 µl). 4-µl droplets containing different concentrations of these mixtures were pipetted into a petri dish that was filled with DI water after solidification and placed in the imaging chamber. [Photoacoustic visualization has been performed by the author]

3.9.7 SERS measurements of gold-coated diatomite

For SERS measurements, diluted suspensions of gold-coated diatomite consisting of one (Diatomite-$(PAH/Au)_1$), three (Diatomite-$(PAH/Au)_3$), and five (Diatomite-$(PAH/Au)_5$) bilayers were mixed with 0.2 mM Rhodamine 6G in an equal volume and left overnight. The Raman spectra from liquid droplets pipetted onto the quartz glass were collected by a confocal Raman spectrometer upon excitation with 633 nm He-Ne laser. A grating with 600 grooves/mm was used throughout. Spectra were registered in the Raman-shift range 600–1700 cm^{-1} at laser power 6.1 mW with 20 s acquisition time and averaged on 10 accumulations. Baseline correction was provided by instrument-embedded software (LabSpec6, HORIBA France SAS, France) after the signal acquisition. [SERS measurements were performed with the help of Anastasiia Merdalimova]

Chapter 4. Monitoring and characterization of diatom colonies

This chapter demonstrates results of monitoring and characterization of diverse diatom cultures throughout their extended cultivation within controlled laboratory environments. The most of the results presented here are part of the following published articles:

- [155] **Cvjetinovic J**, Salimon I, Novoselova M, Sapozhnikov Ph, Shirshin E, Yashchenok A, Kalinina O, Korsunsky A, Gorin D. Photoacoustic and fluorescence lifetime imaging of diatoms. *Photoacoustics.* 2020; 18; 100171;
- [162] **Cvjetinovic J**, Perkov S, Kurochkin M, Sergeev I, German S, Bedoshvili Ye, Davidovich N, Korsunsky A, Gorin D. Concentration dependence of optical transmission and extinction of different diatom cultures. *Journal of Biomedical Photonics and Engineering*. 2023; 9(1):1-9;
- [153] **Cvjetinovic J**, Bedoshvili Ye, Nozdriukhin D, Salimon A, Korsunsky A, Gorin D. Photonic tools for evaluating the growth of diatom colonies during long-term batch cultivation. *Journal of Physics: Conference Series*. 2022; 2172; 012011;
- [163] **Cvjetinovic J**, Nozdriukhin D, Bedoshvili Ye, Salimon A, Korsunsky A, Gorin A. Assessment of diatom growth using fluorescence imaging. *Journal of Physics: Conference Series*. 2021; 1984; 012017;
- [154] **Cvjetinovic J**, Bedoshvili Ye, Nozdriukhin D, Efimova O, Salimon A, Volokitina N, Korsunsky A, Gorin D. In situ fluorescence/photoacoustic monitoring of diatom algae. *SPIE Proceedings* Dynamics and Fluctuations in Biomedical Photonics XVIII; 2021; 11641; 116410G.

All experimental results in this Chapter were obtained and analyzed by the author if not stated otherwise. The diatom incubator was fabricated by Daniil Nozdriukhin, the optical setup for monitoring the growth was fabricated by Dr Maxim Kurochkin and Sergei Perkov, the microfluidic cell was fabricated by Dr Sergei German. The utilization of Figures in this Chapter is granted by the Elsevier (the publisher of Photoacoustics journal), Samara National Research University (the publisher of Journal of Biomedical Photonics and Engineering), IOP Publishing Ltd (the publisher of Journal of Physics: Conference series), SPIE (the publisher of SPIE Proceedings Dynamics and Fluctuations in Biomedical Photonics XVIII) Copyright Policy.

4.1 Background

Monitoring the growth of diatoms during cultivation is crucial for optimizing their growth conditions and achieving high biomass production. Several techniques can be used to monitor the growth of diatoms during cultivation, such as optical density, dry weight, chlorophyll concentration, and cell counting.

1. Optical density measurements: Optical density (OD) measurement is a rapid and non-destructive method of measuring the biomass concentration of diatoms.[167] This method measures the amount of light scattered or absorbed by the cells in a culture using a spectrophotometer which can be related directly to cell mass or cell number. As the cell concentration increases, the OD increases proportionally, allowing for real-time monitoring of the culture growth. However, this method does not provide information about the cell size and morphology of the diatoms.

2. Dry weight measurement: Dry weight measurement is a destructive method that estimates the biomass concentration of diatoms by weighing the dried cell pellets. This method is accurate and provides information about the cell size and morphology

of the diatoms, but it requires the destruction of the entire cell culture and is time-consuming.[168]

3. Chlorophyll concentration measurement: Chlorophyll concentration measurement is a reliable method for monitoring the growth of photosynthetic diatoms, as it reflects the photosynthetic activity of the cells. This method involves the extraction of chlorophyll from the cells using organic solvents and subsequent measurement of the chlorophyll absorbance using a spectrophotometer. However, this method does not provide information about the cell count or cell size of the diatoms.[169]

4. Cell counting: Cell counting is a direct and accurate method of measuring the concentration of diatoms in a culture. This method involves the use of a microscope and a hemocytometer to count the number of cells in a given volume of the culture. Cell counting provides information about the cell size, morphology, and viability of the diatoms. However, it is a time-consuming and labor-intensive method.[170,171]

Each of the above-mentioned methods has its advantages and limitations. Since microalgal cells are usually dispersed in the medium, estimating their biomass remains difficult. It is therefore impossible to perform direct gravimetric measurements due to the concentration of cells required. OD (turbidity) and chlorophyll fluorescence indirectly estimate microalgal biomass, but are susceptible to faulty measurements caused by light-cell interference. Depending on the application and the specific requirements, one or more of these methods can be used to optimize the growth conditions of diatoms and achieve high biomass production.[169–171]

This thesis introduces an alternative approach to growth monitoring utilizing both commercially available and custom-developed optical setups. Optical methods can

be used for monitoring the growth of diatoms, and two notable techniques are photoacoustic (optoacoustic) imaging and fluorescence-based methods.[153,154]

1. Photoacoustic imaging: Photoacoustic visualization is non-invasive, high-resolution imaging technique that utilizes laser light to produce acoustic waves within the sample, which can be detected by ultrasound transducers[172]. It is readily used to collect meaningful acoustic signals from complex biological objects with unprecedented spatial accuracy of detection of their components containing light-absorbing molecules. The excitation of hierarchically finer scale objects—light-absorbing chromophore molecules (melanin, hemoglobin, water, lipid, etc.)—ultimately converts to the vibrations of much bigger, hierarchically larger-scale objects such as cell organelles (e.g., melanosomes) or whole cells (erythrocytes)[173,174]. The flow of energy across hierarchical levels of organization is associated with the changes in the underlying physical phenomena according to size and scale effects[175]. The frequencies of these vibrations, recorded owing to the optically driven acoustic signal, range from 1 MHz to 100 MHz, which is of the same order of magnitude as the eigenfrequencies of capsular mechanical objects having sub- and micrometer sizes[176]. Very limited data[177,178] are available on the photoacoustic studies of single-cell organisms—both prokaryotes (e.g., cyanobacteria) and eukaryotes (e.g., diatoms)—which contain light-absorbing chromophores such as chlorophyll or carotenoids. The photoacoustic visualization of such living objects may have a number of ecological, biotechnological, and biomedical applications, such as the remote and rapid control over microbial cultures and media, cell studies, sanitary control, and aquaculture. The photoacoustic technique is very interesting from the standpoint of observations of diatoms in their natural environments and also during culturing. It is potentially possible

to install photoacoustic tools in vessels or in harbor constructions that are used to monitor diatoms in aquatic environments. Owing to laser irradiation and subsequent absorption of light by the diatom chromophores, the photoacoustic method is promising for studying the activity of these objects in their natural environments, as well as for monitoring their growth in bioreactors or aquaculture installations by means of the imaging of colonies. In this thesis, photoacoustic measurements were performed using RSOM Explorer P50 setup, as described in the section 3.2.3.

2. Fluorescence-based methods: Fluorescence imaging and spectroscopy are highly sensitive techniques that have been widely used to monitor phytoplankton. Two types of light-harvesting pigments of diatoms are well documented[63,179,180]: chlorophylls and carotenoids. The predominant form of chlorophyll observed in diatoms is chlorophyll a, which absorbs energy in the violet-blue and orange-red regions[63,179,181]. Unlike many other types of algae, diatoms also contain chlorophyll c, which absorbs mostly blue and red light[63]. The main carotenoid identified in diatoms is fucoxanthin, which absorbs light in the blue-to-green region of the spectrum[63,179,180]. Therefore, fluorescence-based methods can be used to monitor the chlorophyll content and the growth of diatoms.[170] For example, by measuring the fluorescence intensity emitted by the chlorophyll in a culture using a fluorometer, the chlorophyll concentration and the growth rate of the diatoms can be estimated. Fluorescence-based methods are non-destructive, fast, and sensitive, and can be used to monitor the growth of diatoms in real-time. The absorption range of different algae pigments is shown in Figure 33.

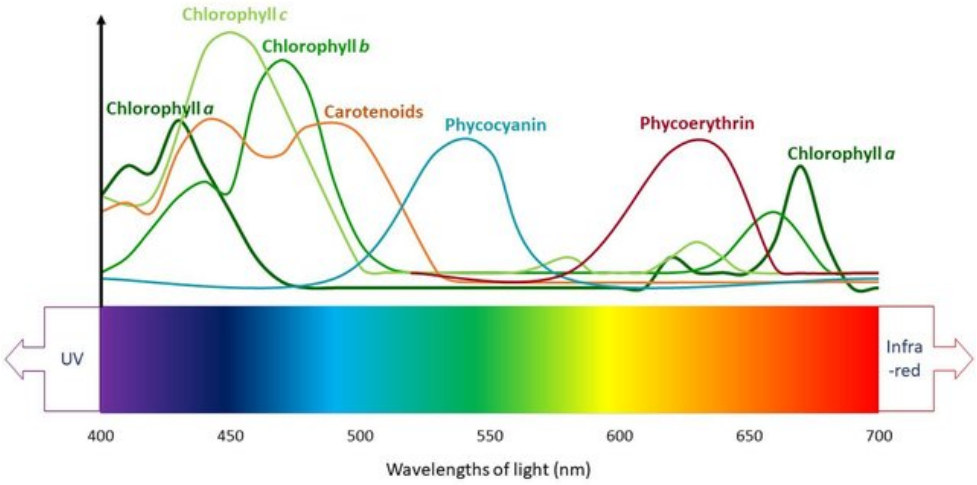

Figure 33. Absorption range of different algae pigments[182]

The results on optical monitoring of diatom growth using RSOM Explorer P50 and IVIS SpectrumCT setups are presented separately based on the division of the cultures by natural environment and form: freshwater pennate and marine centric diatoms.

4.2 Monitoring of freshwater pennate diatoms

A. sibiricum diatoms isolated from the Baikal Lake were cultivated over 70 days in the incubator (Figure 34) and monitored using raster scanning optoacoustic mesoscopy (RSOM) approach and IVIS SpectrumCT In vivo Imaging system.

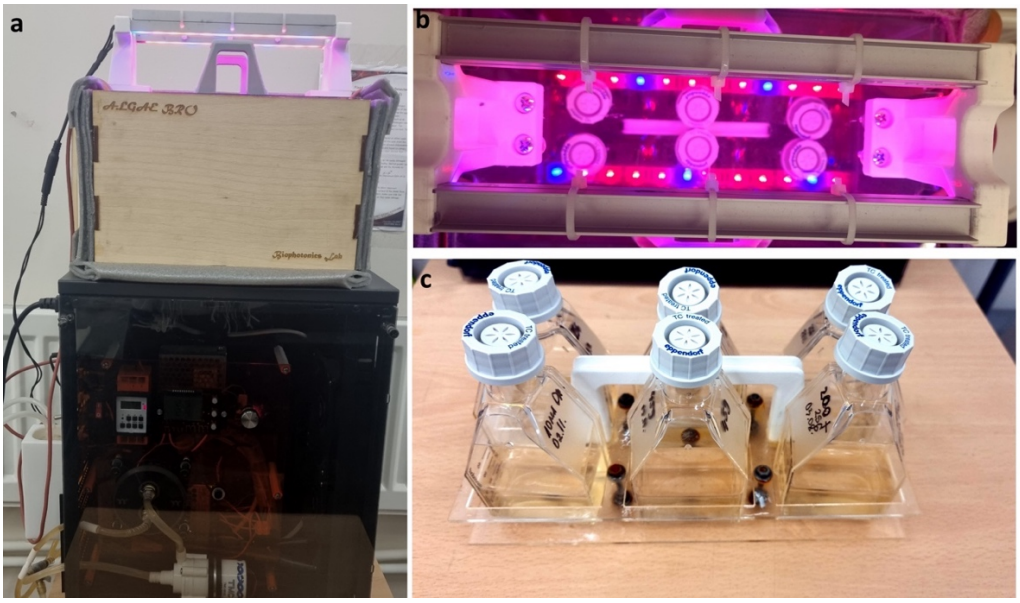

Figure 34. Photography of: a) incubator, b) LED strip above cell culture flasks, c) cell culture flasks with diatoms.

In light of the impracticality of conventional cell counting during long-term cultivation, spectroscopic techniques were employed to showcase the monitoring capabilities of RSOM and IVIS. Furthermore, valuable insights into the state of diatoms can be derived from extinction and fluorescence spectra. Notably, anomalies or shifts in the spectra may serve as indicators of stressors or alterations in the physiological state of the diatom algae. This set of monitoring techniques, as believed, will be further widely used in aquaculture and incubator practice to facilitate the harvesting of diatom algae and diatom-derived bioactive substances for pharmaceutical and biomedical purposes.

A. sibiricum are monoraphid pennate diatoms with bilateral symmetry, whose raphe is present only on one valve of the frustule, as shown in Figure 35a. Valves are

dorsiventral, with rounded apices. Their length ranges from 9.8 to 18.7 µm, while the width is 4.5–6.0 µm. Distal raphe ends are curved toward the ventral margin.

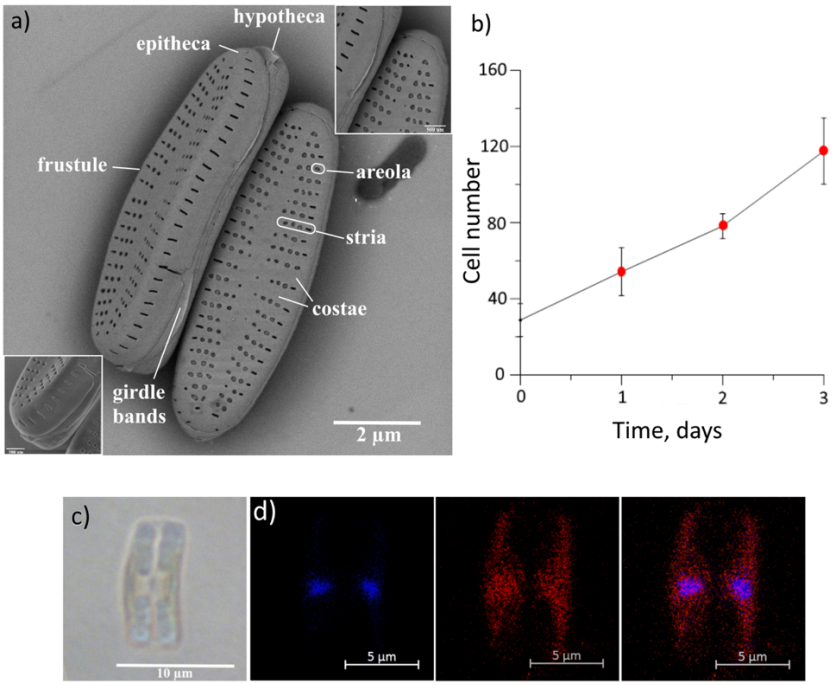

Figure 35. A. sibiricum: a) SEM image, b) culture growth during three days after inoculation, c) optical image of two diatoms during cell division, d) confocal images of: cells fixed formaldexyde and stained with DAPI (blue, nucleus; red, chlorophyll).

The growth kinetics of a periodic culture of diatoms is very similar to the growth kinetics of prokaryotic organisms[183]. In this case, the lag phase and the onset of the exponential growth of the culture were observed by cultivating diatoms in microvolumes. The conventional method involving cell counting over the initial four days of cultivation showed a steady growth of the culture (Figure 35b). After four days of culture, counting was difficult due to the formation of cell clusters. Light microscopy

image of *A. sibiricum* during the cell division is shown in Figure 35c. A confocal laser microscopy was used during the first days of culturing to observe the DNA material of DAPI-labeled cells (Figure 35d). Nuclei, located in the center of the cells, had an oval shape (Figure 35d). The red fluorescence of the chloroplasts was excited with 647 nm wavelength. Chloroplasts occupy most of the cells, which is also confirmed by light images. The state of chloroplasts and cell division indicate the viability of the culture.

Further growth was more accurately monitored by proposed methods—fluorescence visualization using IVIS imaging system and photoacoustic measurements with RSOM setup. Since the studied species are benthic (that is, they live on substrates [184]), and capable of secreting a lot of mucus and forming cell clusters[185], the main difficulty in counting cells in microvolume in a well-plate is the impossibility of selecting adequate aliquots and plotting growth curves with sufficiently large technical errors. The proposed methods for assessing chlorophyll, which do not require the extraction of cells from the medium, increase the accuracy of experiments.

The results of fluorescence visualization of *A. sibiricum* in cell culture flasks during 100 days of cultivation using IVIS SpectrumCT imaging system are shown in Figure 36a, b. The average radiant efficiency increases with increasing incubation time up to 45 days, followed by a steady decrease. The result indicates that after 45 days, the population of living cells begins to decline, probably due to the lack of necessary nutrients, since batch cultivation implies that nutrients are provided only at the beginning without further addition. However, during 100 days of monitoring, the occurrence of the final death phase could not be observed. The fluorescence spectra collected during the cultivation demonstrate an emission band, which is attributable to chlorophyll a (Figure 36c). The fluorescence intensity at 680 nm and IVIS imaging

results were also compared. According to Figure 36d, the maximum values were obtained after 45 days of incubation, which corresponds well with the results obtained with the IVIS.

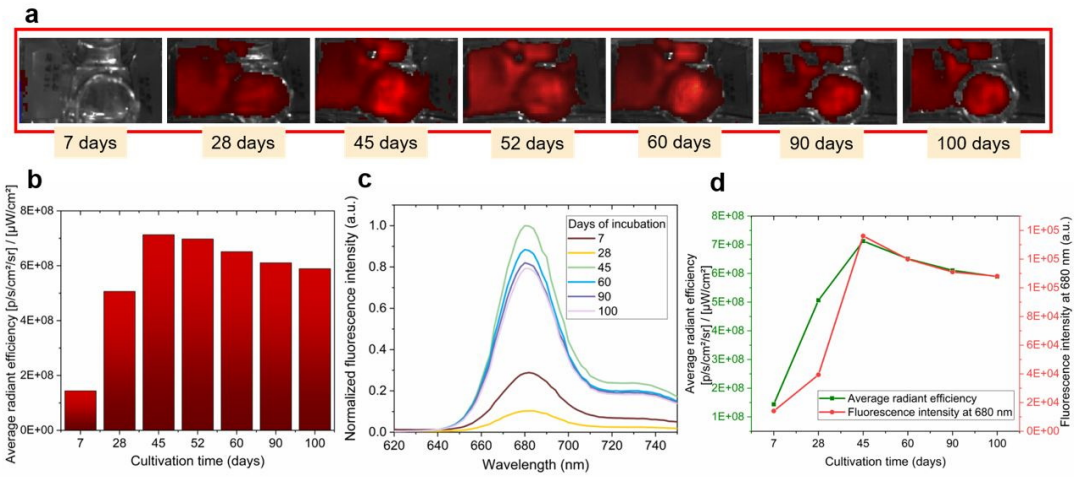

Figure 36. (a) Images of cell culture flasks containing diatoms obtained using the IVIS platform (top view), (b) The average radiant efficiency of diatoms during the cultivation period, (c) Normalized fluorescence spectra of *A. sibiricum* cells, (d) Comparison of fluorescence intensity at 680 nm and average radiant efficiency depending on the cultivation time.

Diatoms exhibit strong photoacoustic signals owing to the presence of chlorophylls and carotenoids that absorb very well the 532 nm wavelength upon illumination. Figure 37a shows the images of diatom-agarose droplets obtained after 7, 28, 45, 60, 90, and 100 days of cultivation using the RSOM system. The dependence of the mean pixel intensity signal on the incubation time is illustrated in Figure 37b. The highest intensity of the photoacoustic response was achieved after 45 days of cultivation. Before mixing with agarose, cells in DM medium have to be properly shaken. However, this diatom species tends to aggregate due to secreted mucilage,

which explains why the red signal at 11-33 MHz is higher. The extinction spectra shown in Figure 37c demonstrate peaks attributable to chlorophyll a and c and the carotenoid fucoxanthin. By comparing the extinction and photoacoustic signals in two frequency ranges (Figure 37d), it can be concluded that they are in good agreement. Thus, the spectroscopic characterization confirmed the results obtained using the IVIS and RSOM imaging systems and proved their capabilities in assessing the growth of diatoms.

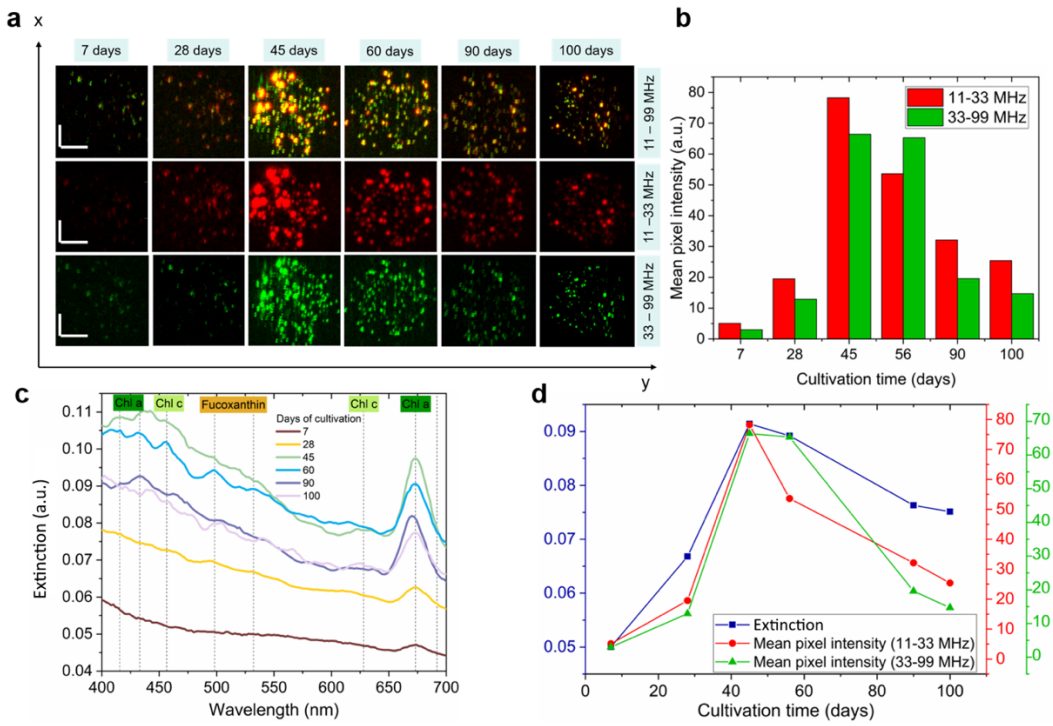

Figure 37. (a) RSOM images of *A. sibiricum* diatoms mixed with agarose gel at 11-99 MHz, 11-33 MHz (red), 33-99 MHz (green) after 7, 28, 45, 60, 90, and 100 days of cultivation. Scale bar: x, y-axis – 0.5 mm. Red color corresponds to a low-frequency signal emitted by larger samples. A high- frequency signal, shown with green bars, is emitted by smaller structures. (b) The dependence of mean pixel intensity on the cultivation time, (c) Extinction spectra collected at different periods of cultivation,

(d) Comparison of extinction at 523 nm and mean pixel intensities at 11-33 MHz and 33-99 MHz, as functions of the cultivation time.

4.3 Monitoring of the growth of marine centric diatoms

The same techniques were employed for monitoring of the growth of marine centric diatoms, which were cultivated on the windowsill, as described in Materials and methods section: *Coscinodiscus* sp. (strain 21.0407-OA) and *B. titiana* (strain 0.0212-OH) (Figure 38a,b, respectively). IVIS results are shown in Figure 38c, d.

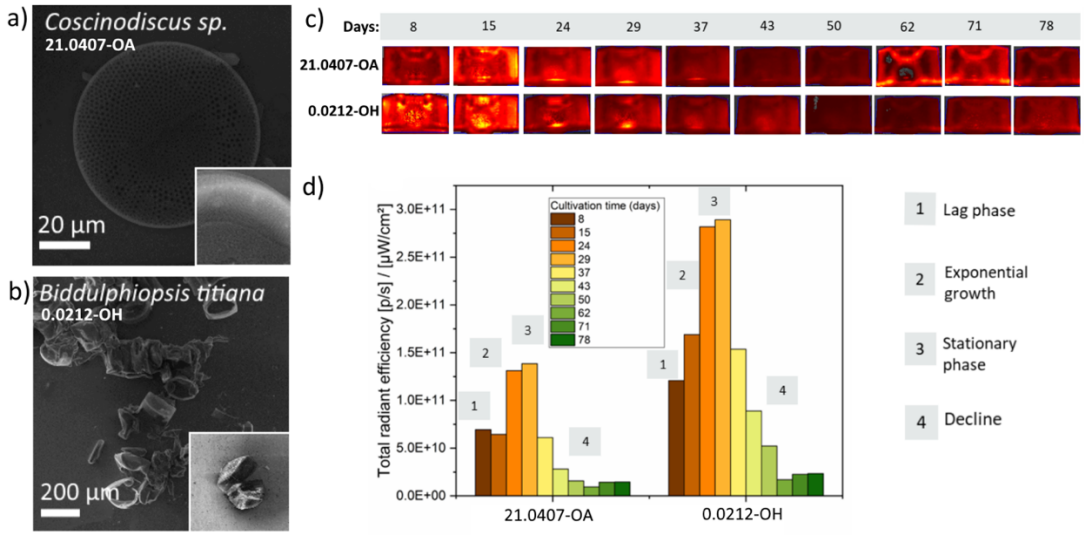

Figure 38. SEM images of: a) *Coscinodiscus* sp. (21.0407-OA), b) *B. titiana* (0.0212-OH). c) Images of flasks containing diatoms obtained using IVIS imaging system, d) Total radiant efficiency depending on the cultivation time of both strains.

The total radiant efficiency in both cases increases with increasing cultivation time up to 30 days, followed by a decrease in intensity (Figure 38b, c). The result indicates that the cells, after slow division, begin to die. One of the reasons for

inhibition of cell growth and death is the lack of essential nutrients, as nutrients are provided only at the beginning. In addition, the passing of the mitotic cell cycle is inhibited by the products of cell metabolism that accumulate in the “old” culture.

The fluorescence spectra obtained during cultivation show an emission band that is attributed to chlorophyll *a* (Figure 39a, c). According to Figure 39b, d the maximum values were obtained after 30 days of incubation, which is in good agreement with the results obtained using the IVIS system.

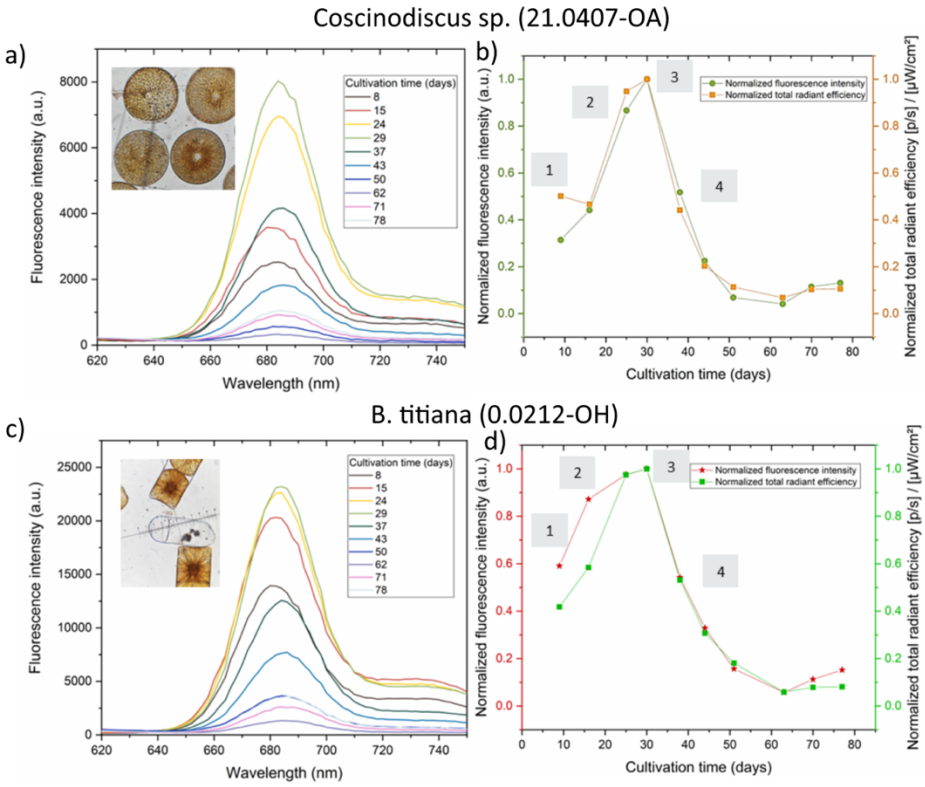

Figure 39. Fluorescence spectra of: a) *Coscinodiscus* sp., c) *B. titiana*. Comparison of normalized fluorescence intensity at 680 nm and normalized total radiant efficiency depending on the cultivation time of: b) *Coscinodiscus* sp., d) *B. titiana*. 1-lag phase, 2-exponential growth, 3-stationary phase, 4-decline.

To monitor the growth of diatoms using RSOM, cultures of *C. oculus-iridis* (strain 0.1211-OD), *Coscinodiscus* sp. (strain 21.0407-OA), *B. titiana* (strain 0.0212-OH) and *U. acus* (strain 15k 595) were mixed with agarose gel and measured on days 7, 15, 25 and 32 of cultivation, as described in the Materials and Methods section. The resulting images are shown in Figure 40.

Using the RSOM system, an optoacoustic signal from diatoms was successfully obtained (Figure 40a), excited by a laser with a wavelength of 532 nm. The dependence of the average pixel intensity signal on the cultivation time is shown in Figure 40b for each species. The signal intensity increases with cultivation time, reaching a maximum value after 32 days of cultivation for all cases except for strain 21.0407-OA, where the maximum is reached after 25 days. Typically, the signal in the 11-33 MHz frequency range, which occurs from larger samples, is more intense, which may also indicate possible cell aggregation and insufficient mixing of the suspension. Insufficient agitation could also result in a stronger signal in the 33-99 MHz frequency range for strain 21.0407-OA after 25 days of cultivation. The most intense signal comes from the largest species, *B. titiana*. In this case, the resolution of the microscope is large enough to receive a signal from one cell.

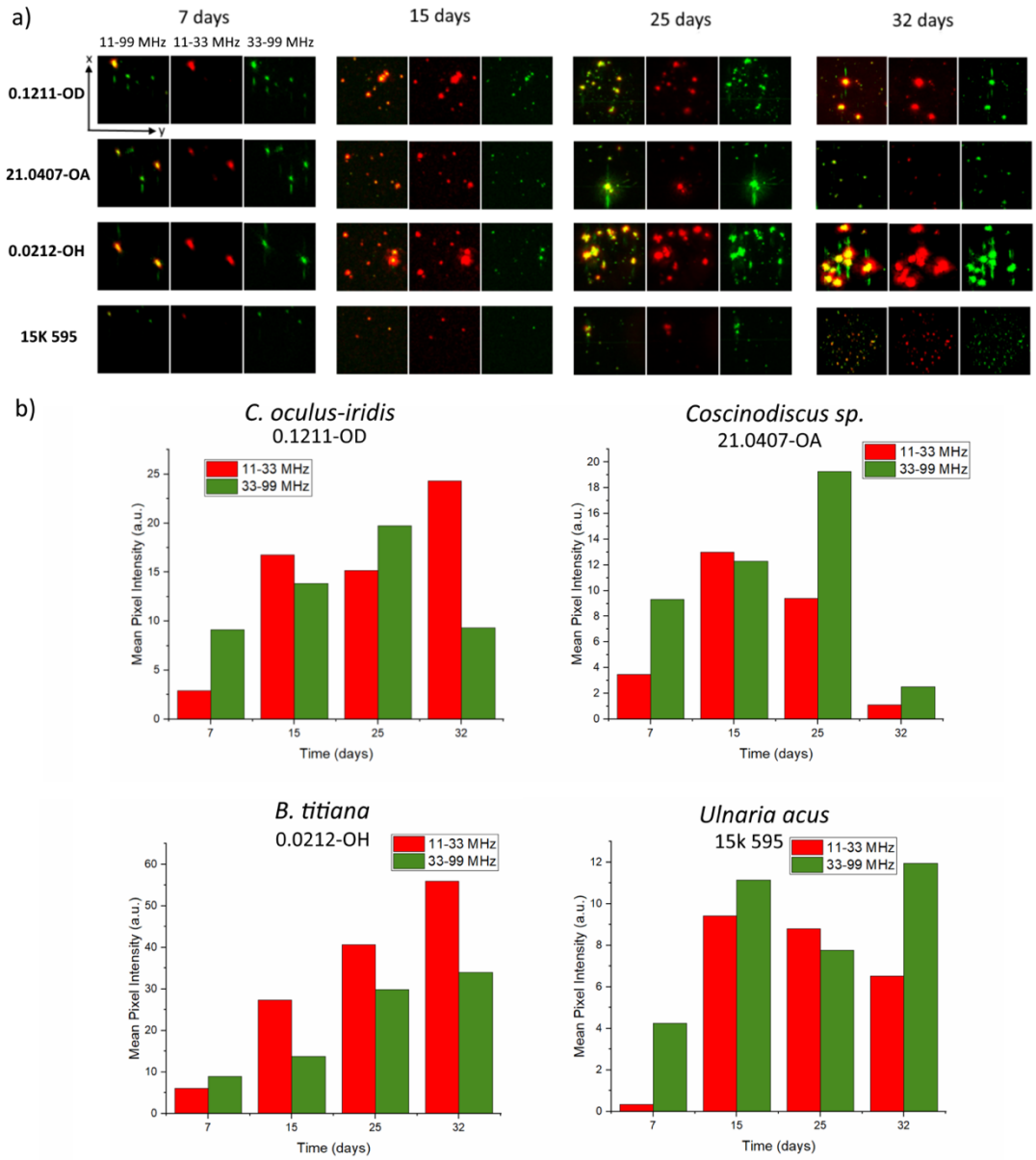

Figure 40. a) RSOM images of 4 different cultures obtained during 32 days of cultivation, b) Mean pixel intensity vs. cultivation time for all strains.

Monitoring of the growth of three different diatom species (*Coscinodiscus* sp., strain 21.0407-OA; *B. titiana*, strain 0.0212-OH, *U. acus*, strain 15k 595) was also carried out using the spectrophotometric method. The extinction spectra obtained during long-term cultivation of diatoms are shown in Figure 41a-c. In addition, graphs

of the time-dependence of the extinction of the main pigments (chlorophyll *a*, fucoxanthin, chlorophyll *c*), normalized to the maximum, were plotted (Figure 41d-f).

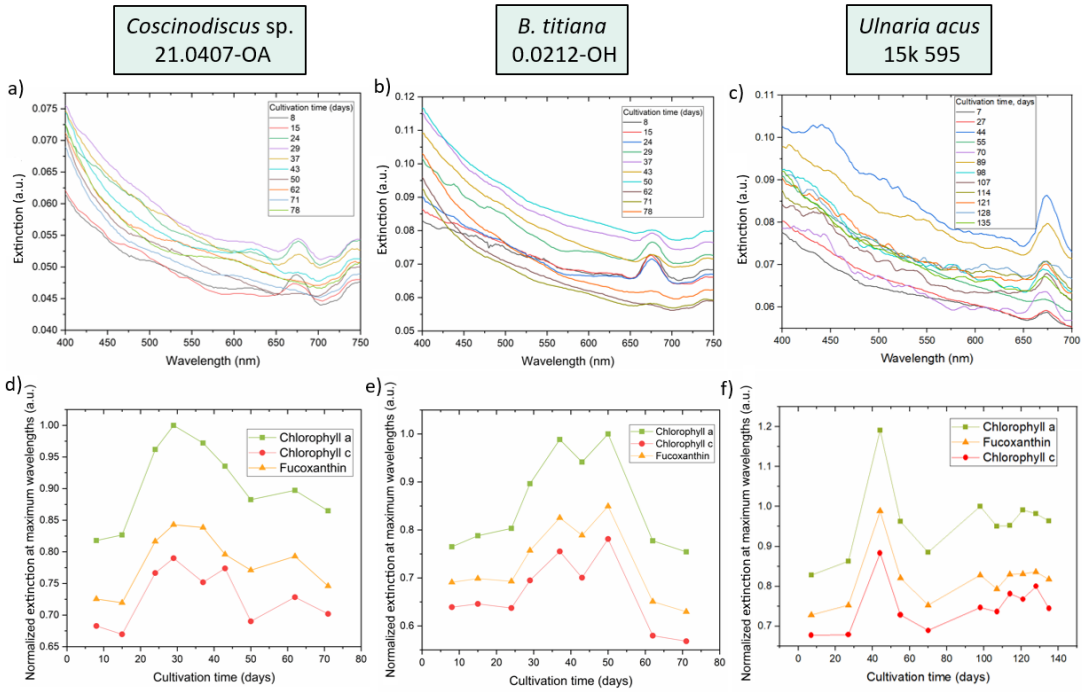

Figure 41. Extinction spectra of: a) *Coscinodiscus* sp., b) *B. titiana*, c) *Ulnaria acus*. Normalized extinction at maximum wavelengths of: d) *Coscinodiscus* sp., e) *B. titiana*, f) *Ulnaria acus*.

The obtained spectra correlate well with the optoacoustic measurements carried out during 32 days of cultivation. Maximum values are observed after 30 days in the case of marine species *Coscinodiscus* sp. and *B. titiana* (Figure 41d, e) and 44 days for *U. acus* (Figure 41f), after which a drop is observed.

Insufficient mixing before measurement could be a potential factor contributing to the observed drops in values on the graph (Figure 41d-f). In addition, with continuous long-term cultivation, artifacts are possible due to a lack of nutrients or contamination

by other algae and bacteria. Also, decomposing pigments outside a living cell are not very stable compounds and can potentially affect the change in the spectra. The data obtained by IVIS, RSOM, spectrophotometry and fluorescence spectroscopy are in good agreement in the case of marine cultures.

At the outset of the cultivation, cell counting was conducted during the initial four days, allowing for the observation of both the lag phase and the commencement of exponential growth within the culture. However, small species of diatoms begin to form clusters a few days after seeding, which makes the counting almost impossible with more prolonged cultivation.[153,163] In the context of evaluating diatom growth during prolonged cultivation, the methods presented, which harness fluorescence and photoacoustic signals, constitute a valuable, rapid, and efficient alternative. These techniques offer numerous benefits in comparison to the traditional method of cell counting. Notably, they enable the rapid assessment of diatom growth without requiring extensive sample preparation. Methods like cell counting and optical density measurements are valuable for assessing diatom abundance, but they lack spatial resolution. The proposed techniques offer non-invasive monitoring of diatoms without the need for additional labels or dyes. The IVIS platform allows direct imaging of diatoms in cell culture flasks, eliminating the need for extraction of the sample and reducing the risk of introducing the contaminants to the diatom medium. It facilitates imaging of up to six cell culture flasks simultaneously within a minute. The IVIS system provides a resolution of 20 μm, whereas RSOM Explorer P50 offers a higher resolution of 10 μm. Consequently, with small cells, both systems primarily capture signals from colonies. However, when dealing with larger centric diatoms, RSOM allows for separate resolution. It is worth noting that the methods presented are particularly well-

suited for long-term cultivation monitoring. For studies focused solely on the initial growth phase over the first few days, the standard cell counting method may be the preferred choice.

4.4 Monitoring changes in diatom concentrations

4.4.1 Photoacoustic imaging

The first photoacoustic visualization of diatom algae is reported in this sub-section below. Figure 42a-c shows clearly that the photoacoustic signal from *K. amoena* was successfully obtained. The dependence of the photoacoustic signal (represented as the volume of 3D objects (diatoms), Figure 42d) on the diatom concentration shows that the volume of the 3D objects emitting the acoustic signal and the mean pixel intensity increased with the diatom concentration. As shown in Figure 42e, a low-frequency signal (shown with red bars) is emitted by a greater number of 3D objects than a high-frequency signal (shown with green bars), whereas a high-frequency signal (33–99 MHz) shows a higher mean pixel intensity than a low-frequency signal within the whole concentration range (Figure 42f). The photoacoustic signal from K. amoena can still be detected at a minimal concentration of 3 cells/µl (Figure 42f).

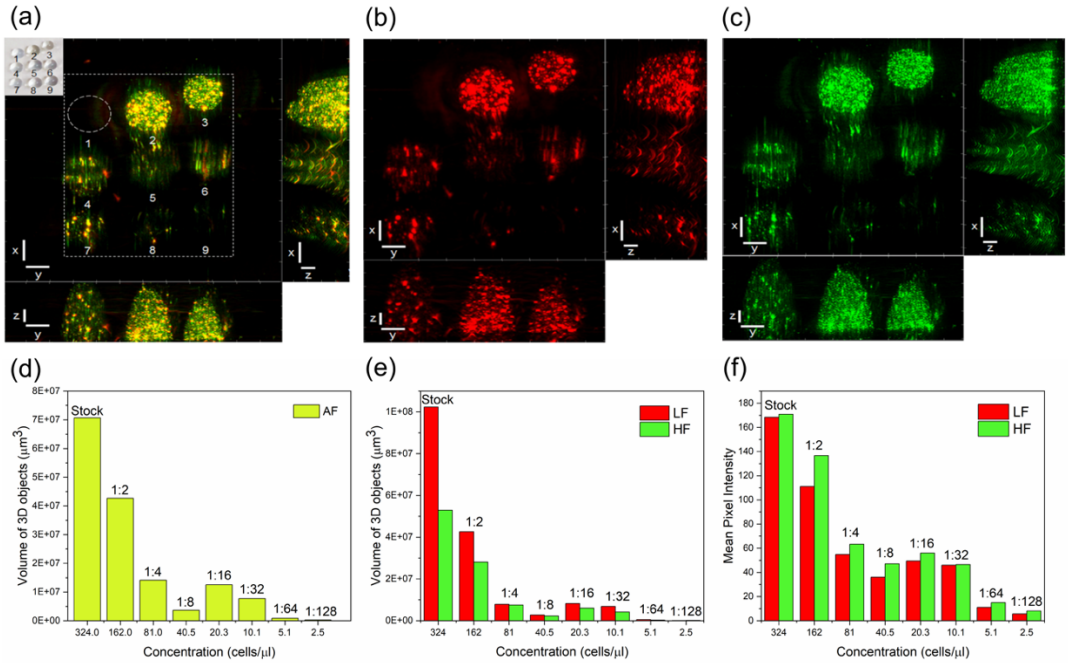

Figure 42. (a) RSOM image of different concentrations of *K. amoena* embedded in agarose gel at frequencies of 11–99 MHz. Inset: Photograph of different dilutions of *K. amoena* in agarose gel drops, where 1 – Agarose gel; 2 – Stock suspension; Diluted suspensions: 3 - 1:2; 4 – 1:4; 5 – 1:8; 6 – 1:16; 7 – 1:32; 8 – 1:64; 9 – 1:128. (b) RSOM image of *K. amoena* at low frequencies (LF). (c) RSOM image of *K. amoena* at high frequencies (HF). Scale bar (a,b,c): x-axis – 1 mm, y-axis – 1 mm, z-axis – 0.2 mm. (d) Volume of 3D objects vs. the concentration of diatoms mixed with agarose gel. AF – all frequencies. (e) Volume of 3D objects vs. the concentration of diatoms. (f) Mean pixel intensity vs. the concentration of diatoms mixed with agarose gel.

The interrelation between the volume of diatoms in gel and the volume of 3D objects emitting a photoacoustic signal remains an important issue for discussion in view of the development of fidelity techniques for the quantitative analysis of diatom

colonies. The volume of diatoms in an agarose gel drop, V_d, is calculated from the volume of one diatom cell, the concentration of diatom cells cd, and the volume of agarose gel drop V_{gel} by using equation:

$$V_d = \left(\frac{4}{3}\right)\pi abc \cdot c_d \cdot V_{gel} \quad (2)$$

The diatom cell is approximated as an ellipsoid, where a, b, c are the length, width, and height, respectively. The volume of agarose gel drop V_{gel} is 10 µl. As one can see from the data in Table 3, there is a wide span of the "volume of 3D objects to the volume of diatoms" ratio for different dilutions of the diatoms in gel.

Table 3 Comparison of the volume of 3D objects obtained by using the ImageJ program with the calculated volume of diatom cells in an agarose gel drop

Dilutions	Volume of 3D objects (ImageJ) / Volume of diatoms in gel (Calculated)
Stock suspension	31
1:2	38
1:4	25
1:8	13
1:16	89
1:32	109
1:64	24
1:128	13

First of all, the volume of 3D objects is one to two orders of magnitude larger than that of the diatoms. Second, this ratio seems independent of dilution, which hints that the volume of 3D objects is not related to the volume of separate diatom cells but to the volume of cell assemblies containing a number of cells. The resolution of the PA microscope is not high enough to resolve separate diatoms, and the volume of the gel surrounding separate cells is detected as the volume apparently emitting a photoacoustic signal. Another important issue is the nature of the structural element that emits the

signal. The chloroplast grains are the obvious candidates; therefore, the distribution and absorption efficiency of the chloroplast grains inside the frustules may contribute to the intensity of the photoacoustic signal.

On the other hand, the frequencies of acoustic signals emitted by diatoms may correspond to the eigenfrequencies of the natural oscillations of vibrating silica frustules, which can be described as capsular mechanical objects (membrane-shaped shells) having sub- and micrometer sizes[148,176]. Low frequency modes require less energy for excitation; therefore, even diatoms located deeper in the gel or those partly shadowed receive sufficient energy to excite these low frequencies, ultimately giving rise to 3D objects emitting an acoustic signal. High-frequency vibrations require a higher excitation energy and emit a more intense signal, which varies proportionally to the square of the frequency.

The extinction value for K. amoena at 532 nm (Figure 43a) is consistent with the photoacoustic signal observed (Figure 43b), indicating an agreement between them. This agreement suggests that chlorophyll a and c, along with fucoxanthin present in diatoms, can be considered as the main light absorbers responsible for the photoacoustic effect. A more exact contribution of each chromophore to the detected acoustic signal remains an open question, because it should be examined taking into account molar absorption coefficient of every chromophore at the wavelength of the laser and the volume fraction and spatial distribution of the chromophores in the frustule.

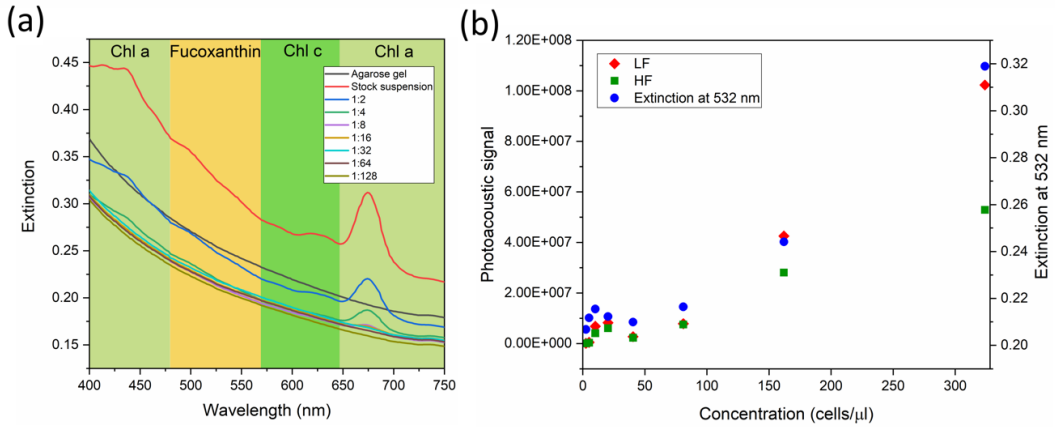

Figure 43. (a) Extinction spectra of different concentrations of *K. amoena* embedded in agarose gel. Chl a – chlorophyll a, Chl c – chlorophyll c. (b) Dependence of photoacoustic signal and extinction at 532 nm on concentration of diatoms mixed with agarose gel.

The application of photoacoustics to bacteria, algae, and other nonhuman natural objects is a relatively undeveloped area that leaves lacunae of knowledge and unexplored opportunities in biotechnology. Separate small diatom cells are not resolved because of the instrumental limitations, whereas diatom clusters and colonies are clearly visualized, which is of utmost importance for aquaculture monitoring. This successful demonstration of the working principle of photoacoustics for the visualization of diatom colonies promises further developments toward the photoacoustic imaging of individual cells. The fundamental cell studies related to the careful continuous characterization of algal colonies could be substantially improved, facilitated, automated, and simplified if supported by large 3D probes.

Given the significant role of diatoms in Earth's biosphere, it is surmised that these findings may open avenues for various applications, primarily associated with the expeditious assessment of sea, fresh, and waste water. In these contexts, the diatom

concentration is indicative of both ecological well-being and biomass productivity. Recent advances in diatom biofuel[186], aquaculture[187], and the management of plastic waste in the world ocean[188] suggest that the use of rapid and remote monitoring systems based on the photoacoustic effect may find interesting applications.

4.4.2 Monitoring of diatom concentration changes using a developed optical setup

A device consisting of LED illumination with a central wavelength of 505 nm that allows monitoring changes in diatom concentrations was described in the Experimental section 3.2.6. Marine centric and freshwater pennate diatoms with different morphologies, sizes and volumes were measured to prove the ability of the developed setup to track changes in their concentrations. Sample probes were taken for measurements during the stationary phase of growth. All studied cultures are shown and described in Table 4 and Figure 44. Table 4 indicates that among the 7 strains, B. titiana exhibits the largest diameter and volume, while A. formosa is the smallest. Overall, the size of the studied pennate diatoms is relatively small in comparison to centric species.

Table 4. The size and morphology of the studied diatom cultures

No.	Diatom culture (strain number)	Type	Shape	Diameter, µm	Length (height), µm	Volume, μm^3
1	*Biddulphiopsis titiana* (0.0212-OH)	marine centric	rectangular with round corners	132	255	$3.5 \cdot 10^6$
2	*Coscinodiscus oculus-iridis* (0.1211-OD)	marine centric	disc-shaped	31	10	$7.5 \cdot 10^3$
3	*Coscinodiscus* sp. (21.0407-OA)	marine centric	cylindrical	27	36	$2.1 \cdot 10^4$
4	*Amphipleura sp.* (Ov 466)	freshwater pennate	elliptical	7	57	$2.2 \cdot 10^3$
5	*Hannaea baicalensis* (BK 479)	freshwater pennate	banana-shaped	7	65	$2.5 \cdot 10^3$
6	*Asterionella formosa* (BZ 33)	freshwater pennate	single: elongated, star-shaped colonies	5	85	$1.7 \cdot 10^3$
7	*Ulnaria acus* (15k 595)	freshwater pennate	needle-shaped	5	175	$3.4 \cdot 10^3$

Brightfield images of centric (Figure 44a-d) and pennate diatom cells (Figure 44i-l) show how the chloroplast color changes from yellow to golden brown depending on the strain. Fluorescence images demonstrate distribution of chlorophyll throughout the cells (Figure 44e-h, m-p). In the case of *Biddulphiopsis titiana* (0.0212-OH), whose size is around 250 µm, chloroplasts partly fill the volume from both sides (Figure 44e). On the other hand, chloroplasts in *Coscinodiscus* species (0.1211-OD, 21.0407-OA) are more densely packed and have oval shape (Figure 44f-h). Figures 44c, g show a side view of C*oscinodiscus oculus-iridis* in the process of division. Chloroplasts in the case of freshwater cultures *Amphipleura* sp. (Ov 466) and *Ulnaria acus* (15k 595)

occupy most of the cells (Figure 44m, p), while in *Hannaea baicalensis* (BK 479) and *Asterionella formosa* (BZ 33) they are distributed in the form of grains (Figure 44n, o).

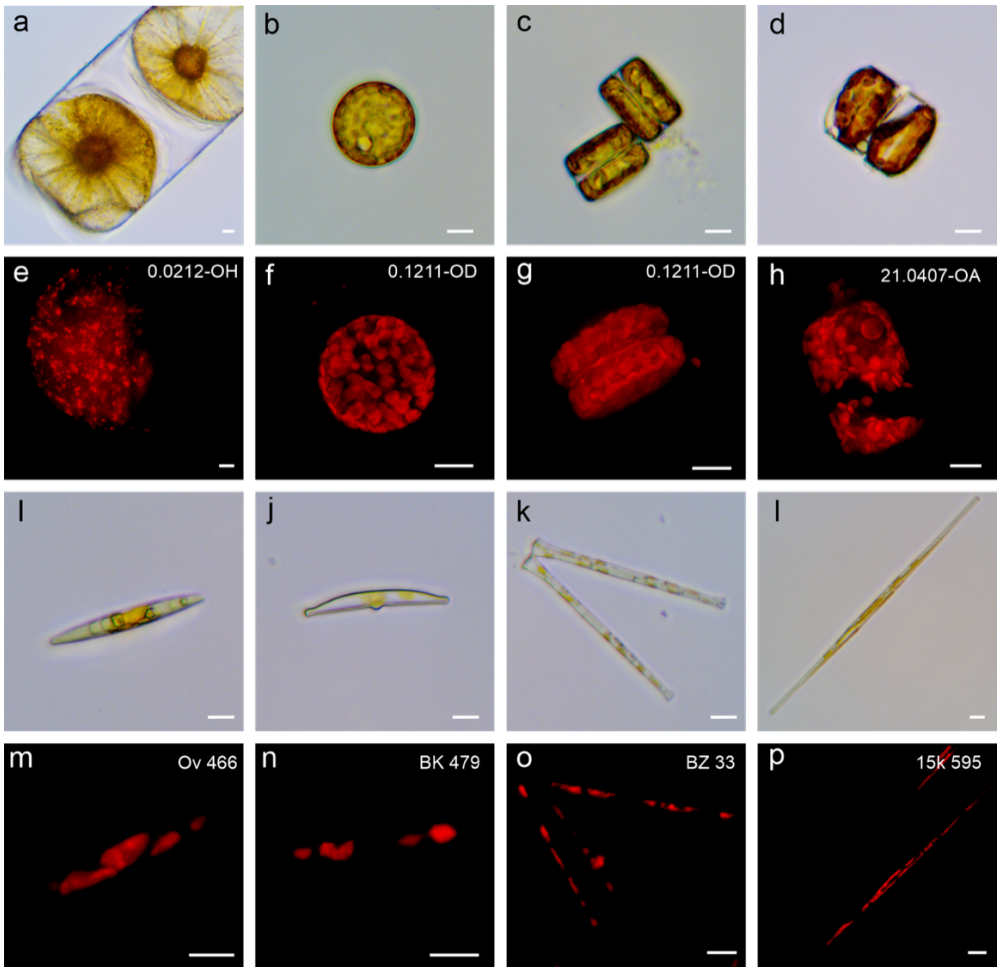

Figure 44. Brightfield microscopy images of marine centric diatoms: (a) *Biddulphiopsis titiana* (0.0212-OH), *Coscinodiscus oculus-iridis* (0.1211-OD): (b) top view, (c) side view, (d) *Coscinodiscus* sp. (21.0407-OA). Fluorescence images of marine centric diatoms: (e) 0.0212-OH, 0.1211-OD: (f) top view, (g) side view, (h) 21.0407-OA. Brightfield microscopy images of freshwater pennate diatom strains: (i) *Amphipleura* sp. (Ov 466), (j) *Hannaea baicalensis* (BK 479), (k) *Asterionella formosa* (BZ 33), (l) *Ulnaria acus* (15k 595). Fluorescence images of freshwater pennate diatoms: (m) Ov 466, (n) BK 479, (o) BZ 33, (p) 15k 595.

The results of measurements obtained using experimental setup described in sub-section 3.2.6 are demonstrated in Figure 45. For each diatom strain the measured light intensity values were normalized to the nutrient medium light intensity values, and the concentration values were multiplied by the number of cells in mL, calculated on the microscope for each diatom strain. Standard deviation, that was calculated from 12000 measurements for each sample, cannot be seen on graph because error bars do not exceed the size of a dot. The observed dependence of the measured light intensity on the relative concentration of diatoms was approximated by the linear fit for each diatoms strain.

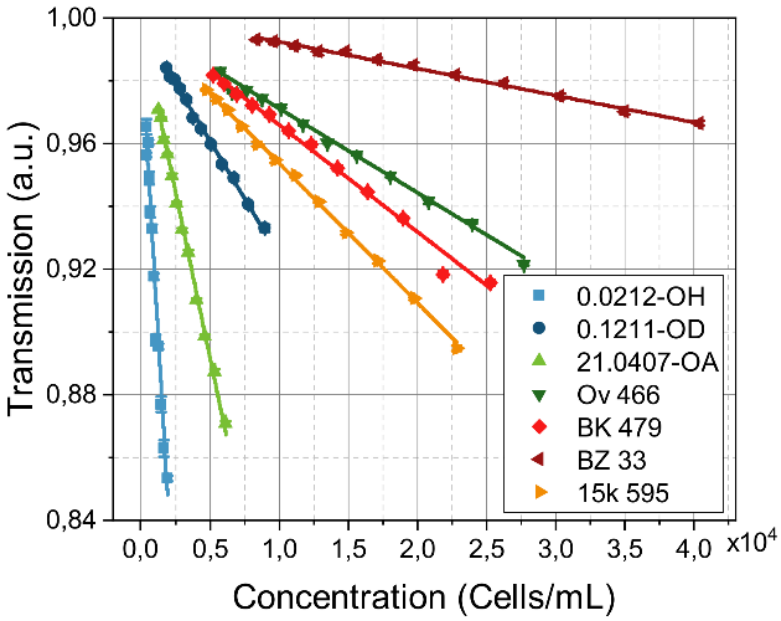

Figure 45. Optical measurements of diatom cultures. Light intensity as a function of the relative concentration of diatom cells. Light intensity was normalized on the measurements of nutrient medium. Scatter plot represents measured values, solid lines represent linear fit.

It can be seen that all values have high correlation with the linear fit, and are in a good agreement with Bouguer-Lambert-Beer law, which states that sample's optical density has linear dependence on light absorber's concentration: $A = \varepsilon lC$, where A - absorbance, ε - molar extinction coefficient, l - optical path, C - concentration.

To demonstrate the advantages of our system over conventional spectrophotometric approach and investigate opportunities for future development of the device, the extinction and fluorescence intensity measurements were made. Figure 46a demonstrates extinction spectra for initial concentrations of 7 diatom strains. The dependence of diatoms extinction on the concentration is demonstrated in Figure 46b. For all strains measured values were approximated by the linear fit.

Figure 46c demonstrates fluorescence intensity spectra for initial concentrations of 7 diatom strains (excitation wavelength: 430 nm). It can be seen that all strains exhibit fluorescence except for nutrient medium and BK 479 strain. This observation correlates with the absence of extinction peak of chlorophyll *c* in BK 479, that should be located near 680 nm. Brightfield microscopic images and the growth curve allow to assume, that this strain was in the transition between stationary growth phase and the last (death) phase during measurements. The composition and quantity of pigments is not constant and depends on the intensity of light, its quality, the content of nutritional elements in water, as well as on the growth phase and the characteristics of diatom vital activity[63,189]. The amount of chlorophyll rather decreases at the end of the stationary phase of growth without renewal of the medium. Thus, fluorescence and extinction measurements of diatoms at the wavelength of 680 nm might be a potential marker of the diatom growth phase.

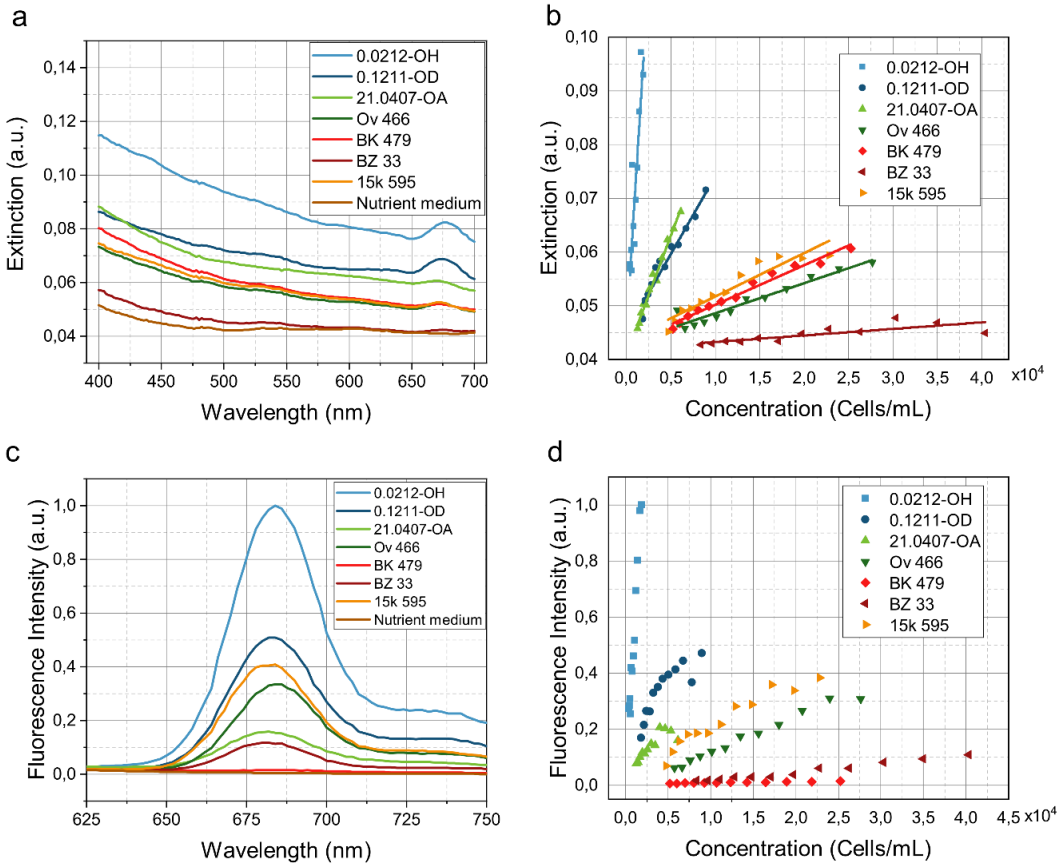

Figure 46. Spectrophotometric and fluorescence measurements of diatoms. (a) Extinction spectra. (b) Dependence of extinction (λ = 505 nm) on the diatom concentration. Scatter plot represents extinction values normalized on the nutrient medium extinction. Solid lines represent linear fit. (c) Fluorescence intensity spectra. Excitation wavelength: 430 nm. (d) Dependence of fluorescence intensity on the diatom concentration. Scatter plot represents fluorescence intensity values normalized on the nutrient medium values.

Also, Figure 46d shows the dependence of fluorescence intensity on the concentration for 7 diatom strains (excitation wavelength: 430 nm, emission wavelength: 680 nm). One can observe, that marine centric diatom cultures (strain No. 0.0212-OH, 0.1211-OD and 21.0407-OA) exhibit stronger fluorescence dependence on

concentration than pennate diatom cultures (strain No. 15k 595, Ov 466, BK 479, BZ 33).

The coefficients of determination (COD) for all linear fits are shown in Table 5. It can be seen, that for all strains spectrophotometric measurements demonstrate lower COD values, than optical measurements on the custom setup, which indicates higher accuracy of the last. This can be explained by the difference in the sensing volume. According to the manufacturer, the spot size of the light beam is 0.7 mm in diameter. The optical path for 200 µL sample is 6.25 mm, thus the sensing volume is V = 2.405 mm^3. In contrast to that, our setup has a spot size of light beam scaled to 1.5 mm in diameter, and the optical path is 10 mm. Therefore, the sensing volume in our setup is V = 17.67 mm^3, which is 7 times greater than in spectrophotometer. This allows our setup to average values more accurately even for small diatom cell concentrations.

Table 5. Comparison of the coefficient of determination (COD) for spectrophotometric measurements with optical measurements on the custom device.

Diatom strain	Spectrophotometer, COD	Custom device, COD
0.0212-OH	0.840	0.981
0.1211-OD	0.954	0.997
21.0407-OA	0.983	0.998
Ov 466	0.929	0.996
BK 479	0.975	0.993
BZ 33	0.638	0.995
15k 595	0.901	0.999

It can be noted from Figures 45, 46, that slopes of linear fits differ between diatom strains. To be more precise, slope of linear fit is connected to shape and volume of a strain, and this dependence is demonstrated in Figure 47. One can clearly see the monotonic dependence of the slope on the volume of diatom cells, that was extracted

from the Table 4. The relation between slopes of linear fits and diatom volume is similar in both extinction and transmission measurements and mostly determined by the extinction coefficient, that combines absorption and scattering properties of diatoms. This knowledge could be used for more accurate tuning of the photodetector sensitivity for monitoring of each diatom strain and for characterization of diatom biomass.

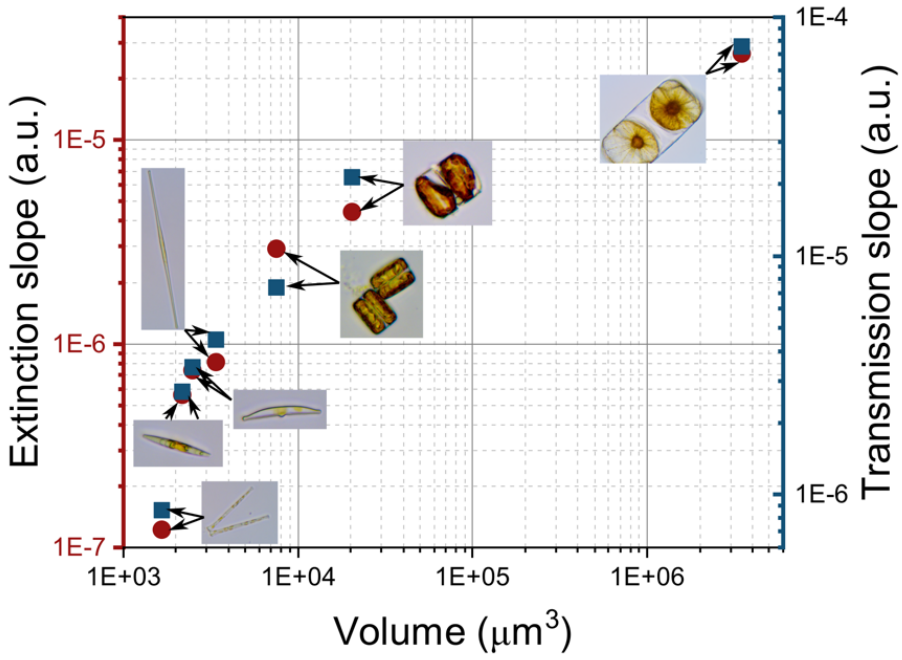

Figure 47. The dependence of linear fit slopes on the volume of diatom cells. The red circles represent slopes of linear fit in extinction measurements. The blue squares represent absolute values of slopes of linear fit in transmission measurements on the custom-made setup.

4.5 Summary

In summary, freshwater pennate and marine centric diatom cultures were cultivated in the specially designed bioreactor and windowsill under specific conditions optimized for their growth. The growth of diatom colonies was monitored using

fluorescence and photoacoustic visualization using IVIS SpectrumCT In Vivo Imaging System and RSOM Explorer P50, which allowed for rapid evaluation of diatom growth without the need for extensive sample preparation. The fluorescence and photoacoustic signals acquired from various species of freshwater pennate diatom (*A. sibiricum*) and marine centric diatoms (*Coscinodiscus* sp., *B. titiana*) exhibit a correlation with their respective growth phases. Notably, the highest signal intensity from *A. sibiricum* was observed following 45 days of cultivation in the bioreactor, while the signals from the marine centric diatoms peaked at 30 days of cultivation. The utilization of fluorescence and photoacoustic signals offers a valuable and efficient alternative for assessing diatom growth owing to the rapid, non-invasive evaluation of growth without extensive sample preparation. By eliminating complex procedures and reducing the risk of contamination in the diatom culture, these proposed methods offer reliable monitoring of diatom growth dynamics. Consequently, these approaches hold great potential for large-scale diatom cultivation aimed at carbon dioxide extraction purposes.

The study revealed that the photoacoustic signal from K. amoena diatoms mixed with agarose gel decreases by approximately 20 times when the diatom concentration reaches a level of 3 cells/l. This observed correlation between the extinction value of K. amoena at 532 nm and the corresponding photoacoustic signal emphasize the concentration-dependent behavior of the photoacoustic signal in relation to diatom abundance and highlight the significant contribution of chlorophylls and carotenoids in facilitating the overall signal generation process within diatom samples. Furthermore, the successful utilization of the photoacoustic principle for visualizing diatom colonies holds potential for the rapid assessment of water bodies, where diatom concentration serves as a vital indicator of ecological well-being and biomass productivity.

Moreover, capabilities of transmission measurements using fabricated optical setup at the wavelength of 505 nm for seven diatom strains were demonstrated and compared to the spectrophotometric approach. As a result, the linear dependence of measured transmission on the diatom concentration was observed with high accuracy for all strains having different shapes and sizes. The LED-based setup, being portable and cost-effective, provides a practical alternative for diatom concentration measurements in field settings and resource-limited environments. The outlined approach holds promise for ongoing diatom monitoring in bioreactors. Further refinement could involve incorporating transmission measurements at 680 nm and fluorescence measurements with matching emission wavelengths. Additionally, fine-tuning the sensitivity of the photodetector based on the derived linear fit dependencies on diatom volume could enhance the methodology.

Chapter 5. Visualization of living and cleaned individual diatoms

This chapter details the investigation of individual diatoms through the application of various methodologies employed to visualize both intact living cells and purified frustules devoid of organic constituents. SEM and FLIM images were obtained and described by the author, while CLSM images were acquired together with Dr Yekaterina Bedoshvili. All samples were prepared by the author.

5.1 Background

Diatoms are classified based on their morphology and nanopatterned structures of their silica cell walls, allowing for accurate identification and classification. The study of diatom morphology and structure enables the characterization and classification of different diatom species, helping to understand their ecological roles and interactions. The changes in the diatom community structure and morphology are considered early warning signals of environmental impacts, such as pollution, eutrophication, and climate change. The study of diatom morphology and structure can, therefore, facilitate the detection of environmental changes and help develop management strategies for maintaining sustainable ecosystems. Understanding the diatom morphology and structure can also enable the design of custom-shaped silica structures with specific chemical and physical properties for targeted applications. The conservation and application of diatoms rely on the in-depth knowledge of their morphology and structure, making this an important research area with a broad spectrum of scientific and technological implications.

The combination of scanning electron microscopy, confocal laser scanning microscopy, and fluorescence lifetime imaging microscopy offers complementary

benefits for observing and understanding diatoms. Here's a rationale for using each of these methods enables better and faster understanding and classification of diatoms:

- SEM provides high-resolution imaging, allowing for detailed observation of the morphology and structural features of diatoms. It provides information about their shape, size, and fine structures but only at the surface level[27].

- CLSM can exploit the intrinsic autofluorescence properties of diatoms or facilitate the use of fluorescent dyes/probes to visualize specific cellular components[190]. This technique provides information about the distribution, localization, and dynamics of various biomolecules within diatoms. It also allows for optical sectioning, which enables the acquisition of focused images at different depths within the diatom structure. This ability to obtain 3D images helps in understanding the spatial arrangement of different cellular components and structures within diatoms[24].

- FLIM is a powerful tool for studying biological structures by measuring the fluorescence decay rate of molecules[155,191–193]. This technique has recently found use in many applications, because it can provide both information on the location of specific fluorophores and on their local environment[191,193,194]. As an intrinsic property of a fluorophore, the fluorescence lifetime depends on temperature, pH, concentration, polarity, the presence of fluorescence quenchers, and internal factors that are connected with fluorophore structure[194,195]. Therefore, it is important to understand the state of the fluorophore in diatoms.

5.2 Morphology of frustules of different species

The morphology of diatom frustules after purification from organic material by acid-treatment was studied using SEM (Figure 48).

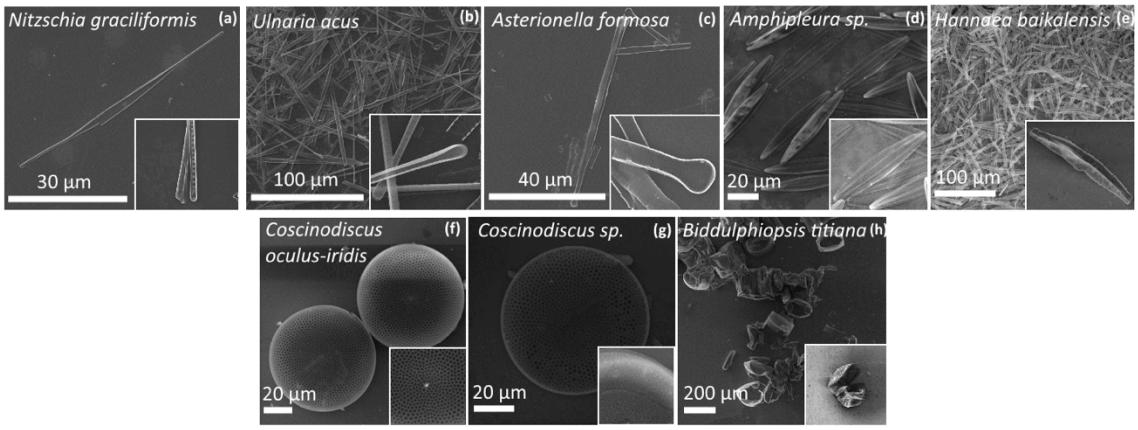

Figure 48. SEM images of different pennate: (a) *Nitzschia graciliformis*, (b) *Ulnaria acus*, (c) *Asterionella formosa*, (d) *Amphipleura* sp., (e) *Hannaea baikalensis* and centric diatom frustules: (f) *Coscinodiscus oculus-iridis*, (g) *Coscinodiscus* sp., (h) *Biddulphiopsis titiana*. Insets: enlarged view of individual frustules.

When writing the names of diatom species, it is customary to follow the binomial nomenclature format, which includes the genus name, species name, and the name of the author(s) who first described the species.

a) *Nitzschia graciliformis* Lange-Bertalot & Simonsen

The cells are solitary needle-shaped, with two chloroplasts, one at each end of the cell. Valves are straight lanceolate, sharply narrowed to very thin ends. The keel runs along the edge of the cell; it contains a canal-suture with central pores. Fibulae, supports on which the tube of the canal-like suture is held, are located along the entire length of the leaf. The two median brooches are widely spaced and form a central knot.

Terminal nodules are visible at the ends of the valves. Rows of areolas are distinguishable only in an electron microscope. The species is widely distributed in the pelagic zone of the lake Baikal, as well as in the river Selenga and in the Selenga shallow water.

b) *Ulnaria acus* (Kützing) Aboal

Cells are solitary, needle-shaped, two large chloroplasts are elongated along the valves. The valves are narrow towards the ends gradually narrowing; the axial field in the center of the valve is narrowly linear. Two-lipped outgrowths are located at each end of the valve. At each end is a pore field - the ocellulimbus. It is one of the mass dominant species of phytoplankton in the pelagial of Lake Baikal.

c) *Asterionella formosa* Hassall

Cells are rod-shaped, connected in stellate colonies. Chloroplasts are small. The frustule is narrowly linear with widened ends, of which the basal end is wider than the head. Axial field narrowly linear, transverse rows of areoles consist of single areoles. At the ends of the valve there are two-lipped outgrowths, the slit of which opens on the outer surface with a hole much larger than the pores. Small irregular spines are located on the border of the front part of the valve and the bend. At the apical ends of both valves, there are fields of small pores arranged in short rows in the direction of the central axis of the valve. The species is widespread in the lake Baikal from spring to autumn.

d) *Amphipleura* sp. Kutzing

Valves linear-lanceolate and very narrow, gradually tapering to rounded ends. The suture branches are greatly shortened and only slightly increase in length as the valve length increases. On the branches of the seam, the seam is surrounded by two

longitudinal ribs. The rows of areolas are very small and visible only under optimal lenses and illumination in a light microscope. The outer distal and proximal ends of the suture are straight. The strain was isolated from the river Yenisei.

e) *Hannaea baicalensis* Genkal, Popovskaya & Kulikovskiy

Cells are rod-shaped, slightly crescent-shaped, solitary. The single chloroplast is pressed against the girdle rims. The valves are crescent-curved with capitate ends, the suture is absent. Rows of areoles are parallel, interrupted in the middle on the ventral side of the valve, where a unilaterally convex field is located. The axial field is narrow-linear. There are two-lipped outgrowths at the ends of the valve. The species is widespread in the littoral zone of the lake Baikal.

f) *Coscinodiscus oculus-iridis* (Ehrenberg) Ehrenberg

Coscinodiscus oculus-iridis is chosen for the study of mechanical and optical properties. In order to comprehensively assess the mechanical properties of Coscinodiscus oculus-iridis and understand their interplay with its structure, the morphology and topography of this diatom will be detailed in Chapter 6, dedicated to the study of mechanical properties. This contextual information is crucial for a thorough examination of its mechanical behavior.

g) *Coscinodiscus* sp.

A species with a taxonomic position that has not yet been clarified by us. Cells are solitary, while frustule is cylindrical. The valves are flat. Chloroplasts are multiple, granular, in a healthy cell evenly distributed throughout the volume of the cytoplasm. At the time of measurements, the cell diameter of the strain *Coscinodiscus* sp. (Black Sea) 21.0407-OA varied from 28 to 35 μm.

The genus *Coscinodiscus* includes 221 species[20]. Representatives of the genus, apparently, are exclusively marine, with the exception of species with an unclear taxonomic position. This large genus requires taxonomic revision as there is a lot of variation at the ultrastructural level. Several species formerly in this genus have been moved to the genus *Thalassiosira*, others to *Actinocyclus* - many of the changes concern species living in tropical lakes.

h) *Biddulphiopsis titiana* (Grunow) Stosch & Simonsen

Cells are rectangular with rounded corners, forming short chains that can attach to a substrate (usually other algae). The contour of the valve is oval to semicircular with deep vertical mantles. When viewed from the girdle, the surfaces of the valves look slightly convex. Areoles occluded by mouths (variant of velum) scattered over elongated central area, arranged radially in single row outside it. On the apexes there are areas with smaller pores, forming rather indistinct false eyes (pseudocellus). The edge of the mantle is slightly extended inward, forming a pseudo-septum. Next to the pseudocellus there is a row of rimoportulae, sometimes forming an irregular ring around them. The waistband consists of four closed rings. The marginal edges of the rims have short thin protrusions with a few inclusions of pores, inside which there is a smooth platform. The areoles run in rows down the rims and have single or multiple elongated mouths. Small, lamellar, multiple plastids occur in the peripheral cytoplasm and in strands extending from a prominent central nucleus. This widespread marine genus consists of two species, *B. titiana* and *B. membranacea*.

The cell ultrastructure examined using a transmission electron microscope is described in Appendix B.

5.3 Distribution of chloroplasts in selected diatom species

Laser scanning microscopy (LSM) was used to observe the DNA material of diatom cells and newly formed valves during division. Confocal images of pennate species (*U. acus*, *N. graciliformis*, *Amphipleura* sp., *A. formosa*) after staining are shown in Figure 49. Newly formed valves are visible on all images (Figure 49a-j). In the case of *Amphipleura* sp. chloroplasts are clearly visible and occupy the central part of the cell (Figure 49e-h). The chloroplast structure is visualized using TEM (Appendix A) and thoroughly reviewed in the study by Bedoshvili et al.[196]

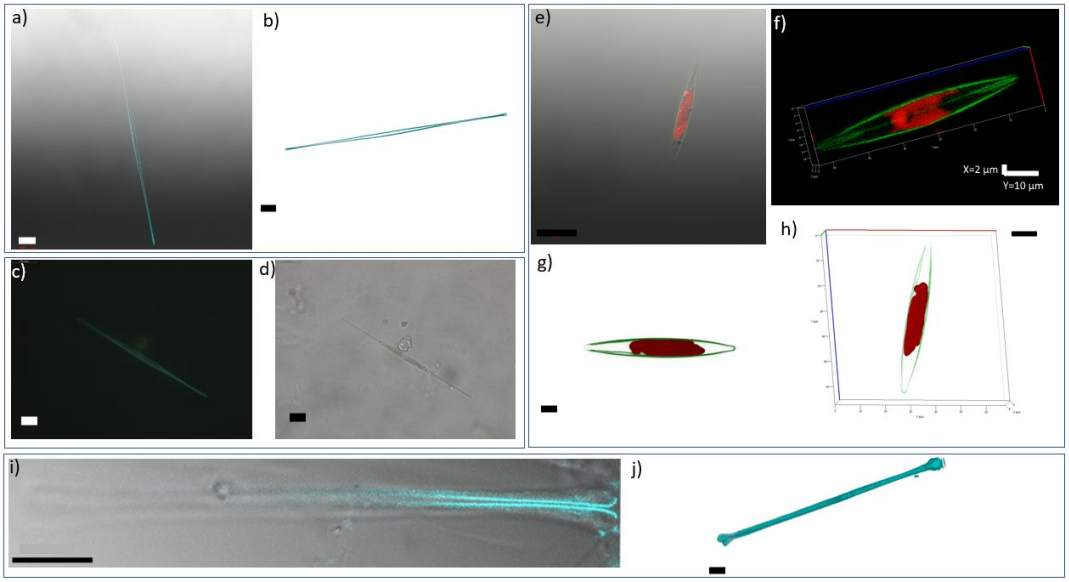

Figure 49. Visualization of pennate diatoms using laser scanning microscopy. a) Confocal image of *U. acus* (15k 595) after PDMPO staining, b) 3D confocal image of U. acus, c) Fluorescent image of *N. graciliformis*, d) Bright field image of *N. graciliformis*, e) Confocal image of *Amphipleura* sp. (Ov 466) after PDMPO staining, f) 3D confocal image of a dividing cell of *Amphipleura* sp., g)-h) 3D images of *Amphipleura* sp., i) Confocal image of *A. formosa* (BZ 33) after PDMPO staining, j) 3D -confocal image of *A. Formosa*. Scale bar: a, b, c, d, i, h - 10 µm; e, g, j – 5 µm.

Confocal images of a marine culture of *C. oculus-iridis* after staining are shown in Figure 50. According to Figure 50a, b, g, the nuclei located in the center of the cells are round. Oval-shaped chloroplasts are rather densely distributed inside the cells (Figure 50a, c, d, f, g). The formation of new valves (represented in green) is shown in Figure 50a-g. The state of chloroplasts and cell division indicate the viability of the culture.

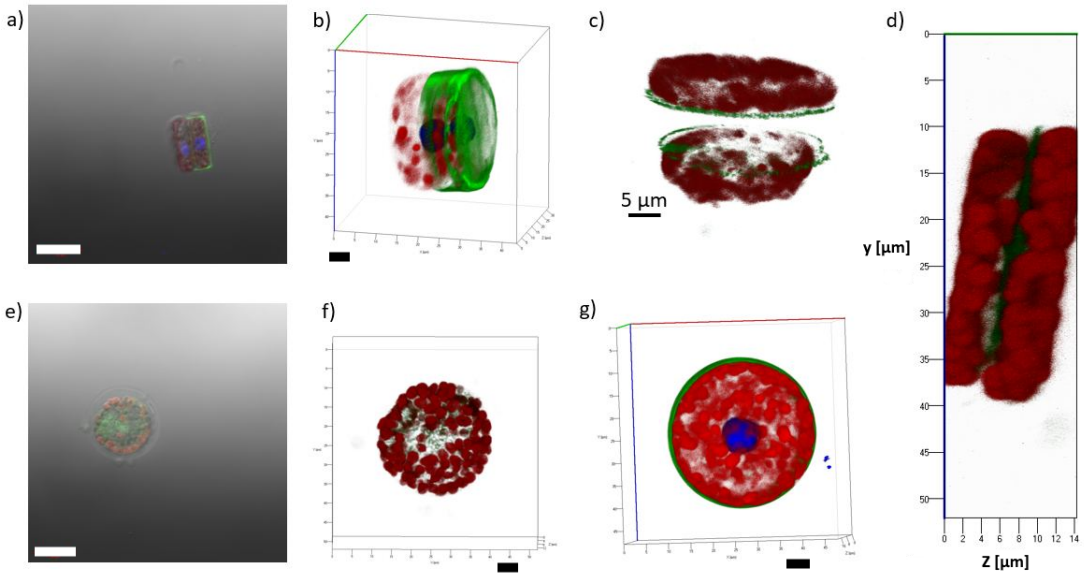

Figure 50. Visualization of *C. oculus-iridis* (strain 0.1211-OD) using laser scanning microscopy. a) Confocal image of a fixed *C. oculus-iridis* cell stained with LysoTracker Yellow and DAPI (lateral view), b) 3D image of a dividing cell with nuclei (lateral view), c) 3D image of a divided cell without a nucleus, d) 3D image image of a dividing cell, e) Confocal image of a fixed *C. oculus-iridis* cell (top view), f) 3D image of a cell without a nucleus (top view), g) 3D image of a cell with a nucleus (top view). Red: chlorophyll autofluorescence, green: newly formed valves, blue: nucleus. Scale bar: a, e – 20 µm; b, c, f, g – 5 µm.

5.4 FLIM visualization

When chloroplasts absorb photons of light, the energy is typically utilized in various photochemical reactions associated with photosynthesis[197]. These photochemical reactions involve the conversion of light energy into chemical energy, enabling the synthesis of carbohydrates and other organic compounds. The absorbed energy can take different paths within the chloroplasts[197]. A significant portion of the absorbed energy is utilized for photochemical processes, such as the excitation of reaction centers and electron transport in the photosynthetic apparatus. These reactions occur rapidly, within picoseconds or nanoseconds, resulting in the conversion of the absorbed energy into chemical energy. In the context of fluorescence, the absorbed energy that is not utilized in photochemical reactions can be re-emitted as fluorescence emission. The time it takes for this fluorescence emission to occur, known as fluorescence lifetime, is influenced by the efficiency of energy transfer processes within the chloroplasts.[197]

According to the study by Falkowski et al.[197], the observed lifetimes of isolated chlorophyll *a* molecules vary between approximately 3.0 to 5.1 nanoseconds, with the specific range dependent on the polarity of the solvent. Correspondingly, these measured lifetimes correspond to quantum yields that range from 20% to 32%. In living cells, fluorescence lifetimes are even shorter, approximately ranging from 0.3 to 1.5 nanoseconds. This reduction in fluorescence lifetime in living cells arises due to a significant portion of the absorbed energy being utilized in photochemical reactions, reflecting the physiological state of the cells[198]. Therefore, the absorption of energy by chloroplasts in living cells influences their fluorescence lifetimes by directing a substantial amount of the absorbed energy towards photochemical reactions, rather than

fluorescence emission. The more energy that is utilized in photochemical processes, the shorter the fluorescence lifetime becomes. It is well known that diatoms use the mechanism of nonphotochemical quenching of chlorophyll *a* fluorescence to dissipate excess energy and prevent overexcitation of the photosynthetic apparatus[199].

The bright-field transmission and FLIM images of different pennate diatom species (*K. amoena*, *Haslea karadagensis*, *A. sibiricum*, *E. silesiacum*) are shown in Figure 51.

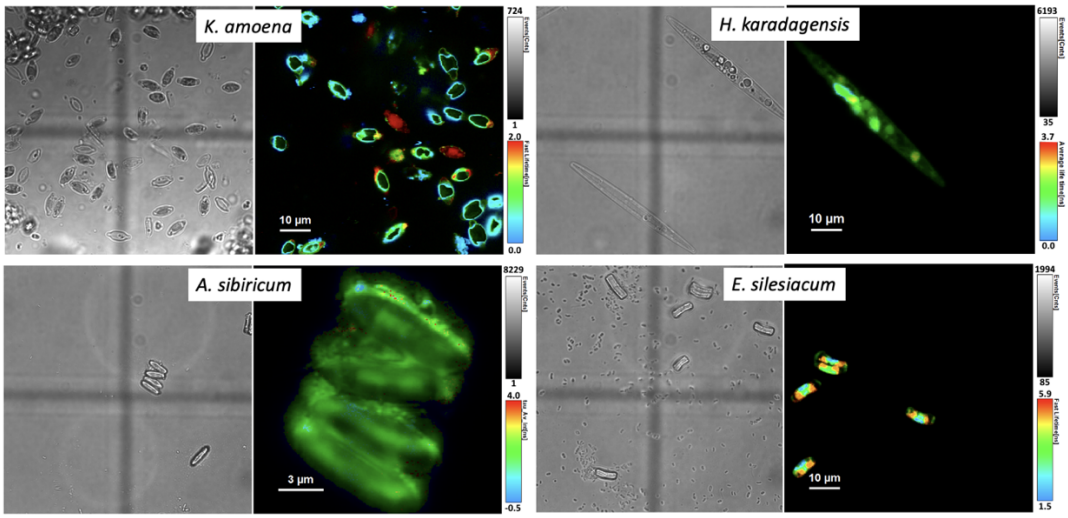

Figure 51. Transmission bright field (left) and FLIM images (right) of different pennate diatoms. Excitation wavelength: 638 nm (*K. amoena*), 402 nm (*H. karadagensis*, *A. sibiricum*, *E. silesiacum*)

FLIM results demonstrate that diatoms generally have a very short yet changeable average lifetime—from 0.5 ns up to 2 ns. The fluorescence signal in diatoms primarily arises from chlorophyll *a*, as evidenced by the utilization of a detection system incorporating a 402-nm and 638-nm excitation laser and a 690-nm bandpass filter, which specifically targets chlorophyll *a* emissions. The fluorescence lifetime detection system

captures a range of lifetimes associated with chlorophyll *a* in diatoms. This is likely attributed to the intricate physiology and cellular state of diatoms. Factors such as cell cycle phase, metabolic activity, and environmental conditions can influence energy transfer dynamics and dissipative processes within the chloroplast, thereby causing variations in fluorescence lifetimes. Additionally, the observed discrepancies in fluorescence lifetimes can potentially be attributed to variations in pigment concentration within diatoms. Some diatom species exhibit non-uniform pigment distribution within their frustules, resulting in partial filling of the diatom frustule volume with pigments. The fill factor of the frustule, specifically the degree to which the pigments or chloroplasts fill the volume within diatoms, can potentially have implications for the fluorescence lifetime of diatom chloroplasts as it influences the intracellular distribution and concentration of pigments, which are determinants of the fluorescence properties exhibited by diatoms[200,201]. In diatoms where pigments only partly fill the frustule volume, the distribution and availability of pigments within the chloroplasts may be altered. This can lead to variations in the fluorophore density, pigment-protein associations, and the extent of self-shielding within the chloroplasts[197,201,202]. Consequently, these changes can affect the rates of non-radiative energy dissipation, light harvesting efficiency, and overall photochemical performance, thereby influencing the fluorescence lifetime.

The specific mechanisms underlying the relationship between the fill factor or chloroplast density within the frustule and the fluorescence lifetime of diatom chloroplasts require further investigation. In-depth analysis of the influences of fill factor and chloroplast density on the fluorescence properties of diatom chloroplasts would enhance our understanding of the intricate interplay between structure, function, and

photosynthetic performance in these organisms. Additionally, studies comparing different diatom species with varying frustule fill factors and pigment concentrations would help elucidate species-specific adaptations and optimize the interpretation of fluorescence lifetime data.

The transmission bright field image of *E. sibiricum* reveals the presence of bacterial contamination, indicating a deviation from an ideal diatom culture condition. The presence of bacteria in an aged diatom culture medium can potentially impact the accuracy of fluorescence lifetime measurements of chlorophyll. This phenomenon arises due to the interactions between bacteria and diatoms, which may alter the physiological state of the diatoms and affect their chlorophyll fluorescence properties. Bacterial contamination can have various effects on diatoms, including changes in nutrient availability, alterations in light conditions, and potential interactions with the diatom's cellular processes. Bacterial contamination in the nutrient medium may compete with diatoms for essential nutrients, such as nitrogen and phosphorus[203]. This competition can potentially limit the availability of these nutrients for diatoms, leading to changes in their chlorophyll content and subsequent alterations in fluorescence lifetime. Bacteria also naturally produce and release various metabolites into their surroundings during growth and metabolic processes which might interact with the diatoms, potentially affecting their physiological processes[204]. Bacterial contamination can lead to physical interactions between bacteria and diatom cells[205]. These interactions may result in cell damage, changes in cell morphology, or disruptions to cellular processes. The direct impact of bacterial interactions on diatom cells can alter the functioning and organization of the photosynthetic apparatus, influencing chlorophyll fluorescence properties, including fluorescence lifetime. In this context, conducting a comparative analysis between the

fluorescence lifetime values of chlorophyll in the aged and contaminated diatom culture medium and a younger, uncontaminated culture medium becomes crucial. By comparing these two scenarios, one can assess the potential influence of bacterial contamination on the fluorescence lifetime measurements of chlorophyll.

The bright-field transmission and FLIM images of different centric diatom species (*C. oculus-iridis*, *Coscinodiscus* sp., *B. titiana*) are shown in Figure 52.

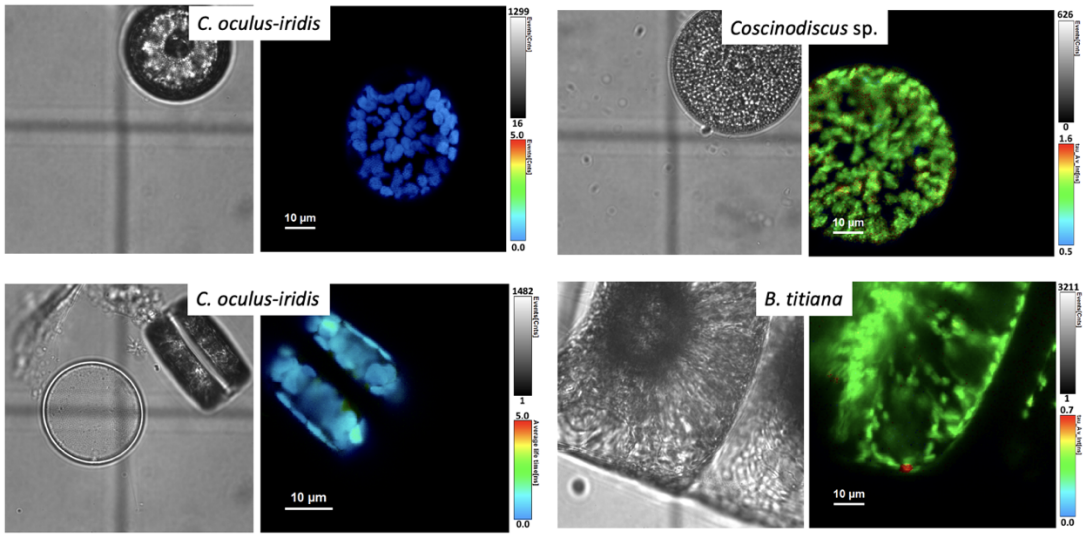

Figure 52. Transmission bright field (left) and FLIM images (right) of different centric diatoms. Excitation wavelength: 402 nm.

Transmission bright field images reveal the intricately ornamented silica frustule of marine centric diatoms, devoid of any observable fluorescence signal (Figure 52, left bottom). FLIM images of marine centric (Figure 52) and pennate diatoms (Figure 51) reveal a distinct difference in the compactness of chloroplast arrangement. Specifically, FLIM images demonstrate a tightly packed configuration of chloroplast grains within the centric diatoms, while the pennate ones exhibit a comparatively looser

arrangement. This distinction in chloroplast organization highlights the morphological variability between these two diatom groups. In the specific case of *C. oculus-iridis*, FLIM images provide a comprehensive view of chloroplast distribution both from a top-down perspective and from a lateral viewpoint. The distribution of chloroplasts in the frustules is also demonstrated using Operetta High Content Imaging System in Figure 44.

Analysis of fluorescence lifetimes reveals a relatively uniform distribution within individual centric diatom cells. However, the specific fluorescence lifetime values vary depending on the diatom species, spanning a range from 0.4 to 0.8 nanoseconds. These variations in fluorescence lifetimes reflect differences in the specific physiological properties and other parameters mentioned above as well as characteristics inherent to each diatom species under study[196].

5.5 Summary

In this chapter, different pennate and centric diatom species are described using SEM, CLSM, and FLIM in terms of their morphology and chloroplast distribution. Upon SEM observation, it is evident that there are distinct morphological differences between various pennate and centric diatom species. These disparities are primarily manifested in aspects such as valve shape, size, ornamentation, and the arrangement of striae or costae. Additionally, variations in the presence of processes, such as rimoportulae or raphe, further differentiate these species. This comprehensive morphological diversity underscores the taxonomic significance of SEM imaging for diatom classification and identification.

Living diatom cells were studied using different fluorescence-based techniques, such as confocal laser scanning microscopy and FLIM, owing to the presence of the

main fluorophore – chlorophyll. CLSM and FLIM images of marine centric diatoms and pennate diatoms show a noticeable difference in the compactness of chloroplast arrangement. Centric diatoms have tightly packed chloroplast grains, while pennate diatoms have a comparatively looser arrangement.

The FLIM results show that pennate diatoms generally have a short and variable average lifetime, ranging from 0.5 ns to 2 ns. The fluorescence lifetime detection system records a range of lifetimes linked to chlorophyll a in diatoms upon excitation with a 402 nm laser. Factors such as the phase of the cell cycle, metabolic activity, and environmental conditions can affect energy transfer dynamics and dissipative processes within the chloroplast, leading to variations in fluorescence lifetimes. Additionally, differences in pigment concentration within diatoms may contribute to observed discrepancies in fluorescence lifetimes. The presence of bacteria in aged diatom culture medium can also impact the accuracy of fluorescence lifetime measurements of chlorophyll. The range of fluorescence lifetimes of centric diatoms spans from 0.4 to 0.8 nanoseconds. Analysis of fluorescence lifetimes reveals a relatively uniform distribution within individual centric diatom strains, but the specific values vary depending on the diatom species.

Chapter 6. Mechanical properties of diatoms

In this chapter, the mechanical properties of *Coscinodiscus oculus-iridis* diatom silica frustules are characterized, along with air-dried and wet cells containing organic material, under both static and dynamic loading conditions. The results on mechanical properties of diatom algae presented here are published in **Cvjetinovic J**, Luchkin S, Statnik E, Davidovich N, Somov P, Salimon A, Korsunsky A, Gorin D. Revealing the static and dynamic nanomechanical properties of diatom frustules—Nature's glass lace. *Scientific Reports*. 2023; 13, 5518: 1-12[39]. Figures, prepared by the author, are reproduced with permission from Springer Nature. The AFM measurements were performed by Dr Sergei Luchkin, while *in situ* SEM nanoindentation was performed with the help of Pavel Somov and Eugene Statnik. Results were analyzed by the author. The subsequent section of this chapter presents the outcomes pertaining to the numerical and experimental study of vibrational modes exhibited by diatom frustules. These research findings have been recently accepted for publication in *Applied Physics Letters* (Cvjetinovic J. et al. Probing vibrational eigenmodes in diatom frustules via combined *in silico* computational study and atomic force microscopy experimentation, Applied Physics Letters).

6.1 Background

For the present study the centric diatom *Coscinodiscus oculus-iridis* was chosen as a representative sample with some of the most interesting variations in structural elements that can affect their mechanical and photonic properties. Cleaned frustules composed of two halves with distinct outer and inner surfaces were investigated, along with diatom cells, both wet and dried, containing organic components (Figure 53a).

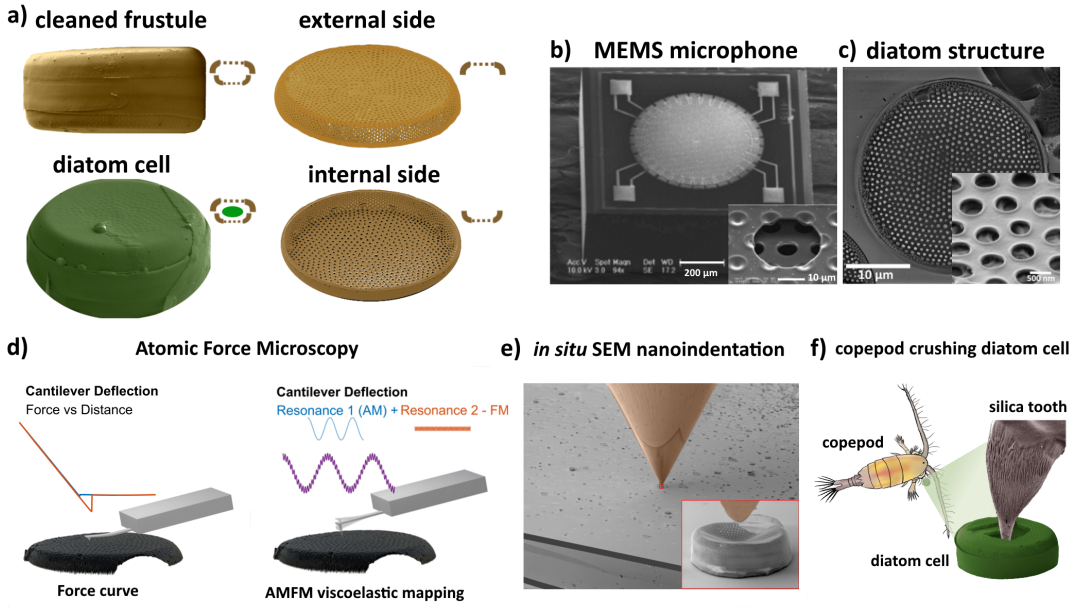

Figure 53. Study objects, biomimetic approach and research methodology. a) Samples used in this study: cleaned frustule (organic matter removed), external and internal sides of cleaned frustules, diatom cell containing organic components, b) SEM images of the MEMS microphone and the membrane perforation (inset). Adapted with a permission from[146]. c) SEM image of diatom frustule showing the porous structure (inset), d) Schematic diagrams of two modes of AFM measurement: force vs distance and amplitude modulation-frequency modulation (AMFM), e) In situ nanoindentation inside SEM column, f) Schematic illustration of a copepod crushing diatom cell with the help of a silica tooth as an example of indentation in nature.

The state of the sample interrogated is indicated by the small cartoons shown in the upper right corner to aid understanding. The striking similarity between diatom valves and the membranes used in modern MEMS microphones[146] (Figure 53b) is shown in Figure 53c. Two different AFM modes used in this study are schematically illustrated in Figure 53d, whilst *in situ* nanoindentation in the SEM column is shown in

Figure 53e. The details of these experimental approaches are explained in the Experimental section. The mechanical contact between a sharp indenter and diatom frustule is a frequent occurrence in nature in the course of interaction with marine zooplankton. This natural contact mirrors the interaction observed during *in situ* SEM nanoindentation (Figure 53e). For example, several species of copepods use the force of their mandibles to crush diatoms using silica-tipped parts called opal teeth[206], as illustrated in Figure 53f.

The following is the underlying reasoning for employing each method in this chapter:

- Firstly, the morphology and topography were examined using SEM and AFM, which serve as potent instruments for obtaining high-resolution nanoscale surface images. By examining the surface features and dimensions of the samples, we gain insights into their structural characteristics, such as surface topography, pore distributions, and pore sizes. Understanding the morphology is crucial for subsequent analyses and interpretations of the material properties.
- The AFM is used not only for surface scanning, but more importantly for the Young's modulus measurements. The AFM technique provides valuable information about the mechanical behavior and stiffness of the material and generates real-space images by “feeling” the sample surface rather than “looking at” it[207]. By quantifying the Young's modulus, one can assess the material's ability to withstand deformation under applied stress and understand its mechanical response.
- The subsequent compliance analysis aims to complement the Young's modulus measurements by examining the material's capability to withstand mechanical

stresses without failure and contributes to a comprehensive understanding of the material's mechanical properties.

- By employing AFM, local indentations can be made, providing more detailed information about the material. However, in this case, the structure is not completely deformed, as in the case of *in situ* SEM nanoindentation. By conducting indentation tests while observing the sample under SEM, one can directly observe the structure deformation behavior under static and dynamic loading which is important for future applications as MEMS devices. Each of these methods offers valuable insights into the mechanical strength and response of the diatom structures at both micro and nanoscales.
- Studying the vibration characteristics using COMSOL calculations and AFM methods[208] provides deeper insights into the structural dynamics of the material and its potential applications in vibration-based systems.

6.2 Morphology and topography study: from micro to nanoscale

Figure 54 shows morphology and topography of *Coscinodiscus oculus-iridis* first identified by Ehrenberg in 1839. The frustule shown in Figure 54a consists of two valves: the upper epitheca and the lower hypotheca, connected by a series of siliceous rings called girdle bands. The diameter of valves ranges from 30 to 70 µm, while their height varies from 10 to 15 µm, although much larger size ranges can be found in literature. The cross-sectional view of a diatom frustule after FIB (Figure 54b, c) demonstrates the multi-layered hierarchical structure of the cell wall, formed by orthosilicic acid in silica deposition vesicle[24,133]. The wall thickness is in the 0.3-1.5 µm range. The disk-shaped valve faces are slightly depressed in the central area, which

is frequently less silicified than the peripheral region[209]. The outer thin perforated silica layer called cribrum (Figure 54d, e, j) consists of a regularly spaced array of 40-70 nm pores (cribellum)[210] (Figure 54f, m). The pore-to-pore distance in one array is around 100 nm. The honeycomb-like chambers called areolae are open to the cell interior via rimmed circular openings (Figure 54g) – foramen with a diameter of around 0.2-0.5 μm (Figure 54h, i). The porous pattern of the cribrum layer is located exactly above the foramen. The rimoportula openings having the shape of a pair of lips are distributed along the perimeter of the internal valve (Figure 54h). On the external valve face, the rimoportula opening is a simple, round aperture, through which they extrude polysaccharides and other carbon compounds. AFM topography images (Figure 54j-m) show that the surface of the air-dried live diatom cell containing organic material is not flat and monotonously "smoothed", but form a hilly terrain (Figure 54l, m).

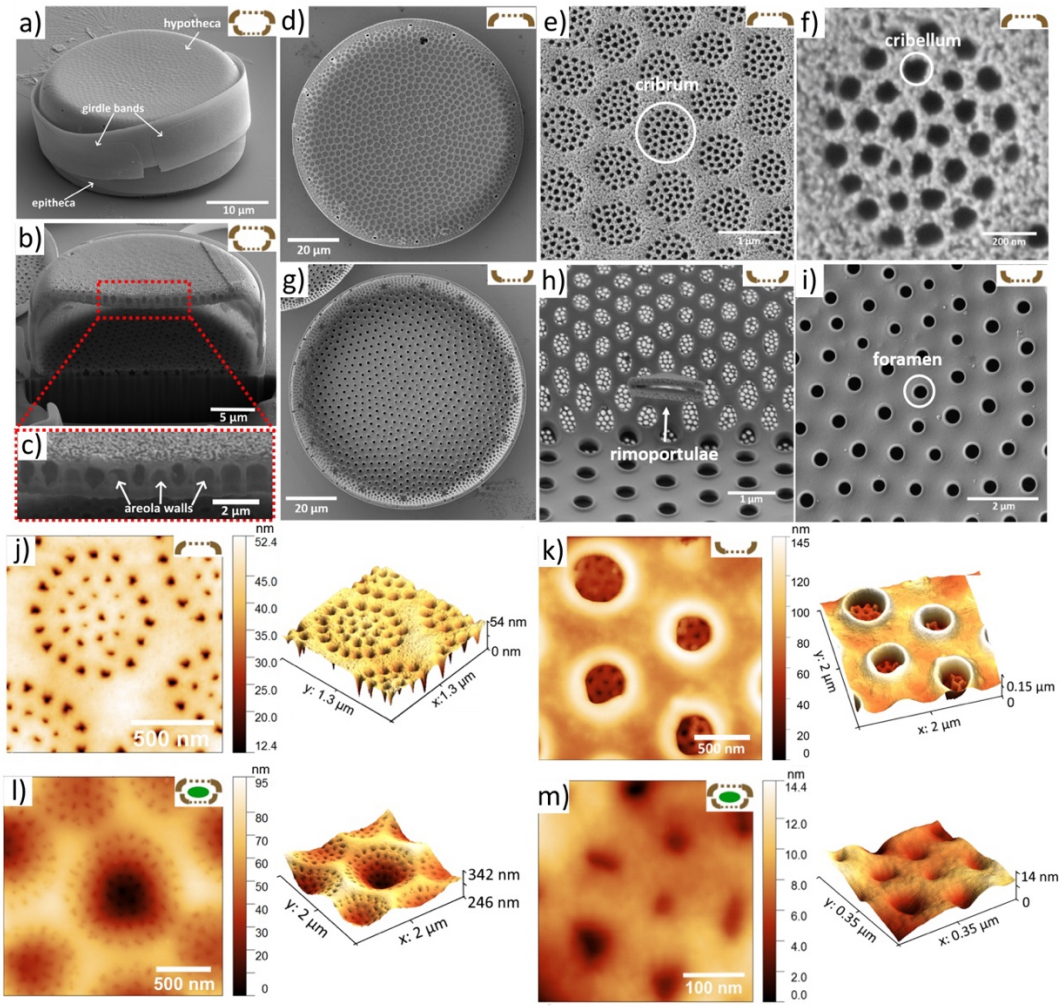

Figure 54. SEM images of: a) the cleaned diatom frustule consisting of a hypotheca and an epitheca joined together by girdle bands, b) the frustule FIB cross-section showing areola walls c, d) outer surface of the valve, e details of the external side of the valve: cribrum, f) cribellum, g) inner surface of the valve, h) details of the internal side of the valve: rimoportulae, i) foramen. AFM topography of: j) an outer surface of the cleaned frustule decorated with porous domes (cribrum), k) foramen holes on the inner surface of a cleaned frustule, l) a surface of a wet diatom cell forming a hilly terrain, m) close view of regularly spaced pores on the outer surface (cribellum) of a wet diatom cell. [39]

Organic components of diatoms can be classified in the following way: 1) an organic casing represented by a thin layer surrounding silica wall, 2) the diatotepum or diatotepic layer located between the plasmalemma and the silica, 3) molecules or organic complexes trapped within the silica, 4) mucilage associated with the cell surface or secreted by diatoms which can be used for motility, adhesion or protection[211]. On the cleaned frustule the perforations on the outermost surface are simple openings (Figure 54j), while on the inner surface they have thickened rims (Figure 54k).

The analogy between the natural appearance of silica diatom frustule lase structure and MEMS (especially microphone membrane) served as a motivation to carefully study diatoms as a mechanical system. Mechanical sensitivity of the MEMS capacitive microphones increases when the thickness of the diaphragm increases[212]. According to the review article[213], the average membrane diameter is 600 μm, while the thickness makes up 1 μm, which corresponds well to the silica frustule thickness.

6.3 AFM and AMFM studies of mechanical properties of diatoms

Figure 55 shows AFM topography and corresponding maps of Young's modulus measured on the inner (Figure 55a, d) and the outer (Figure 55b, e) surfaces of cleaned diatom frustules and on the wet cell containing organic material (Figure 55c, f). The Young's modulus data were obtained by collecting force-distance curves in the elastic regime[214,215].

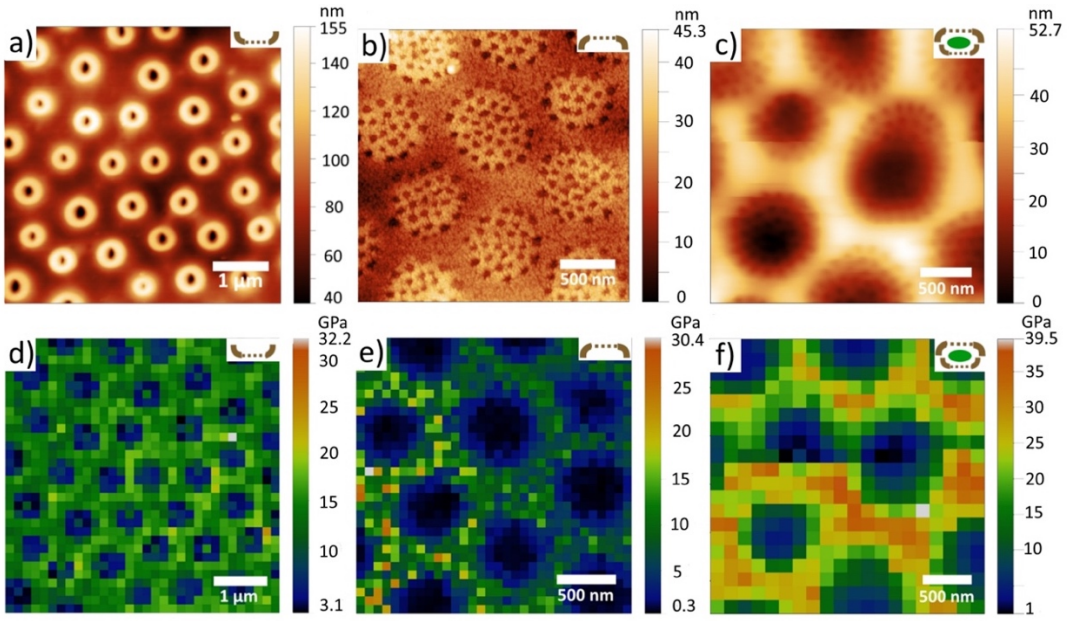

Figure 55. AFM study of cleaned frustules and wet diatom cells. Topography of a measured: a) inner side and b) outer side of cleaned frustule, c) wet diatom cell. Young's modulus of: d) inner and e) outer surface of cleaned frustule, f) wet diatom cell. [39]

The results show that Young's modulus of the thick space between pores is E=15±2 GPa and E=10±4 GPa for the inner and the outer surfaces of cleaned frustules, respectively, while for the wet diatom cell E=25±5 GPa, which was expected considering the support from the organic material trapped inside the frustule. According to study[216], the introduction of molecular water into the silica network leads to an increase of Young's modulus of silica glass at low water content. On the other hand, due to excessive boiling in concentrated nitric acid, the frustule material can become friable and fine structures in some cases may be lost which leads to the lower mechanical performance. Conversely, if the oxidation was weak and the samples were poorly washed, the organic matter lays down on the surface of the frustule as a thin

layer, covering and masking fine structures. The stronger mechanical structure of the internal plate is expected as this layer is the basic framework for building the other porous layers – cribrum and cribellum. Finite element simulation of an isolated pleura of *T. punctigera*[48] showed that the Young's modulus of diatom silica is 22.4 GPa, which is comparable to cortical bone (20 GPa) and in good agreement with our study. Young's modulus of the rims around pores is lower probably because the material of the rims is not clamped in in-plane direction, as shown in Figure 56.

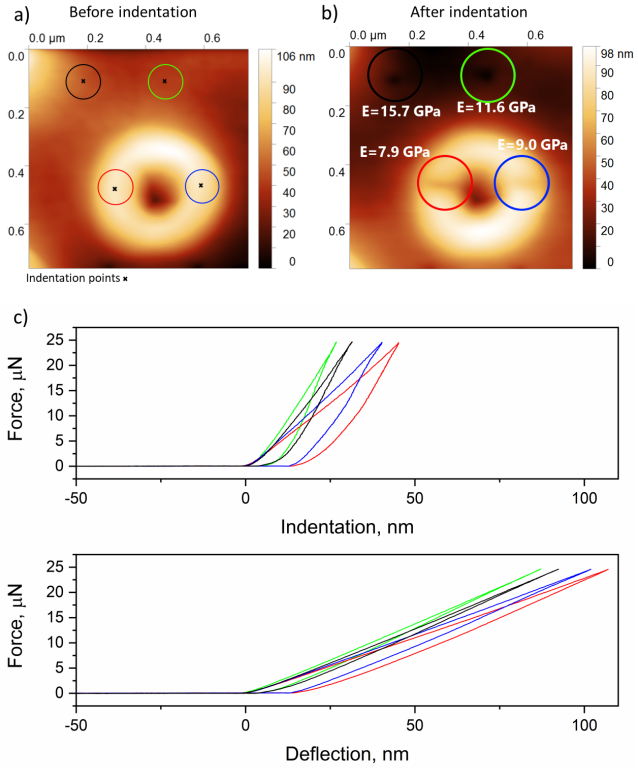

Figure 56. Inner surface of a frustule measured by the stiff diamond probe (k=400 N/m). a) Topography before nanoindentation, b) topography after nanoindentation with indicated Young's modulus values calculated using DMT model, c) force-indentation and force-deflection curves collected at specific indentation points.

39

Indentation was also performed at specific points on the inner surface of the cleaned frustule by applying different indentation forces, as indicated in Figure 57a.

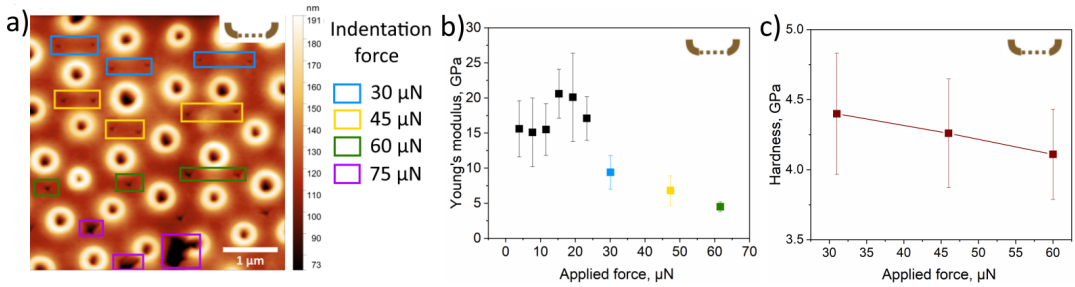

Figure 57. AFM indentation at specific points of a cleaned inner valve. a Inner surface of a frustule measured by the stiff probe after indentation at specific points by applying different indentation force, b Young's modulus calculated using the Derjaguin-Muller-Toropov (DMT) model at different applied forces after averaging over 10 points, c the dependence of hardness on the applied force. [39]

Young's modulus calculated from these data using the DMT model (Figure 57b) show the same trend as for the reference fused silica sample, i.e., correct values are at the applied force below 20 µN where the tip-surface contact geometry may be approximated by a sphere and interaction is mainly elastic. At higher forces the model does not fit well because the contact geometry deviates from the spherical one, while at 75 µN the valve breaks. Hardness calculated as a ratio of the maximum indentation force to the indent area is between 4.0 and 4.5 GPa and slightly decreases with increasing loading force, which is typical for nanohardness measurements (Figure 57c).[217] Similar behaviour was observed on the reference fused silica sample (Figure 32). The hardness of the measured cleaned inner valve was significantly higher as compared to the previously reported[45] values obtained on the outer porous layers

((0.033 - 0.116 GPa) – at the center, (0.076 - 0.120 GPa) – at the edge). The difference in hardness values between the inner valve and cribellum layer is anticipated due to the low thickness of the latter (less than 50 nm). This led to the collapse of the cribellum layer around the indenter tip and the penetration of the tip into the underlying cribrum layer[45]. The cracks were detected in cribellum at relatively low loads (1.5-3 μN), indicating the mechanical weakness of this layer [45].

Young's modulus on the cribrum in Figure 55 appears smaller than on the thicker parts of the sample. It can be explained by the fact that the cribrum is so thin that during force-distance curve acquisition it bends as a membrane even at low applied force (100 nN). In this case the obtained values of Young's modulus do not correctly reflect properties of the material. In order to obtain more accurate results for the cribrum, a gentler AMFM viscoelastic mapping method[218] has been employed. In this method the AFM cantilever scans the sample's surface in the tapping mode in the repulsive regime[219]. The results are shown in Figure 58. The AMFM Young's modulus is up to two times higher than the modulus calculated from the force-distance curves. On the outer surface of the cleaned frustule Young's modulus of the cribrum is about 3 times lower than of the thicker space in between, while on the wet diatom cell, where the inorganic frustule is supported by the organic interior, the difference almost vanishes. This result implies that Young's modulus calculated on the cribrum from the force-distance curves is indeed affected by the membrane effect.

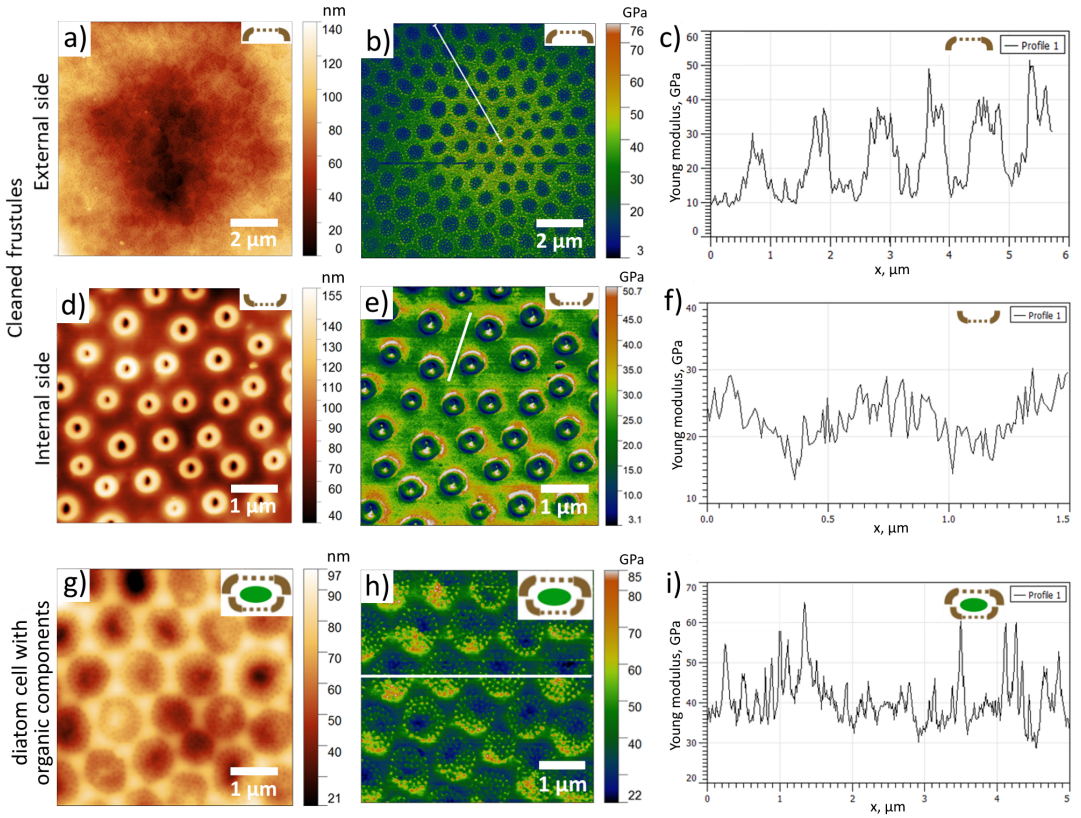

Figure 58. The AMFM study of cleaned frustules and wet diatom cells. External side of the cleaned valve: a) Topography, b) The AMFM Young modulus, c) The AMFM Young modulus profile along the white line shown in Figure 60b. Internal side of the cleaned valve: d) Topography, e) The AMFM Young modulus, f) The AMFM Young modulus profile along the white line shown in Figure 60e. External side of the wet diatom cell: g) Topography, h) The AMFM Young modulus, i) The AMFM Young modulus profile along the white line shown in Figure 60h.

Force, applied to the sample during the force-distance curve acquisition in this study, was in the µN range. Force, applied to the sample during AMFM measurements is hard to quantify, but according literature[220–222], it is in the nN range – single to tenth of nN. It means that the volume of deformed material is higher in the case of force-

distance curves acquisition, which results in two effects: (1) size effect and (2) influence of internal pores effect.

1) The indentation size effect manifests itself as a significant dependence of hardness and elastic modulus from the indentation depth[223]. Usually measured values of mechanical properties increase with decrease in indentation depth, especially when indentation is at the nanoscale.

2) The porous structure of the frustule implies that higher volume of deformed material during the force-distance curve acquisition is more likely to include a void or a void part, which results in smaller elastic modulus as compared with the AMFM measurements, where the probed volume is very small (few nm^3) and localized in the surface vicinity, which reduces the void influence.

6.4 Compliance of cleaned frustules: Static vs. dynamic approach

To get deeper insight into mechanical properties of the cleaned valve, force-distance curves were acquired from the edge towards the center of the outer surface along green lines shown in Figure 59a using the stiff diamond probe. The maximum loading force of 7.7 μN falls into the elastic regime (without indentation) and the frustule's outer surface bends as a membrane under the load. The results showed that the bending increases from the side towards the center of the valve. Young's modulus calculated using the Hertz fitting model decreases as the distance from the edge towards the center of the valve increases.

The data obtained was used in combination with the analytical model for circular membrane deformation given by Melnikov[224]. The Green's function of a point force G(z,ζ) for Kirchhoff plates satisfies the equation:

$$D\nabla^4 G(z,\zeta) = \delta(z-\zeta) \tag{3}$$

where $D = Eh^3/12(1-\nu^2)$ is the flexural rigidity of the diatom valve given in terms of Young's modulus E, thickness h and ν is Poisson's ratio, while $z = r(cos\varphi + i\,sin\varphi)$ and $\zeta = \rho(cos\,\psi + i\,sin\,\psi)$ represent the observation point and the force application point, respectively. The solution is given by:

$$G(z,\zeta) = \frac{1}{8\pi D}\left[\frac{1}{2a^2}(a^2-|z|^2)(a^2-|\zeta|^2) - |z-\zeta|^2 ln\,\frac{|a^2-z\underline{\zeta}|}{a|z-\zeta|}\right] \tag{4}$$

where a is the radius of the diatom. By fitting the model to experimental observations, the membrane flexural rigidity can be used to determine the overall apparent Young's modulus of the diatom valve as a circular membrane. The compliance defined as the measure of the structure deformation under the action of external forces was calculated as the reciprocal of rigidity. The dependence of compliance on the relative radial position calculated using influence function of a point force is shown in Figure 59b. Maximum similarity with the experimental values was achieved at h=477 nm and E=9.35 GPa.

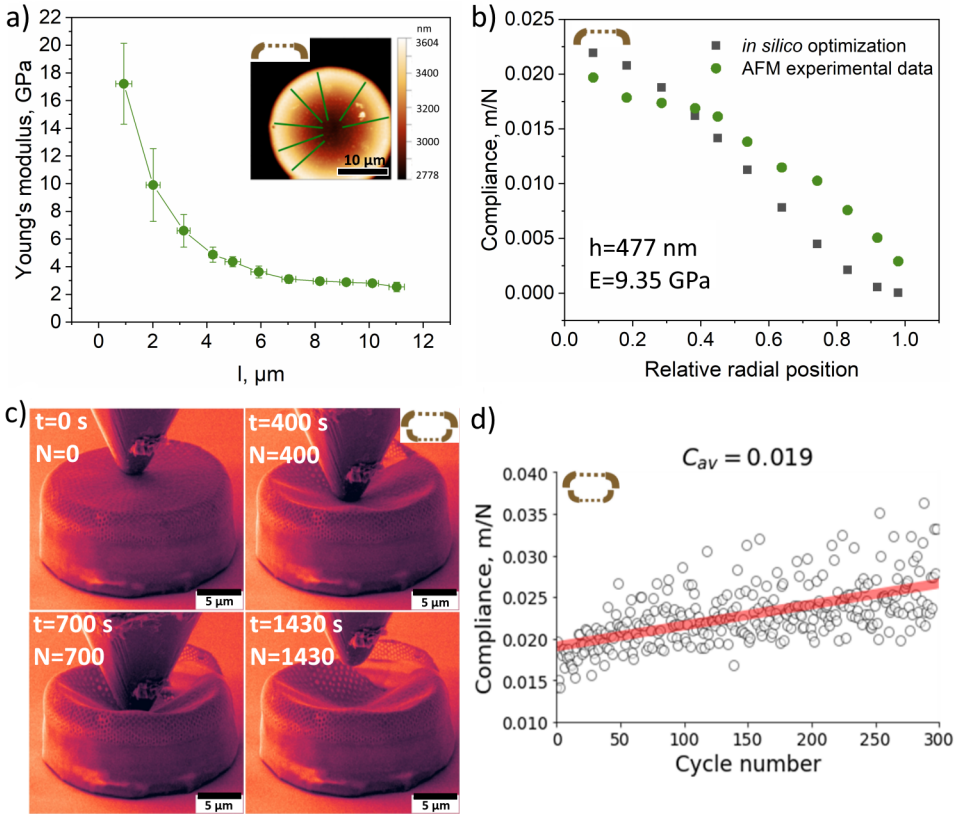

Figure 59. Compliance of cleaned frustules: static vs. dynamic approach. A) Young's modulus depending on the distance from the edge towards the center of the outer surface of the valve. Inset: topography of outer surface of a cleaned frustule. The measurements were carried out using AFM by pressing the diamond probe on the sample with a force of 7.7 μN along each green line. b) Compliance vs. relative radial position calculated using the Green's function of a point force, c) SEM images of whole diatom frustule acquired during different stages of nanoindentation in the SEM column, d) Calculated compliance vs. cycle number. [39]

The results of cyclic loading (amplitude 1 μm, period 1 s) performed on cleaned diatom frustule in the SEM column are shown in Figure 59c and Figure 60. By examining the dependence of displacement on time, and considering sinusoidal motion of diatom frustules represented as $A \cdot \sin(\omega t)$, the stiffness and subsequently compliance

were determined as a function of cycle number, as presented in Figure 59d. Compliance increases with increasing number of cycles. The frustule begins to break along one edge after ca. 300 s, but continues to oscillate during cyclic loading without complete rupture. Figures 60a-d show the analysis of vibration behaviour of upper diatom valve, while Figure 60e-h represent the analysis of the whole frustule.

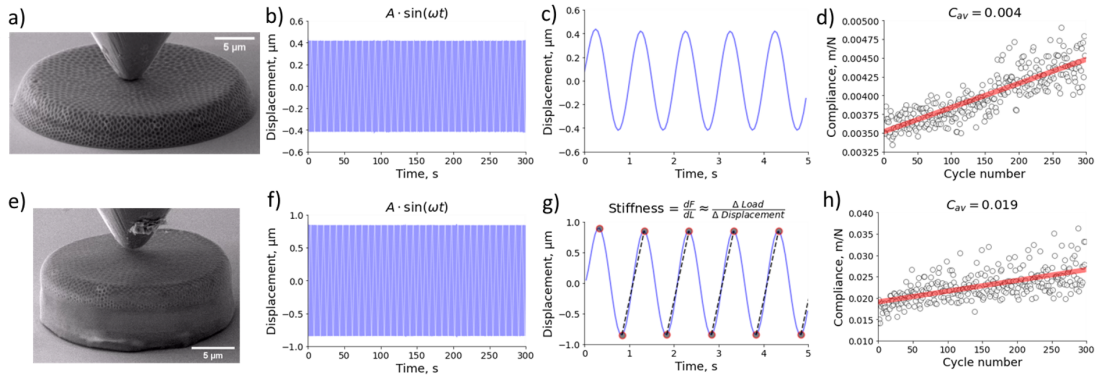

Figure 60. a) SEM image of a measured cleaned diatom upper valve, b) Displacement vs. time, the whole region – 300 seconds, c) Displacement vs. time, a short time interval – 5 seconds, d) Compliance vs. cycle number, e) SEM image of a measured cleaned diatom frustule, f) Displacement vs. time, the whole region – 300 seconds, g) Displacement vs. time, a short time interval – 5 seconds, h) Compliance vs. cycle number. Amplitude 1 µm, period 1s. [39]

The obtained average compliance value of 0.019 m/N for a cleaned diatom frustule, as measured in the dynamic mode during nanoindentation, is comparable to the values of graphene-based MEMS microphones[225,226]. Shubham et al.[147] obtained slightly lower value 7.154×10^{-3} m/N for a semiconstrained polysilicon diaphragm with peripheral and center protrusions on the backplate. In MEMS microphones, compliance refers to the ability of the diaphragm to exhibit sufficient flexibility and sensitivity to

capture sound waves. A higher compliance value indicates that the material can deform more easily under applied forces, resulting in increased sensitivity to sound vibrations. Conversely, a lower compliance value implies a stiffer diaphragm that may exhibit reduced sensitivity to sound. This indicates that the diatom frustule has the potential to be a promising material for MEMS microphone applications. However, further investigations and considerations are necessary to fully assess the suitability and performance of the diatom frustule in actual MEMS microphone designs.

Considering the deformation response of the frustule valve to local indentation illustrated in Figure 61, the total compliance of the system can be written as the sum of the local material compliance under the indenter, C_L, and the global structural compliance C_G:

$$C = \frac{\delta+u}{F} = \frac{\delta}{F} + \frac{u}{F} = C_L + C_G \tag{5}$$

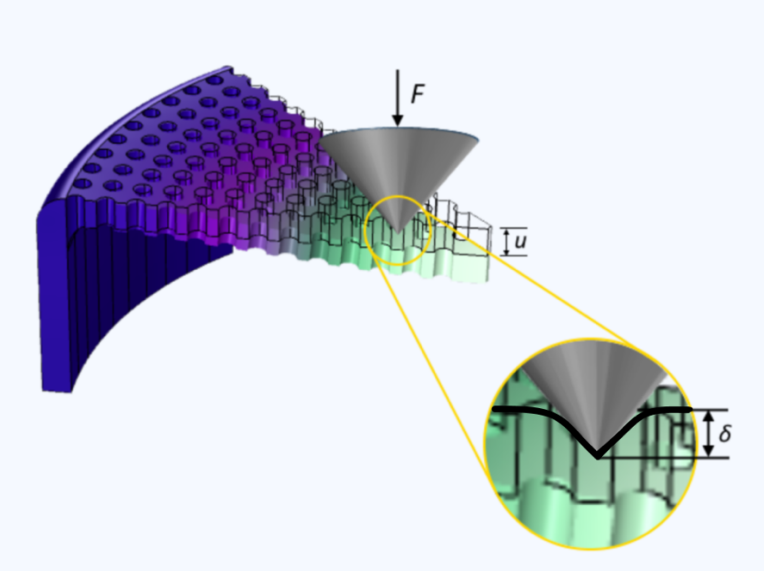

Figure 61. The deformation response of the frustule valve to local indentation

It is well known from the literature for elastic[227,228] as well as plastic indentation[229] that the force-displacement relation is described by a power law function of the type $F \cong \delta^{(1+m)}$, where m>0. Therefore, the local compliance decays with increasing applied force as $C_L \cong F^{-m}$, whilst the global compliance C_G remains appreciably constant within the range of forces for which the structural deflection remains elastic. By the same argument, the local compliance C_L dominates over global compliance C_G for small applied forces. This transition between the two regimes takes place over a range of loads that depend on the material properties and the indenter shape. It can therefore be concluded that both the local material and global structural responses can be interrogated via the suitable choice of loading conditions and indenter tips under the small and large applied forces, respectively. Both local and global effects can be considered together only once the global compliance has been calibrated.

6.5 In situ SEM nanoindentation

Static *in situ* nanoindentation inside SEM was also conducted on dried cells with cellular material (Figure 62a), as well as cleaned diatom frustules (Figure 62b). Their mechanical performance was analyzed based on the force-displacement curves. Static studies lead us to a more precise definition of the module of a material as a whole. Figure 62c shows the force-displacement curves of dried cells, which vary depending on the orientation and size. As can be seen, dried cells 1-4 (diameter, 37-40 μm; height, 11-13 μm) have a similar size and mechanical behavior, which is different from the dried cell 5, whose diameter/height ratio is smaller (diameter, 41 μm; height, 18 μm). On the other hand, a difference in mechanical performance was observed when indenting from the girdle band point a dried cell 6, which was similar in size to cell 5.

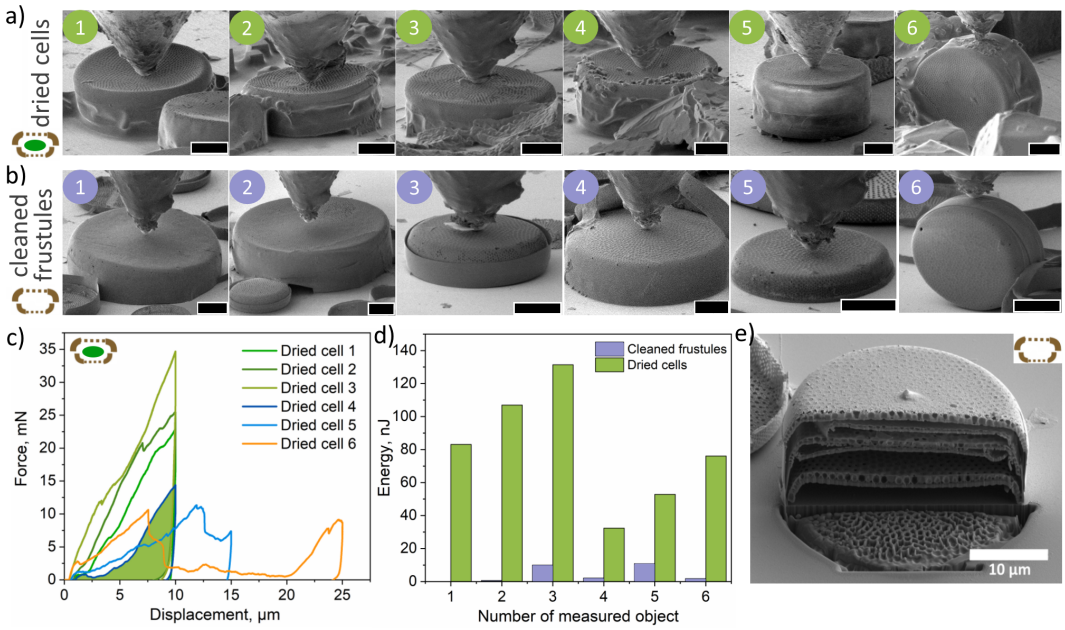

Figure 62. In situ SEM nanoindentation of cleaned frustules and dried diatom cells. a) SEM images of air-dried diatom cells measured by nanoindentation in the SEM column, b) SEM images of cleaned frustules. Scale bar, 10 µm. c) Force-displacement curves obtained during indentation of dried cells, d) Calculated area under the force-displacement curves of dried and cleaned diatoms equal to work done, e) The case of a layered structure of the frustules of some diatoms, potentially responsible for difference in the obtained force-distance curves. [39]

The nature of the curves of cleaned frustules and dried cell with organic material is different (Figure 62c, 63). The force-distance curve for dried cells with organic material exhibits a steeper slope and higher forces than the cleaned frustules. The higher forces indicate a greater strength and the ability of the material to withstand deformation owing to the presence of organic materials. In the case of cleaned frustules, the area under the curve is typically smaller compared to dried cells with organic material

(Figure 62d). This suggests that less energy is required to deform the cleaned frustules, indicating a lower resistance to indentation.

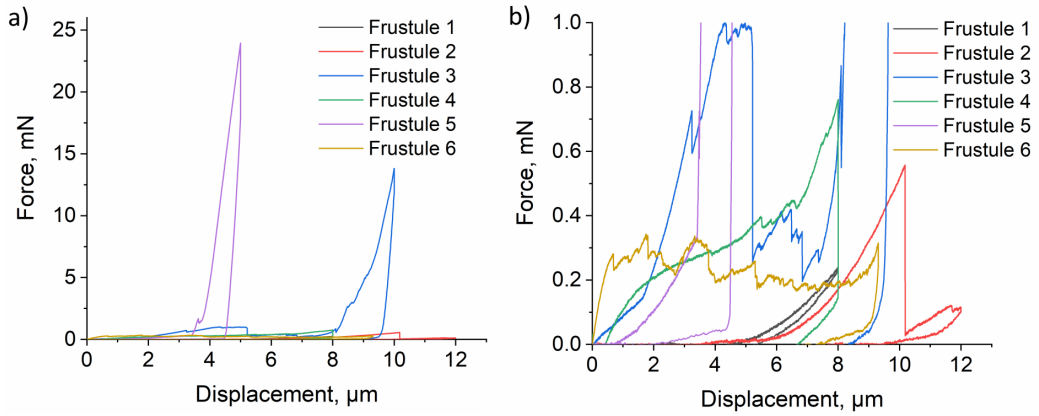

Figure 63. Force-displacement curves of cleaned frustules obtained by in situ SEM nanoindentation. a) force-displacement curves for forces up to 25 mN, b) magnified view of force-displacement curves for forces up to 1 mN. [39]

The presence of multiple small peaks or a "noisy" behavior in force-distance curves of some cleaned frustules can be attributed to several factors related to the material's structure and mechanical properties. Cleaned frustules may exhibit surface roughness at the microscale or nanoscale due to the cleaning process or inherent characteristics of the frustule structure. When the indenter makes contact with the rough surface, it encounters variations in the local mechanical properties of the material, causing the force to fluctuate and result in the “jagged” force-distance curve. Moreover, the presence of heterogeneities in the frustule material or residual organic or inorganic matter on the frustule surface can lead to a force-distance curve that deviates from a smooth, continuous pattern, displaying abrupt changes or fluctuations instead. The differences between the mechanical response of different diatom samples can also be

attributed to the layered “burger” structure within the frustule of some diatoms, as demonstrated in Figure 62e. This situation can occur in old cultures when the process of cell division is corrupted and formation of the valves is not accompanied by cytokinesis. The combination of organic and inorganic components in diatom cells, leading to their superior mechanical characteristics, can serve as an inspiration for layer-by-layer assembly, which can be used to modify the inorganic substrate for the manufacture of multilayer composites.[230]

There is a strong correlation between MEMS' performance and the mechanical properties of the materials they are constructed from[231]. By selecting, designing, fabricating, and packaging materials in accordance with mechanical properties, some of the mechanical failure modes may be eliminated[232]. Polysilicon, the most frequently used MEMS material, has Young’s modulus mostly in the range between 160 and 180 GPa, similar to single-crystal silicon (160 – 190 GPa)[232]. Silicon-carbide and silicon-nitride are also promising MEMS materials having Young’s modulus values determined by indentation method of 395 GPa and 101 – 251 GPa, respectively[232]. Silicon oxide is often included in MEMS devices (e. g. as a sacrificial material in polysilicon surface micromachining), but has low stiffness and strength (64 GPa)[232].

6.6 Vibrational eigenmodes of diatom frustules

Over the recent years, there has been a surge of interest in leveraging natural structures as a source of inspiration for innovative engineering solutions, showing the potential of biomimicry. One particularly intriguing avenue of research involves the utilization of diatom algae frustules for fabricating an array of micro- and

nanoelectronic devices[92,132,233–235]. As already mentioned in this chapter, the high mechanical strength, small size, low density, optical properties and tailored nanostructures of diatom frustules, have inspired researchers to explore their potential in the development of MEMS and NEMS devices with improved performance, efficiency, and longevity[39,148,236]. The dimensional and structural congruence observed between diatom exoskeletons and advanced devices, including PICs and MEMS microphones, represents a promising foundation for exploring additional avenues in the realm of nanotechnology component development through the application of biomimetics and biotechnology[39,144,146].

The resonance frequencies of MEMS devices play a crucial role in their design and performance optimization as they determine the dynamic behavior of the devices and significantly impact their functionality, efficiency, and reliability. Hence, understanding the resonance frequency characteristics of MEMS devices inspired by diatom algae frustules is of paramount importance. Resonance frequencies play also an important role in the characterization of other biological objects, including red blood cells[237], bacteria[238,239], virus[240], algae[241], etc. Zinin et al.[238] found that the natural vibrations of specific bacteria are in MHz range by solving the dispersion equation using a shell model that accounts for the elastic properties of the membrane and the associated viscosities of the cytoplasm and the surrounding fluid.

Vibrational modes of diatom silica frustules have been the subject of research, but primarily through the utilization of FEM as reported by Abdusatorov et al.[148] who explored the potential of using diatom silica frustules for vibrational MEMS applications. The results showed that diatom frustules have natural frequencies in the range between several MHz and tens of MHz and are determined by the stiffness and

density of the material, the valve diameter, and the wall thickness of the frustules. Gutierrez et al.[242] investigated the mechanics of centric diatom frustules using the FEM in combination with morphology and material properties obtained from SEM and mechanical tests respectively. The study reveals that the first ten deformation modes correlate noticeably well with deformation patterns observed through SEM. A quadratic correlation was observed between the pore size and the critical buckling load, alongside a cubic relationship between the thickness of the frustule and the critical buckling load. The findings in this research provide insights into the mechanical response of diatom frustules that can aid the realization of tailored properties in new bio-inspired materials, in particular for nanotechnology applications, but also for advanced metamaterials and optomechanical devices.

Despite these notable advancements, further exploration and experimental validation of the resonance frequency characteristics of MEMS devices inspired by diatom algae frustules are warranted. The first experimental study of vibrational modes of a diatom silica frustule was conducted, and the obtained results were compared with computational data. The numerical simulations utilize FEA to model the dynamic response of the frustules. This numerical approach allows for the evaluation of resonance frequencies based on the frustules' geometric and material properties, providing insights into their inherent mechanical behavior.

To experimentally validate the numerical findings and provide precise measurements of resonance frequencies of individual diatoms, two different methods to register vibrations were employed using an AFM optical detection system: (1) collection of frequencies of thermal vibrations and (2) an external mechanical excitation followed by detection via a lock-in amplifier. These experimental techniques allow for

the direct observation of the frustules' dynamic behavior, providing valuable data for comparison with the numerical simulations.

The centric diatom *Coscinodiscus oculus-iridis* (Ehrenberg) Ehrenberg, 1840 (phylum Bacillariophyta, class Coscinodiscophyceae) was used as a model, as in the study of mechanical properties. This diatom was chosen because its shape is simple to model, it has a “microphone” pattern, and it may even be studied by analytic mathematics using Bessel functions. First, numerical calculations of eigenfrequencies of diatom frustule were performed, taking into account its geometry, silica density, Young’s modulus, and Poisson’s ratio (Table 6) and applying Comsol Multiphysics Structural Mechanics module to obtain the simulation results, as illustrated in Figure 64a.

Table 6. Diatom model parameters

Frustule diameter	D=60/70/72 μm
Frustule thickness	t=1 μm
Frustule height	15 μm
Pore diameter	0.6 μm
Silica density	ρ=2300 kg/m^3
Poisson’s ratio	ν=0.17
Young’s modulus	E=15 GPa

For experimental validation samples were prepared by welding a frustule to an AFM Si cantilever chip by FIB, followed by sputtering a ~ 30 nm thick layer of gold on top of the frustule in order to increase laser reflectance (Figure 64b). The AFM

measurements were performed by obtaining frequencies of thermal vibrations from a still sample (Figure 64c), and by measuring the amplitude-frequency response from the sample which was externally excited by a piezodriver (Figure 64d).

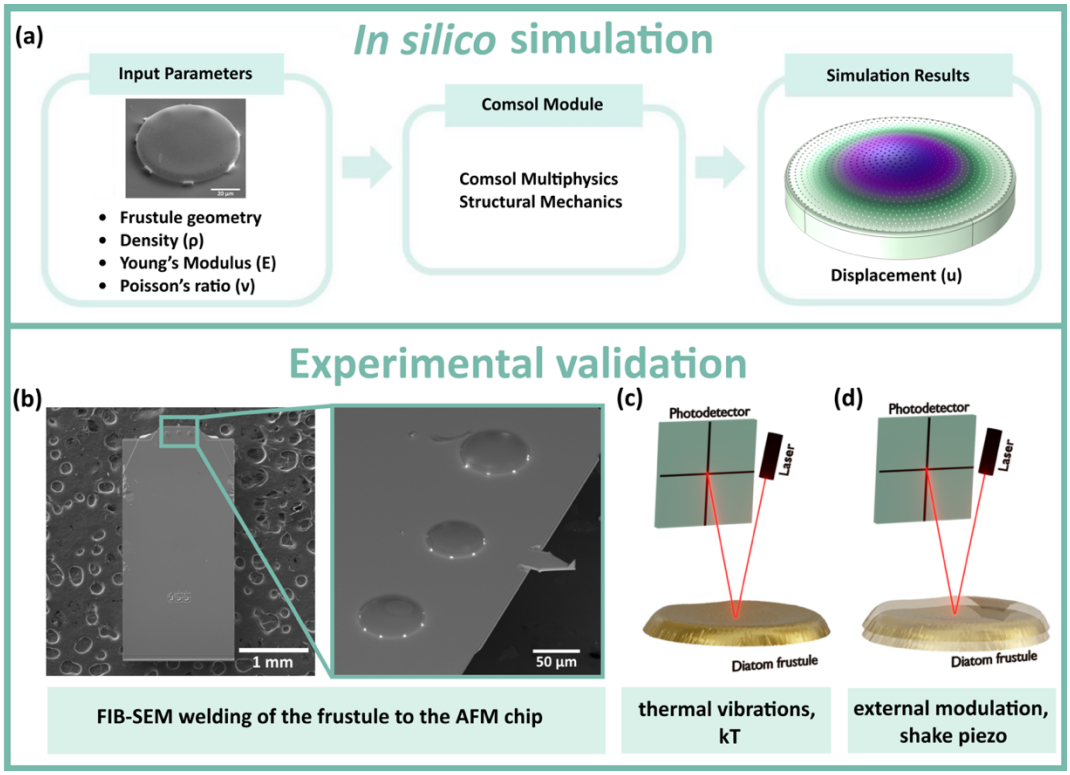

Figure 64. a) Flowchart of modelling steps using COMSOL Multiphysics. b) SEM image of AFM chip after FIB-assisted welding of diatom frustules, right: enlarged view of the samples. Schematic illustrations of two AFM approaches: c) thermal vibrations, d) external modulation.

The thermal frequency spectra obtained from different parts of the diatom frustule are shown in Figure 65a. They show that the vibration amplitude is position sensitive which corroborate the computational results, shown in Figure 65b. The experimental eigenfrequency values closely match those obtained by COMSOL

calculations (1.93, 3.20, 3.65, 4.68, 5.43, 7.68 MHz) and highlighted by the color bars. The majority of the resonance peaks were ascertained through measurements conducted on the elevated region of the valve.

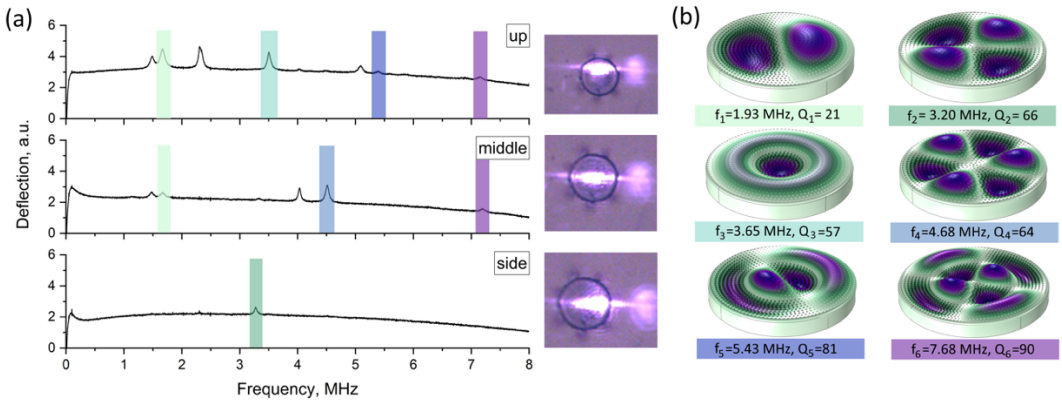

Figure 65. a) Experimental frequencies of thermal vibrations collected from different parts of the diatom frustule, as shown in the optical microscopy insets on the right side. The spectra were smoothed to avoid spurious spectral lines. The raw spectra are shown in Appendix B. b) Calculated vibrational eigenmodes of diatom frustules with indicated frequencies and quality factors.

Quality factors ranging from 21 to 90 were calculated using the peaks in Figure 66 (Table 7). The quality factor (Q) was calculated based on the obtained thermal frequency spectra using the equation: $Q = f / \Delta f$, where f is the resonance frequency, and Δf represents the full-width at half-maximum (FWHM) of the resonance peak. The rigid nature of the diatom's silica cell wall contributes to the preservation of oscillation energy, resulting in high-quality oscillations characteristic of these microorganisms. As demonstrated in the work by Zinin, quality factors for different types of cells range from 0.8 (*E. coli*) to 23.2 (*D. Carota*).[238] It appears feasible for various types of bacteria

characterized by a rigid cell wall to exhibit natural oscillations with a sufficiently high quality factor. While higher quality factors are generally desired in MEMS microphones to improve their sensitivity and performance, quality factors below 100 can still be suitable for certain applications with specific requirements, for example where a wider bandwidth is required rather than high sensitivity[243,244].

Experimentally obtained and calculated resonance frequencies as well as calculated quality factors are shown in Table 7. Intensity of the obtained peaks is position sensitive. This effect depends on the relative size of a laser spot and a frustule. In this study, the laser spot was sufficiently small to resolve different surface vibration amplitude at different parts of the frustule, which depends of the vibration mode. Instead of being a limitation, this approach provides advantages, particularly in cases where a smaller laser spot size enables high-resolution mapping of surface displacement. This means that more detailed information about surface vibrations can be obtained. Additionally, the small laser spot can be easily enlarged by defocusing the optical system, ensuring that the spot covers the entire surface of the frustule.

Table 7. Experimentally obtained and calculated resonance frequencies and quality factors

Calculated frequency, MHz	Position	Peak №	Resonance frequency, MHz	FWHM, MHz	Q
0.93	Side up	1	1.48	0.09	16
1.93		2	1.67	0.08	21
3.20		3	2.32	0.08	28
3.65		4	3.50	0.06	57
4.68		5	5.09	0.08	64
5.43		6	5.40	0.07	81
6.38		7	7.16	0.13	56
7.68	Middle	1	1.48	0.07	21
		2	1.68	0.07	24
		3	4.03	0.06	67
		4	4.51	0.07	64
		5	7.19	0.08	90
	Middle-side	1	3.28	0.05	66

Amplitude-frequency spectra of different parts of the diatom frustule obtained by external mechanical excitation are shown in Figure 66. Besides the pronounced background signal from the substrate in the frequency range below 1.5 MHz, two peaks can be distinguished at about 2 MHz, which is in agreement with the data on frequencies of thermal vibrations.

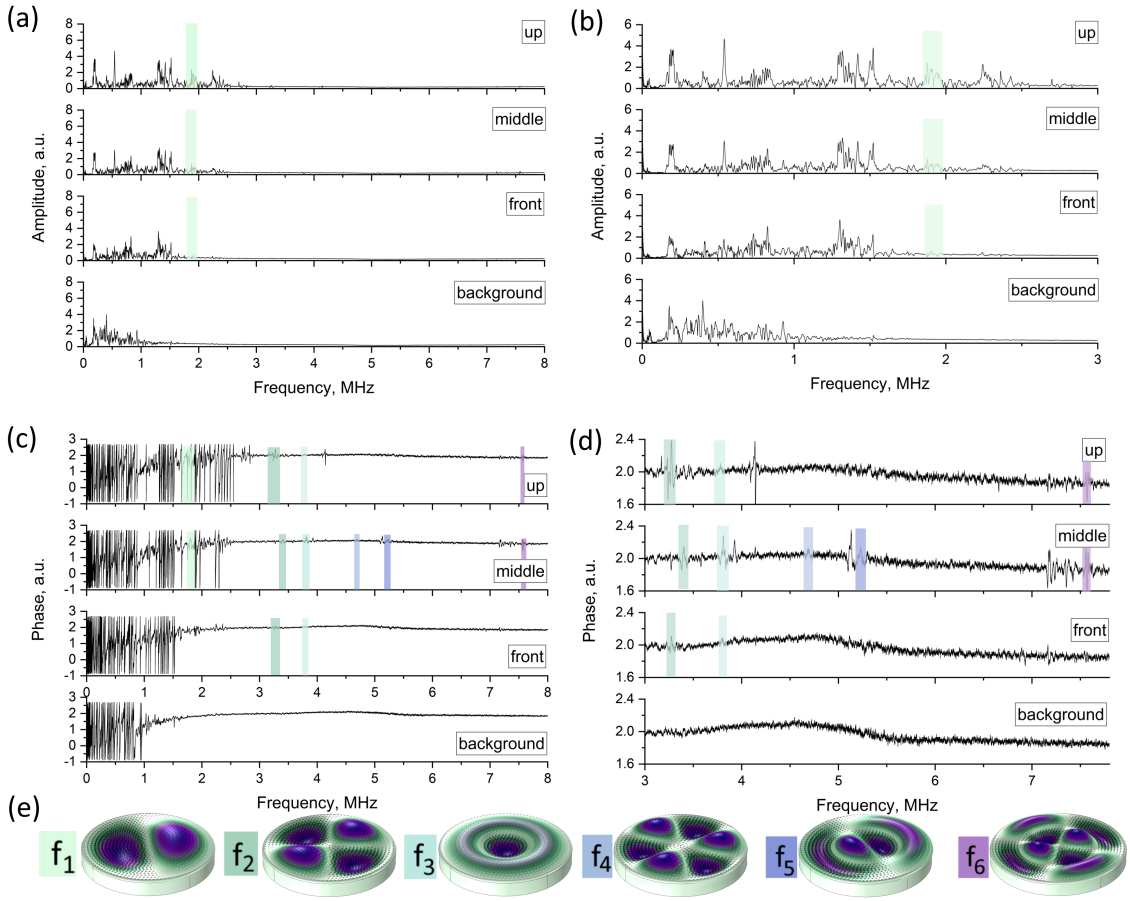

Figure 66. Amplitude-frequency spectra of different parts of diatom frustules obtained by mechanical excitation in the region: a) 0-8 MHz, b) 0-3 MHz. Phase frequency spectra collected at different positions in the region: c) 0-8 MHz, d) 3-7.8 MHz.

The both techniques were also applied to measure three diatom frustules with diameters of 60, 70 and 72 μm, as shown in Figure 67. Table 8 shows calculated resonance frequencies for all three diatom frustules.

Table 8. Calculated resonance frequencies for diatom frustules with diameters 60, 70 and 72 μm

Mode №	Calculated frequency for D=60 μm, MHz	Calculated frequency for D=70 μm, MHz	Calculated frequency for D=72 μm, MHz
1	1.29	0.93	0.89
2	2.62	1.93	1.82
3	4.35	3.20	3.03
4	4.96	3.65	3.45
5	6.36	4.68	4.43
6	7.30	5.43	5.14
7	8.67	6.38	6.04
8	9.66	7.68	7.28

The resonance frequencies of diatom frustules are inversely proportional to the diameter. The frustule with a diameter of 60 μm has a higher resonance frequency compared to the two larger frustules. On the other hand, the frustule with a diameter of 72 μm has the lowest resonance frequency among the three. Due to its larger diameter, the frustule exhibits a relatively softer structure, resulting in a lower natural frequency.

The measured frequencies of thermal vibrations possess position sensitivity, but had much lower amplitude. The mechanical excitation vibrations showed resonance peaks at about 2 MHz (Figure 67), as in the case discussed above.

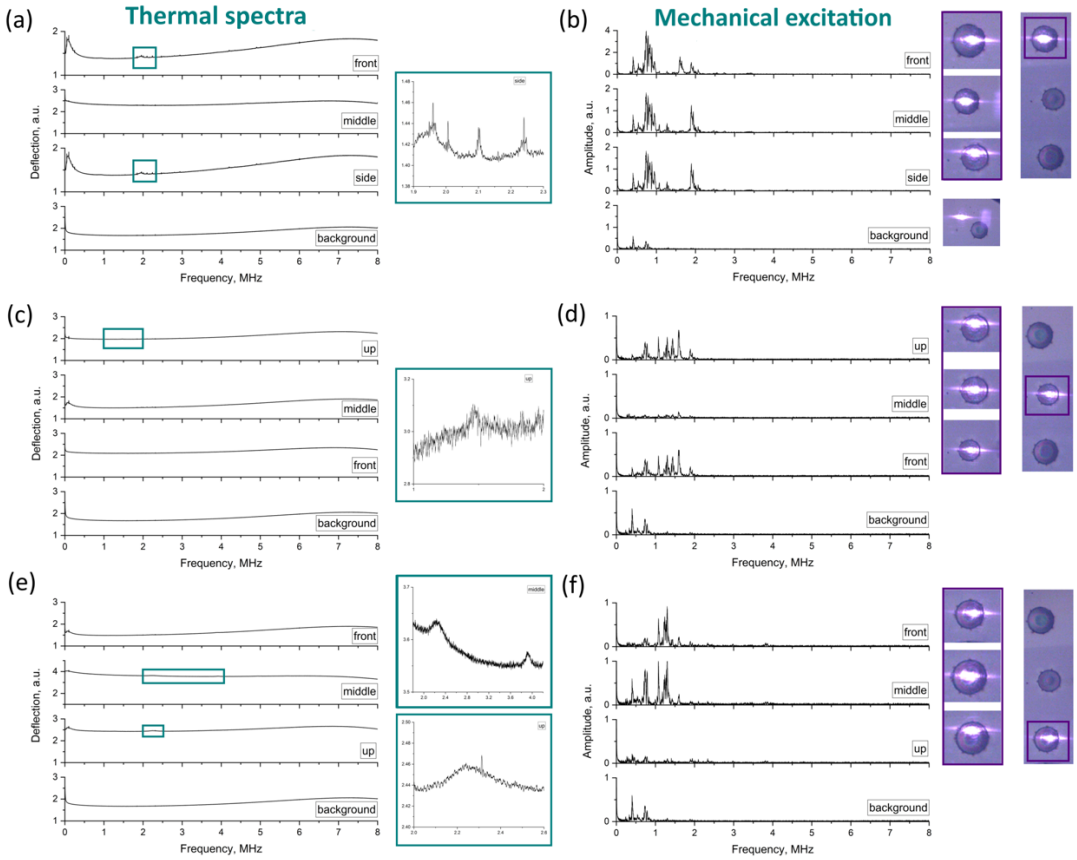

Figure 67. Thermal vibration spectra of diatoms with diameter: (a) 72 µm, (c) 60 µm, (e) 70 µm, with enlarged view of peaks on the right. Externally modulated vibration spectra of the same diatoms. Optical microscopy images of the samples and positions of the laser spot are shown on the right.

Different sensitivity for different samples might be explained either by different properties of the samples or by specifics of the optical detection system of AFM. The optical detection system is optimized to measure an AFM cantilever deflection angle rather than direct displacement [245]. The incident laser beam is reflected from a

cantilever into a photodetector. The cantilever deflection $\Delta\theta = \frac{3}{2}\frac{\Delta z}{l}$, where Δz is the cantilever displacement and l is the cantilever length, leads to change in the laser reflection by $2\Delta\theta$ and shift of the laser spot on the photodetector, which is measured. This means that the measured vibration amplitude depends not only on the actual surface displacement, but also on how this displacement is transferred into the reflection angle, which depends on the laser position on the surface and the surface geometry. The sample which demonstrated the highest vibration amplitudes possess a 1.5 μm dome-shaped valve in the middle (Figure 68), and the valve slope may facilitate transfer of the surface displacement into the change of laser reflection angle. Surface with lower curvature may transfer surface displacement into the change of laser reflection angle to lesser extent, which may explain the observed variation in vibration amplitudes obtained from different samples.

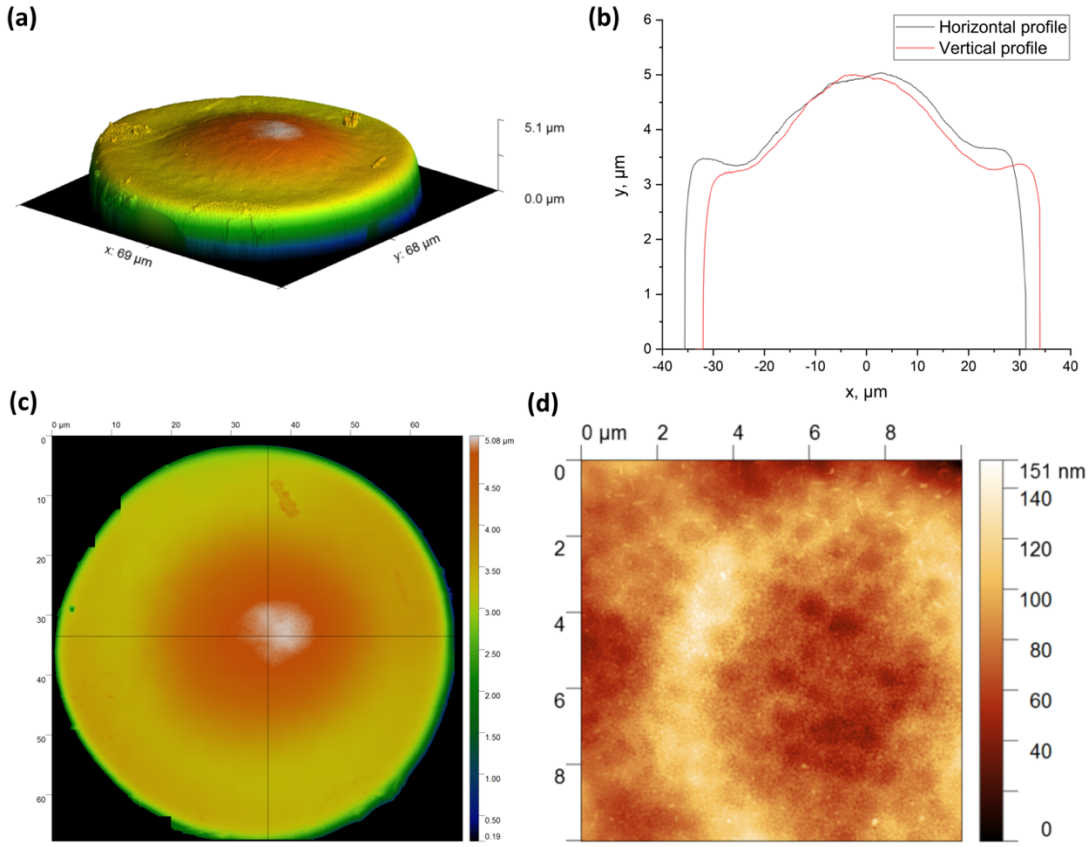

Figure 68. a) 3D AFM image of the diatom frustule. b) Horizontal and vertical profiles of diatom frustule as shown in the image c). d) Topography of the surface layer.

The deformation modes of the diatom frustule are similar to those of circular membranes, which are described by Bessel functions[246]. Gutierrez et al.[242] highlighted the importance of considering the curvature of the dome-shaped valve in the creation of a computer-aided design (CAD) model approximating a centric diatom frustule. However, they pointed out that a different curvature could be used instead of that chosen for the CAD model, or the frustule could be considered flat, suggesting that such changes are unlikely to significantly change the deformation modes of the structure. In this study, a flat diatom frustule has been considered based on the SEM images.

The simplified model utilized in this study disregards the intricate and multi-layered structure of diatom frustules, comprising three distinct layers possessing varying thickness, pore sizes, and pore distributions, as well as the dome in the middle (Figure 68 a-c). Such structural complexity is known to impact the mechanical properties of diatom frustules, thereby potentially influencing their vibrational characteristics.

The resonance frequency is detremined by two competing factors, namely mass and stiffness due to the porosity of the membrane. As the number of pores increases, the mass of the membrane decreases, which can lead to an increase in the resonance frequency. On the other hand, as the number of pores increases, the stiffness of the membrane decreases, which leads to a decrease in the resonance frequency. The porosity of diatom frustules varies a lot depending on the layer. For example, the porosity of the cribrum layer of *Coscinodiscus* sp. (25.2 ± 2.5%) is significantly higher than that of the cribellum (7.5 ± 1.2%)[131]. Another study showed that when the diameter scale, pore size, and density of diatom frustules decrease, their natural frequencies increase[148]. Besides, frustules with lower stiffness and thickness vibrate at lower frequencies than frustules with higher stiffness and thickness.

Han Je et al. designed a surface-micromachined capacitive microphone consisting of a membrane center hole and back-plate supports with improved sensitivity and frequency response, which looks similar to diatom frustule[146]. In the proposed microphone, the resonance frequency of the back-plate is increased from 86 to 853 kHz by the back-plate supporting beams. Westerveld et al.[144] fabricated a ultrasound sensor based on silicon photonics technology, which achieved remarkable sensitivity through the implementation of an innovative optomechanical waveguide. The waveguide

employs two movable components with a highly confined 15 nm air gap, consisting of a silicon dioxide lower cladding and an upper cladding (membrane) structure. The performance of the resulting 20 μm sensor operating within the range 3-30 MHz, surpasses that of piezoelectric elements of equivalent dimensions by two orders of magnitude.

6.7 Summary

The mechanical characteristics of both cleaned *Coscinodiscus oculus-iridis* frustules and cells with organic content were explored using AFM and *in situ* SEM nanoindentation techniques, considering static and dynamic loading conditions. The Young's modulus of wet diatom cells displayed a notably elevated value ($E = 25 \pm 5$ GPa) compared to cleaned frustules ($E = 15 \pm 2$ GPa for inner surface and $E = 10 \pm 4$ GPa for outer surface). The AMFM viscoelastic mapping method provided Young's modulus values up to twice as high as those calculated from the force-distance curves. This discrepancy can be attributed to the differences in applied forces; force during force-distance curve acquisition was in the μN range, while in AMFM measurements, it was in the nN range. The frustule's porous structure suggests that a higher volume of deformed material in force-distance curve acquisition is more likely to contain a void or a portion of a void. In AMFM, the probed volume is very small (few nm^3) and localized near the surface, minimizing the influence of voids, which leads to higher values Young's modulus values. Besides static *in situ* nanoindentation measurements, the behavior of the frustule was reported for the first time under the cyclic loading, which is vital for the application of diatom-like structures in MEMS devices. The nanoindentation measurements in the dynamic mode showed that the average

compliance of a cleaned frustule is 0.019 m/N, a value comparable to that of graphene-based MEMS microphones.

The intricate architecture of diatom frustules, combined with their unique properties, offer tremendous potential for the development of advanced MEMS devices. The resonance frequencies of *Coscinodiscus oculus-iridis* were determined through numerical simulations in COMSOL Multiphysics, spanning from 1 to 8 MHz. These frequencies were experimentally confirmed using two atomic force microscopy techniques: (1) measuring thermal vibration frequencies and (2) applying an external mechanical excitation and detecting the response with a lock-in amplifier. The resulting quality factors, ranging from 21 to 90, provide versatility for applications with distinct requirements, particularly in situations prioritizing a broader bandwidth over high sensitivity. The author believes that these findings will contribute to a deeper understanding of the relationship between the structural attributes of diatom frustules and the resonance frequencies of MEMS devices, enabling the development of more efficient and optimized devices for a wide range of applications.

Chapter 7. Optical properties of diatoms

In this chapter the mechanisms behind diatom optical response have been presented and analyzed using approaches like the Fourier modal method. By studying how the structural features of diatom frustules are optimized for enhancing the interaction of light with chloroplasts, we can gain valuable insights into improving their photosynthetic efficiency. Numerical simulations have been performed by Prof. Sergey Dyakov. Extinction spectra and FLIM images were acquired by the author.

7.1 Background

Diatoms provide a model system for understanding how to engineer microscale and nanoscale structures with precise control over their optical properties. Analyzing the diffraction of light by diatoms under different conditions also enables their properties to be applied for biosensing, such as detecting shifts in factors like pH, salinity, temperature, and the presence of chemicals[84].

When studying diatom frustule, two important factors need to be considered from an optical point of view. The first factor is the physical dimension of the periodic structure, which includes the number of porous silica layers, the thickness of each layer, and the size of the holes within the material[8]. These parameters can affect how the structure interacts with light, including how it scatters, diffracts, or guides light. The second factor is the refractive index contrast, which is created by the complementarity of silica (with a refractive index of approximately 1.45), water (with a refractive index 1.33) and air pores (with a refractive index of 1) in the visible range[8]. Previous studies primarily focused on purified materials under air conditions, ensuring a relatively favorable refractive index contrast for enabling and quantifying specific optical properties like light diffraction through silica/air patterns[62,247]. Overall, understanding

these two factors is important for studying the optical properties of silica-based materials, particularly in relation to how they interact with light. Diatom valves with periodic patterns of holes can resemble a photonic crystal slab waveguide, enabling light-matter interaction[8].

In this chapter, the optical phenomena displayed by periodic microscale structures in diatom frustules within a water environment, such as light diffraction and interference, were modeled using the Fourier modal method.

7.2 The diatom model

The numerical model of diatom *C. oculus-iridis* for optical simulations has been made based on the SEM and AFM images shown in Figures 53, 69.

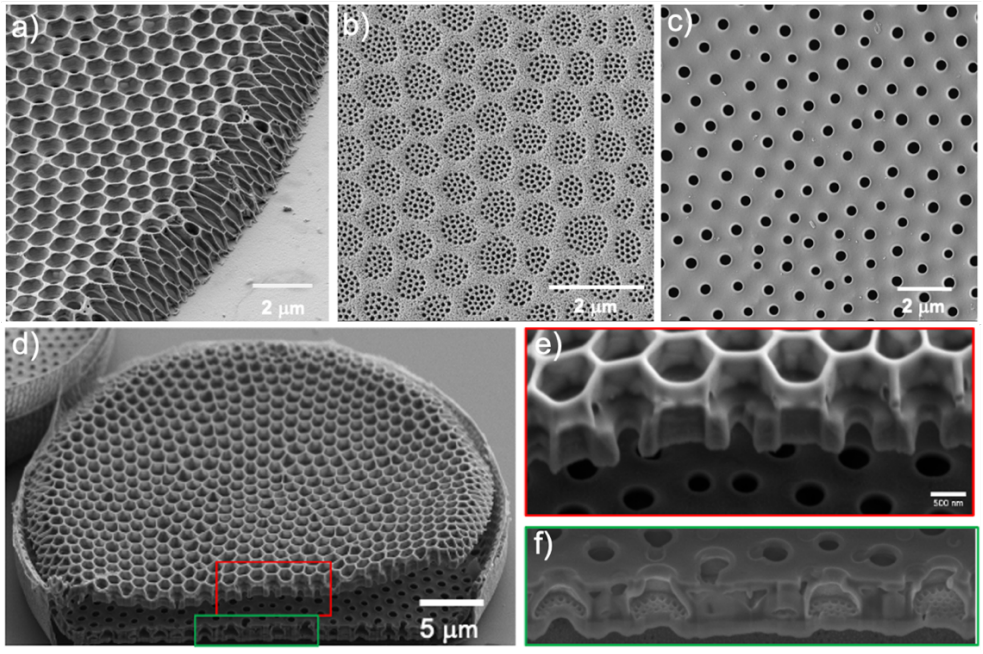

Figure 69. SEM images of C. oculus-iridis. Top view of: a), b) upper layers, c) inner layer. Cross sections of: d) the whole frustule, e) upper layer, f) inner layer.

The 3D numerical model for optical simulations and the corresponding pattern of the dielectric permittivity in each elementary layer is shown in Figure 70.

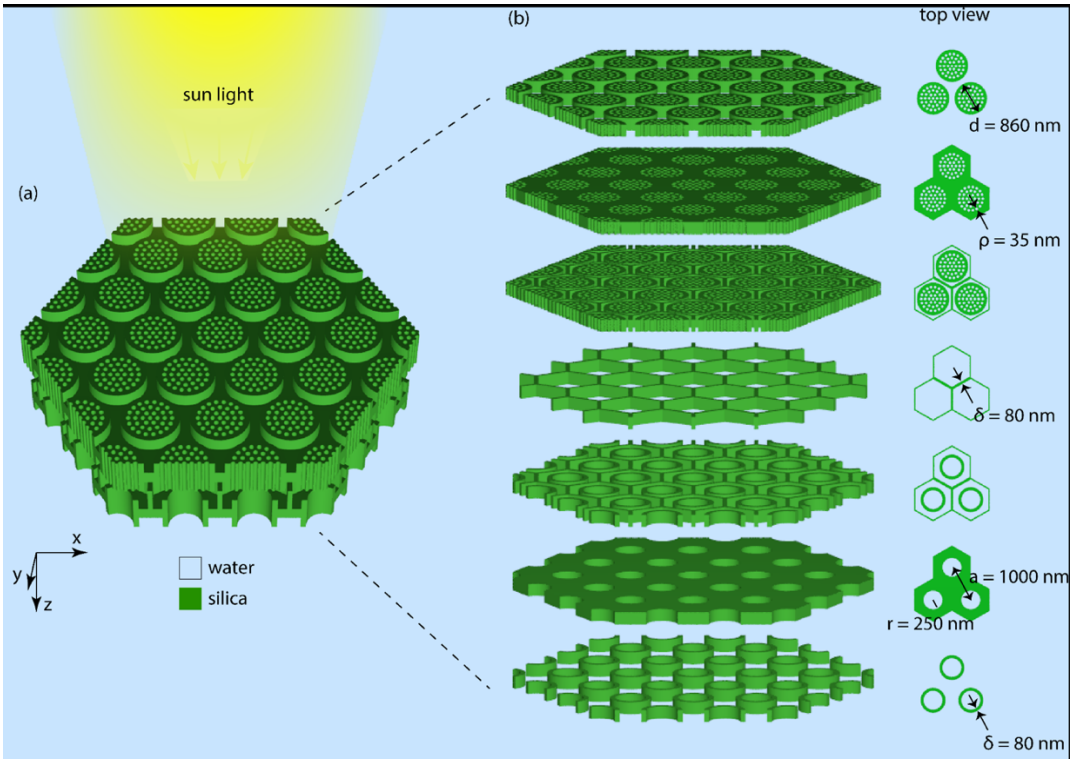

Figure 70. The schematic of a 3D model of diatom frustule including structural parameters used for calculations. Blue: water ($n = 1.33$), green: silica ($n = 1.45 \pm 0.03i$)

7.3 Reflection and transmission

The numerical calculations of reflection and transmission of diatoms were obtained using the formalism of Fourier modal method. The structure is subjected to an incident plane wave, allowing for the expansion of the plane wave into Fourier harmonics. To achieve an optimal trade-off between computational efficiency and accuracy, the Fourier series employed in this chapter is truncated at 97 harmonics (see Appendix D for convergency check). The reflection and transmission in the main channels correspond to the coefficient of the linear combination of $e^{i(k_x x + k_y y + k_z z)}$ at the main harmonic (where k is wave vector). Summing the coefficients of linear

combinations of $e^{i(k_x x+k_y y+k_z z)}$, without the main harmonic, facilitates the calculation of transmission and reflection spectra for all diffraction channels. The results obtained for the main, diffraction and all channels are shown in Figure 71 (incidence from top) and Figure 72 (incidence from bottom).

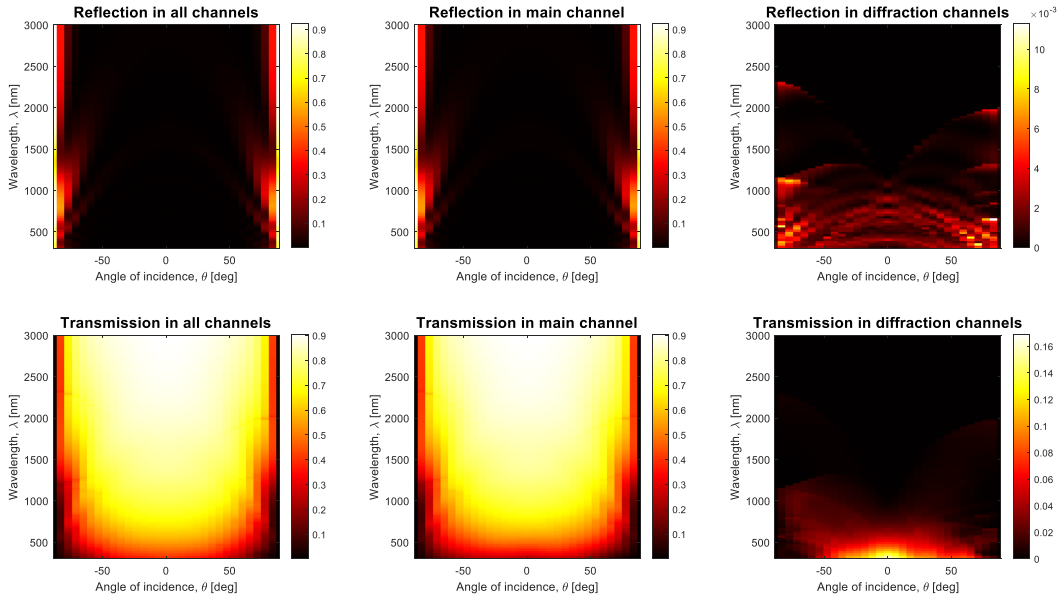

Figure 71. Reflection (upper row) and transmission (bottom row) of diatoms in main, diffraction and all channels. Incidence from the top.

The appearance of peaks in the reflection spectra within the diffraction channel is a result of diffraction on the periodic structure of the frustule. Specifically, in the main channel, reflection is primarily observable at angles near the normal incidence and absent at other angles, which aligns with the small contrast between the refractive indices of the medium (water) and the frustule material (silica). In the case of short wavelengths (400-500 nm), the transmittance within the diffraction channel remains above zero for all incident angles. However, as the wavelength increases, the

transmittance progressively diminishes and eventually reaches zero. This behavior holds true for all incidence angles.

The intensity of reflection displays variation when comparing incident plane wave from the bottom and top, while transmission remains unchanged when the incident plane wave is from the bottom (Figure 72).

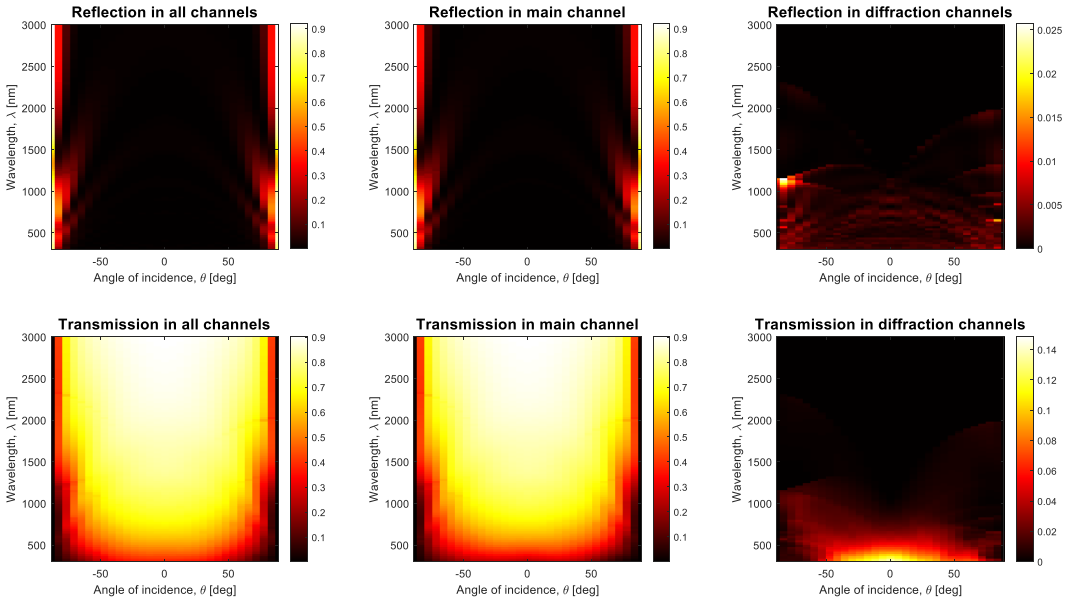

Figure 72. Reflection (upper row) and transmission (bottom row) of diatoms in main, diffraction and all channels. Incidence from the bottom.

For calculations of transmission spectra, the small absorption of the silica shell is taken into account. Water absorption is not taken into account, since it is very small for these wavelengths. The scattering, which occurs due to imperfections and non-periodicity, cannot be accounted for while using the Fourier modal method. The transmission spectra of a non-periodic structure and the diatom frustule in the main, diffraction and all channels in the case of a normal incidence is shown in Figure 73.

The term "non-periodic structure" refers to a silica structure without pores, possessing equivalent thickness to that of the diatom frustule.

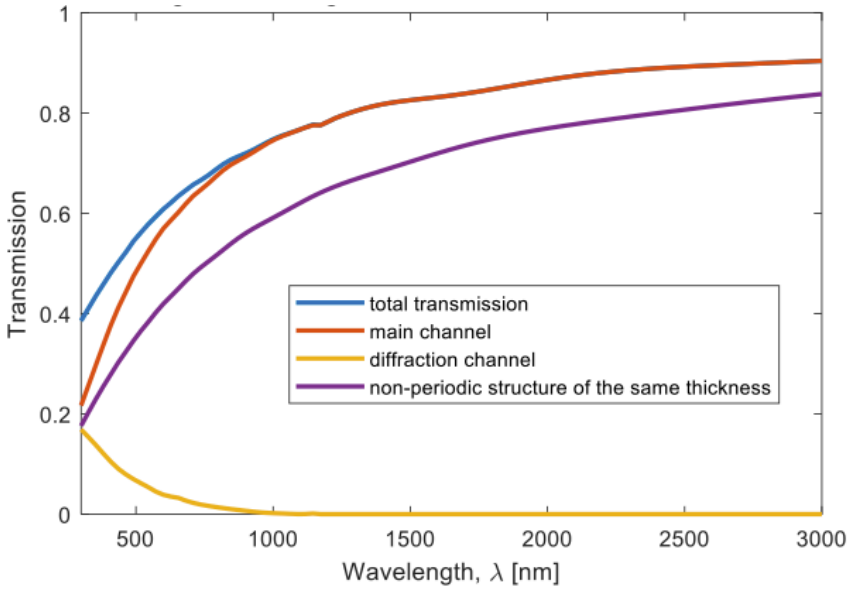

Figure 73. The transmission spectra of diatoms and non-periodic structure of the same thickness.

Due to diffraction, the periodic structure of the diatom frustule enhances the transmittance of light in the region λ = 400–500 nm by approximately 1.5–2 times when compared to a homogeneous layer of the same silica material. This layer has the same thickness as the diatom frustule but lacks its periodic porous structure. If we were to consider ourselves as diatoms, what would be more advantageous in terms of utilizing light: having a porous shell with a periodic perforated structure or a non-periodic hard shell? The non-periodic structure permits less light transmission, whereas the perforated shells enable more light to pass through, particularly in wavelength regions where chlorophyll *a* demonstrates absorption peaks (Figure 74a). The absorption of water is minimal just in the region of wavelengths 400-500 nm. Optically speaking, it

is favorable for a diatom to possess a perforated shell. Besides chlorophyll *a*, the absorption spectra of living diatoms demonstrate peaks attributable to chlorophyll *c* and carotenoid fucoxanthin[63]. On the other hand, the spectra of cleaned frustules show no peaks, as expected, since the organic content was removed during acid treatment (Figure 74b).

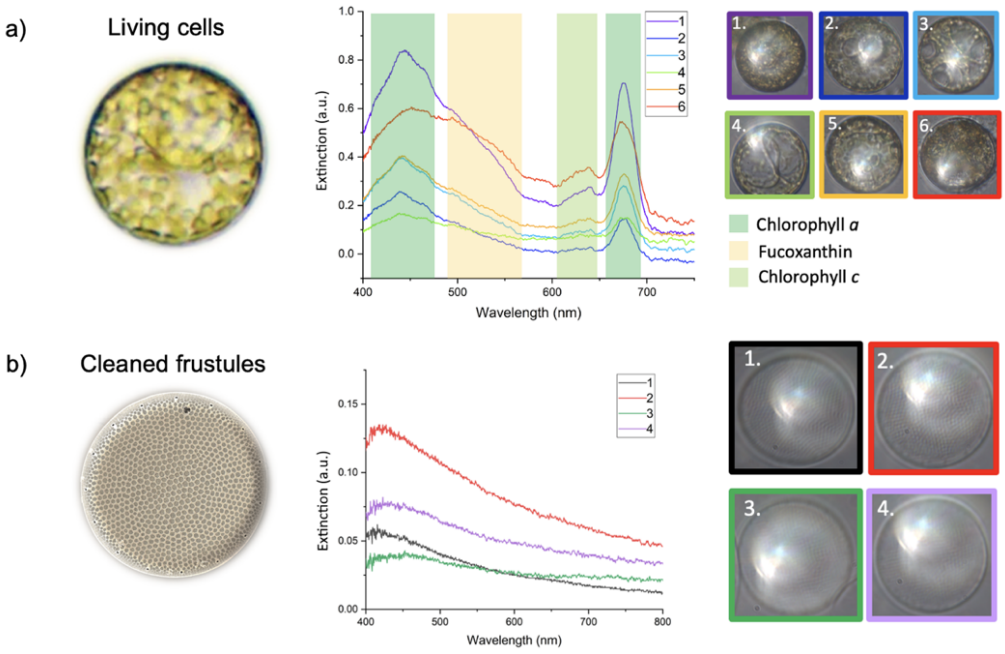

Figure 74. Absorption spectra of: a) individual living diatoms, b) individual cleaned frustules with corresponding images showing where the spectra were collected.

7.3.1. The solar spectra at different depths in water

When investigating the light intensity distribution inside diatom frustules, it is necessary to choose the appropriate wavelength of incident light. By comprehending the solar spectra at the depths where diatoms are commonly located in water, and choosing the suitable incident light wavelength, a meaningful context for studying the light intensity distribution inside diatom frustules can be established. The solar spectra at different depths in water (D65 illuminant) as well as modelled color of water as a

function of depth are shown in Figure 75 (Color matching functions: CIE 1931; normalization: overlap integral of solar spectrum at sea level with Y-function equals to 1.)

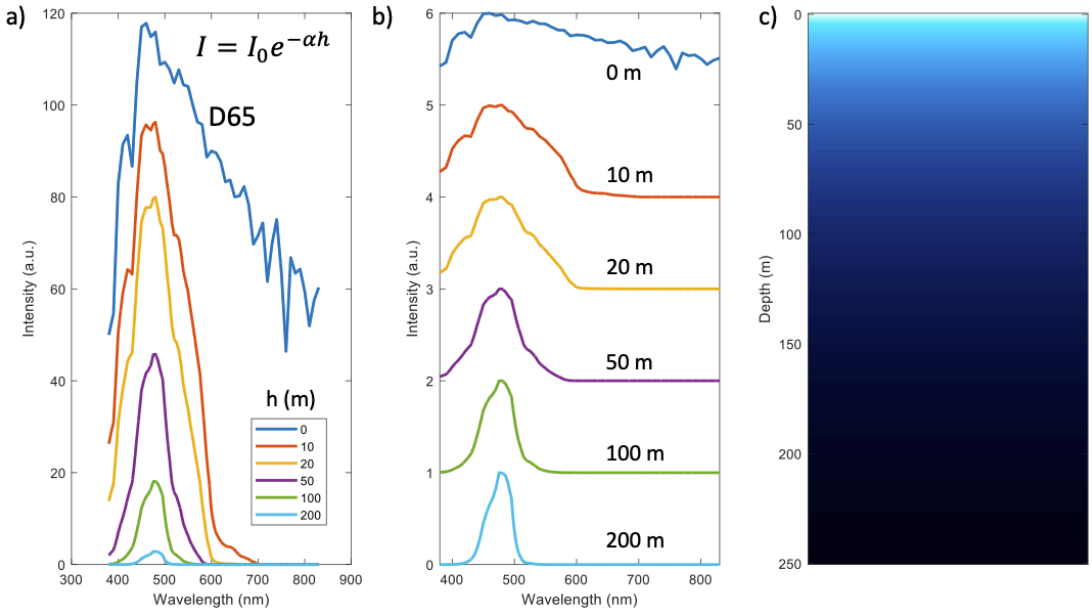

Figure 75. a) Solar spectra and b) normalized solar spectra at different depths in water, c) modelled color of water as a function of depth.

As sunlight penetrates into water, its spectral composition changes due to absorption and scattering properties of water (Figure 75a-c). The primary factors that influence the spectral composition of light in water are water depth and water clarity. The solar angle also affects the spectral composition of light in water through its impact on scattering and absorption processes[248]. As the solar angle increases, shorter wavelengths are attenuated to a greater extent, causing a shift towards longer wavelengths. The rate of absorption of different wavelengths of light in water varies with depth, leading to distinct changes in the solar spectrum at different depths. In some

cases, like algae blooms, the surface water can appear green due to chlorophyll, while in other cases, it can have a brownish or yellowish hue due to the presence of dissolved organic matter. At shallow depths up to 1 meter, the visible spectrum of sunlight dominates, with red and yellow wavelengths being absorbed more rapidly than green and blue. At depths greater than 3 meters, there is a significant drop in the amount of visible light, and the spectrum contains mostly blue and ultraviolet light. The water appears very dark blue or black in the deepest parts of the ocean, where sunlight is absent (Figure 75c). The availability of different wavelengths of light affects the photosynthesis rates of primary producers, the visual perception and behavior of predators and prey, and the distribution and abundance of different species in the water column.

Diatoms, since they are predominantly autotrophs, need enough light, so they inhabit the so-called euphotic zone in water bodies, which extends from the surface to the depth of the compensation point (where photosynthesis exceeds respiration). Usually, this depth corresponds to about 1% of the solar radiation coming to the surface of the water. In practice, the euphotic zone extends for several tens of meters, up to 150–200 m. *Coscinodiscus oculus-iridis* used here as a model, represents a marine species obtained from samples from the Tsushima Strait (Sea of Japan). Since this is a planktonic species, it soars in the water column and lives at depths of up to several tens of meters.

7.4 Light intensity distribution

7.4.1 Light intensity at specific incident angles

The first results of light intensity simulation at λ=420 nm (θ=0°, φ=0°) are shown in Figure 76. Figure 76 shows the interference pattern within vertical and horizontal cross-sections of the diatom. The obtained interference pattern looks very similar to Talbot interference pattern[249]. The resulting Talbot interference pattern can be visualized as a series of repeating frustule patterns with varying intensity, where the bright regions correspond to constructive interference and the dark regions to destructive interference. This interference phenomenon can be explained by the periodicity and symmetry of the frustule structure.

While the Talbot effect is a well-known phenomenon in the near-field optics of diffraction gratings[250], it is frequently omitted or not thoroughly examined in diatom-related studies, except for mentions by De Stefano et al.[73] and Ghobara et al. [251] In their study[251], Ghobara et al. demonstrated that pennate frustules of *Gomphonema parvulum* exhibit effective light modulation due to their unique ultrastructure. The modulation is highly influenced by light wavelength and refractive index. These observations suggest that certain optical phenomena are correlated with the presence of integrated optical components, such as guided-mode resonance and the Talbot effect linked to the grid-like structure. Meanwhile, other phenomena are more closely associated with the size parameter rather than the specific optical component, such as the generation of photonic jets.

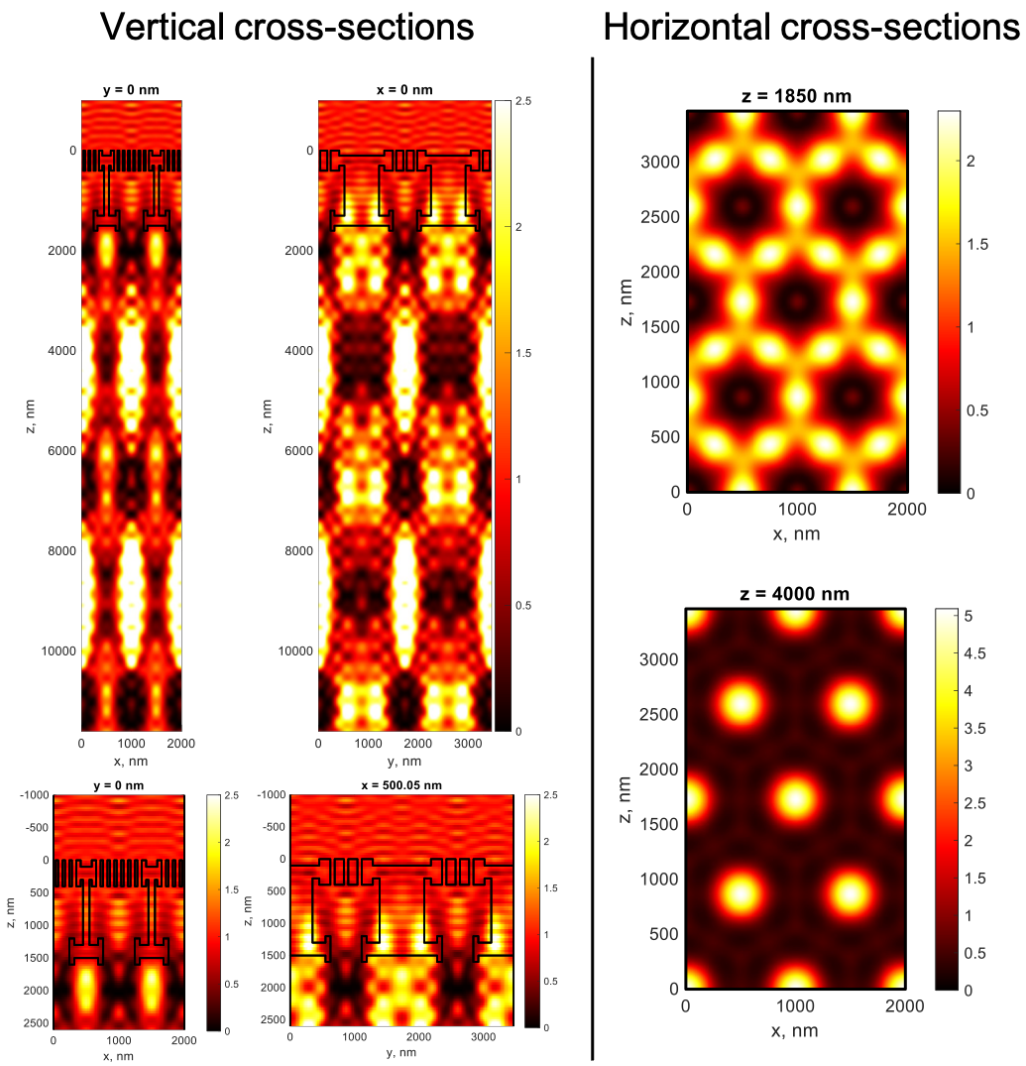

Figure 76. Light intensity simulation at λ=420 nm, θ=0°, φ=0° on the surface of the frustule.

Light intensity at λ=420 nm, θ=45°, φ=0° is shown in Figure 77.

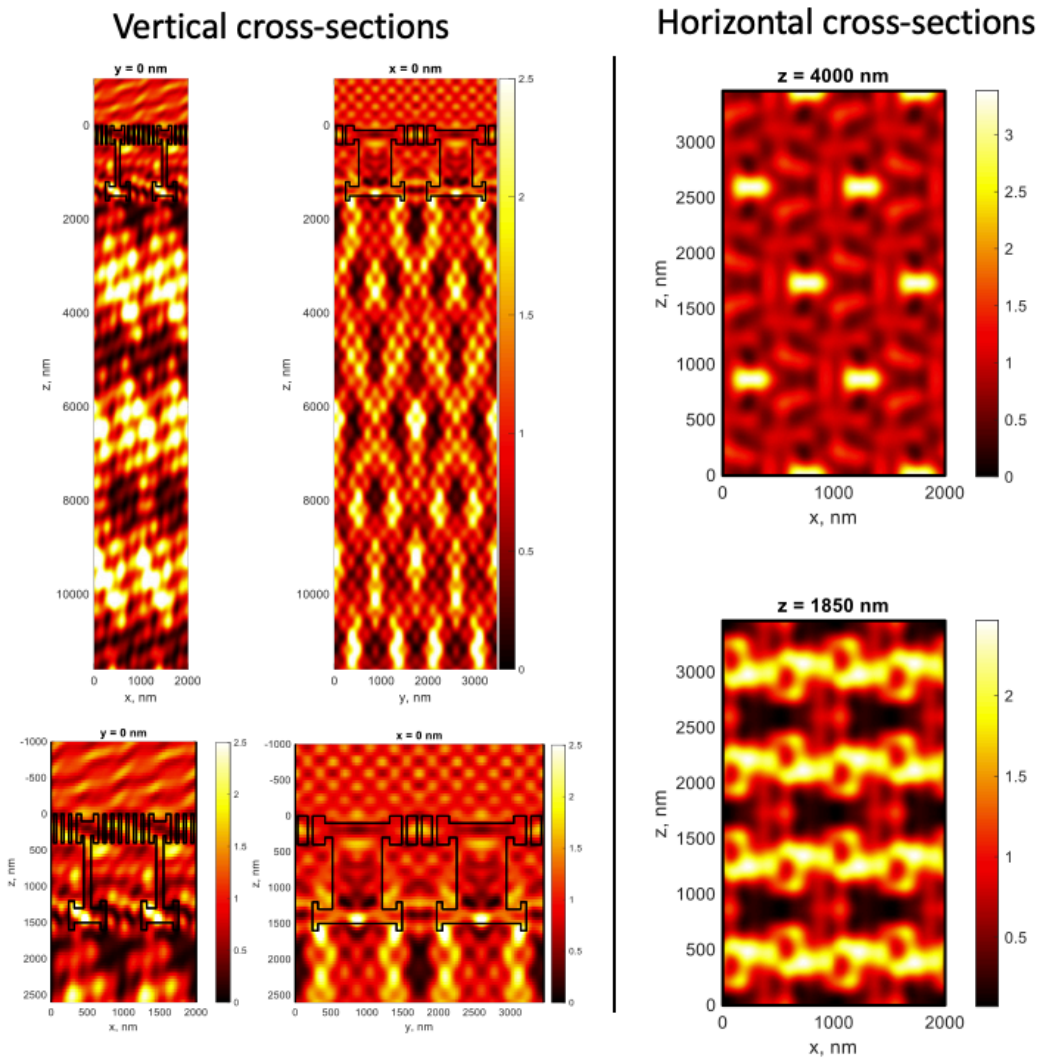

Figure 77. Light intensity simulation at λ=420 nm, θ=45°, φ=0° on the surface of the frustule.

7.4.2 Light intensity integrated over all incident angles and all polarizations

To comprehensively assess whether a perforated frustule offers advantages in terms of light absorption by chloroplasts, it is insufficient to solely consider the light intensity at incident angles of θ=90° or θ=45°. The distribution of light intensity at all angles and with all polarizations needs to be examined and be averaged across these conditions. The light intensity is normalized to the intensity of a plane wave

propagating in water. Here two different model structures were considered: structure 1 “with cavity” – the whole frustule, and structure 2 “without cavity” – only one valve (Figure 78).

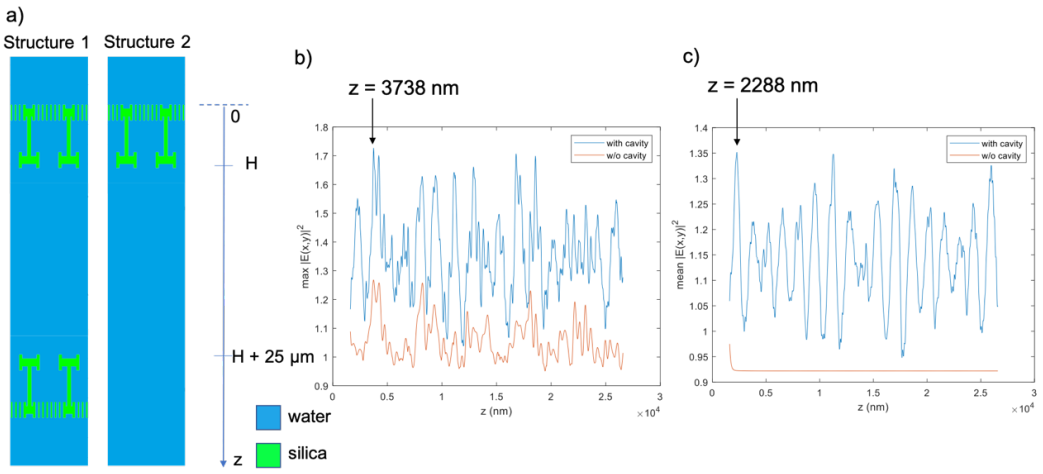

Figure 78. a) Vertical cross-sections of two model structures: 1 (with cavity) and 2 (without cavity). b) Maximal and c) mean light intensity over a horizontal cross-section with coordinate z for both structures (with and without cavity).

The graph in Figure 78b,c represents the maximal and mean light intensities over horizontal cross-sections depending on the z coordinate. Both maximal and mean light intensities are higher in the case of a structure with cavity, due to the reflection of light and occurrence of Fabry Perot resonances. At bright points, for a structure with two valves, the maximum light intensity is 1.7, and for a structure with one half, the maximum is 1.25 (Figure 78). For a structure without cavity, the mean light intensity is slightly less than 1 because there is reflection and the exponential decay of light intensity indicates that the structure is a weak waveguide. The presence of a cavity

along the plane leads to a 1.35-fold increase in the integrated light intensity compared to the case without such a structure.

Figure 79 shows the cross-section of light intensity distribution at the coordinates z=2288 nm z=3738 nm, which correspond to the point where the mean and maximal light intensities are 1.7 and 1.35 times larger for the structure with cavity, respectively. The light intensity in the case of a structure with a cavity integrated over the plane is 1.35 times larger than that of the incident light, and in the case of a structure without a cavity it is slightly less than 1.

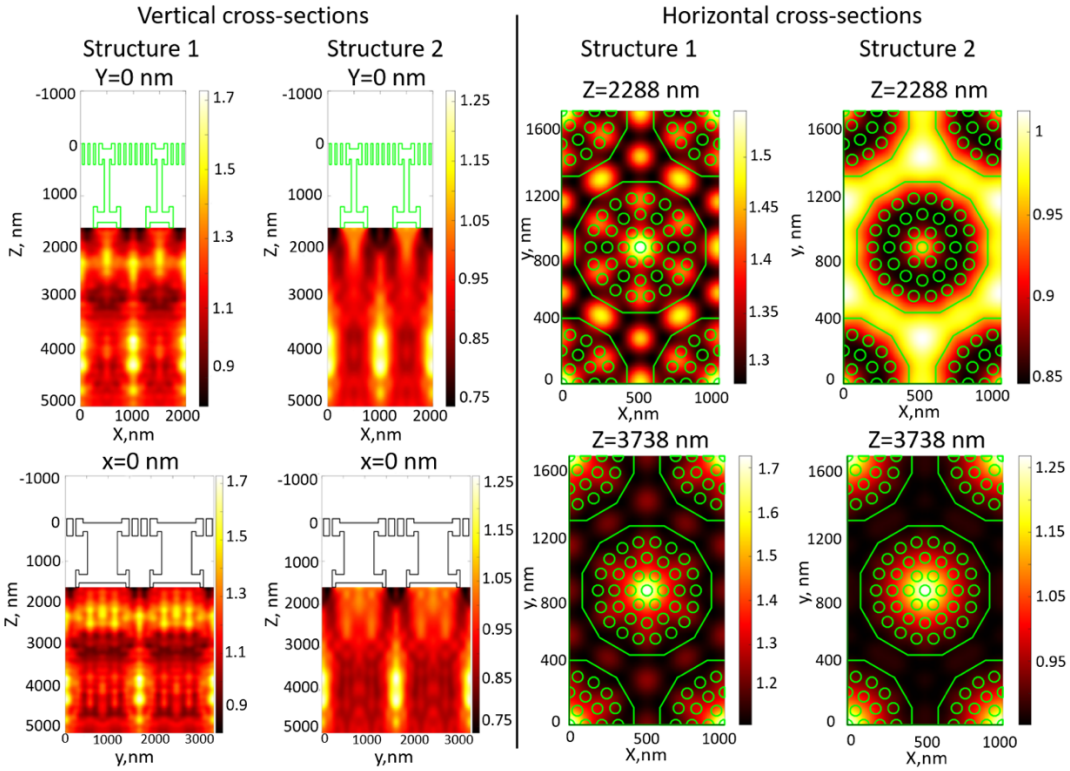

Figure 79. Left: Vertical cross-sections of light intensity distribution for structure 1 (with cavity) and structure 2 (without cavity). Right: Horizontal cross-sections of light intensity distribution at the coordinates z=2288 nm and nm z=3738 nm for structure 1 (with cavity) and structure 2 (without cavity).

The green lines in Figure 79 (right) represent contours of the structure and are superimposed with horizontal cross-sections of light intensity distribution for visual evaluation. In essence, the periodic porous silica structure controls the diffraction of light such that the light intensity increases under the holes where the chloroplasts are located, as demonstrated in Figure 80. FLIM data displayed here as color-coded intensity images, where the color of each pixel corresponds to the fluorescence decay rate, reveal details about the distribution of chloroplasts inside diatom frustules, such as their overall density and spatial variability. A higher fluorescence decay rate corresponds to a shorter fluorescence lifetime represented by orange-red color in Figure 80. It means that the chloroplasts located along the periphery of the frustule exhibit faster decay kinetics, leading to a more rapid decrease in fluorescence intensity over time. This phenomenon can be attributed to a range of factors, encompassing interactions with molecular environments, energy transfer processes, or quenching mechanisms, as detailed in section 5.4. However, it necessitates additional investigation and a more extensive dataset for conclusive understanding.

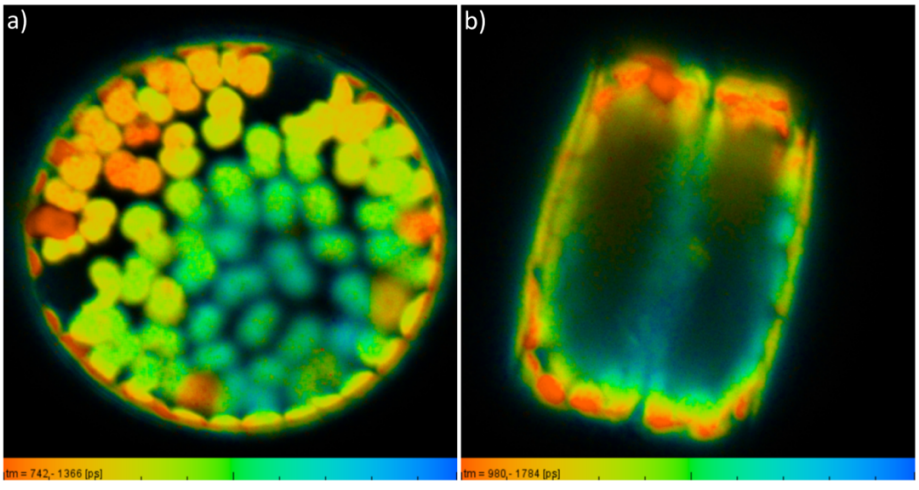

Figure 80. FLIM images of *C. oculus-iridis* showing distribution of chloroplasts in the frustule: a) top view, b) side view.

7.4.3 Light intensity depending on the distance between two valves and polarization

In the previous section 7.4.3, the light intensity was calculated for a fixed distance between two valves, equal to 25 μm, and averaged over all incidence angles and polarizations. S- and P-polarizations were also analyzed separately by taking into account different distance between valves starting from g=5 μm to g=25 μm with the step of 5 μm (Figure 81, 82, Appendix D).

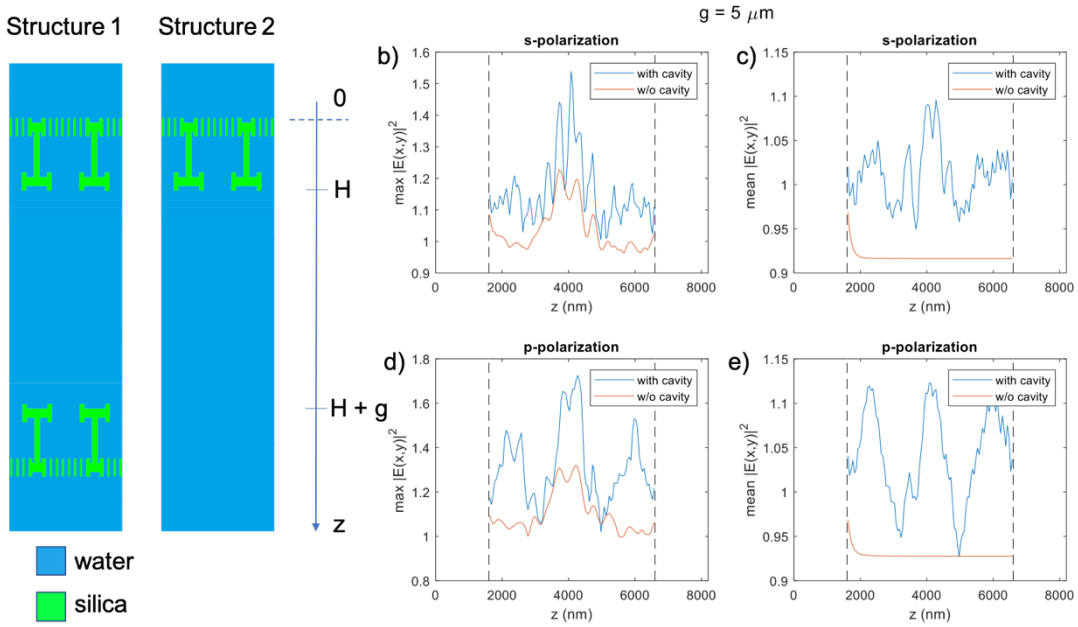

Figure 81. a) Two model structures: 1 - with cavity and 2 - without cavity for distance between valves g=5μm. Maximal light intensity distribution calculated for: b) S- and d) P- polarizations. Mean light intensity distribution calculated for: c) S- and e) P- polarizations.

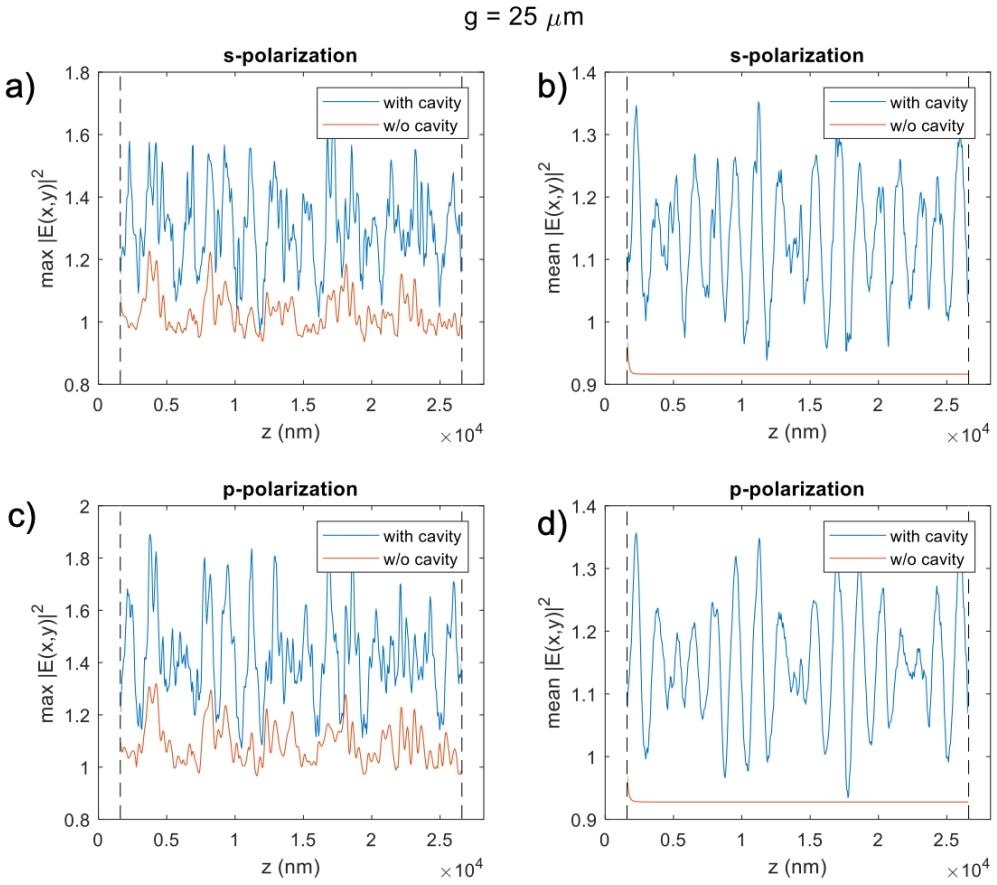

Figure 82. Maximal light intensity distribution calculated for two model structures for distance between valves g=25μm: a) S- and c) P- polarizations. Mean light intensity distribution calculated for: b) S- and d) P- polarizations.

In a structure with two shells (valves), not only diffraction occurs, but also interference of two modes that propagate along positive and negative z-direction, and therefore, as in any optical cavity structure of this kind, there are points at which the incident light intensity is amplified both locally and on average over z-coordinate. The dielectric permittivity contrast in this particular structure is small, and therefore the light intensity enhancement is small, but it is still present. In a structure with one valve, only diffraction occurs, so although the light intensity can be amplified locally, it is

constant on average along the z-coordinate, with the exception of the region near the shell, where near fields associated with the shell itself make a contribution. The similarities in the dependence of maximal light intensity on the z-coordinate for a specific distance between upper and lower valve, regardless of S- or P-polarization, indicates that polarization might not play a conclusive role in the enhancement of light intensity. In contrast, when comparing frustules of different height, significant deviations arise in the dependency of the maximal light intensities on the z-coordinate between S- and P-polarizations. These variations imply that the distributions of light intensities are influenced differently at varying heights within the frustule structure. The observed discrepancies, thus, highlight the importance of sample height as one of determining factors in shaping the light intensity distributions for different polarization states.

7.4.4 Chloroplast migration in diatom frustules: responses to varied light intensity conditions

While the standard situation, as depicted in Figure 80, illustrates a typical configuration of chloroplasts inside diatom frustule, it is essential to note that under varying light intensity conditions, chloroplasts have been observed to exhibit dynamic migration. When exposed to low-intensity light, diatom chloroplasts move to the cell periphery to capture incoming light, while under high-intensity light they move towards the cell center to reduce the amount of light absorbed and maintain photosynthesis efficiency[252,253]. The chloroplast migration in diatom algae is mediated by actin filaments, which form a cytoskeletal network inside the cells[254]. Actin filaments extend from the cell periphery towards the chloroplasts, binding to them and pulling them

towards their desired location in the cell. During this process, the actin filaments and other associated proteins form a dynamic and flexible structure that allows for the movement and positioning of the chloroplasts.

The process of chloroplast migration in diatom algae occurs relatively rapidly [254], with chloroplasts changing their location within a few minutes of changes in light condition. Chloroplasts are also able to orient themselves within the cytoskeleton in a way that maximizes their exposure to light and minimizes the amount of shading from other chloroplasts. By optimizing their chloroplast positioning, diatoms can regulate their photosynthetic efficiency and minimize photodamage from excess light exposure. This can be especially important in environments with variable light conditions, where diatom algae must be able to quickly adapt to changing levels of irradiance. By delving into the mechanisms governing light distribution within frustules, we gain valuable insights into the optimization of photosynthesis under different light regimes. This understanding is closely linked to chloroplast migration patterns, shedding light on how cells adapt to varying light conditions for optimal photosynthesis. Together, these research avenues contribute to our comprehensive grasp of the intricate relationship between light and photosynthetic organisms. They offer crucial insights into the physical and biological mechanisms employed by these organisms to harness and utilize light energy effectively.

7.5 Summary

This chapter is related to the numerical study of optical properties of *Coscinodiscus oculus-iridis* frustule in water by using Fourier modal method. A periodic structure of diatom frustule due to diffraction increases the transmittance of light in the region λ = 400–500 nm as well as light intensity compared to a silica

homogenous layer. Interestingly, this is the same range where chlorophyll *a*, a pigment involved in photosynthesis, absorbs light most effectively. Simultaneously, water exhibits minimal absorption within this specific range of wavelengths. The simulation results reveal a distinct interference pattern of light intensity beneath the diatom frustule under varying incident light polarization and sample heights. The interference patterns facilitate the spatial concentration of light within the frustule, leading to a more effective utilization of light by the chloroplasts situated beneath the cell wall. Therefore, this structural feature of diatom frustules appears to be optimized for maximizing the interaction of light with chloroplasts, potentially enhancing photosynthetic efficiency.

The analysis of light intensity distribution across various structures indicates that the inclusion of a cavity-containing structure (frustule with two valves) enhances both the maximum and mean light intensities. In comparison to scenarios lacking such a structure, the maximal and mean light intensities surpass the incident field by 1.7 and 1.35 times, respectively. This can be attributed to the reflection of light and the occurrence of Fabry Perot resonances. On the other hand, a structure without a cavity exhibits a slightly lower mean light intensity, close to 1, due to reflection and the exponential decay indicating its weak waveguide characteristics. These findings highlight the importance of structural features, such as the presence of a cavity, in modulating the light intensity. Further experimental exploration will shed light on the intricate interplay between the frustule structure and the resultant light intensity distributions. Such insights hold promising potential for advancing our understanding of the optical properties and functionalities of diatom frustules, ultimately fostering the development of novel optical devices and technologies inspired by these micro-scale structures.

Chapter 8. Modification of diatomite

In this chapter a modification of diatomite – a soft, loose, and fine-grained siliceous sedimentary rock composed of the remains of fossilized diatoms – by gold nanoparticles using layer-by-layer technology in combination with a freezing-induced loading approach is demonstrated. The obtained composite structures are characterized by dynamic light scattering, extinction spectroscopy, SEM and TEM, photoacoustic imaging technique, and tested as a platform for surface-enhanced Raman scattering (SERS) using Rhodamine 6G. The results presented here are published in article **Cvjetinovic J**, Merdalimova A, Kirsanova M, Somov P, Salimon A, Korsunsky A, Gorin D. SERS Platform Based on Diatomite Modified by Gold Nanoparticles Using a Combination of Layer-by-Layer Assembly and Freezing-Induced Loading Method. *Physical Chemistry Chemical Physics*. 2022; 24: 8901-8912. [94] The author prepared the samples, measured extinction spectra and zeta potential, performed photoacoustic visualization. SEM and TEM measurements were performed in Advanced Imaging Core Facility at Skolkovo Institute of Science and Technology. SERS measurements were conducted with the help of Anastasiia Merdalimova. As per the guidelines provided by RSC Publishing, no permission is needed for the reproduction of the entire article in this thesis, considering I am the author.

8.1 Gold nanoparticle characterization

Gold nanoparticles (AuNPs) can be synthesized using different approaches depending on the desired size, shape, and surface functionality.[255] Owing to the unique features of gold nanospheres[256], such as size- and shape-related optoelectronic properties (surface plasmon resonance), good biocompatibility, low toxicity, large surface-to-volume ratio, they have been exploited for a wide range of applications in

bionanotechnology, diagnostics, imaging, etc.[255,257] The surface plasmon resonance occurs when the frequency of an impinging electromagnetic field equals the frequency of self-oscillations of electron plasma in a nanoparticle.[258]AuNPs have also been widely used as photoacoustic contrast agents in recent years.[259] Given the abovementioned facts, in this study, AuNPs were utilized to modify the diatomite surface, aiming to achieve excellent photoacoustic and enhanced SERS signals.

According to bright-field TEM (BF-TEM) image in Figure 83a, the spherical gold nanoparticle sizes follow a normal distribution with an average diameter of 19 ± 5 nm (Figure 83b). The obtained gold nanoparticles have an absorption peak at 524 nm, as shown in Figure 83c. The absorption band results from the collective oscillation of the conduction electrons due to the resonant excitation by the incident photons.[260]

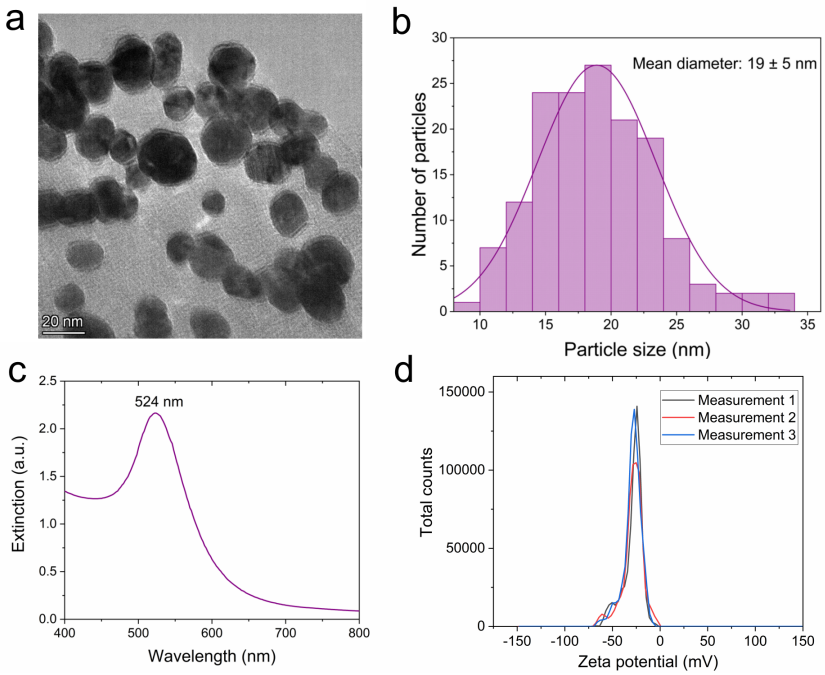

Figure 83. a) Typical BF-TEM image of gold nanoparticles (scale bar, 20 nm), b) Size distribution histogram of synthesized gold nanoparticles, c) Extinction spectrum of AuNPs, d) Zeta potential distribution of AuNPs.

Zeta potential measurements showed that the nanoparticles have an average surface charge of -29.3 ± 0.9 mV, indicating that their stability is on the borderline between incipient instability and moderate stability [261].

8.2 Characterization of gold-coated diatomite

For the deposition of gold nanoparticles onto the surface of diatomite, the LbL technique was applied for the first time in combination with freezing-induced loading. PAH, as one of the most popular positively charged polyelectrolytes, according to the scheme shown in Figure 84a covers the negatively charged surface of the diatomite and subsequently attracts the negatively charged gold nanoparticles. The LbL+FIL process can be repeated several times, which makes it possible to obtain a high efficiency of nanoparticle deposition. Here, the process has been applied up to five times, which resulted in hybrid materials based on diatomite with different coverage by gold nanoparticles. Figure 84b shows the measured extinction spectra of bare AuNPs and gold-coated diatomite hybrid materials consisting of different number of layers. The amplitude of the absorption peak corresponding to gold increases with the rising number of deposition cycles up to three. Subsequently, a decrease was observed, which may be attributed to two processes. First, with each layer deposition, the weakly adsorbed polyelectrolytes and nanoparticles had to be removed by rinsing with deionized water at least three times, resulting in the loss of a certain amount of nanoparticles. Second, according to spectrum of gold-coated diatomite composites consisting of five PAH/AuNPs bilayers, the band at ca. 525 nm practically disappears. The long tail observed in the region 560-700 nm indicates the presence of aggregates.

Thus, the number of small nanoparticles which absorb well at ca. 525 nm decreases, while the number of larger aggregates of various shapes increases.

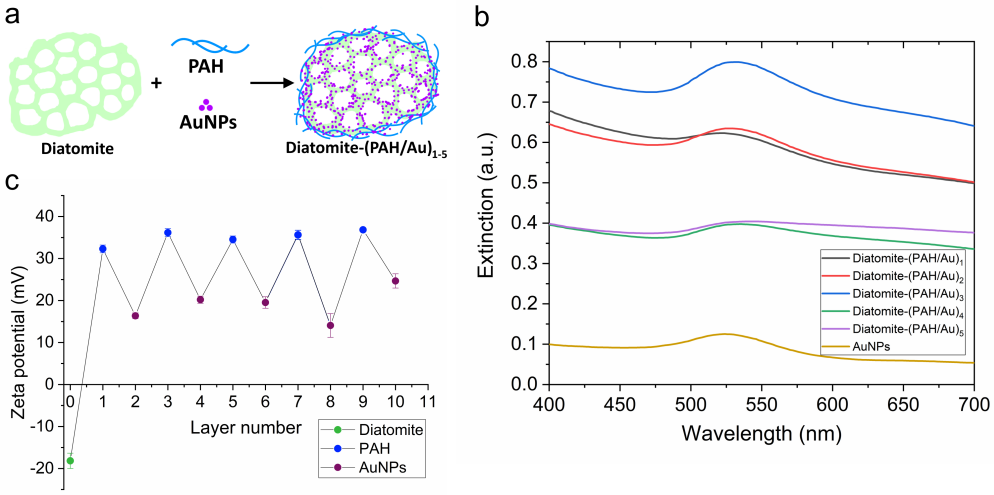

Figure 84. a) A schematic representation of layer-by-layer approach, b) Extinction spectra of AuNPs and diatomite decorated with different number of PAH/AuNPs bilayers, c) Zeta potential depending on the layer number.

Figure 84c shows the change of zeta potential after depositing polyelectrolyte and AuNPs depending on the layer number. Even though the AuNPs are negatively charged, no surface charge change was observed upon deposition on PAH-coated diatomite. This suggests that AuNPs didn't completely cover the surface of diatomite as polyelectrolyte.

8.3 SEM study of degree of coverage of diatomite surface by gold

SEM images of diatomite decorated with one, three, and five PAH/AuNPs bilayers are shown in Figure 85. The difference in the level of coverage of the diatomite surface by AuNPs is clearly evident. One PAH/AuNPs bilayer leads to insufficient

coverage, which significantly increases as the number of bilayers increases. Nanoparticles are in some places located more at the edges, along the rim, but they can also be observed around the pores. SEM images illustrate that the diatomite surface is not entirely covered with AuNPs, explaining the obtained zeta potential distribution. Usually, nanoparticles at low concentrations are homogenously adsorbed on the substrates, but at higher concentrations, they tend to form clusters. Some nanoparticles get deposited in the proximity of other particles because, at high concentrations, all the favored sites at the polyelectrolyte surface become immediately occupied.[262,263] Generally, the deposition of a polycation on a surface previously treated and partially covered with negatively charged nanoparticles will occur predominantly on the nanoparticles' surface.[262,264] Subsequently, in the case of multilayer gold deposition, further anionic AuNPs also bind to locations of previously deposited AuNPs, and therefore, clusters are formed.

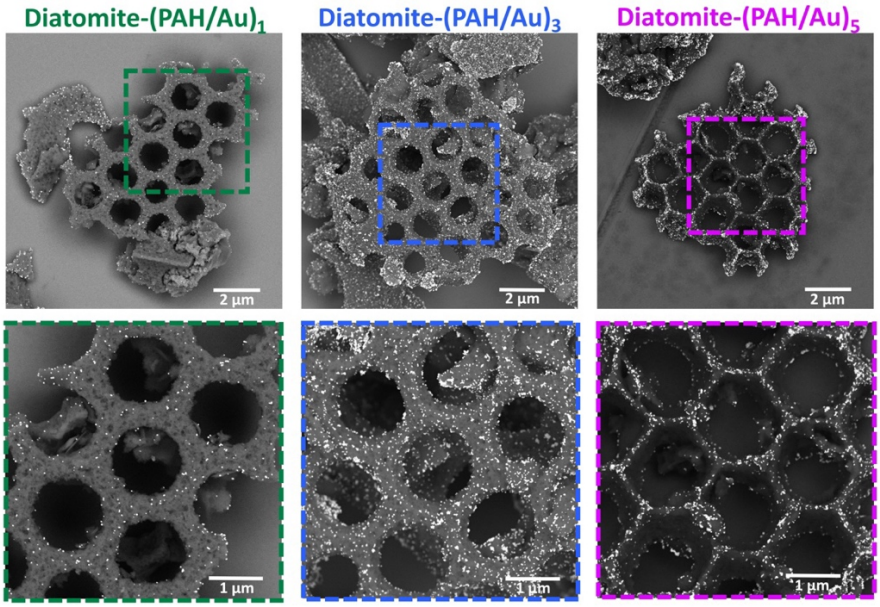

Figure 85. SEM images of gold-coated diatomite consisting of one (left), three (middle), and five (right) PAH/AuNPs bilayers.

8.4 TEM and STEM-EDX study

Overview HAADF-STEM and BF-TEM images of a sample consisting of three PAH/AuNPs bilayers (Diatomite-(PAH/Au)$_3$) are shown in Figure 86a-d. In the HAADF-STEM images, the contrast is proportional to squared atomic number, and heavy gold nanoparticles appear as bright spots, while in the BF-TEM the color scheme is different and AuNPs look dark. The diatomite is covered with a dense layer of AuNPs which tend to form clusters, especially along the edges. STEM-EDX maps and spectra confirmed the presence of AuNPs on the surface of diatomite, composed of silica (Figure 86e,f).

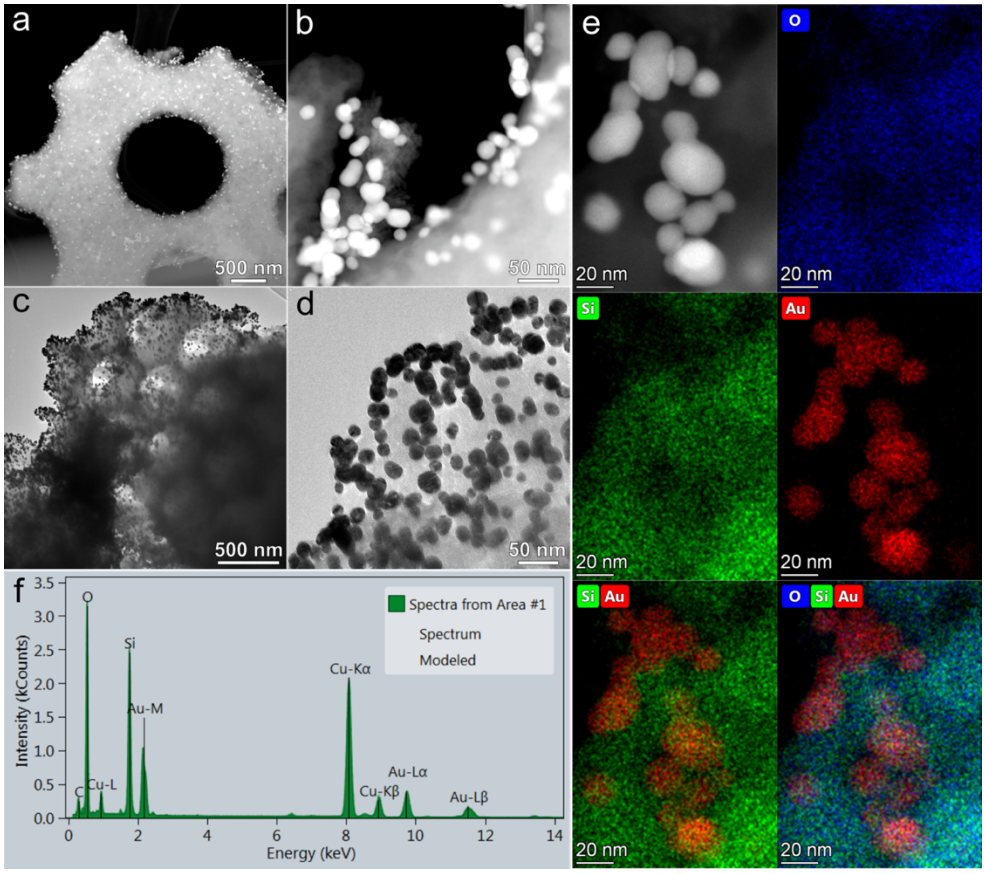

Figure 86. Diatomite-(PAH/Au)$_3$: a, b) HAADF-STEM image, c, d) TEM images, e) HAADF-STEM image, corresponding elemental EDX maps and f) EDX spectrum.

The dominant peaks in the EDX spectrum arise from oxygen, silicon and gold, as expected. The C and Cu signals are attributed to the supporting TEM grid, though the carbon can be present also due to residual organics in the diatomite powder. The presence of Fe can be explained by the nature of diatomite which is composed of 2.5 wt. % iron oxide; as well, Fe-K can be interpreted as an escape peak of intensive Cu-Kα line.

8.5 Analysis of degree of diatomite functionalization by gold nanoparticles using photoacoustic imaging

The generated photoacoustic pressure waves are linearly dependent on the absorption coefficient[265], which is proportional to the concentration of gold nanoparticles. Therefore, this method can be utilized as an *in situ* technique to characterize the degree of modification of diatom biosilica surfaces with AuNPs. The photoacoustic signals from the gold-coated diatomite composites were collected using RSOM technique. RSOM images of all the fabricated samples are shown in Figure 87. A 2-fold dilution was performed here to demonstrate the dependence of the signal intensity on the concentration of such hybrid materials. The number of applied PAH/AuNPS bilayers increases from the left to the right side. The images show the signal over the entire frequency range from 11 to 99 MHz. A low-frequency signal in the 11-33 MHz range, emitted by larger particles is shown with red color, while the green-colored high-frequency signal (33-99 MHz) corresponds to smaller objects. The signal decreases with the decrease in concentration, as expected. The red-colored signal is usually higher indicating the aggregation of gold nanoparticles, especially at higher concentrations. On the other hand, the high frequency signal is higher in the case of smaller number of layers and lower concentrations.

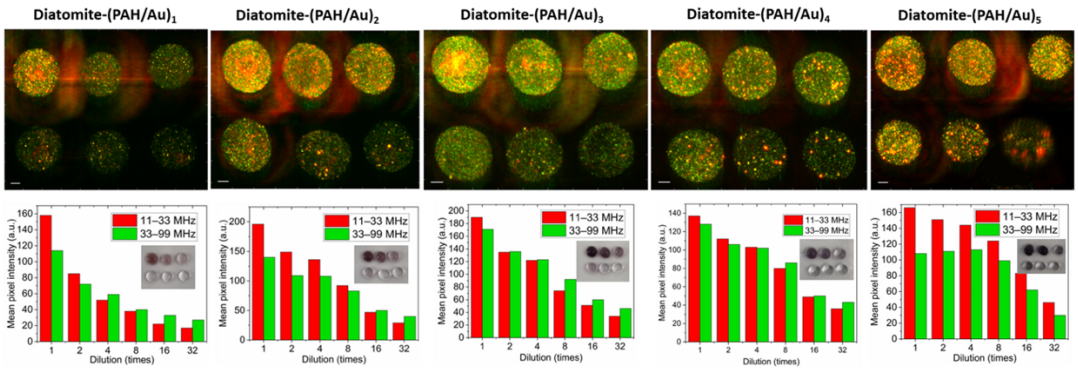

Figure 87. RSOM images of 2-fold diluted diatomite coated with different number of PAH/AuNPs bilayers (up) and the corresponding mean pixel intensity depending on the dilution (down).

Figures 88a-c illustrate the RSOM signal from the bare AuNPs and stock suspensions of diatomite covered with different number of PAH/AuNPS bilayers in the frequency range 11-99 MHz, 11-33 MHz and 33-99 MHz, respectively. Upon comparing the collected signals from all samples, it can be concluded that the highest value was obtained from the sample with three bilayers (Figure 88d). Additionally, a comparison was made between the extinction at 532 nm and mean pixel intensities in both frequency channels (Figure 88e), revealing a good correlation between extinction and signal in the frequency range from 33 to 99 MHz. Low frequency signal deviations can be explained by the tendency of particles to accumulate in the center of the droplet and probably insufficient mixing before measurements.

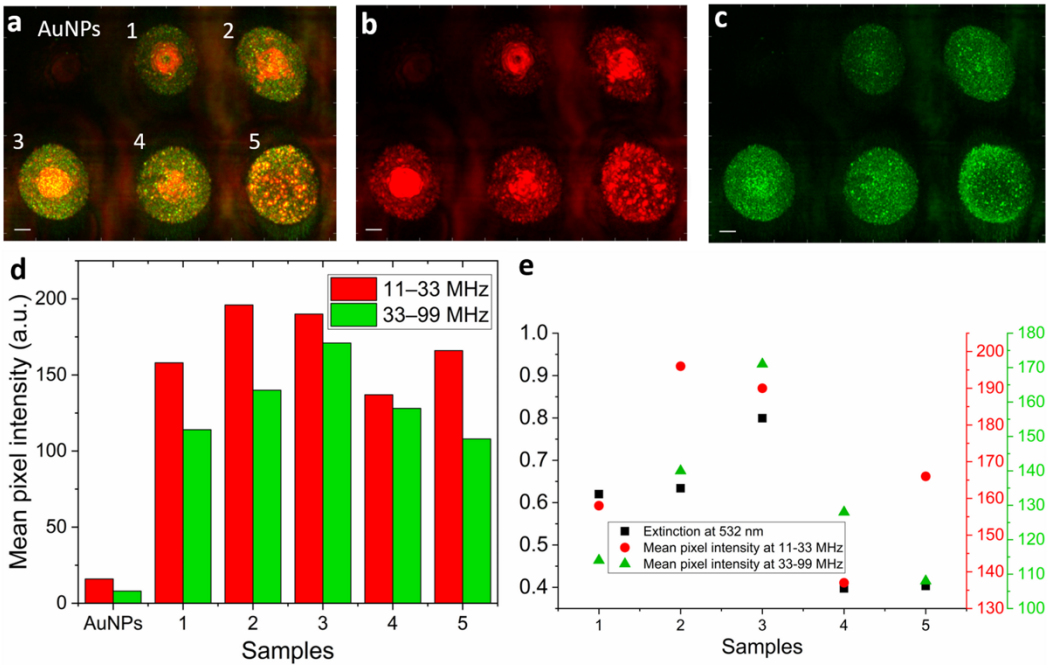

Figure 88. RSOM images of gold nanoparticles and stock suspensions of diatomite coated with different number of PAH/AuNPs bilayers at: a) 11-99 MHz, b) 11-33 MHz, c) 33-99 MHz frequency range, d) Mean pixel intensity depending on the sample, e) comparison of the extinction at 532 nm and mean pixel intensities at 11-33 and 33-99 MHz. 1-Diatomite-$(PAH/Au)_1$, 2-Diatomite-$(PAH/Au)_2$, 3-Diatomite-(PAH/Au)3, 4-Diatomite-$(PAH/Au)_4$, 5-Diatomite-$(PAH/Au)_5$. Scale bar, 200 µm.

The signal from the bare AuNPs is very low when compared to that of AuNPs deposited on the diatomite surface. As already mentioned, the gold-based nanoparticles have been widely used as photoacoustic contrast agents owing to their strong and tunable optical absorption that results from surface plasmon resonance (SPR) effect. When illuminated with a pulsed laser, AuNPs absorb light and generate substantial heat that can sometimes result in their melting. This problem can be solved by silica coating as it lowers the interfacial thermal resistance between gold and the surrounding medium. Moreover, some studies have shown the amplification of photoacoustic

signals and the stability generated by silica-coated gold compared to pure gold caused by a decrease in the thermal resistance of gold to the solvent.[266–268]

8.6 Gold-decorated diatomite as a SERS platform

The potential of diatomite decorated by AuNPs to serve as a SERS platform was tested using Rhodamine 6G as a model analyte. The resulting Raman and SERS spectra of droplets on a glass slide containing bulk Rhodamine 6G, as well as bare diatomite and diatomite coated with one, three and five PAH/AuNPs bilayers incubated with Rhodamine 6G are shown in Figure 89.

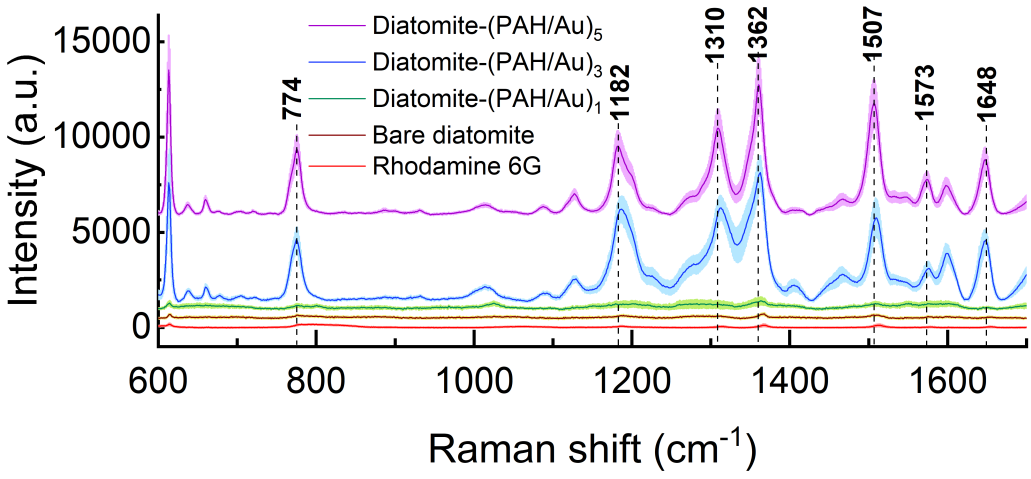

Figure 89. Surface-enhanced Raman spectra of Rhodamine 6G obtained using gold-coated diatomite hybrid materials with a different number of PAH/AuNPs bilayers.

A variety of strong bands corresponding to Rhodamine 6G on the gold-coated diatomite can be identified. Rhodamine 6G provides an intense peak at 613 cm^{-1}, which is assigned to C–C–C ring in-plane bending.[269] The vibrational mode of 660 cm^{-1} band is due to a symmetric deformation localized in the phenyl ring.[270] 774 cm^{-1} corresponds

to the C–H out-of-plane bending vibration, while 1127 and 1182 cm^{-1} are C–H in-plane bending. [269] Peaks at 1310, 1362, 1507, 1573, 1648 cm^{-1} are assigned to the aromatic C–C stretching vibrations. [269]

Figure 89 illustrates strong enhancement of SERS signal from Rhodamine 6G using diatomite coated with three and five PAH/AuNPs bilayers compared with bare analyte. Droplets of Rhodamine 6G with Diatomite-$(PAH/Au)_3$ or Diatomite-$(PAH/Au)_5$ substrates provided approximately 50 times stronger signal from the analyte, calculated at peaks ca. 1362 and 1507 cm^{-1} (Table 9). Insufficient coverage of diatomite with AuNPs in the presence of only one PAH/Au bilayer resulted in a lack of notable enhancement in the signal from Rhodamine 6G.

Table 9. Raman and SERS intensities

R6G			Diatomite-$(PAH/Au)_3$				Diatomite-$(PAH/Au)_5$			
Peak position, cm^{-1}	Mean intensity I_{RS}, a.u.	RSD	Peak position, cm^{-1}	Mean intensity I_{SERS}, a.u.	RSD	$\frac{I_{SERS}}{I_{RS}}$	Peak position, cm^{-1}	Mean intensity I_{SERS}, a.u.	RSD	$\frac{I_{SERS}}{I_{RS}}$
1368	122	41%	1363	7081	11%	58	1362	6426	26%	53
1512	120	44%	1509	4723	22%	39	1507	5523	27%	46

Spectra were collected at a set of points on the surface of the samples, showing a consistent and reproducible scattering pattern without large variability in the intensity in the case of samples coated with three and five bilayers. A quantitative evaluation of the reproducibility of the spectra in terms of average relative standard deviation (RSD) over the intensities of the prominent Rhodamine 6G Raman peaks are provided in Appendix D. The enhancement factor (EF) was calculated as follows[271]:

$$EF = \frac{I_{SERS}/N_{surf}}{I_{RS}/N_{vol}} \quad (6)$$

where I_{RS}, I_{SERS} are Raman and SERS intensities of Rhodamine 6G, N_{surf} is the average number of Rhodamine 6G molecules adsorbed onto the gold-coated diatomite composite in the scattering area for the SERS measurements, and N_{vol} is the number of Rhodamine 6G molecules present in the bulk scattering volume for spontaneous Raman scattering measurements. For the EF estimation, Raman modes at 1362 and 1507 cm^{-1} were used, as they correspond to benzene ring stretching and are the most prominent ones. The detailed calculation steps are provided in Appendix D. The SERS EF for diatomite coated with three PAH/AuNPs bilayers was calculated to be 6×10^3. Therefore, hybrid materials based on diatomite decorated with gold nanoparticles can be utilized as a low-cost and easy to fabricate SERS platform.

The signal enhancement introduced by diatomite decorated with gold nanoparticles can be explained in a number of ways. Given that a diatomite has a high specific surface area, AuNPs can be adsorbed not only on the surface but also around the pores using LbL technique in combination with FIL.[272] Dense gold coating in an ordered manner creates numerous ‘‘hot spots’’ and ensures high SERS enhancement and reproducibility. During the deposition, AuNP clusters are formed, which is indicated by long tail in the extinction spectra of diatomite coated with three and five PAH/AuNPs bilayers (Figure 84b) and confirmed by photoacoustic imaging (Figure 87, 88). Strong SERS enhancement in the case of multilayer deposition, which is absent in the case of one bilayer, is probably resulting from the increase in the number and efficiency of SERS ‘‘hot spots’’ caused by the aggregation of AuNPs with the deposition procedures. One potential approach to mitigate the effects of non-uniform nanoparticle distribution could involve the creation of "hot volumes" using arrays of weakly coupled metal nanohelices, as demonstrated in[273]. The application of a

continuous metallic thin film might also facilitate a more uniform SERS signal across a hybrid substrate[102,274].

8.7 Summary

Here, the capabilities of gold-coated diatomite as a SERS platform were demonstrated. The combination of LBL and FIL hybrid material fabrication approaches optimized the spatial distribution of AuNPs and numerous "hot spots" on the nanostructured silica substrate, resulting in a 6×10^3 enhancement of the Raman signal from Rhodamine 6G.

The degree of coverage of the diatomite surface by gold nanoparticles was assessed using photoacoustic imaging using 532 nm laser, as gold nanoparticles are known to act as photoacoustic contrast agents and absorb well green light. After evaluating the gathered photoacoustic signals across all samples, it can be deduced that the sample featuring three PAH/AuNPs bilayers exhibited the highest signal intensity. This observation was further corroborated by SEM analysis and extinction spectra measurements. Using gold-coated diatomite as a SERS platform offers several advantages and some disadvantages.

Advantages of using gold-coated diatomite as SERS platform:

1. Diatomite is an abundant and naturally occurring material, making it a cost-effective and environmentally friendly option as a substrate for SERS.

2. The intricate structure of diatomite provides a high surface area, which can enhance the adsorption of analyte molecules and improve SERS signal intensity.

3. Diatomite is generally considered biocompatible, which makes it suitable for potential applications, such as bioimaging or biosensing.

4. Diatomite has good mechanical stability, which can ensure the durability of the SERS substrate during repeated measurements or handling.

5. The properties of the gold nanoparticles on the diatomite surface, such as size, shape, and interparticle distance, can be tailored to optimize SERS enhancement by controlling the synthesis parameters.

Disadvantages:

1. Reproducibility: Achieving consistent and reproducible coverage of gold nanoparticles on the diatomite surface can be challenging, leading to variations in SERS enhancement between different substrates.

2. Diatomite is a natural material composed of numerous intricate pieces with a broad size distribution and a range of shapes. The irregularity in particle size and shape can lead to variations in the SERS enhancement factor across the substrate. This can affect the reproducibility of SERS.

3. The stability of gold-coated diatomite as a SERS platform under harsh chemical or environmental conditions needs to be carefully evaluated to ensure its performance in practical applications.

Chapter 9. Conclusions and Outlook

This thesis focuses on the investigation of diatom algae at three distinct levels, namely diatom colonies in suspension, individual living diatoms cells and cleaned frustules, and diatomite powder. Based on the findings presented in this thesis, the following main conclusions can be drawn:

I. Characterization and monitoring of diatom colonies

- The fluorescence and photoacoustic signals obtained from different species of freshwater pennate diatom (*A. sibiricum*) and marine centric diatoms (*Coscinodiscus* sp., *B. titiana*) exhibit a dependence on their growth phase. The highest signal intensity from *A. sibiricum* was achieved after 45 days of cultivation in the bioreactor. Conversely, the signals from the marine centric diatoms reached peak values after 30 days of cultivation. In the realm of diatom growth assessment during long-term cultivation, the presented methods leveraging fluorescence and photoacoustic signals emerge as a valuable, expeditious, and effective alternative. These methods offer several advantages over traditional cell counting, including the capacity for rapid evaluation of diatom growth without necessitating extensive sample preparation. By eliminating the need for cumbersome procedures and minimizing the risk of contamination introduced into the diatom medium, the proposed methods prove highly advantageous for accurate and reliable monitoring of diatom growth dynamics. Consequently, these approaches hold substantial promise within the context of large-scale diatom cultivation for carbon dioxide extraction purposes.
- Upon subjecting *K. amoena* diatoms, embedded in agarose gel, to 532 nm illumination, the photoacoustic signal decreases approximately 20 times when

reaching a concentration level of 3 cells/µl. The obtained agreement between the extinction value of *K. amoena* at 532 nm and the corresponding photoacoustic signal supports the assertion that chlorophylls and carotenoids serve as the primary light absorbers responsible for the photoacoustic effect in diatoms as 532 nm laser light is absorbed by these chromophores within diatoms. These findings highlight the concentration-dependent behavior of the photoacoustic signal in relation to diatom abundance and emphasize the significant contribution of chlorophylls and carotenoids to the overall signal generation process within diatom samples. Furthermore, the successful demonstration of the photoacoustic principle for visualizing diatom colonies has the potential to open avenues for various applications pertaining to the rapid assessment of water bodies, where diatom concentration serves as an indicator of ecological well-being and biomass productivity.

- Using a fabricated optical device consisting of LED illumination with a central wavelength of 505 nm, a linear dependence of the measured transmission on the concentration of diatoms was obtained with high accuracy for 7 strains of diatoms of various shapes and volumes. The observed monotonic dependence of the extinction and transmission slope on the volume of diatom cells is primarily governed by the extinction coefficient, which encompasses the absorption and scattering properties of diatoms.

II. Optical and mechanical properties of individual diatoms

- The mechanical properties of both cleaned *Coscinodiscus oculus-iridis* frustules and cells containing organic material were investigated utilizing AFM and *in situ* SEM nanoindentation techniques under static and dynamic loading

conditions. The Young's modulus of wet diatom cells exhibited a significantly higher value ($E = 25 \pm 5$ GPa) in comparison to cleaned frustules ($E = 15 \pm 2$ GPa for inner surface and $E = 10 \pm 4$ GPa for outer surface). The dynamic nanoindentation measurements unveiled that the average compliance of a cleaned frustule is 0.019 m/N, aligning with literature values observed graphene-based MEMS microphones. Diatoms present a diverse array of attributes that hold promise for effectively addressing fundamental challenges in bionics, particularly in the application of their exoskeleton principles for the creation of highly efficient microelectromechanical and photonic devices.

- The structure–mechanical properties relationship has a direct impact on the vibrational properties of the frustule as a complex micrometer-sized mechanical system. The numerically calculated resonance frequencies of Coscinodiscus oculus-iridis, ranging from 1 to 8 MHz, have been experimentally validated using two atomic force microscopy approaches: (1) measurement of frequencies of thermal vibrations and (2) an external mechanical excitation followed by detection with a lock-in amplifier. The calculated quality factors, ranging from 21 to 90, may find suitability in specific applications with distinct requirements, such as instances where a broader bandwidth is prioritized over high sensitivity.
- A periodic structure of *Coscinodiscus oculus-iridis* frustule, calculated using the formalism of Fourier modal method, due to diffraction increases the transmittance of light in the region λ = 400–500 nm up to 2 times when compared to the same silica material with the same thickness. The generated interference patterns inside the diatom frustule can play role in the efficient collection and channeling of light to the chloroplasts. These patterns optimize

light absorption, and potentially enhance the overall photosynthetic efficiency of diatoms.

III. Functionalization of diatomite powder

- By employing a novel technique that combines layer-by-layer assembly and freeze-induced loading, the surface of diatomite was successfully modified with gold nanoparticles. This approach effectively fine-tuned the spatial distribution of gold nanoparticles on the nanostructured silica substrate, resulting in a 6×10^3 enhancement of the Raman signal from Rhodamine 6G. Functionalizing diatom surface with nanoparticles offers a versatile platform with broad applications in environmental monitoring, materials science, and photonics.

Based on the findings of the research, the following future plans can be outlined:

I. Characterization and monitoring of diatom colonies

- The thesis highlights the potential of using fluorescence and optoacoustic methods for monitoring of growth of diatoms. The future work will also focus on developing optical methods for monitoring the activity of diatoms in utilization of carbon dioxide during long-term cultivation in bioreactors.

II. Optical and mechanical properties of individual diatoms

- The research conducted in this thesis provides insights into the mechanical properties and structural characteristics of diatoms. Building upon this knowledge, future work will focus on the fabrication and testing of diatom-inspired MEMS devices.
- Experimental study of diatom optical properties: The numerical exploration of diatom optical properties outlined in this thesis lays a groundwork for subsequent

studies in this domain. Future research endeavors will encompass experimental studies with the objective of probing the distribution of light within the diatom frustule and its impact on the chloroplasts.

- Building upon the research on diatom-chloroplast interaction, future work can explore novel techniques for manipulating diatom chloroplasts. Optical tweezers can be used to precisely position and manipulate individual chloroplasts inside diatoms. Investigating the precise manipulation and control of diatom chloroplasts can open up new possibilities for studying their photosynthetic activity and understanding their interaction with light.

III. Functionalization of diatoms

- The research on diatom structures and their mechanical properties can guide future work on the fabrication of composite materials incorporating diatoms. Integration of diatoms within matrices or polymers can lead to the development of lightweight, high-strength materials with unique structural properties. Exploring the fabrication techniques, material characterization, and applications of these diatom-based composites can be an exciting avenue for further research.

Appendix A

Monitoring of the division of diatoms in a microfluidic cell

Monitoring the division of diatoms using a microfluidic cell offers several advantages and allows for a more detailed understanding of the division process and its underlying mechanisms. It offers a powerful and versatile approach for studying this essential biological process and advancing our knowledge of diatom biology. Additionally, the insights gained from division monitoring can have applications in various fields, such as biotechnology, bioengineering, and environmental monitoring[275–277].

Here are some reasons why division monitoring specifically through microfluidic cells is valuable:

1. Microfluidic cells provide a controlled and stable environment for studying diatom division. Factors such as nutrient availability, temperature, pH, and light intensity can be precisely regulated, ensuring optimal conditions for division experiments which enables us to study the influence of specific environmental parameters on the division process and observe the effects of any variations[278].

2. Microfluidic devices allow for real-time observation of diatom division under a microscope which facilitates detailed monitoring of the various stages of division, including the formation of the division plane and daughter cell separation. By recording these processes, we can analyze the division kinetics, identify potential abnormalities or variations, and gain insights into the timing and coordination of the division process[279].

3. Microfluidic systems can accommodate multiple channels or compartments, allowing for the simultaneous observation of numerous diatoms undergoing division.

This high-throughput capability enables the collection of large datasets, enhancing statistical significance and enabling more robust quantitative analysis among different diatom species, individual cells, or within a population[280].

4. Microfluidic-based monitoring enables the quantification and characterization of various division parameters. These parameters may include division duration, growth rates, cell size, daughter cell symmetry, and the occurrence of asymmetric division events. By quantitatively analyzing these parameters across different conditions, researchers can identify patterns, correlations, and potential mechanisms regulating diatom division[279].

5. Microfluidic cells can support long-term observations of diatom division by tracking changes over time and capturing rare or infrequent events, extending beyond the limitations of conventional laboratory techniques[280].

Figure 90 shows the division of *Coscinodiscus oculus-iridis* in a flow cell at a temperature of 21°C, a CO_2 concentration in the gas receiver of 0.05 vol.% and a nutrient medium flow rate of 10 µl/min.

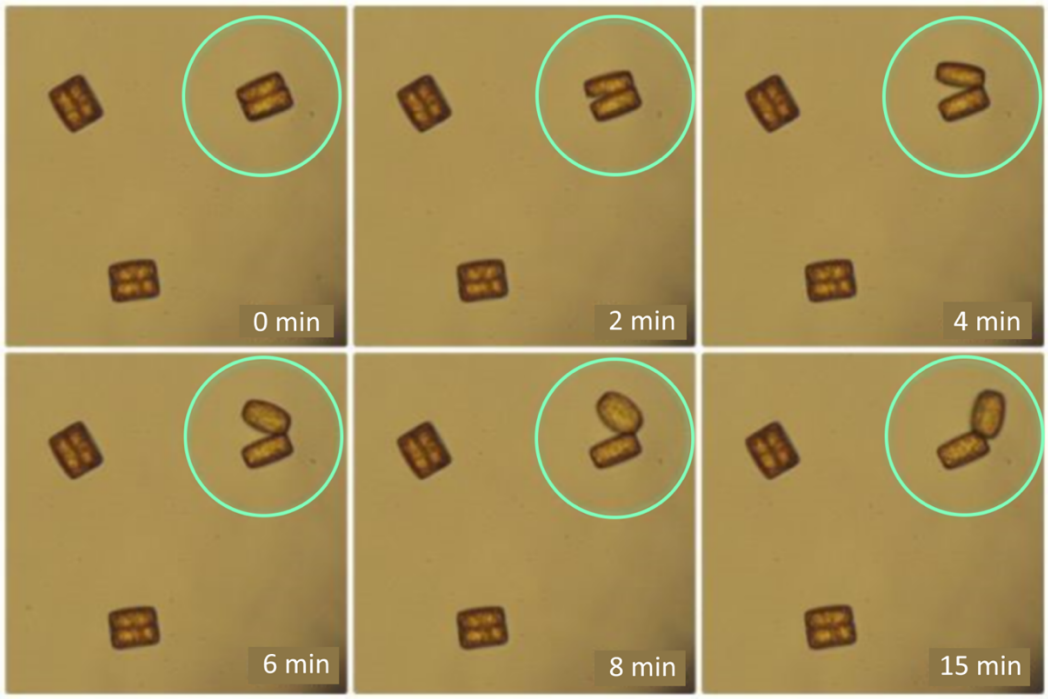

Figure 90. Division of C. oculus-iridis in the microfluidic cell

Figure 91 shows an example of a microfluidic cell temperature profile and images taken at different times while monitoring the division of the diatom Coscinodiscus oculus-iridis. Monitoring was performed at a nutrient medium flow rate of 10 µl/min and a CO_2 concentration in the gas receiver of 0.05 vol.%. Lowering the temperature to 10°C slows down the division of *Coscinodiscus oculus-iridis*. When the temperature rises to 23°C for 3 hours, cell division is observed. The images show that part of the algae is carried away by the flow of the nutrient medium during the observation. Therefore, further optimization of the channel configuration is required in order to reduce the flow rate directly in the field of visual observation. Thus, the device allows for several days to carry out in situ monitoring of the process of division of individual cells with the possibility of varying the concentration of CO_2, temperature and flow rate of the nutrient medium.

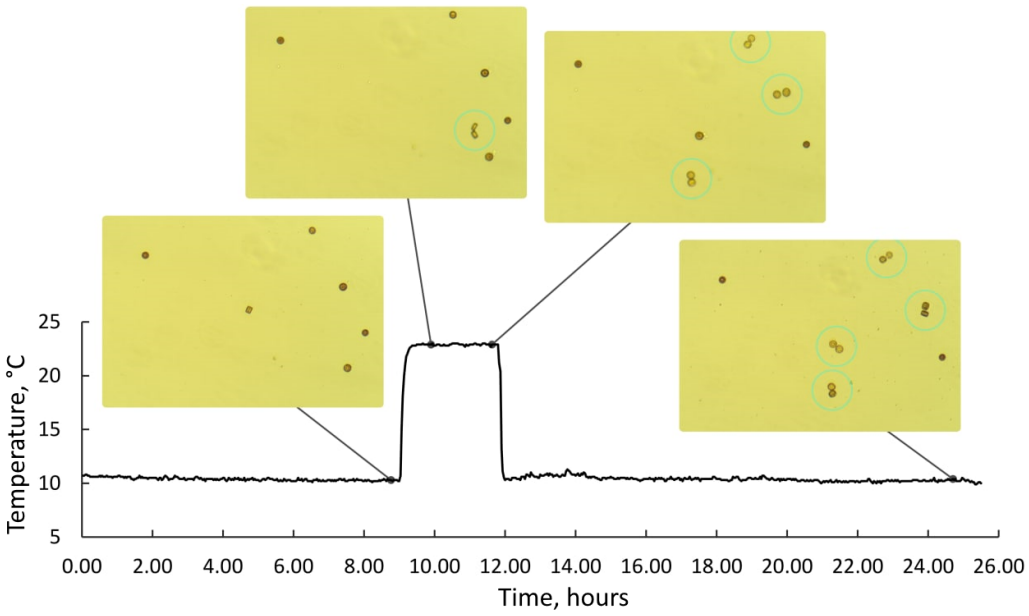

Figure 91. Monitoring of the division of *C. oculus-iridis* in the microfluidic cell during temperature changes.

Appendix B

Cell ultrastructure

To study the ultrastructure, the prepared sections of diatoms were examined using a transmission electron microscope.

Ulnaria acus (Kützing) Aboal

The internal structure of the cells of *Ulnaria acus* (Kützing) Aboal (=Synedra acus Kützing 1844) corresponds to previously obtained data [281] (Figure 92).

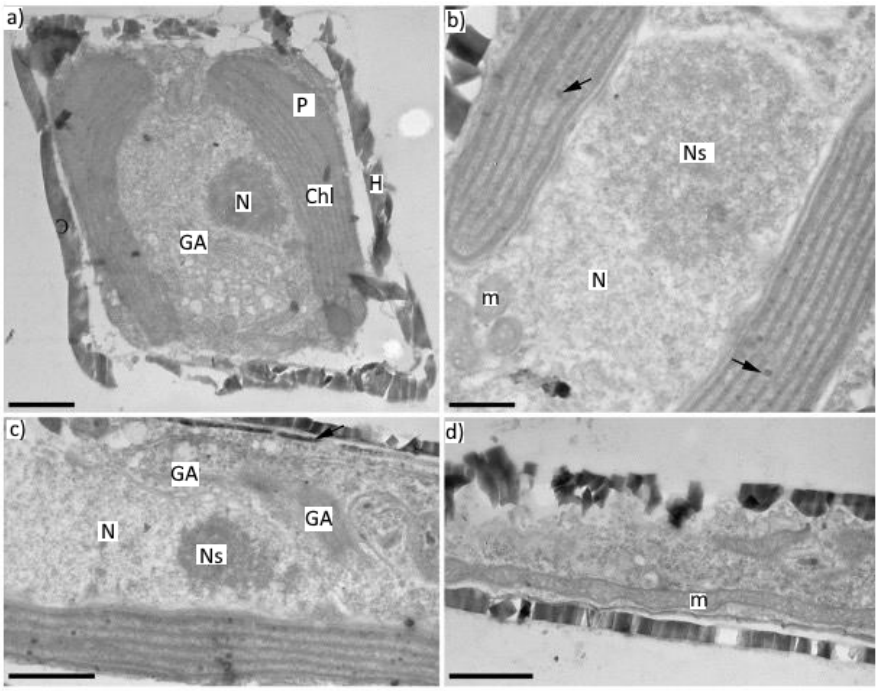

Figure 92. Structural details of *Ulnaria acus* 15K595 cells (TEM). Cross sections - a, b; longitudinal sections, c, d. The arrows in Figure 1b show plastoglobules, and in Figure 1c, a fragment of the forming girdle rim. Symbols: GA - Golgi apparatus; H - hypotheca; m - mitochondrion; P - pyrenoid; E - epitheca; N – nucleus, NS - nucleolus. Scale: a, c, d – 1 μm; b – 500 nm.

Cross sections show a nucleus with a large nucleolus through the center of the cell, between two chloroplasts (Figure 92a-c). Chloroplasts are pressed against the

valves and have an indistinct pyrenoid (Figure 92a, b). A few plastoglobuli are located between the thylakoids (Figure 92b). On sections of many cells, there are emerging girdle rims (Figure 92c). The Golgi apparatuses are adjacent to the nucleus (Figure 92a, c). Mitochondria on transverse sections are small rounded (Figure 92b), and on longitudinal sections they are elongated and can reach a length of more than 4 μm (Figure 92d).

Coscinodiscus oculus-iridis (Ehrenberg) Ehrenberg

The cell ultrastructure of *Coscinodiscus oculus-iridis* (Ehrenberg) Ehrenberg has not been previously described. On sections, the nucleus with a large nucleolus is located in the center of the cell, surrounded by chloroplasts and lipid droplets, or can be shifted to the girdle rims (Figure 93a). The bulk of the cell is occupied by the vacuole (Figure 93a). Numerous chloroplasts are pressed to the cell periphery, have a rounded pyrenoid (Figure 93b), thylakoids are packed in stacks of three and can form anastomoses (Figure 93d), plastoglobuli are located between the thylakoid stacks (Figure 93e). In all sections, the polysaccharide layer adjacent to the valve is clearly visible (Figure 93c). Mitochondria are oblong, most often pressed against the cell periphery (Figure 93c). On the periphery of the cytoplasm, there are vesicles transporting mucus to the plasmalemma (Figure 93e).

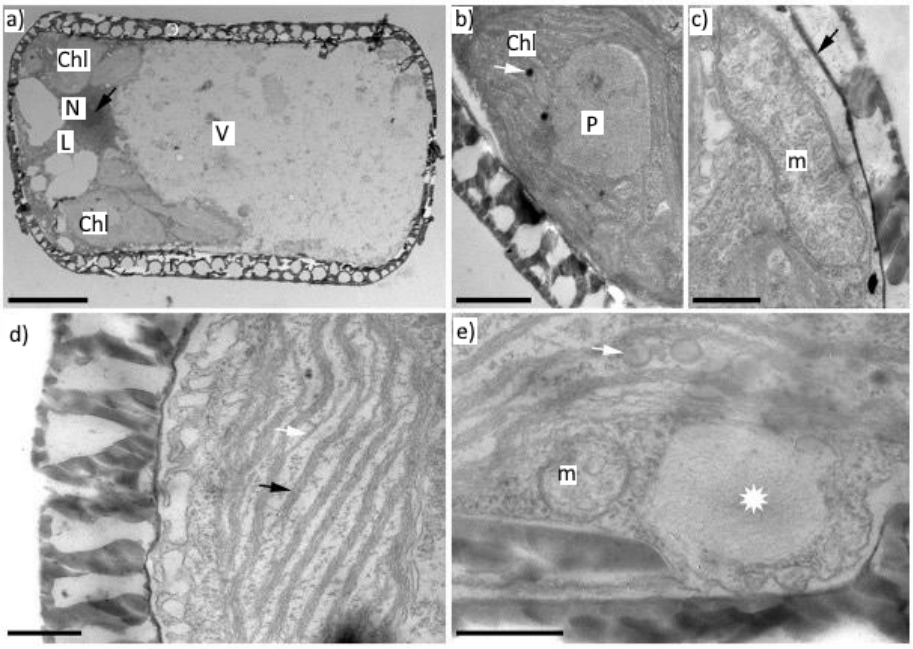

Figure 93. Details of the cell structure of *Coscinodiscus oculus-iridis*. a) general view of the cell, cross section, the arrow shows the nucleolus; b) section through the chloroplast (arrow – plastoglobules); c) section through the mitochondrion (arrow— polysaccharide layer); d) fragment of a chloroplast section (black arrow, thylakoid; white arrow, anastomosis between stacks of thylakoids); e) Section fragment through the chloroplast (arrow – plastoglobule) and transport vesicle (asterisk). Scale: a – 5 μm; b – 1 μm; c-e - 500 nm. Designations as in the previous Figure 92.

Hannaea baicalensis Genkal, Popovskaya & Kulikovskiy

The ultrastructure of *Hannaea baicalensis* Genkal, Popovskaya & Kulikovskiy is described for the first time. The only chloroplast is pressed against the shell from the side of the girdle rims and is distinguished by a large pyrenoid located in the center of the chloroplast (Figure 94a, b). Stacks of thylakoids are not numerous - from 4 to 7 on a chloroplast section (Figure 94a-c), plastoglobuli are located between the thylakoids (Figure 94b). The nucleus is adjacent to the pyrenoid; it can be shifted to one of the

lobes of the chloroplast (Figure 94a, b). Mitochondria are small and irregular in shape (Figure 94d). There are several Golgi apparatuses in the cell, but on the cut, as a rule, it is one and is adjacent to the nucleus (Figure 94b) or to the chloroplast (Figure 94e).

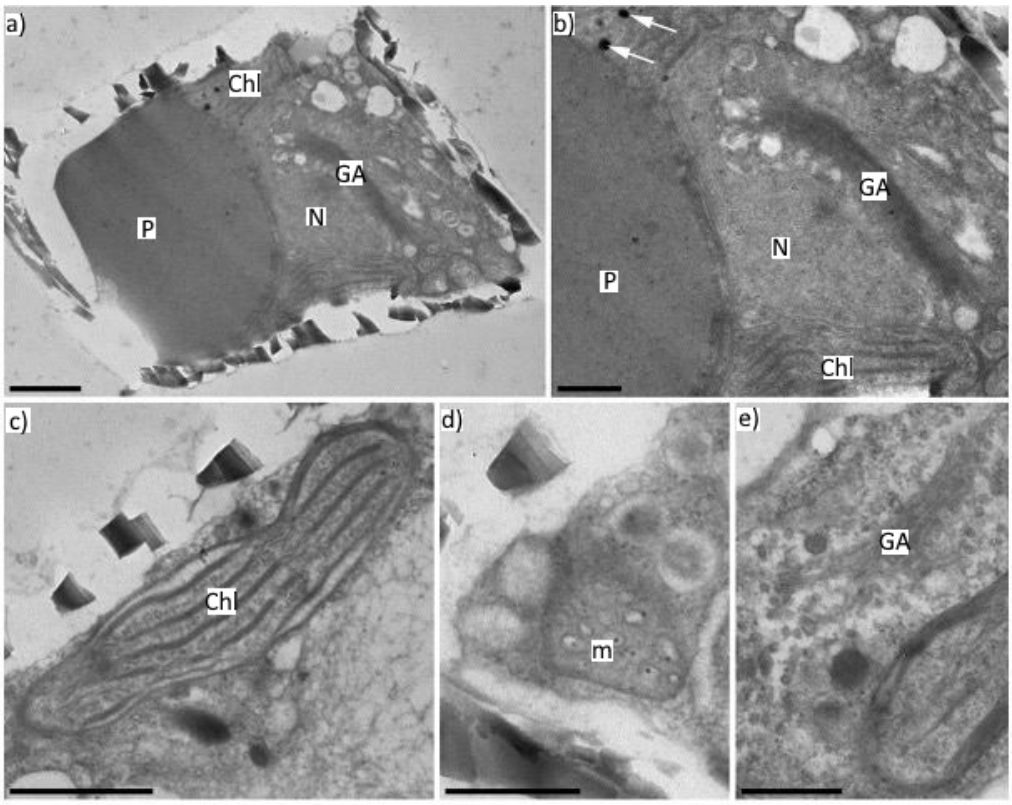

Figure 94. Details of the cell structure of *Hannaea baicalensis*. A) general view of the cell, cross section; b) enlarged fragment of figure 48a; c) section through a part of the chloroplast without a pyrenoid; d) cross section of mitochondria; e) section of the Golgi apparatus adjacent to the chloroplast. Scale: a, c – 1 μm; b, d, e – 500 nm. Designations as in Figure 92.

Appendix C

The raw thermal frequency spectra of diatom frustule at different positions are shown in Figure 95.

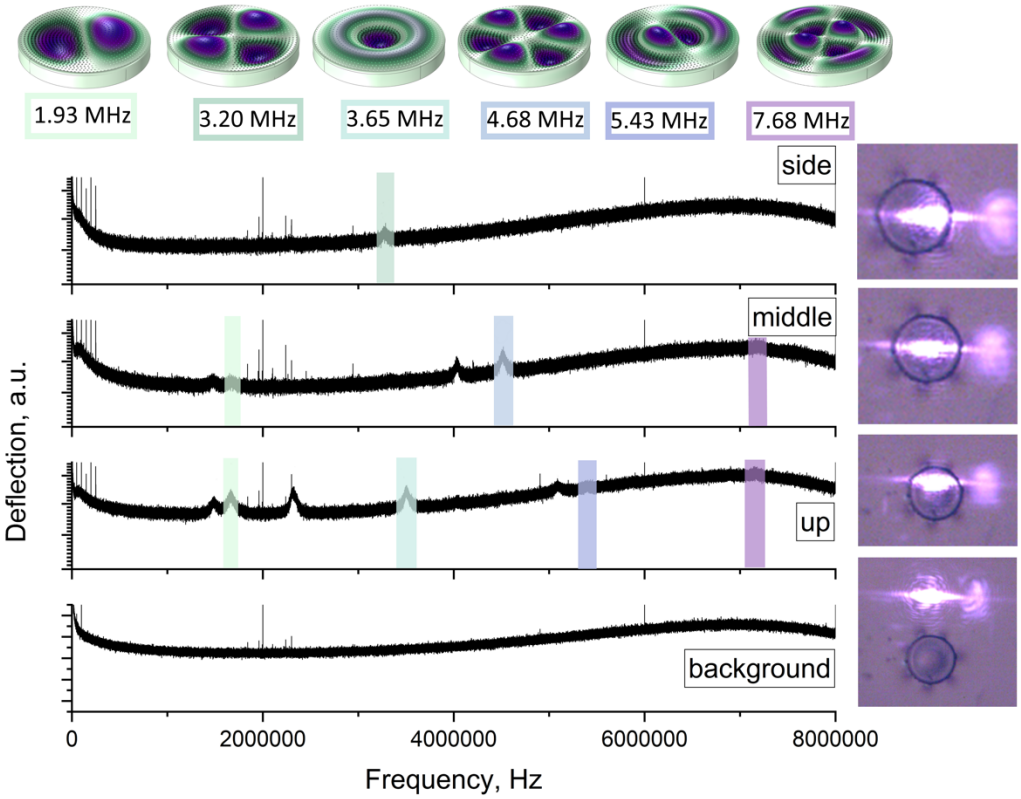

Figure 95. Raw spectra of frequencies of thermal vibrations of the diatom frustule collected at different spots.

Appendix D

Numerical simulations of optical properties using Fourier modal method

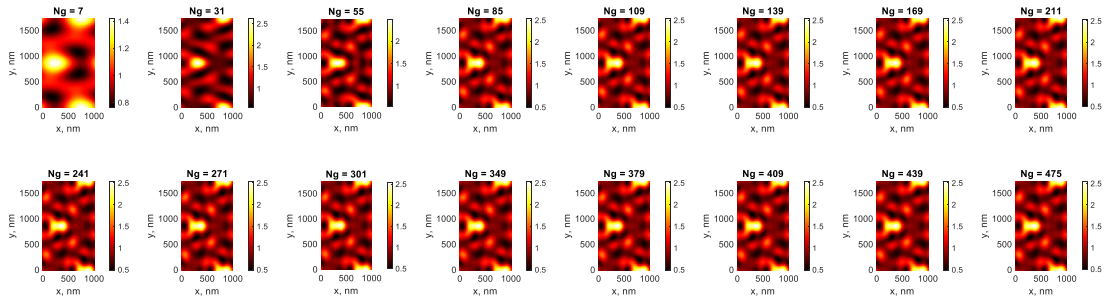

Figure 96. Convergency check in Fourier modal method. In simulation, Ng=97 is used.

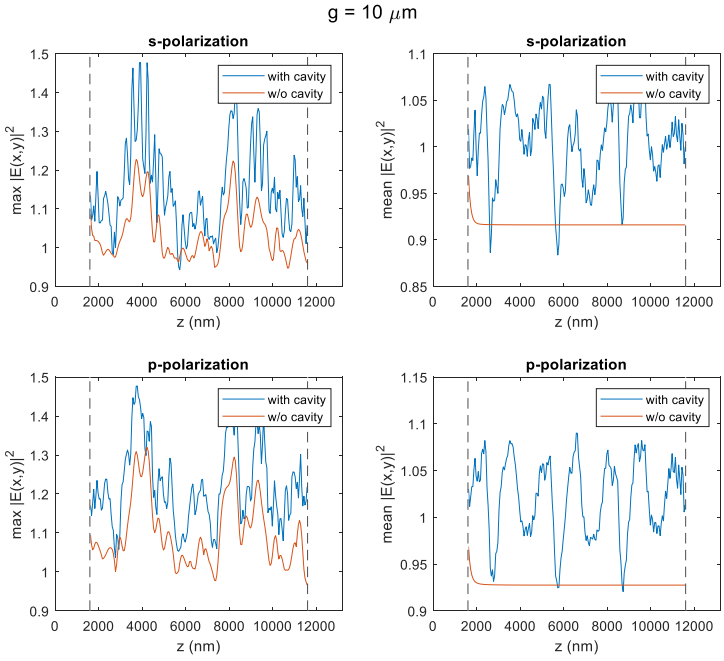

Figure 97. Maximal and mean light intensity distribution calculated for two model structures for distance between valves g=10 μm for S- and P- polarizations.

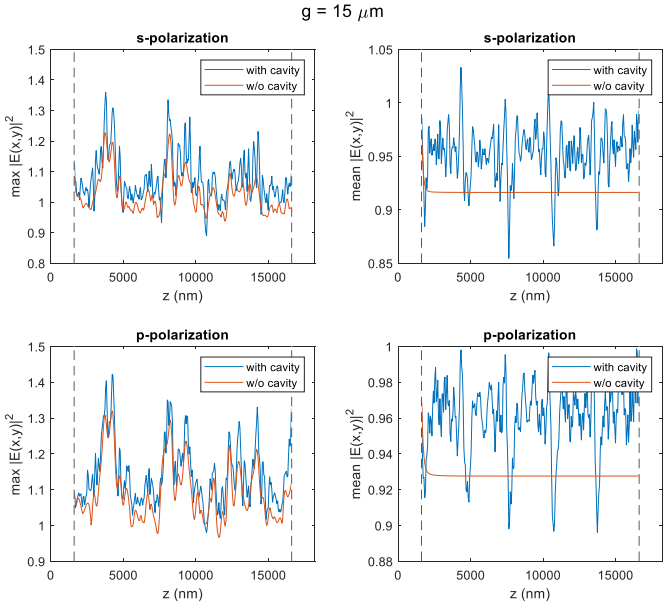

Figure 98. Maximal and mean light intensity distribution calculated for two model structures for distance between valves g=15 μm for S- and P- polarizations.

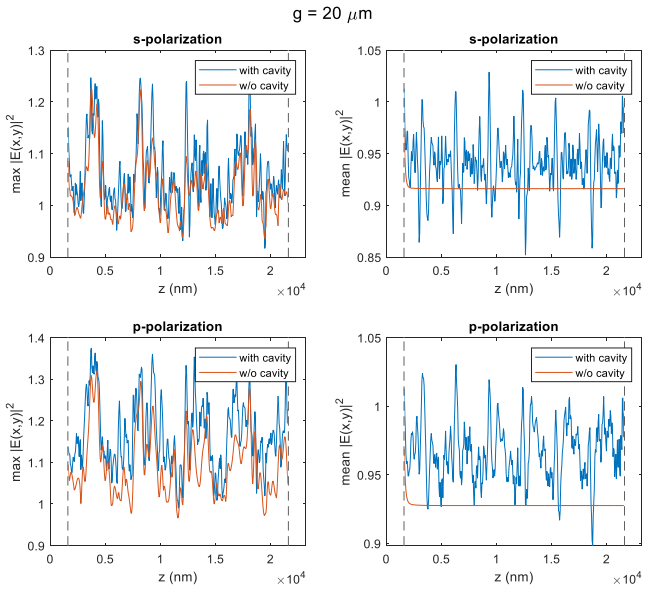

Figure 99. Maximal and mean light intensity distribution calculated for two model structures for distance between valves g=20 μm for S- and P- polarizations.

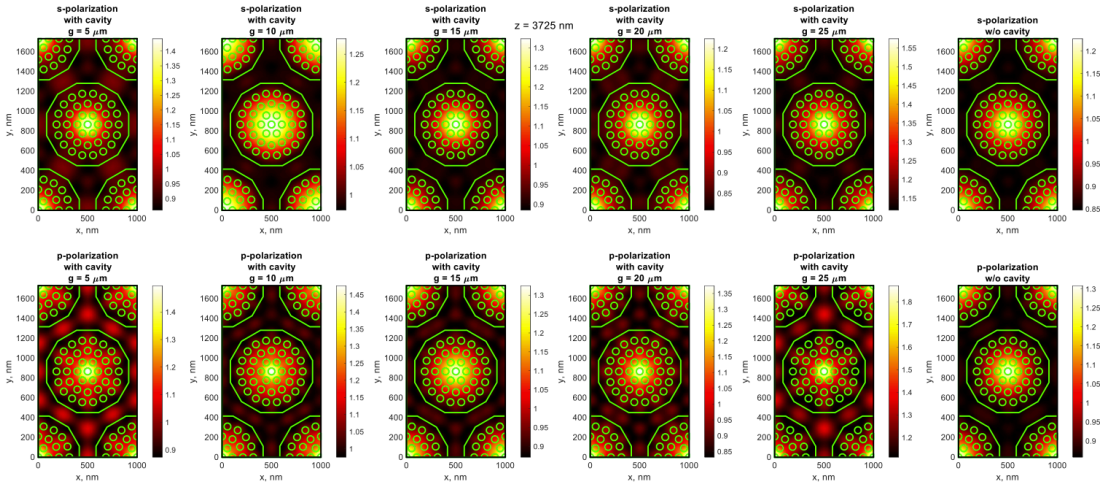

Figure 100. Light intensity calculated for: S- (upper row) and P-polarization (bottom row), within horizontal cross-sections of samples with height g=5, 10, 15, 20, 25 μm.

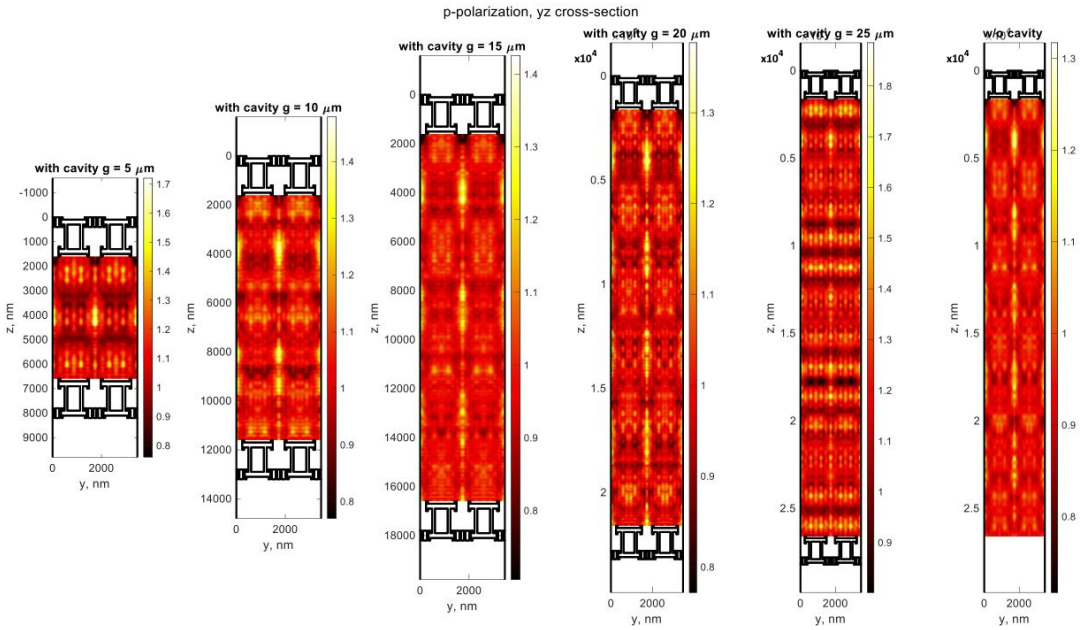

Figure 101. Light intensity calculated for P-polarization within vertical cross-sections of samples with height g=5, 10, 15, 20, 25 μm in yz plane.

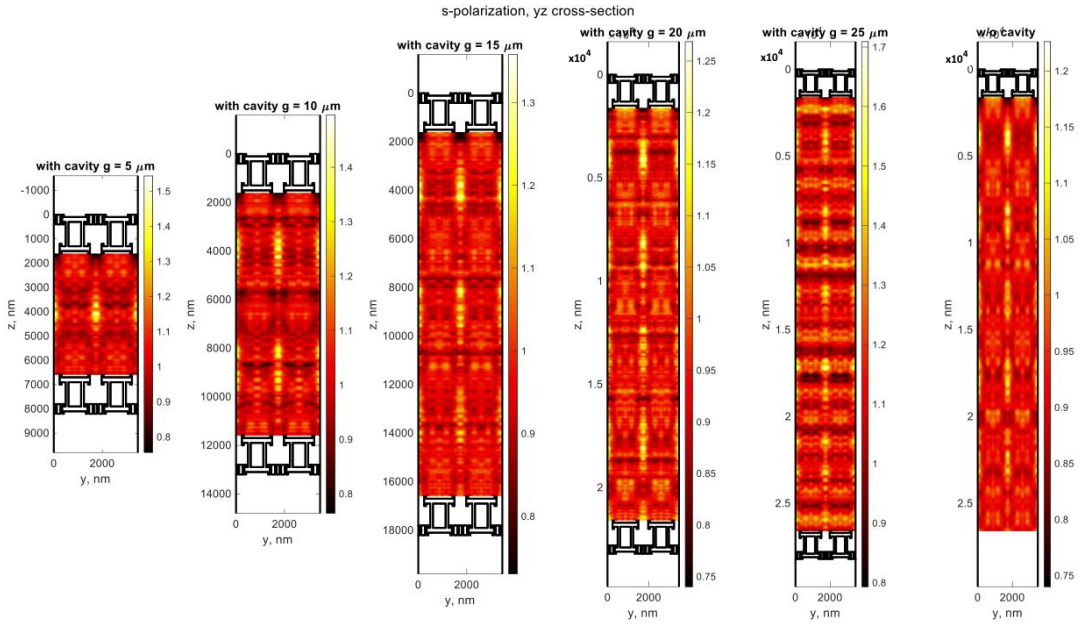

Figure 102. Light intensity calculated for S-polarization within vertical cross-sections of samples with height g=5, 10, 15, 20, 25 μm in yz plane.

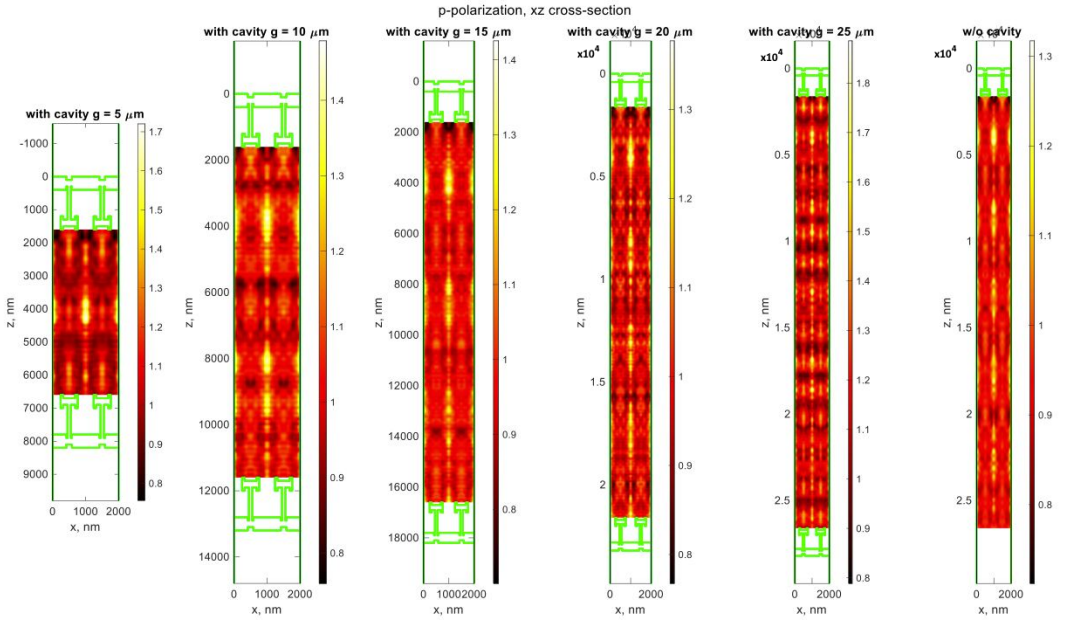

Figure 103. Light intensity calculated for P-polarization within vertical cross-sections of samples with height g=5, 10, 15, 20, 25 μm in xz plane.

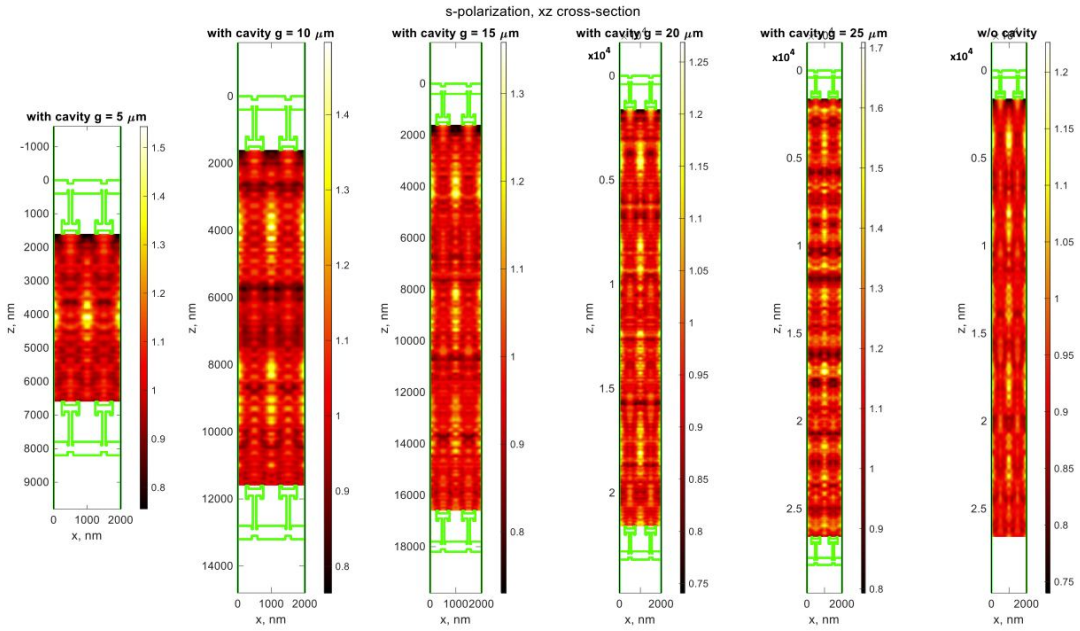

Figure 104. Light intensity calculated for S-polarization within vertical cross-sections of samples with height g=5, 10, 15, 20, 25 μm in xz plane.

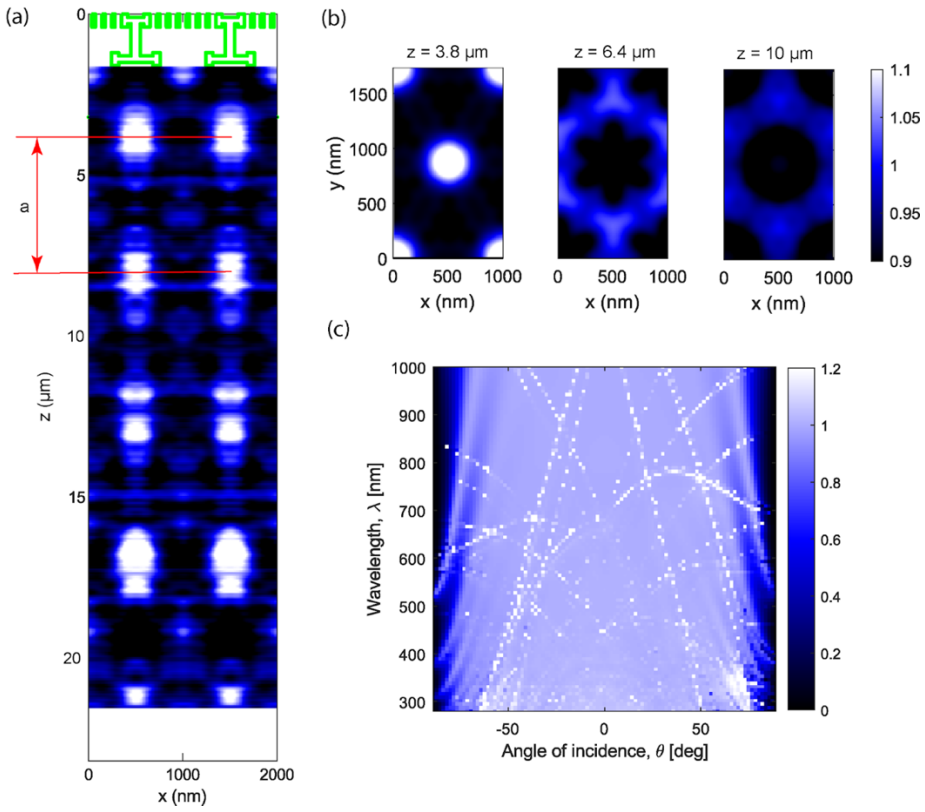

Figure 105. Light intensity distribution inside the diatom frustule calculated for the wavelength λ=450 nm: a) Vertical cross-section, b) Horizontal cross-sections at z=3.8 μm, z=6.4 μm, z=10 μm. c) The dependence of wavelength of incident light on the angle of incidence.

Appendix E

SERS measurements justification

1. Choosing traces of Raman scattering

For each diatomite-based sample type, 9-10 measurements were taken. Then for each sample type intensity distribution of the modes around 1362 and 1509 cm^{-1} was analyzed, and measurements with amplitudes in the lower quartile (1-2 measurements per sample type) were excluded. Therefore, each sample type had 7-9 measurements that were used for further calculation of mean trace and its standard deviation, as shown in Figure 100.

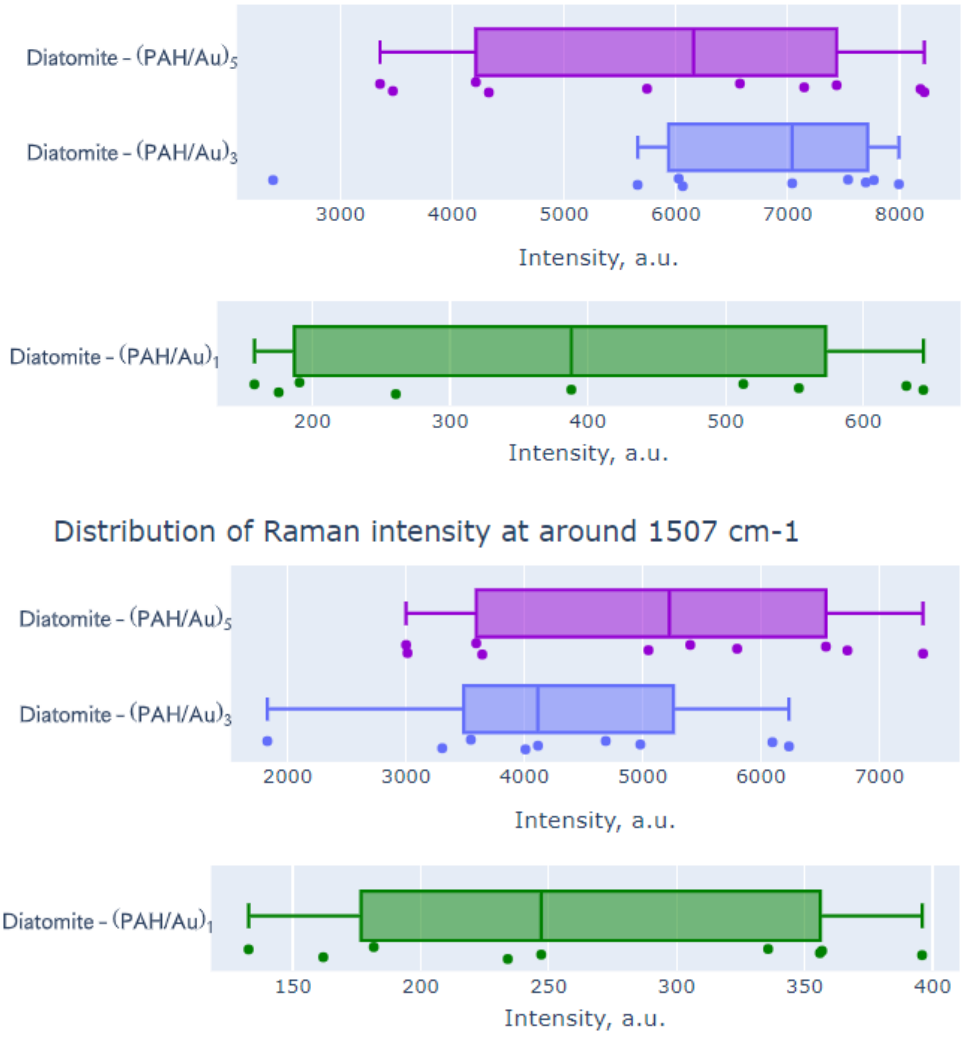

Figure 106. Distributions of peak intensities of two prominent peaks of Rhodamine 6G (1362 cm^{-1} – up, 1509 cm^{-1} – down).

In Table 9, mean intensity values and their relative standard deviations (RSD) are calculated for each pair of prominent Rhodamine 6G (R6G) Raman peaks detected. For a general enhancement factor (EF) estimation for the substrates, Raman modes at 1362 and 1509 cm^{-1} were used, as they correspond to benzene ring stretching and are the most prominent ones.

2. Enhancement Factor Calculation

The enhancement factor was calculated using equation (6), as shown in the section 8.8.

2.1. Determination of N_{surf}

To determine the average number of R6G molecules adsorbed onto the gold-coated diatomite composite in the scattering area, concentrations of bulk R6G before and after incubation with Diatomite-$(PAH/AuNPs)_3$ were estimated by means of the calibration curve built for R6G absorption at 500 nm.

To absorb R6G on diatomite coated with PAH/AuNPs layers, 120 µL of 200 µM R6G, that equals to 24 nmoles, were mixed with 120 µL of Diatomite-$(PAH/AuNPs)_3$ with concentration $c_{Dt} = 1.3 \cdot 10^8$ particles/mL, that equals to $N_{Dt} = 1.56 \cdot 10^7$ particles in solution.

According to spectroscopic data obtained, the concentration of non-absorbed R6G after incubation with gold-coated diatomite was 72 µM, that equals to 17.3 nmoles. It was presumed that the rest of R6G molecules, $n_{R6G}^{abs} = 6.7$ nmol, were

absorbed on gold-coated diatomite composites, therefore on average 1 diatomite absorbed $2.8 \cdot 10^8$ particles:

$$\frac{N_{R6G}}{N_{Dt}} = \frac{n_{R6G}^{abs} \cdot N_A}{c_{Dt} \cdot V_{Dt}} = 2.6 \cdot 10^8 \text{ molecules/particle}$$

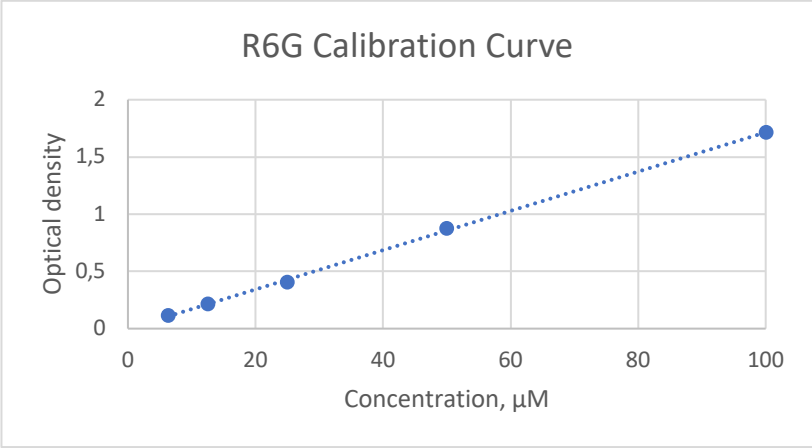

Figure 107. Calibration curve for R6G

Raman spectrometer was equipped with an objective having magnification M = 10 and the pinhole size Φ was set to 100 µm. Therefore, the laser spot size radius way be estimated as[282]:

$$r \approx \frac{\Phi}{2 \cdot 1.4 \cdot M} = 3.57$$

Then the laser spot area

$$S = \pi r^2 = 40 \text{ µm}^2$$

The size is obviously greater than that of the diatomite, therefore it is assumed that a SERS signal is obtained from a single diatomite particle. Additionally, it is assumed that only half of the intensity that could be obtained from one diatomite is

collected, as irradiation and detection are provided from just one side, in a backscattering mode. Furthermore, only molecules in vicinity of AuNPs are enhanced, and according to SEM images (Figure 86) 15.5% of diatomite surface is covered with AuNPs, therefore

$$N_{surf} = \frac{1}{2} \cdot \frac{\mathrm{N_{R6G}}}{\mathrm{N_{Dt}}} * 15.5\% = 2 \cdot 10^7 \text{ molecules}$$

2.2. Determination of N_{vol}

Liquid drop height *h* is around 0.5 mm. Assuming that for a given objective the whole height participates in Raman scattering, the volume participating may be found as

$$V_{RS} = S \cdot h = \ 2 \cdot 10^4 \ \mu m^3$$

Therefore, the number of R6G molecules participating in Raman scattering is

$$N_{vol} = V_{RS} \cdot c_{R6G} \cdot N_A = \ 2 \cdot 10^4 \mu m^3 \cdot 200 \cdot 10^{-21} \frac{mol}{\mu m^3} \cdot 6.02 \cdot 10^{23} \frac{1}{mol} =$$

$2.4 \cdot 10^9$ molecules

2.3. Determination of the Enhancement Factor

Thus, according to equation (6) and data from Table 9, the EF may be estimated as:

$$EF = \frac{I_{SERS}}{I_{RS}} \cdot \frac{N_{vol}}{N_{surf}} \approx 6 \cdot 10^3$$

Bibliography

1. Nelson, D. M., Tréguer, P., Brzezinski, M. A., Leynaert, A. & Quéguiner, B. Production and dissolution of biogenic silica in the ocean: Revised global estimates, comparison with regional data and relationship to biogenic sedimentation. *Global Biogeochem Cycles* **9**, 359–372 (1995).
2. Field, C. B., Behrenfeld, M. J., Randerson, J. T. & Falkowski, P. Primary production of the biosphere: Integrating terrestrial and oceanic components. *Science (1979)* **281**, 237–240 (1998).
3. Sethi, D., Butler, T. O., Shuhaili, F. & Vaidyanathan, S. Diatoms for Carbon Sequestration and Bio-Based Manufacturing. *Biology* **9**, 217 (2020).
4. Yang, R., Wei, D. & Xie, J. Diatoms as cell factories for high-value products: chrysolaminarin, eicosapentaenoic acid, and fucoxanthin. *Crit Rev Biotechnol* **40**, 993–1009 (2020).
5. Chen, J. *et al.* Recent Progress on Systems and Synthetic Biology of Diatoms for Improving Algal Productivity. *Front in Bioeng and Biotech,* 10 (2022).
6. Korsunsky, A. M., Sapozhnikov, P. V., Everaerts, J. & Salimon, A. I. Nature's neat nanostructuration: The fascinating frustules of diatom algae. *Materials Today* **22**, 159–160 (2019).
7. Guillard, R. & Sieracki, M. Counting Cells in Cultures with the Light Microscope. *Algal Culturing Techniques* 239–252 (2005)
8. Mcheik, A. *et al.* Optical properties of nanostructured silica structures from marine organisms. *Frontiers in Marine Science* vol. 5 (2018).
9. Fuhrmann, T., Landwehr, S., El Rharbl-Kucki, M. & Sumper, M. Diatoms as living photonic crystals. *Applied Physics B 2004 78:3* **78**, 257–260 (2004).

10. Kamińska, A., Sprynskyy, M., Winkler, K. & Szymborski, T. Ultrasensitive SERS immunoassay based on diatom biosilica for detection of interleukins in blood plasma. *Anal Bioanal Chem* **409**, 6337–6347 (2017).

11. Chamuah, N. *et al.* A naturally occurring diatom frustule as a SERS substrate for the detection and quantification of chemicals. *J Phys D Appl Phys* **50**, (2017).

12. Pannico, M. *et al.* Electroless Gold-Modified Diatoms as Surface-Enhanced Raman Scattering Supports. *Nanoscale Res Lett* **11**, (2016).

13. Collins, S., Rost, B. & Rynearson, T. A. Evolutionary potential of marine phytoplankton under ocean acidification. *Evol Appl* **7**, 140–155 (2014).

14. Salimon, A. I. *et al. On the Mathematical Description of Diatom Algae: From Siliceous Exoskeleton Structure and Properties to Colony Growth Kinetics, and Prospective Nanoengineering Applications* in The *Mathematical Biology of Diatoms,* ed. Janice L. Pappas, Scrivener Publishing LLC, 63-102 (2023).

15. Medlin, L. K., Kooistra, W. H. C. F., Sims, P. & Wellbrock, U. Is the origin of the diatoms related to the end-Permian mass extinction? *Nova Hedwigia* **65**, 1–11 (1997).

16. Harwood, D. M. & Nikolaev, V. A. Cretaceous Diatoms: Morphology, Taxonomy, Biostratigraphy. *Short Courses in Paleontology* **8**, 81–106 (1995).

17. Haeckel, E. Kunstformen der Natur, Bibliographisches Institut, Leipzig-Vienna, 1904.

18. Salimon, A. I. *et al.* A Mini-Atlas of diatom frustule electron microscopy images at different magnifications. in *Materials Today: Proceedings* vol. 33 1924–1933 (Elsevier Ltd, 2020).

19. Charles Darwin. On the origin of species by means of natural selection, or the preservation of favoured races in the struggle for life. John Murray, p.502 (1859).

20. AlgaeBase :: Listing the World's Algae. https://www.algaebase.org/.

21. Aitken, Z. H., Luo, S., Reynolds, S. N., Thaulow, C. & Greer, J. R. Microstructure provides insights into evolutionary design and resilience of Coscinodiscus sp. frustule. *Proc Natl Acad Sci U S A* (2016).

22. Mishra, M., Arukha, A. P., Bashir, T., Yadav, D. & Prasad, G. B. K. S. All new faces of diatoms: Potential source of nanomaterials and beyond. *Frontiers in Microbiology* (2017).

23. Jain, S. Marine Diatoms in *Fundamentals of Invertebrate Palaeontology,* Springer Geology, Springer Science and Business Media Deutschland GmbH, 131–142 (2020).

24. Bedoshvili, Y., Gneusheva, K., Popova, M., Morozov, A. & Likhoshway, Y. Anomalies in the valve morphogenesis of the centric diatom alga Aulacoseira islandica caused by microtubule inhibitors. *Biol Open* **7**, (2018).

25. Nemoto, T., Best, P. B., Ishimaru, K., & Takano, H. Diatom films on whales in South African waters. *Sci. Rep. Whales Res. Inst*. **32**, 97-103 (1980).

26. Falciatore, A., Jaubert, M., Bouly, J. P., Bailleul, B. & Mock, T. Diatom molecular research comes of age: Model species for studying phytoplankton biology and diversity[open]. *Plant Cell* (2020).

27. Zgłobicka, I. *et al.* Insight into diatom frustule structures using various imaging techniques. *Scientific Reports 2021 11:1* **11**, 1–10 (2021).

28. Zhang, D. Y. *et al.* Bio-manufacturing technology based on diatom micro- and nanostructure. *Chinese Science Bulletin* **57**, 3836–3849 (2012).

29. Bruder, K. & Medlin, L. K. Morphological and molecular investigations of naviculoid diatoms. II. Selected genera and families. *Diatom Research* **23**, 283–329 (2008).

30. De Tommasi, E., Gielis, J. & Rogato, A. Diatom Frustule Morphogenesis and Function: a Multidisciplinary Survey. *Mar Genomics* **35**, 1–18 (2017).

31. Aguirre, L. E. *et al.* Diatom frustules protect DNA from ultraviolet light. *Scientific Reports 2018 8:1* **8**, 1–6 (2018).

32. Romann, J. *et al.* Wavelength and orientation dependent capture of light by diatom frustule nanostructures. *Sci Rep* **5**, (2015).

33. Sprynskyy, M. *et al.* Naturally organic functionalized 3D biosilica from diatom microalgae. *Mater Des* (2017)

34. Sardo, A., Orefice, I., Balzano, S., Barra, L. & Romano, G. Mini-review: Potential of diatom-derived silica for biomedical applications. *Applied Sciences (Switzerland)* vol. 11 (2021).

35. Zahajská, P., Opfergelt, S., Fritz, S. C., Stadmark, J. & Conley, D. J. What is diatomite? *Quaternary Research (United States)* **96**, 48–52 (2020).

36. Aggrey, P. *et al.* On the diatomite-based nanostructure-preserving material synthesis for energy applications. *RSC Adv* **11**, 31884–31922 (2021).

37. Hamm, C. E. *et al.* Architecture and material properties of diatom shells provide effective mechanical protection. (2003)

38. Fabritius, H. O., Sachs, C., Triguero, P. R. & Raabe, D. Influence of structural principles on the mechanics of a biological fiber-based composite material with hierarchical organization: The exoskeleton of the lobster homarus americanus. *Advanced Materials* **21**, 391–400 (2009).

39. Cvjetinovic, J. *et al.* Revealing the static and dynamic nanomechanical properties of diatom frustules-Nature's glass lace. *Sci Rep* **13**, 5518 (2023).

40. Sumper, M. A Phase Separation Model for the Nanopatterning of Diatom Biosilica. *Science (1979)* **295**, 2430–2433 (2002).

41. Zgłobicka, I. *et al.* Visualization of the internal structure of Didymosphenia geminata frustules using nano X-ray tomography. *Sci Rep* **7**, (2017).

42. Taveri, G., Grasso, S., Gucci, F., Toušek, J. & Dlouhy, I. Bio-Inspired Hydro-Pressure Consolidation of Silica. *Adv Funct Mater* **28**, (2018).

43. Sumper, M. & Kröger, N. Silica formation in diatoms: the function of long-chain polyamines and silaffins. *J. Mater. Chem.* **14**, 2059–2065 (2004).

44. Subhash, G., Yao, S., Bellinger, B. & Gretz, M. R. Investigation of mechanical properties of diatom frustules using nanoindentation. *J Nanosci Nanotechnol* **5**, 50–56 (2005).

45. Losic, D., Short, K., Mitchell, J. G., Lal, R. & Voelcker, N. H. AFM nanoindentations of diatom biosilica surfaces. *Langmuir* **23**, 5014–5021 (2007).

46. Losic, D., Pillar, R. J., Dilger, T., Mitchell, J. G. & Voelcker, N. H. Atomic force microscopy (AFM) characterisation of the porous silica nanostructure of two centric diatoms. *Journal of Porous Materials 2006 14:1* **14**, 61–69 (2006).

47. Almqvist, N. *et al.* Micromechanical and structural properties of a pennate diatom investigated by atomic force microscopy. *J Microsc* **202**, 518–532 (2001).

48. Hamm, C. E. *et al.* Architecture and material properties of diatom shells provide effective mechanical protection. *Nature 2003 421:6925* **421**, 841–843 (2003).

49. Wegst, U. G. K. & Ashby, M. F. The mechanical efficiency of natural materials. *Philosophical Magazine* **84**, 2167–2186 (2004).

50. Moreno, M. D., Ma, K., Schoenung, J. & Dávila, L. P. An integrated approach for probing the structure and mechanical properties of diatoms: Toward engineered nanotemplates. *Acta Biomater* **25**, 313–324 (2015).

51. Luo, S. & Greer, J. R. Bio-Mimicked Silica Architectures Capture Geometry, Microstructure, and Mechanical Properties of Marine Diatoms. *Adv Eng Mater* (2018) doi:10.1002/adem.201800301.

52. Topal, E. *et al.* Numerical and experimental study of the mechanical response of diatom frustules. *Nanomaterials* **10**, 1–14 (2020).

53. Yao, S., Subhash, G. & Maiti, S. Analysis of nanoindentation response of diatorp frustules. *J Nanosci Nanotechnol* **7**, 4465–4472 (2007).

54. Parker, A. R. *Natural photonic structures: an overview*. *Optical Biomimetics* (Woodhead Publishing Limited, 2012). doi:10.1533/9780857097651.1.

55. Vukusic, P. & Sambles, J. R. Photonic structures in biology. *Nature* **424**, 852–855 (2003).

56. Parker, A. R. & Townley, H. E. Biomimetics of photonic nanostructures. *Nat Nanotechnol* **2**, 347–353 (2007).

57. Mcheik, A. *et al.* Optical properties of nanostructured silica structures from marine organisms. *Frontiers in Marine Science* vol. 5 (2018).

58. Romann, J., Valmalette, J.-C., Røyset, A. & Einarsrud, M.-A. Optical properties of single diatom frustules revealed by confocal microspectroscopy. *Opt Lett* **40**, 740 (2015).

59. Lamastra, F. R. *et al.* Diatom frustules decorated with zinc oxide nanoparticles for enhanced optical properties. *Nanotechnology* **28**, (2017).

60. Yamanaka, S. *et al.* Optical properties of diatom silica frustule with special reference to blue light. *J Appl Phys* **103**, 074701 (2008).

61. Tranell, G., Røyset, A. & Noren, A. K. *Characterization of Structure and Optical Properties of Diatoms for improved Solar Cell Efficiency*. (2011).

62. Ferrara, M. A. *et al.* Optical properties of diatom nanostructured biosilica in Arachnoidiscus sp: Micro-optics from mother nature. *PLoS One* **9**, (2014).

63. Kuczynska, P., Jemiola-Rzeminska, M. & Strzalka, K. Photosynthetic pigments in diatoms. *Mar Drugs* **13**, 5847–5881 (2015).

64. De Tommasi, E. *et al.* UV-shielding and wavelength conversion by centric diatom nanopatterned frustules. *Sci Rep* **8**, 1–14 (2018).

65. Ellegaard, M. *et al.* The fascinating diatom frustule—can it play a role for attenuation of UV radiation? *J Appl Phycol* **28**, 3295–3306 (2016).

66. Martynov, N. & Stolyarov, S. Theory of wave propagation in periodic structures. *Soviet Journal of Quantum Electronics* **8**, 1056 (2007).

67. De Tommasi, E. Light Manipulation by Single Cells: The Case of Diatoms. *Journal of Spectroscopy* **2016**, (2016).

68. Noyes, J., Sumper, M. & Vukusic, P. Light manipulation in a marine diatom. *J Mater Res* **23**, 3229–3235 (2008).

69. Goessling, J. W. *et al.* Structure-based optics of centric diatom frustules: modulation of the in vivo light field for efficient diatom photosynthesis. *New Phytologist* **219**, 122–134 (2018).

70. Richard, B. & Hoover, M. J. *Part of the Optics Commons Recommended Citation Recommended Citation Hoover*. *Journal of the Arkansas Academy of Science* vol. 24 (1970).

71. De Tommasi, E. *et al.* Light micro-lensing effect in biosilica shells of diatoms microalgae. in *Micro-Optics 2008* vol. 6992 69920F (SPIE, 2008).

72. Kieu, K. *et al.* Structure-based optical filtering by the silica microshell of the centric marine diatom Coscinodiscus wailesii. *Opt Express* **22**, 15992 (2014).

73. Stefano, L. De, Rendina, I., Stefano, M. De, Rea, I. & Moretti, L. Lensless light focusing with the centric marine diatom Coscinodiscus walesii. *Optics Express, Vol. 15, Issue 26, pp. 18082-18088* **15**, 18082–18088 (2007).

74. De Tommasi, E. *et al.* Multi-wavelength study of light transmitted through a single marine centric diatom. *Optics Express, Vol. 18, Issue 12* **18**, 12203–12212 (2010).

75. Knight, J. C. Photonic crystal fibres. *Nature* **424**, 847–851 (2003).

76. Chen, X., Wang, C., Baker, E. & Sun, C. Numerical and experimental investigation of light trapping effect of nanostructured diatom frustules. *Sci Rep* **5**, 1–9 (2015).

77. Yoneda, S., Ito, F., Yamanaka, S. & Usami, H. Optical properties of nanoporous silica frustules of a diatom determined using a 10 μm microfiber probe. *Jpn J Appl Phys* **55**, (2016).

78. Yoon, H. & Goorsky, M. S. A systematic study of the structural and luminescence properties of P-type porous silicon. *MRS Online Proceedings Library* **378**, 893–898 (1995)

79. Cullis, A. G., Canham, L. T. & Calcott, P. D. J. The structural and luminescence properties of porous silicon. *Journal of Applied Physics* vol. 82 909–965 Preprint at https://doi.org/10.1063/1.366536 (1997).

80. De Tommasi, E. *et al.* Intrinsic photoluminescence of diatom shells in sensing applications. in *Optical Sensors 2009* vol. 7356 735615 (SPIE, 2009).

81. De Stefano, L., Rendina, I., De Stefano, M., Bismuto, A. & Maddalena, P. Marine diatoms as optical chemical sensors. *Appl Phys Lett* **87**, 1–3 (2005).

82. Bismuto, A., Setaro, A., Maddalena, P., De Stefano, L. & De Stefano, M. Marine diatoms as optical chemical sensors: A time-resolved study. *Sens Actuators B Chem* **130**, 396–399 (2008).

83. Townley, H. E., Woon, K. L., Payne, F. P., White-Cooper, H. & Parker, A. R. Modification of the physical and optical properties of the frustule of the diatom Coscinodiscus wailesii by nickel sulfate. *Nanotechnology* **18**, (2007).

84. De Stefano, L. *et al.* Marine diatoms as optical biosensors. *Biosens Bioelectron* **24**, 1580–1584 (2009).

85. Camargo, E. *et al.* Chemical and optical characterization of Psammodictyon panduriforme (Gregory) Mann comb nov (Bacillariophyta) frustules. *Opt Mater Express* **6**, 1436 (2016).

86. Arteaga-Larios, N. V., Nahmad, Y., Navarro-Contreras, H. R., Encinas, A. & García-Meza, J. V. Photoluminescence shift in frustules of two pennate diatoms and nanostructural changes to their pores. *Luminescence* **29**, 969–976 (2014).

87. Rea, I. & De Stefano, L. Recent advances on diatom-based biosensors. *Sensors (Switzerland)* vol. 19 Preprint at https://doi.org/10.3390/s19235208 (2019).

88. Zaman, S., Hassan, M. M., Hasanuzzaman, M. & Baten, M. Z. Coscinodiscus diatom inspired bi-layered photonic structures with near-perfect absorptance accompanied by tunable absorption characteristics. *Opt Express* **28**, 25007 (2020).

89. De Stefano, L. *et al.* Nano-biosilica from marine diatoms: A brand new material for photonic applications. *Superlattices Microstruct* **46**, 84–89 (2009).

90. Tommasi, E. De, Tommasi, E. De, Luca, A. C. De & Luca, A. C. De. Diatom biosilica in plasmonics: applications in sensing, diagnostics and therapeutics [Invited]. *Biomedical Optics Express, Vol. 13, Issue 5, pp. 3080-3101* **13**, 3080–3101 (2022).

91. Jeffryes, C. *et al.* Electroluminescence and Photoluminescence from Nanostructured Diatom Frustules Containing Metabolically Inserted Germanium. *Advanced Materials* **20**, 2633–2637 (2008).

92. Tommasi, E. De *et al.* Optics with diatoms: towards efficient, bioinspired photonic devices at the micro-scale. **8792**, 99–104 (2013).

93. Jeffryes, C., Campbell, J., Li, H., Jiao, J. & Rorrer, G. The potential of diatom nanobiotechnology for applications in solar cells, batteries, and electroluminescent devices. *Energy Environ Sci* **4**, 3930–3941 (2011).

94. Cvjetinovic, J. *et al.* A SERS platform based on diatomite modified by gold nanoparticles using a combination of layer-by-layer assembly and a freezing-induced loading method. *Physical Chemistry Chemical Physics* **24**, 8901–8912 (2022).

95. Kong, X. *et al.* Plasmonic nanoparticles-decorated diatomite biosilica: extending the horizon of on-chip chromatography and label-free biosensing. *J Biophotonics* **10**, 1473–1484 (2017).

96. Roychoudhury, P., Bose, R., Dąbek, P. & Witkowski, A. Photonic Nano-/Microstructured Diatom Based Biosilica in Metal Modification and Removal—A Review. *Materials 2022, Vol. 15, Page 6597* **15**, 6597 (2022).

97. Leonardo, S., Prieto-Simón, B. & Campàs, M. Past, present and future of diatoms in biosensing. *TrAC Trends in Analytical Chemistry* **79**, 276–285 (2016).

98. Viji, S. *et al.* Diatom-Based Label-Free Optical Biosensor for Biomolecules. *Appl Biochem Biotechnol* **174**, 1166–1173 (2014).

99. Selvaraj, V., Muthukumar, A., Nagamony, P. & Chinnuswamy, V. Detection of typhoid fever by diatom-based optical biosensor. *Environmental Science and Pollution Research* **25**, 20385–20390 (2018).

100. Kong, X. *et al.* Chemical and biological sensing using diatom photonic crystal biosilica with in-situ growth plasmonic nanoparticles. *IEEE Trans Nanobioscience* **15**, 828–834 (2016).

101. Vona, D. *et al.* Light emitting silica nanostructures by surface functionalization of diatom algae shells with a triethoxysilane-functionalized π-conjugated fluorophore. *MRS Adv* **1**, 3817–3823 (2016).

102. De Tommasi, E. & De Luca, A. C. Diatom biosilica in plasmonics: applications in sensing, diagnostics and therapeutics [Invited]. *Biomed Opt Express* **13**, 3080 (2022).

103. Rogato, A. & De Tommasi, E. Physical, chemical, and genetic techniques for diatom frustule modification: Applications in nanotechnology. *Applied Sciences (Switzerland)* **10**, 1–23 (2020).

104. Delasoie, J. & Zobi, F. Natural diatom biosilica as microshuttles in drug delivery systems. *Pharmaceutics* **11**, 1–21 (2019).

105. Kim, J., Seidler, P., Wan, L. S. & Fill, C. Formation, structure, and reactivity of amino-terminated organic films on silicon substrates. *J Colloid Interface Sci* **329**, 114–119 (2009).

106. Ruggiero, I. *et al.* Diatomite silica nanoparticles for drug delivery. *Nanoscale Res Lett* **9**, 1–7 (2014).

107. Bariana, M., Aw, M. S., Kurkuri, M. & Losic, D. Tuning drug loading and release properties of diatom silica microparticles by surface modifications. *Int J Pharm* **443**, 230–241 (2013).

108. Losic, D. *et al.* Surface functionalisation of diatoms with dopamine modified iron-oxide nanoparticles: toward magnetically guided drug microcarriers with biologically derived morphologies. *Chemical Communications* **46**, 6323 (2010).

109. Terracciano, M. *et al.* Silica-Based Nanovectors: From Mother Nature to Biomedical Applications. *Algae - Organisms for Imminent Biotechnology* (2016) doi:10.5772/63191.

110. Terracciano, M. *et al.* Surface bioengineering of diatomite based nanovectors for efficient intracellular uptake and drug delivery. *Nanoscale* **7**, 20063–20074 (2015).

111. George, J. *et al.* Metabolic Engineering Strategies in Diatoms Reveal Unique Phenotypes and Genetic Configurations With Implications for Algal Genetics and Synthetic Biology. *Front Bioeng Biotechnol* **8**, (2020).

112. Stukenberg, D., Zauner, S., Dell'Aquila, G. & Maier, U. G. Optimizing CRISPR/cas9 for the diatom Phaeodactylum tricornutum. *Front Plant Sci* **9**, (2018).

113. Huang, W. & Daboussi, F. Genetic and metabolic engineering in diatoms. *Philosophical Transactions of the Royal Society B: Biological Sciences* vol. 372 (2017).

114. Jeffryes, C., Gutu, T., Jiao, J. & Rorrer, G. L. Two-stage photobioreactor process for the metabolic insertion of nanostructured germanium into the silica microstructure of the diatom Pinnularia sp . **28**, 107–118 (2008).

115. Jeffryes, C., Gutu, T., Jiao, J. & Rorrer, G. L. Metabolic Insertion of Nanostructured TiO 2 into the Patterned Biosilica of the Bioreactor Cultivation Process. **2**, 2103–2112 (2008).

116. Jeffryes, C., Gutu, T., Jiao, J. & Rorrer, G. L. Peptide-mediated deposition of nanostructured TiO2 into the periodic structure of diatom biosilica. *J Mater Res* **23**, 3255–3262 (2008).

117. Bandara, T. M. W. J., Furlani, M., Albinsson, I., Wulff, A. & Mellander, B. E. Diatom frustules enhancing the efficiency of gel polymer electrolyte based dye-sensitized solar cells with multilayer photoelectrodes. *Nanoscale Adv* **2**, 199–209 (2020).

118. Xiao, X. *et al.* A Visible-NIR Responsive Dye-Sensitized Solar Cell Based on Diatom Frustules and Cosensitization of Photopigments from Diatom and Purple Bacteria. *J Chem* **2020**, (2020).

119. Machill, S. *et al.* Analytical studies on the incorporation of aluminium in the cell walls of the marine diatom Stephanopyxis turris. *BioMetals* **26**, 141–150 (2013).

120. Zhang, G. *et al.* Preparation of silicate-based red phosphors with a patterned nanostructure via metabolic insertion of europium in marine diatoms. *Mater Lett* **110**, 253–255 (2013).

121. Basharina, T. N. *et al.* The Effect of Titanium, Zirconium and Tin on the Growth of Diatom Synedra Acus and Morphology of Its Silica Valves. *Silicon* **4**, 239–249 (2012).

122. Gannavarapu, K. P., Ganesh, V., Thakkar, M., Mitra, S. & Dandamudi, R. B. Nanostructured Diatom-ZrO2 composite as a selective and highly sensitive enzyme free electrochemical sensor for detection of methyl parathion. *Sens Actuators B Chem* **288**, 611–617 (2019).

123. Brzozowska, W. *et al.* "Outsourcing" Diatoms in Fabrication of Metal-Doped 3D Biosilica. *Materials 2020, Vol. 13, Page 2576* **13**, 2576 (2020).

124. Delalat, B. *et al.* Targeted drug delivery using genetically engineered diatom biosilica. *Nature Communications 2015 6:1* **6**, 1–11 (2015).

125. Zobi, F. Diatom Biosilica in Targeted Drug Delivery and Biosensing Applications: Recent Studies. *Micro 2022, Vol. 2, Pages 342-360* **2**, 342–360 (2022).

126. Sun, X. W., Zhang, Y. X. & Losic, D. Diatom silica, an emerging biomaterial for energy conversion and storage. *J Mater Chem A Mater* **5**, 8847–8859 (2017).

127. Cassaignon, S., de Maleprade, R., Nassif, N. & Livage, J. From Living Light to Living Materials. *Mater Today Proc* **1**, 209–215 (2014).

128. Li, A., Zhao, X., Duan, G., Anderson, S. & Zhang, X. Diatom Frustule-Inspired Metamaterial Absorbers: The Effect of Hierarchical Pattern Arrays. *Adv Funct Mater* **29**, 1809029 (2019).

129. Kumari, S., Min, K. H., Kanth, B. K., Jang, E. K. & Pack, S. P. Production of TiO2-deposited Diatoms and Their Applications for Photo-catalytic Degradation of Aqueous Pollutants. *Biotechnology and Bioprocess Engineering 2020 25:5* **25**, 758–765 (2020).

130. Köhler, L. *et al.* Are Diatoms "Green" Aluminosilicate Synthesis Microreactors for Future Catalyst Production? *Molecules 2017, Vol. 22, Page 2232* **22**, 2232 (2017).

131. Losic, D., Rosengarten, G., Mitchell, J. G. & Voelcker, N. H. Pore architecture of diatom frustules: potential nanostructured membranes for molecular and particle separations. *J Nanosci Nanotechnol* **6**, 982–989 (2006).

132. Korsunsky, A. M. *et al.* Siliceous diatom frustules - A smart nanotechnology platform. *Mater Today Proc* **33**, 2032–2040 (2020).

133. Gordon, R., Losic, D., Tiffany, M. A., Nagy, S. S. & Sterrenburg, F. A. S. The Glass Menagerie: diatoms for novel applications in nanotechnology. *Trends Biotechnol* **27**, 116–127 (2009).

134. Rabiee, N. *et al.* Diatoms with invaluable applications in nanotechnology, biotechnology, and biomedicine: Recent advances. *ACS Biomater Sci Eng* **7**, 3053–3068 (2021).

135. Truong, H. T., Nguyen, T. D. & Nguyen, H. Q. Nanocomposite of silver nanoparticles/diatomite against pathogenous bacteria for catfish. *Aquac Rep* **16**, 100286 (2020).

136. Sun, H. *et al.* Biocompatible silver nanoparticle-modified natural diatomite with anti-infective property. *J Nanomater* **2018**, (2018).

137. Jantschke, A., Herrmann, A. K., Lesnyak, V., Eychmüller, A. & Brunner, E. Decoration of diatom biosilica with noble metal and semiconductor nanoparticles (<10 nm): Assembly, characterization, and applications. *Chem Asian J* **7**, 85–90 (2012).

138. Fischer, C. *et al.* Gold nanoparticle-decorated diatom biosilica: A favorable catalyst for the oxidation of d-glucose. *ACS Omega* **1**, 1253–1261 (2016).

139. Kong, X. *et al.* Plasmonic nanoparticles-decorated diatomite biosilica: extending the horizon of on-chip chromatography and label-free biosensing. *J Biophotonics* **10**, 1473–1484 (2017).

140. Onesto, V. *et al.* Silica diatom shells tailored with Au nanoparticles enable sensitive analysis of molecules for biological, safety and environment applications. *Nanoscale Res Lett* **13**, 1–9 (2018).

141. Villani, M. *et al.* Transforming diatomaceous earth into sensing devices by surface modification with gold nanoparticles. *Micro and Nano Engineering* **2**, 29–34 (2019).

142. Terracciano, M., Napolitano, M., De Stefano, L., De Luca, A. C. & Rea, I. Gold decorated porous biosilica nanodevices for advanced medicine. *Nanotechnology* **29**, (2018).

143. Briceño, S., Chavez-Chico, E. A. & González, G. Diatoms decorated with gold nanoparticles by In-situ and Ex-situ methods for in vitro gentamicin release. *Materials Science and Engineering C* **123**, (2021).

144. Westerveld, W. J. *et al.* Sensitive, small, broadband and scalable optomechanical ultrasound sensor in silicon photonics. *Nat Photonics* **15**, 341–345 (2021).

145. Bogaerts, W. *et al.* Basic structures for photonic integrated circuits in Silicon-on-insulator. *Optics Express, Vol. 12, Issue 8, pp. 1583-1591* **12**, 1583–1591 (2004).

146. Je, C. H., Lee, J., Yang, W. S., Kim, J. & Cho, Y. H. A surface-micromachined capacitive microphone with improved sensitivity. *Journal of Micromechanics and Microengineering* **23**, 055018 (2013).

147. Shubham, S. *et al.* A Novel MEMS Capacitive Microphone with Semiconstrained Diaphragm Supported with Center and Peripheral Backplate Protrusions. *Micromachines 2022, Vol. 13, Page 22* **13**, 22 (2021).

148. Abdusatorov, B., Salimon, A. I., Bedoshvili, Y. D., Likhoshway, Y. V. & Korsunsky, A. M. FEM exploration of the potential of silica diatom frustules for vibrational MEMS applications. *Sens Actuators A Phys* **315**, 112270 (2020).

149. Gebeshuber, I. C. *et al.* Exploring the innovational potential of biomimetics for novel 3D MEMS. *Adv Mat Res* **74**, 265–268 (2009).

150. Kim, K., Liang, Z., Liu, M. & Fan, D. E. Biobased High-Performance Rotary Micromotors for Individually Reconfigurable Micromachine Arrays and Microfluidic Applications. *ACS Appl Mater Interfaces* **9**, 6144–6152 (2017).

151. Kawahara, T. *et al.* On-chip microrobot for investigating the response of aquatic microorganisms to mechanical stimulation. *Lab Chip* **13**, 1070–1078 (2013).

152. Aggrey, P. *et al.* In Situ Formation of Nanoporous Silicon on a Silicon Wafer via the Magnesiothermic Reduction Reaction (MRR) of Diatomaceous Earth. *Nanomaterials 2020, Vol. 10, Page 601* **10**, 601 (2020).

153. Cvjetinovic, J. *et al.* Photonic tools for evaluating the growth of diatom colonies during long-term batch cultivation. *J Phys Conf Ser* **2172**, 012011 (2022).

154. Cvjetinovic, J. *et al.* In situ fluorescence/photoacoustic monitoring of diatom algae. 8 (2021) doi:10.1117/12.2588254.

155. Cvjetinovic, J. *et al.* Photoacoustic and fluorescence lifetime imaging of diatoms. *Photoacoustics* **18**, 100171 (2020).

156. Davidovich, N. A., Davidovich, O. I. & Podunay, Y. The diatom culture collection at Karadag Scientific Station (Crimea). *Marine Biological Journal* **2**, 18–28 (2017).

157. Andersen, R. A. *Algal Culturing Techniques*.

158. Medlin, L. K. & Kaczmarska, I. Evolution of the diatoms: V. Morphological and cytological support for the major clades and a taxonomic revision. *Phycologia* **43**, 245–270 (2004).

159. Polyakova, S. L., Davidovich, O. I., Podunay, Y. A. & Davidovich, N. A. Modification of the ESAW culture medium used for cultivation of marine diatoms. *Marine Biological Journal* **3**, 73–80 (2018).

160. Shishlyannikov, S. M. *et al.* A procedure for establishing an axenic culture of the diatom Synedra acus subsp. Radians (Kütz.) Skabibitsch. From Lake Baikal. *Limnol Oceanogr Methods* **9**, 478–484 (2011).

161. Thompson, A. S., Rhodes, J. C. & Pettman, I. Culture collection of algae and protozoa : catalogue of strains 1988. in (1988).

162. Cvjetinovic, J. *et al.* Concentration Dependence of Optical Transmission and Extinction of Different Diatom Cultures. *J Biomed Photonics Eng* 010303 (2023) doi:10.18287/jbpe23.09.010303.

163. Cvjetinovic, J. *et al.* Assessment of diatom growth using fluorescence imaging. *J Phys Conf Ser* **1984**, 012017 (2021).

164. Croce, R. & Van Amerongen, H. Natural strategies for photosynthetic light harvesting. *Nature Chemical Biology 2014 10:7* **10**, 492–501 (2014).

165. Bedoshvili, Y. D., Kaluzhnaya, O. V. & Likhoshway, Y. V. The frustules morphogenesis of aulacoseira baicalensis in the natural population. *Journal of Advanced Microscopy Research* **7**, 219–223 (2012).

166. Salakhova, N. S., Fradkin, I. M., Dyakov, S. A. & Gippius, N. A. Fourier modal method for moiré lattices. *Phys Rev B* **104**, (2021).

167. Griffiths, M. J., Garcin, C., van Hille, R. P. & Harrison, S. T. L. Interference by pigment in the estimation of microalgal biomass concentration by optical density. *J Microbiol Methods* **85**, 119–123 (2011).

168. Touliabah, H. E., Abdel-Hamid, M. I. & Almutairi, A. W. Long-term monitoring of the biomass and production of lipids by Nitzschia palea for biodiesel production. *Saudi J Biol Sci* **27**, 2038–2046 (2020).

169. Knefelkamp, B., Carstens, K. & Wiltshire, K. H. Comparison of different filter types on chlorophyll-a retention and nutrient measurements. *J Exp Mar Biol Ecol* **345**, 61–70 (2007).

170. Schagerl, M., Siedler, R., Konopáčová, E. & Ali, S. S. Estimating Biomass and Vitality of Microalgae for Monitoring Cultures: A Roadmap for Reliable Measurements. *Cells* **11**, (2022).

171. Esra Erçetin Bursa Teknik Üniversitesi, V., Esra Dökümcüoğlu, V. & Yılmaz, M. *Assessment of Cell Counting Method Based on Image Processing for a Microalga Culture*. *MedFAR* vol. 3 (2020).

172. Manohar, S. & Razansky, D. Photoacoustics: a historical review. *Adv Opt Photonics* **8**, 586 (2016).

173. Li, C. & Wang, L. V. Photoacoustic tomography and sensing in biomedicine. *Phys Med Biol* **54**, (2009).

174. Wang, L. V. & Hu, S. Photoacoustic tomography: In vivo imaging from organelles to organs. *Science* vol. 335 1458–1462 (2012).

175. Korsunsky, A. M. & Salimon, A. I. On the paradigm of Hierarchically Structured Materials, in conjunction with the Virtual Special Issue on Functional Materials. *Mater Des* **158**, 1–4 (2018).

176. Systems, M. M., Abdusatorov, B., Everaerts, J., Salimon, A. I. & Korsunsky, A. M. On the prospects of using Biogenic Silica for. **0958**, (2019).

177. Lamastra, F. R. *et al.* Photoacoustic Spectroscopy Investigation of Zinc Oxide/Diatom Frustules Hybrid Powders. *Int J Thermophys* **39**, 1–10 (2018).

178. Pinchasov, Y., Porat, R., Zur, B. & Dubinsky, Z. Photoacoustics: A novel tool for the determination of photosynthetic energy storage efficiency in phytoplankton. *Hydrobiologia* **579**, 251–256 (2007).

179. Akimoto, S. *et al.* Excitation relaxation dynamics and energy transfer in fucoxanthin–chlorophyll a/c-protein complexes, probed by time-resolved fluorescence. *Biochimica et Biophysica Acta (BBA) - Bioenergetics* **1837**, 1514–1521 (2014).

180. Millie, D. F., Schofield, O. M. E., Kirkpatrick, G. J., Johnsen, G. & Evens, T. J. Using absorbance and fluorescence spectra to discriminate microalgae. *Eur J Phycol* **37**, 313–322 (2002).

181. Burson, A., Stomp, M., Greenwell, E., Grosse, J. & Huisman, J. Competition for nutrients and light: testing advances in resource competition with a natural phytoplankton community. *Ecology* **99**, 1108–1118 (2018).

182. Hedlund, C. & Hagman, C. Phytoplankton in humic and colored Nordic lakes. *MINA fagrapport* 66.

183. Sullivan, C. W. Diatom mineralization of silicic acid. II. Regulation of $Si(OH)_4$ transport rates during the cell cycle of Navicula pelliculosa. *J Phycol* **13**(1), 86-91(1977).

184. Kulikovskiy, M., Lange-Bertalot, H., Witkowski, A. & Khursevich, G. Achnanthidium sibiricum (Bacillariophyceae), a new species from bottom sediments in Lake Baikal. *Arch Hydrobiol Suppl Algol Stud* (2011) doi:10.1127/1864-1318/2011/0136-0077.

185. Bedoshvili, Y. D. *et al.* Frustule morphogenesis of raphid pennate diatom Encyonema ventricosum (Agardh) Grunow. *Protoplasma* **255**, (2018).

186. Wang, J. K. & Seibert, M. Prospects for commercial production of diatoms. *Biotechnology for Biofuels* **10**, (2017).

187. Li, X. L. *et al.* A novel growth method for diatom algae in aquaculture waste water for natural food development and nutrient removal. *Water Science and Technology* **75**, 2777–2783 (2017).

188. Salimon, A. I., Everaerts, J., Sapozhnikov, P. V, Statnik, E. S. & Alexander, M. On Diatom Colonization of Porous UHMWPE Scaffolds. **II**, 4–8 (2018).

189. Holdsworth, E. S. Effect of growth factors and light quality on the growth, pigmentation and photosynthesis of two diatoms, Thalassiosira gravida and Phaeodactylum tricornutum. *Marine Biology 1985 86:3* **86**, 253–262 (1985).

190. Grigoryeva, N. & Chistyakova, L. Confocal Laser Scanning Microscopy for Spectroscopic Studies of Living Photosynthetic Cells. in *Color Detection* (eds. Zeng, L.-W. & Cao, S.-L.) Ch. 3 (IntechOpen, 2019). doi:10.5772/intechopen.84825.

191. Chang, C. W., Sud, D. & Mycek, M. A. Fluorescence Lifetime Imaging Microscopy. *Methods Cell Biol* **81**, 495–524 (2007).

192. Elson, D. *et al.* Biomedical Applications of Fluorescence Lifetime Imaging. *Opt Photonics News* **13**, 26 (2002).

193. Becker, W. Fluorescence lifetime imaging - techniques and applications. *J Microsc* **247**, 119–136 (2012).

194. Chen, L. C., Lloyd, W. R., Chang, C. W., Sud, D. & Mycek, M. A. *Fluorescence lifetime imaging microscopy for quantitative biological imaging*. *Methods in Cell Biology* vol. 114 (Elsevier Inc., 2013).

195. Korczyński, J. & Włodarczyk, J. [Fluorescence lifetime imaging microscopy (FLIM) in biological and medical research]. *Postepy Biochem* **55**, 434–40 (2009).

196. Bedoshvili, Y. D., Popkova, T. P. & Likhoshway, Y. V. Chloroplast structure of diatoms of different classes. *Cell tissue biol* **3**, 297–310 (2009).

197. Falkowski, P. G., Lin, H. & Gorbunov, M. Y. What limits photosynthetic energy conversion efficiency in nature? Lessons from the oceans. *Philosophical Transactions of the Royal Society B: Biological Sciences* **372**, 2–8 (2017).

198. Holzwarth, A. R. Fluorescence lifetimes in photosynthetic systems. *Photochemistry and Photobiology* vol. 43 707–725 (1986).

199. Lavaud, J. & Lepetit, B. An explanation for the inter-species variability of the photoprotective non-photochemical chlorophyll fluorescence quenching in diatoms. *Biochim Biophys Acta Bioenerg* **1827**, 294–302 (2013).

200. Bernard, S., Probyn, T. A. & Quirantes, A. *Simulating the optical properties of phytoplankton cells using a two-layered spherical geometry*. *Biogeosciences Discuss* vol. 6 (2009).

201. Mann, D.G. Chloroplast morphology, movements and inheritance in diatoms. In BR Chaudhary, SB Agrawal, eds, Cytology, Genetics and Molecular Biology of Algae. SPB Academic Publishing, Amsterdam, pp 249–274, 1996.

202. Wu, H., Roy, S., Alami, M., Green, B. R. & Campbell, D. A. Photosystem II photoinactivation, repair, and protection in marine centric diatoms. *Plant Physiol* **160**, 464–476 (2012).

203. Koedooder, C. *et al.* Diatom-bacteria interactions modulate the composition and productivity of benthic diatom biofilms. *Front Microbiol* **10**, (2019).

204. Amin, S. A., Parker, M. S. & Armbrust, E. V. Interactions between Diatoms and Bacteria. *Microbiology and Molecular Biology Reviews* **76**, 667–684 (2012).

205. Cirri, E. *et al.* Associated Bacteria Affect Sexual Reproduction by Altering Gene Expression and Metabolic Processes in a Biofilm Inhabiting Diatom. *Front Microbiol* **10**, (2019).

206. Michels, J., Vogt, J. & Gorb, S. N. Tools for crushing diatoms – opal teeth in copepods feature a rubber-like bearing composed of resilin. *Scientific Reports 2012 2:1* **2**, 1–6 (2012).

207. Korayem, M. H., Ebrahimi, N. & Sotoudegan, M. S. Frequency response of atomic force microscopy microcantilevers oscillating in a viscous liquid: A comparison of various methods. *Scientia Iranica* **18**, 1116–1125 (2011).

208. Laurent, J., Steinberger, A. & Bellon, L. Functionalized AFM probes for force spectroscopy: Eigenmode shapes and stiffness calibration through thermal noise measurements. *Nanotechnology* **24**, (2013).

209. Sancetta, C. Three species of Coscinodiscus Ehrenberg from North Pacific sediments examined in the light and scanning electron microscopes. *Micropaleontology* **33**, 230–241 (1987).

210. Gogorev, R. M., Chudaev, D. A., Stepanova, V. A. & Kulikovskiy, M. S. Russian and English terminological glossary on morphology of diatoms. *Nov Sist Nizs Rast* **52**, 265–309 (2018).

211. Tesson, B. & Hildebrand, M. Characterization and Localization of Insoluble Organic Matrices Associated with Diatom Cell Walls: Insight into Their Roles during Cell Wall Formation. *PLoS One* **8**, e61675 (2013).

212. Loboda, V. V & Salamatova, U. V. CAPACITIVE MEMS MICROPHONES FOR MEDICAL APPLICATIONS. *Computing, Telecommunications and Control* **14**, 65–78 (2021).

213. Zawawi, S. A., Hamzah, A. A., Majlis, B. Y. & Mohd-Yasin, F. A review of MEMS capacitive microphones. *Micromachines* vol. 11 Preprint at https://doi.org/10.3390/MI11050484 (2020).

214. Heuberger, M., Dietler, G. & Schlapbach, L. Mapping the local Young's modulus by analysis of the elastic deformations occurring in atomic force

microscopy I Mapping the local Young's modulus by analysis of the elastic deformations occurring in atomic force microscopy. *Nanotechnology* **6**, (1995).

215. Butt, H. J., Cappella, B. & Kappl, M. Force measurements with the atomic force microscope: Technique, interpretation and applications. *Surface Science Reports* vol. 59 1–152 (2005).

216. Mei, H. *et al.* Effects of water on the mechanical properties of silica glass using molecular dynamics. *Acta Mater* **178**, 36–44 (2019).

217. Bhushan, B. & Koinkar, V. N. Nanoindentation hardness measurements using atomic force microscopy. *Appl Phys Lett* **64**, 1653 (1998).

218. Garcia, R. & Proksch, R. Nanomechanical mapping of soft matter by bimodal force microscopy. *Eur Polym J* **49**, 1897–1906 (2013).

219. García, R. & Pérez, R. Dynamic atomic force microscopy methods. *Surf Sci Rep* **47**, 197–301 (2002).

220. Hu, S. & Raman, A. Analytical formulas and scaling laws for peak interaction forces in dynamic atomic force microscopy. *Appl Phys Lett* **91**, (2007).

221. Hölscher, H. Quantitative measurement of tip-sample interactions in amplitude modulation atomic force microscopy. *Appl Phys Lett* **89**, (2006).

222. Bielefeldt, H. & Giessibl, F. J. A simplified but intuitive analytical model for intermittent-contact-mode force microscopy based on Hertzian mechanics. *Surf Sci* **440**, L863–L867 (1999).

223. Niu, X., Dong, G., Li, X., Geng, X. & Zhou, J. Effect of indentation depth and strain rate on mechanical properties of Sn0.3Ag0.7Cu. *Microelectronics Reliability* **128**, 114429 (2022).

224. Melnikov, Y. A. Influence Functions of a Point Force for Kirchhoff Plates with Rigid Inclusions. *Journal of Mechanics* **20**, 249–256 (2004).

225. Todorović, D. *et al.* Multilayer graphene condenser microphone. *2d Mater* **2**, (2015).

226. Baglioni, G. *et al.* Ultra-sensitive graphene membranes for microphone applications. *Nanoscale* **15**, 6343–6352 (2023).

227. Korsunsky, A. M. The influence of punch blunting on the elastic indentation response. *J Strain Anal Eng Des* **36**, 391–400 (2001).

228. Korsunsky, A. M. & Constantinescu, A. The influence of indenter bluntness on the apparent contact stiffness of thin coatings. *Thin Solid Films* **517**, 4835–4844 (2009).

229. Korsunsky, A. M. & Constantinescu, A. Work of indentation approach to the analysis of hardness and modulus of thin coatings. *Materials Science and Engineering: A* **423**, 28–35 (2006).

230. Podsiadlo, P. *et al.* Ultrastrong and stiff layered polymer nanocomposites. *Science (1979)* **318**, 80–83 (2007).

231. Stanimirović, Z. & Stanimirović, I. Mechanical Properties of MEMS Materials. in *Micro Electronic and Mechanical Systems* (ed. Takahata, K.) Ch. 11 (IntechOpen, 2009).

232. Stanimirović, Z. & Stanimirović, I. Mechanical Properties of MEMS Materials. in *Micro Electronic and Mechanical Systems* (ed. Takahata, K.) (IntechOpen, 2009). doi:10.5772/7010.

233. Pan, J., Cai, J., Zhang, D., Wang, Y. & Jiang, Y. Micro-arraying of nanostructured diatom microshells on glass substrate using ethylene-vinyl

acetate copolymer and photolithography technology for fluorescence spectroscopy application. *Physica E Low Dimens Syst Nanostruct* **44**, 1585–1591 (2012).

234. Jeffryes, C., Campbell, J., Li, H., Jiao, J. & Rorrer, G. The potential of diatom nanobiotechnology for applications in solar cells, batteries, and electroluminescent devices. *Energy and Environmental Science* vol. 4 3930–3941 Preprint at https://doi.org/10.1039/c0ee00306a (2011).

235. Parkinson, J. & Gordon, R. Beyond micromachining: the potential of diatoms. *Trends Biotechnol* **17**, 190–196 (1999).

236. Simovic-Pavlovic, M., Bokic, B., Vasiljevic, D. & Kolaric, B. Bioinspired NEMS—Prospective of Collaboration with Nature. *Applied Sciences (Switzerland)* **12**, (2022).

237. Ackerman, E. Resonances of biological cells at audible frequencies. *The bulletin of mathematical biophysics* 13, 93-106 (1951).

238. Zinin, P. V., Allen, J. S. & Levin, V. M. Mechanical resonances of bacteria cells. *Phys Rev E Stat Nonlin Soft Matter Phys* **72**, (2005).

239. Zinin, P. V. & Allen, J. S. Deformation of biological cells in the acoustic field of an oscillating bubble. *Phys Rev E Stat Nonlin Soft Matter Phys* **79**, (2009).

240. Ford, L. H. Estimate of the vibrational frequencies of spherical virus particles. *Phys Rev E Stat Phys Plasmas Fluids Relat Interdiscip Topics* **67**, 3 (2003).

241. Miller, D.K. Effects of a High-Amplitude l-MHz Standing Ultrasonic Field on the Algae Hydrodictyon. *IEEE Trans Ultrason Ferroelectr Freq Control.* **33**, 165-170, (1986).

242. Gutiérrez, A., Gordon, R. & Dávila, L. P. Deformation Modes and Structural Response of Diatom Frustules. *Journal of Materials Science and Engineering with Advanced Technology* **15**, 105–134 (2017).

243. Shah, M. A., Shah, I. A., Lee, D. G. & Hur, S. Design approaches of MEMS microphones for enhanced performance. *Journal of Sensors* vol. 2019 (2019).

244. Williams, M. D., Griffin, B. A., Reagan, T. N., Underbrink, J. R. & Sheplak, M. An AlN MEMS piezoelectric microphone for aeroacoustic applications. *Journal of Microelectromechanical Systems* **21**, 270–283 (2012).

245. Putman, C. A. J., De Grooth, B. G., Van Hulst, N. F. & Greve, J. A detailed analysis of the optical beam deflection technique for use in atomic force microscopy. *J Appl Phys* **72**, 6–12 (1992).

246. Gordon, R. & Tiffany, M. A. Possible Buckling Phenomena in Diatom Morphogenesis. in *The Diatom World* (eds. Seckbach, J. & Kociolek, P.) 245–271 (Springer Netherlands, 2011).

247. Kieu, K. *et al.* Structure-based optical filtering by the silica microshell of the centric marine diatom Coscinodiscus wailesii. *Opt Express* **22**, 15992 (2014).

248. Kotilainen, T. *et al.* Patterns in the spectral composition of sunlight and biologically meaningful spectral photon ratios as affected by atmospheric factors. *Agric For Meteorol* **291**, 108041 (2020).

249. Kim, M.-S. *et al.* Fractional Talbot imaging of phase gratings with hard x rays. *J. Lightwave Technol* vol. 25 (2008).

250. Rayleigh, Lord. XXV. On copying diffraction-gratings, and on some phenomena connected therewith . *The London, Edinburgh, and Dublin Philosophical Magazine and Journal of Science* **11**, 196–205 (1881).

251. Ghobara, M., Oschatz, C., Fratzl, P. & Reissig, L. Numerical Analysis of the Light Modulation by the Frustule of Gomphonema parvulum: The Role of Integrated Optical Components. *Nanomaterials* **13**, (2023).

252. Hermanowicz, P., Banaś, A. K., Sztatelman, O., Gabryś, H. & Łabuz, J. UV-B Induces Chloroplast Movements in a Phototropin-Dependent Manner. *Front Plant Sci* **10**, (2019).

253. Furukawa, T., Watanabe, M. & Shihira-Ishikawa, I. Green- and blue-light-mediated chloroplast migration in the centric diatomPleurosira laevis. *Protoplasma* **203**, 214–220 (1998).

254. Sakai, Y. & Takagi, S. Roles of actin cytoskeleton for regulation of chloroplast anchoring. *Plant Signal Behav* **12**, (2017).

255. Yeh, Y. C., Creran, B. & Rotello, V. M. Gold nanoparticles: Preparation, properties, and applications in bionanotechnology. *Nanoscale* **4**, 1871–1880 (2012).

256. Sau, T. K., Rogach, A. L., Jäckel, F., Klar, T. A. & Feldmann, J. Properties and applications of colloidal nonspherical noble metal nanoparticles. *Advanced Materials* **22**, 1805–1825 (2010).

257. Xu, R. X. Multifunctional microbubbles and nanobubbles for photoacoustic imaging. *Contrast Media Mol Imaging* **6**, 401–411 (2011).

258. Amendola, V., Pilot, R., Frasconi, M., Maragò, O. M. & Iatì, M. A. Surface plasmon resonance in gold nanoparticles: A review. *Journal of Physics Condensed Matter* **29**, (2017).

259. Cheheltani, R. *et al.* Tunable, biodegradable gold nanoparticles as contrast agents for computed tomography and photoacoustic imaging. *Biomaterials* **102**, 87–97 (2016).

260. Miller, M. M. & Lazarides, A. A. Sensitivity of metal nanoparticle plasmon resonance band position to the dielectric environment as observed in scattering. *Journal of Optics A: Pure and Applied Optics* **8**, 21556–21565 (2006).

261. Salopek, B., Krasic, D. & Filipovic, S. Measurement and application of zeta-potential. *Rudarsko-geolosko-naftni zbornik* **4**, 147–151 (1992).

262. Yashchenok, A. M. *et al.* Impact of magnetite nanoparticle incorporation on optical and electrical properties of nanocomposite LbL assemblies. *Physical Chemistry Chemical Physics* **12**, 10469–10475 (2010).

263. Bédard, M. F. *et al.* On the mechanical stability of polymeric microcontainers functionalized with nanoparticles. *Soft Matter* **5**, 148–155 (2009).

264. Yashchenok, A. M., Inozemtseva, O. A., Gorin, D. A. & Khlebtsov, B. N. Effect of the size of colloidal gold nanoparticles on the physical parameters of nanocomposite microcapsule shells. *Colloid Journal* **71**, 422–429 (2009).

265. Esenaliev, R. O. Optoacoustic monitoring of physiologic variables. *Front Physiol* **8**, 1–6 (2017).

266. Jokerst, J. V., Thangaraj, M. & Gambhir, S. S. Photoacoustic imaging of mesenchymal stem cells in living mice via silica-coated gold nanorods. in *Photons Plus Ultrasound: Imaging and Sensing 2014* (eds. Oraevsky, A. A. & Wang, L. V.) vol. 8943 89431O (SPIE, 2014).

267. Chen, Y., Xu, C., Cheng, Y. & Cheng, Q. Photostability enhancement of silica-coated gold nanostars for photoacoustic imaging guided photothermal therapy. *Photoacoustics* **23**, 100284 (2021).

268. Chen, Y. S. *et al.* Silica-coated gold nanorods as photoacoustic signal nanoamplifiers. *Nano Lett* **11**, 348–354 (2011).

269. He, X. N. *et al.* Surface-enhanced Raman spectroscopy using gold-coated horizontally aligned carbon nanotubes. *Nanotechnology* **23**, (2012).

270. Watanabe, H., Hayazawa, N., Inouye, Y. & Kawata, S. DFT vibrational calculations of Rhodamine 6G adsorbed on silver: Analysis of tip-enhanced Raman spectroscopy. *Journal of Physical Chemistry B* **109**, 5012–5020 (2005).

271. Le Ru, E. C., Blackie, E., Meyer, M. & Etchegoint, P. G. Surface enhanced raman scattering enhancement factors: A comprehensive study. *Journal of Physical Chemistry C* **111**, 13794–13803 (2007).

272. Chen, J. *et al.* A synergistic combination of diatomaceous earth with Au nanoparticles as a periodically ordered, button-like substrate for SERS analysis of the chemical composition of eccrine sweat in latent fingerprints. *J Mater Chem C Mater* **3**, 4933–4944 (2015).

273. Caridad, J. M. *et al.* Hot-Volumes as Uniform and Reproducible SERS-Detection Enhancers in Weakly-Coupled Metallic Nanohelices. *Sci Rep* **7**, (2017).

274. Gilic, M., Ghobara, M. & Reissig, L. Tuning SERS Signal via Substrate Structuring: Valves of Different Diatom Species with Ultrathin Gold Coating. *Nanomaterials* **13**, (2023).

275. Kim, H. S., Devarenne, T. P. & Han, A. Microfluidic systems for microalgal biotechnology: A review. *Algal Res* **30**, 149–161 (2018).

276. Mesquita, P., Gong, L. & Lin, Y. Low-cost microfluidics: Towards affordable environmental monitoring and assessment. FRLCT **1**, (2022).

277. Campos, C. D. M. & da Silva, J. A. F. Applications of autonomous microfluidic systems in environmental monitoring. *RSC Adv* **3**, 18216–18227 (2013).

278. Aslan Kamil, M. *et al.* An image-guided microfluidic system for single-cell lineage tracking. *PLoS One* **18**, e0288655- (2023).

279. Girault, M., Beneyton, T., del Amo, Y. & Baret, J.-C. Microfluidic technology for plankton research. *Curr Opin Biotechnol* **55**, 134–150 (2019).

280. Luo, C. *et al.* High-throughput microfluidic system for monitoring diffusion-based monolayer yeast cell culture over long time periods. *Biomed Microdevices* **11**, 981–986 (2009).

281. Bedoshvili, Y. D. & Likhoshway, Y. V. *Changing of silica valves of diatom Synedra acus subsp. radians influenced by paclitaxel Bacillariophyta* Tsitologiya **59**(1), 53-61 (2017).

282. Tomba, J. P., Arzondo, L. M. & Pastor, J. M. Depth Profiling by Confocal Raman Microspectroscopy: Semi-empirical Modeling of the Raman Response. *Applied Spectroscopy* 61, (2007).